IMPROVED UNDERSTANDING AND CONTROL OF HIGH-SPEED JET INTERACTION FLOWS

A Dissertation

by

RAVICHANDRA SRINIVASAN

Submitted to the Office of Graduate Studies of
Texas A&M University
in partial fulfillment of the requirements for the degree of

DOCTOR OF PHILOSOPHY

December 2005

Major Subject: Aerospace Engineering

IMPROVED UNDERSTANDING AND CONTROL OF HIGH-SPEED JET INTERACTION FLOWS

A Dissertation

by

RAVICHANDRA SRINIVASAN

Submitted to the Office of Graduate Studies of
Texas A&M University
in partial fulfillment of the requirements for the degree of

DOCTOR OF PHILOSOPHY

Approved by:

Chair of Committee,	Rodney D. W. Bowersox
Committee Members,	Sharath S. Girimaji
	Paul Cizmas
	Simon North
Head of Department,	Helen Reed

December 2005

Major Subject: Aerospace Engineering

ABSTRACT

Improved Understanding and Control of
High-Speed Jet Interaction Flows. (December 2005)
Ravichandra Srinivasan, B. E., Bangalore University;
M.S., The University of Alabama
Chair of Advisory Committee: Dr. Rodney D. W. Bowersox

A numerical study of the flow field generated by injection through diamond-shaped orifices into a high-speed flow is presented in this document. Jet interaction flows have a wide range of applications in the field of engineering. These applications include the use of jets for fuel injection in scramjets, for reaction control of high-speed aerodynamic bodies and as cooling jets for skins of high-speed vehicles. A necessary requirement in the use of transverse jets for these and other applications is a thorough understanding of the physics of the interaction between the jet and freestream. This interaction generates numerous flow structures that include multiple shocks, vortices, recirculation regions and shear layers. This study involves diamond-shaped orifices that have the advantage of generating weaker or attached interaction shocks as compared to circular injectors. These injectors also negate the effects due to the recirculation region that is formed upstream of the injector. This study was undertaken in order to gain further understanding of the flow features generated by diamond-shaped injectors in a high-speed flow.

Numerical simulations were performed using two different levels of turbulence models. Reynolds' Averaged Navier-Stokes (RANS) simulations were performed using the GASP flow solver while Detached-Eddy Simulation (DES) runs were performed using the Cobalt flow solver. A total of fifteen diamond injector simulations were performed using the RANS model for a 15° half-angle diamond injector. The

fifteen simulations spanned over five different injection angles and three jet total pressures. In addition to these, two circular injector simulations were also performed. In addition, low pressure normal injection through diamond and circular orifices simulations were performed using DES. Results obtained from CFD were compared to available experimental data. The resulting flow structure and the turbulent properties of the flow were examined in detail. The normal injection case through the diamond-shaped orifice at the lowest jet total pressure was defined as the baseline case and is presented in detail. In order to study the effect of different components of the vorticity transport equation, an in-house code was used post-process the results from the RANS runs.

ACKNOWLEDGEMENTS

I would like to record my grateful thanks to my research advisor, Dr. Rodney Bowersox, for his guidance and motivation. He has always been accessible and the patience that he demonstrated during the times that I faltered on the course of this work has been invaluable. I greatly appreciate the time that he spent with me in his office in discussing the direction, goal and impact of this research. The conversations that we had on topics in engineering and various other areas were very informative and enjoyable.

I would also like to thank the members of my committee: Dr. Sharath Girimaji, Dr. Paul Cizmas and Dr. Simon North. I have found them to be a source of encouragement and their insight into various aspects of this research has been extremely helpful.

This work would not have been possible without the help of the people at AeroSoft Inc. and Cobalt LLC. Dr. Reece Neel has been a source of great help over the years in guiding me in the use of the GASP flow solver. I have also benefited from the assistance of Dr. James Forsythe in the use of Cobalt and in the generation of unstructured grids. I am indebted to Dr. Craig Hunter and Dr. Shahyar Pirzadeh at NASA for their help in providing the software for the generation of unstructured grids.

The support that I received from my colleagues Huiago Fan, Zakaria Mahmud, Daina Lee, Isaac Ekoto, Dipankar Sahoo, Justin McClellan and Jason Garcia is appreciated. My sincere thanks to Karen Knabe, without whom I would not have been able to finish the paperwork required for this degree.

Finally, I must thank the Air Force Office of Scientific Research and Dr. John Schmisseur for providing the financial support for this research.

TABLE OF CONTENTS

CHAPTER Page

LIST OF FIGURES

FIGURE Page

FIGURE Page

FIGURE Page

FIGURE Page

FIGURE Page

FIGURE Page

CHAPTER I

INTRODUCTION

Background

Since the invention of powered flight, there has been a progression towards faster speeds and greater range in the design requirements of aircraft. An elusive goal has been the ability to fly at hypersonic speeds in aircraft powered by air-breathing engines. Hypersonic speeds are generally defined as speeds greater than five times the speed of sound. Hypersonic flight has numerous potential civilian, military and space applications. A vehicle traveling at hypersonic speeds would be able to provide reliable access to space at reduced cost. Military applications include long range bombers and interceptor missiles. Eventual applications could be in the form of civilian transport aircraft for intercontinental travel.

Research in Hypersonic Airbreathing Propulsion

Hypersonic vehicles, powered by air-breathing propulsion systems, are one of the remaining challenges of high-speed atmospheric flight. During the last two decades there has been resurgent interest in hypersonic research. The National Aerospace Plane (NASP) program was initiated in the 1980s to pursue a hypersonic vehicle development program. The goals of the NASP program required the vehicle to use air-breathing propulsion to accelerate and cruise at hypersonic speeds. The aircraft had to be versatile in its performance so that it could be used for intercontinental travel or enter low earth orbit. In order to achieve this goal, the vehicle's speed had to range from Mach 0 to 25. To operate in the lower Mach number range, efficient

---

This dissertation follows the style of *AIAA Journal*.

subsonic propulsion and aerodynamics were required. The NASP project vehicle, designated X-30, is shown in Fig. 1. The scientific and engineering challenges posed by the requirements of NASP, coupled with substantial increase in budgets and implementation delays led to termination of the program.

NASP has been replaced by the National Aerospace Initiative (NAI). It is an alliance between various governmental organizations including the Department of Defense (DoD) and National Aviation and Space Administration (NASA). The following is an excerpt from the congressional report on NAI.

> The NAI is an integrated, nationally planned and executed science and technology (S&T) development and demonstration initiative focused on solving and demonstrating the fundamental physics associated with advanced high-speed/hypersonic airbreathing systems, advanced rocket systems, and space-based payloads — offering a truly revolutionary advancement in warfighting capability and our ability to utilize space.

The focus areas of the NAI are hypersonic/high-speed research, space access, and space technology. The hypersonic/high-speed research involves development of expendable and reusable technologies. Expendable technologies include supersonic and hypersonic missiles. Under the reusable technology category is the development of long-range strike vehicles and single-state-to-orbit (SSTO) and two-stage-to-orbit (TSTO) propulsion systems.

Various programs have been initiated under the umbrella of NAI. The USAF's HyTech program has the specific goal of developing an expendable liquid hydrocarbon fueled propulsion system. The engine should be able to propel a vehicle to speeds between Mach 4.0 - 8.0. A near term use for this kind of propulsion system

would be in a long-range air-to-surface missile. The Hypersonic Flight Demonstration program (HyFly) is a US Navy endeavor to demonstrated hypersonic flight technology. The eventual goal of this program is a vehicle with a range of 600 nautical miles and cruise speed of about Mach 6.0. Like the HyTech program, the propulsion system will use liquid hydrocarbons as fuel.

The Hyper-X program, under the aegis of NASA, aims to demonstrate a hypersonic vehicle that has a propulsion system powered by hydrogen. The motivation for NASA is to eventually find a replacement for the aging space shuttle fleet. There are three flight demonstration vehicles in the Hyper-X program, the X-43A, X-43B and X-43C. Figure 2 shows a sketch of the X-43 flight demonstration vehicle and also results from a Computational Fluid Dynamics (CFD) simulation of the vehicle. It is an unmanned aircraft powered by hydrogen fuel and expected to fly between Mach 7.0 and Mach 10.0. The initial test of the X-43A flight vehicle failed in 2002 due to a malfunction in the booster. Two successive tests were performed in March and November 2004 in which the flight vehicle reached speeds of Mach 6.8 and 9.6 respectively.

Research in airbreathing hypersonic propulsion is being pursued by other nations around the world. Australia, under the HyShot initiative, successfully flight-tested a Mach 7.6 hypersonic vehicle in 2002. France has ground-tested hypersonic propulsion engines at Mach 6.0 - 7.5. In Asia, countries like Japan, China, and India are also involved in hypersonics research.

Scientific and Engineering Challenges

There are significant challenges that have to be overcome to achieve goals outlined in previous sections. Some of these challenges are listed below.

- Efficient propulsion.
- Thermal management at high-speeds.
- Integration and control of the airframe.
- Structural designs and materials capable of achieving desired strength to weight ratio.

Jet injection has the potential to address many engineering problems in high-speed flow. Specifically, these include fuel injection in scramjets, control of high-speed vehicles, film cooling of components such as gas turbine blades. However, a fundamental understanding of the flowfield physics of transverse jet injection into high-speed flows is required prior to its application to any of the afore mentioned problems.

The flowfield generated by transverse injection into a high-speed flow has been the subject of numerous investigations[1–7]. The flow field generated by injection through a circular orifice is show in Figure 3. As indicated the flow is characterized by numerous shocks and secondary flow structures. The first flow feature encountered in the streamwise direction is the interaction or bow shock produced as a result of the freestream impacting on the injector streamtube. For injector configurations, where δ/d_{eff} is on the order of one or more, a separation region and lambda shock form upstream of the injector port. A horseshoe vortex forms between the jet and the interaction shock. After entering the freestream, the underexpanded jet undergoes a rapid Prandtl-Meyer expansion surrounded by a barrel shock. A shock wave normal to the jet path known as the Mach disk, terminates the barrel shock, and compresses the flow to the effective back-pressure. Downstream of the Mach disk, a counter rotating vortex pair forms within the jet plume. Wake

vortices are also formed. The plume vorticity and turbulent mechanisms induce the required large scale mixing between the jet fluid and the freestream.

Transverse injection of jets into high-speed flows has numerous applications in aerospace engineering. Three relevant applications are discussed below.

Supersonic Combustion Ramjets

The most promising candidate for air breathing, hypersonic propulsion systems is the Supersonic Combustion Ramjet (Scramjet). Research in Scramjets started in the 1950s as an extension of Ramjet engines. Pioneering work was done in the United States by Antonio Ferri at the Brooklyn Polytechnic Institute and General Applied Science Laboratories (GASL). During the same time period, research was also being conducted at Johns Hopkins University's Applied Physics Laboratory and at McGill University.

The components of a Scramjet engine are shown schematically in Figure 4[8]. A Scramjet works on the same principles as that of a ramjet i.e., air is compressed as it passes across a shock wave that is generated by the vehicle. Fuel is injected into this compressed air and the mixture is burned. The exhaust products of combustion are then made to exit the engine through a nozzle at the back. The crucial difference between a Scramjet and Ramjet is that the air inside the combustor is traveling at subsonic speeds in the Ramjet whereas in the Scramjet it is supersonic. This creates substantial problems in designing an efficient engine. The supersonic air flowing through the combustor has a transit time of 2 ms to 3 ms. Fuel has to be injected, mixed efficiently and burned within this short period of time. Thermal management of the system also poses significant challenges. To be able to reach speeds higher than Mach 8, the outer shell of the vehicle has to be actively cooled.

Advanced materials with the capability of withstanding the harsh flight environment have to be developed. Thrust margins for current designs are fairly small. Any design change must take into account the impact on the drag of the engine.

Reaction Control

Transverse control jets are viable alternatives to using aerodynamic surfaces especially under conditions where dynamic pressures are low enough to affect proper aerodynamic surface control. Numerous applications of this technique include rapid maneuvering of high-speed missiles and attitude control of hypersonic vehicles. Other applications also include use in thrust-vectoring nozzles of combat aircraft for greater agility. An understanding of the flowfield generated by transverse injection into high-speed flows is essential for proper design of reaction control jets.

Flow Control

In situations where flight vehicles have to operate under off-design conditions, flow control becomes necessary in order to maintain adequate performance. For example, a scramjet whose inlet is designed for specific flight conditions will perform poorly under off design conditions since the inlet shock will no longer be incident on the cowl lip. It is possible to use transverse jet injection to modify flow characteristics and force the inlet shock back to the intended position. Transverse jets, arranged in specific topologies, have also been used as aerodynamic ramps to increase penetration and mixing within a scramjet. Helium injection through slots has been used to achieve structural reorganization of hypersonic boundary layers.[9] The current leading candidate for flame holding within scramjets is the wall cavity

flame concept.[10;11] This concept has proven effective, however, the cavity induces flow unsteadiness and the cavity has to endure a very harsh environment.

Research Objectives

As mentioned above, the flowfield generated by transverse injection is dominated by strong secondary flow features and viscous-inviscid interactions. Improved understanding of the secondary flow structure, production mechanisms and receptivity to manipulation may offer an opportunity for active or passive control. Hence, the primary research goal of this study is the improved understanding and control of the secondary motion in high-speed jet interaction flowfields. High-fidelity experimental characterization is prohibitively time consuming, especially for parametric studies. Thus, a multi-fidelity numerical approach is undertaken in order to achieve the research goal. This research is part of an Air Force sponsored project on hypersonic jet-interaction flows that includes a Mach 5.0 experimental study. Hence, that experimental configuration was chosen as the test bed for the present study. An added benefit of this is the availability of experimental data for comparison. The contributions of this work to the field of jet interaction flows include

- Evaluation of two-equation and DES turbulence models (chapter V).
- Flowfield understanding using simulation and visualisation tools (chapter VI).
- Quantification of the generation and transport of vorticity (chapter VII).
- Identification of controllable flow features (chapter VIII).
- Parametric database for engineering purposes comprising of information for various injection angles and jet total pressures (chapter VI and appendices).

CHAPTER II

LITERATURE REVIEW

Jet-Into-A-Cross-flow

Injection into a cross-flow is a fundamentally important flow field that has implications across a myriad of military and civil disciplines. Thus, numerous experimental studies, primarily at low-speeds, have been performed to quantitatively assess the mean flow field and qualitatively examine the instantaneous vortical flow features[12–14]. However, studies that contain turbulence data suitable for flow field understanding are exceedingly scarce[14]. Furthermore, the available mean and turbulence data for supersonic flows are also limited. However, some studies were found, and the results of which are integrated into the following the discussions. Hypersonic jet-interaction studies are virtually non-existent.

Injection into a low-speed cross-flow produces a complex flow with at least four distinguishable vortical flow characteristics (Fig. 3). As the jet emerges into the cross-flow, it is curved downstream by the cross-flow. The jet plume cross-section evolves into a cardioidal or “kidney-bean” shape. The counter-rotating vortex pair within the plume is responsible for the distorted plume shape. A number of flow mechanisms are responsible for generating this secondary flow. For example, turning of the flow into the downstream direction creates a pressure gradient across the flow that induces vortical motion. Lateral shearing along the plume edges also contributes to the vorticity. The jet-free stream interaction (separation) creates a horseshoe vortex similar to that of a wing-body junction on an aircraft. The third vortex system consists of jet-shear layer vortices. Lastly, a fourth wake vortex system exists. Until recently, the formation of this unsteady vortex phenomenon had

been attributed to vortex shedding similar the Karman-vortex wake of a cylinder in a cross-flow. Since visualization was possible only by seeding the boundary layer, it was reasoned[15]that the vortices were the result of upstream boundary layer vorticity being transported up into the wake. The process is believed to be the result of "separation event" and eruptions of the boundary layer fluid and vorticity into "tornado-like" structures that begin at the wall and are entrained into the jet flow. However, evidence contradicting this hypothesis has also been presented. For example, the planar laser induced fluorescence concentration measurements[16], show signs of the structures. However in that study, only the jet flow was seeded. Hence, these data may suggest that these structures could in part emanate from the jet and not the wall. Adding to this apparent dilemma, three possible scenarios leading to the formation of the wake vortex system have been suggested[17]. These unsteady phenomena can be very important for future flow control algorithms.

For high-speed flows, the mean flow features are similar to those described above. However, compressibility creates additional features that do not have incompressible counterparts. For example, perpendicular injection of an underexpanded sonic or supersonic jet into a supersonic free stream produces several flow structures. The first of these is a bow shock produced as the free stream impacts the injection streamtube; in this respect the injectant acts as a solid cylindrical body[18]. For injector configurations where injector diameter is greater than the boundary layer thickness, a separation bubble and a lambda shock form slightly upstream of the injector port[1]. After entering the free stream, the jet experiences a rapid Prandtl-Meyer expansion (usually assumed to be an isentropic process) surrounded by a barrel shock[19]. A shock normal to the jet path, known as the Mach disk, terminates the barrel shock, and compresses the flow to the appropriate (i.e., effective) back pressure. As the free stream flow wraps around the jet,

a recompression shock is created. Recent CFD calculations[2] indicate that the recompression shock creates an addition counter-rotating vortex pair that eventually engulfs the original jet induced pair discussed above.

Angled injection is a means of reducing total pressure loss. In either normal or angled injection, the entry of the injectant jet into the mainstream flow can be regarded as a two-stage process[1]. The jet first enters the main flow and remains relatively intact as it expands to the height of the Mach disk. Beyond the Mach disk, the flow turns coaxial to, and accelerates with, the main flow. In the second stage, the jet acts as a coaxial vortex mixing structure. It is this feature that may be useful for boundary layer control (i.e., drag reduction).

During a rather extensive literature review, only a very limited number of studies on injection flows were found that included turbulence measurements. Results from Andreopoulus and Rodi[20], Fric and Roshko[21], Kamotani and Greber[12] were identified for low speed flows and for high-speed flows, the McCann and Bowersox[3] and Bowersox[22] Mach 3.0 studies were located. This finding is consistent with other surveys[14]. Hence, the turbulent flow physics of the injection into a cross-flow are significantly less understood than their mean flow counterpart. However, some limited qualitative insight into the overall structure can be gleaned from the available data. For example the axial turbulence intensity contour plots of Kamotani and Greber[12] indicated that two peaks in the intensity levels existed across the plume. In addition, the peaks were roughly co-located with each of the vortices of the counter rotating vortex pair. Investigating a high-speed angled injection case, McCann and Bowersox[3] found that the turbulent kinetic energy also had two peaks, which were roughly, located just below each vortex with the vortex pair. They deduced that the increased strain rates due to the secondary vortex flow resulted in an increased production of the turbulent kinetic energy. The data of McCann and

Bowersox also demonstrated that the $x-y$ turbulent shear stresses peaked along the plume centerline, and the x-z shear stresses were highly asymmetrical. However, as suggested by Cantwell, the peak turbulence levels along the jet centerline may be the result of an unsteady movement of the vortex pair. It is also important to mention here that a number of experimental studies show an asymmetry in the mean flow. Further, the numerical simulation of a shocked jet also showed signs of an asymmetry. Three possible scenarios have been presented to explain the generation of the asymmetry[22]. The incompressible data of Andreopoulus and Rodi[20] presented the axial variation of the $x-y$ and $x-z$ turbulent shear stresses for two spanwise locations. Unfortunately, the spatial resolution of that study was sparse; hence, only limited quantitative information was available. However, those data showed trends in the turbulence decay rates. Though the limited data available in the literature, in conjunction with a current understanding of the mean flow field, can provide a qualitative impression of the turbulent flow structure, studies with enough detail for turbulence model development and validation are virtually non-existent. This conclusion is supported by the review of Margason[14], and it was also the consensus during the General Discussion session following a recent AGARD meeting (General Discussion, 1993) among a number of key international researchers. Further, Chui et al.[23] and Alverez et al.[24] both indicated that turbulence modeling was the limiting key factor in determining the accuracy of their numerical predictions. Hence, detailed experimental studies are required to develop turbulence models for design applications.

Different injector cross-section geometries have been studied, both numerically and experimentally. It has been found[25] that wedge shaped orifice provide better perfomance in scramjet combustors. Experimental mixing studies have been perfomed using a novel aerodynamic ramp concept at Virgina Polytechnic Institute

and State University[26]. Numerical simulations[27] have also been performed to study the effectiveness of using a aerodynamic ramp to alleviate the effects of nose-down pitching moments. A series of sonic jet injection into a Mach 5.0 freestream was perfomed by Bowersox et al[28]. Diamond shaped injectors were used in this study. This was done in order to reduce the total pressure losses associated with stronger interaction shocks that are generated by circular injectors. Numerous mean flow measurements were performed including five-hole probe measurements of span wise pressure distribution and Mach number at two different axial locations, surface pressure measurements using pressure sensitive paint, surface oil flow and shadowgraph. Particle image velocimetry was used to study the flow along a lateral plane passing through the center of the jet. Turbulence measurements were not reported from this study. A total of three different jet total pressures and five injection angles were used in this series of experiments. It was found that the separation region upstream of the injector grows smaller with decreasing injection angle. A study of total pressure loss based on the interaction shock shape showed that the losses associated with low angled injection were smaller when compared to angled injection.

Overview of Current Prediction Methods

Currently, engineers and scientists rely on an approximate form the governing equations of motion to predict the overall mean flow character of these flows. The Reynolds and Favre averaged forms of the Navier-Stokes equations are universally used to compute low-speed and high-speed flows, respectively.

Associated with the averaging procedure is the requirement for accurate turbulence models. Currently, industry standard eddy viscosity gradient transport

turbulence models, such as Baldwin-Lomax algebraic and $k - \epsilon$ two equation, are extended to more complex flows on an ad hoc basis. However, as discussed in Wilcox[29], current eddy viscosity models are not accurate for three-dimensional, vortex-dominated flows. As discussed in section 2.1, the jet into a cross-flow flow field is dominated by numerous three-dimensional vortex systems; thus, the current prediction methods are not accurate.

In a numerical study of injection into a cross-flow, Chui et al.[23] noted that the predictions of the flow with the eddy viscosity Baldwin-Lomax and Baldwin-Barth models "... compared no better with the experimental data than the laminar flow computation." Alverez et al.[24] reported similar shortcomings. In a survey of 333 articles that covered a 50-year era, Margason (1993)[14] concluded that there is a need for high quality, high fidelity experimental data that will allow for verification of current and future computational fluid dynamic results and to define the unsteady flow characteristics. Also, the during the General Discussion, following the 1993 AGARD (General Discussion, 1993) conference, entitled Computational and Experimental Assessment of Jets in a Cross-flow, there was some surprise that more detailed and high fidelity Laser Doppler and Particle Image Velocimetry data were not available for turbulence model development and evaluation.

Some of the short comings in the availability of turbulence data from experiments may be addressed by the use of higher-order numerical simulations such as DNS and LES/DES. Large-eddy simulations of a low speed, low Reynolds number transverse jet injection from a circular orifice indicate that the farfield CVP is formed due to the mixing layer formed at the lateral edges of the injector[30]. The roll up of the vortical structures have been demonstrated in a study performed using vortex elements[31]. The entrainment of the freestream flow into the jet plume downstream of the injector was also observed.

CHAPTER III

GOVERNING EQUATIONS AND FLOW SOLVERS

Modern computers have the ability to execute repetitive arithmetic calculations at very high speeds. This provides an excellent platform for implementing numerical algorithms in order to obtain solutions to the governing equations of fluid dynamics. This chapter details the techniques used in the field of Computational Fluid Dynamics (CFD) in general and specifically those implemented in the GASP and Cobalt flow solvers which are used in this work.

Governing Equation

The following subsections present the governing equations of fluid dynamics in integral and differential form.

Integral Form

The integral form of the combined system of governing equations for a generic flow involving a single species is

$$\frac{\partial}{\partial t}\iiint_V \mathbf{Q}dV + \iint_A \left(\mathbf{F}\left(\mathbf{Q}\right)\cdot\hat{\mathbf{n}}\right)dA = \iint_A \left(\mathbf{F_v}\left(\mathbf{Q}\right)\cdot\hat{\mathbf{n}}\right)dA + \iiint_V \mathbf{S}dV \qquad (1)$$

where $\mathbf{Q}$ is the vector of conserved quantities:

$$\mathbf{Q} = \left\{ \begin{array}{c} \rho \\ \rho u \\ \rho v \\ \rho w \\ \rho e_o \end{array} \right\}. \tag{2}$$

The inviscid flux term is

$$\mathbf{F}\left(\mathbf{Q}\right) \cdot \hat{\mathbf{n}} = \left\{ \begin{array}{c} \rho \left(\mathbf{V} \cdot \hat{\mathbf{n}}\right) \\ \rho u \left(\mathbf{V} \cdot \hat{\mathbf{n}}\right) + p\hat{n}_x \\ \rho v \left(\mathbf{V} \cdot \hat{\mathbf{n}}\right) + p\hat{n}_y \\ \rho w \left(\mathbf{V} \cdot \hat{\mathbf{n}}\right) + p\hat{n}_x \\ \rho h_o \left(\mathbf{V} \cdot \hat{\mathbf{n}}\right) \end{array} \right\} \tag{3}$$

and the viscous flux term on the right hand side is given by

$$\mathbf{F_v}\left(\mathbf{Q}\right) \cdot \hat{\mathbf{n}} = \left\{ \begin{array}{c} 0 \\ \mathbf{T} \cdot \hat{\mathbf{n}} \\ -\left(\nabla q + \mathbf{T}\mathbf{V}\right) \cdot \hat{\mathbf{n}} \end{array} \right\}. \tag{4}$$

The source term vector, $\mathbf{S}$, is zero for flow where body forces are neglected. The dot product of tensor $\mathbf{T}$ with the normal vector $\hat{\mathbf{n}}$ leads to the column vector

$$\mathbf{T} \cdot \hat{\mathbf{n}} = \left[\begin{array}{c} \tau_{xx}\hat{n}_x + \tau_{xy}\hat{n}_y + \tau_{xz}\hat{n}_z \\ \tau_{yx}\hat{n}_x + \tau_{yy}\hat{n}_y + \tau_{yz}\hat{n}_z \\ \tau_{zx}\hat{n}_x + \tau_{zy}\hat{n}_y + \tau_{zz}\hat{n}_z \end{array} \right]. \tag{5}$$

Differential Form

The integral form of the conservation equations can be converted into a differential form using the Gauss divergence theorem which states that

$$\iiint_V (\nabla \cdot \mathbf{F})\, dV = \iint_A (\mathbf{F} \cdot \hat{\mathbf{n}})\, dA \tag{6}$$

for a vector $\mathbf{F}$ with continuous partial derivatives enclosed by a volume V with surface A and normal vector $\hat{\mathbf{n}}$.

Using Eq. (6), Eq. (1) can be rewritten as

$$\frac{\partial}{\partial t} \iiint_V \mathbf{Q} dV + \iiint_V (\nabla \cdot \mathbf{F}(\mathbf{Q}))\, dA = \iiint_V (\nabla \cdot \mathbf{F_v}(\mathbf{Q}))\, dA + \iiint_V \mathbf{S} dV \tag{7}$$

Ignoring the source vector $\mathbf{S}$ and accumulating terms under a single integral, we get

$$\iiint_V \left[\frac{\partial \mathbf{Q}}{\partial t} + \nabla \cdot \mathbf{F}(\mathbf{Q}) - \nabla \cdot \mathbf{F_v}(\mathbf{Q}) \right] dV = 0 \tag{8}$$

which is true for any arbitrary control volume. Therefore

$$\frac{\partial \mathbf{Q}}{\partial t} + \nabla \cdot \mathbf{F}(\mathbf{Q}) - \nabla \cdot \mathbf{F_v}(\mathbf{Q}) = 0 \tag{9}$$

Equation (9) contains three separate physical principles i.e., conservation of mass, conservation of momentum and conservation of energy. The corresponding equations for these are:

mass conservation

$$\frac{\partial \rho}{\partial t} + \frac{\partial \rho u_i}{\partial x_i} = 0 \tag{10}$$

momentum conservation

$$\frac{\partial \rho u_i}{\partial t} + \frac{\partial \rho u_j u_i}{\partial x_j} = -\frac{\partial p}{\partial x_i} + \frac{\partial \tau_{ji}}{\partial x_j} \tag{11}$$

and energy conservation

$$\frac{\partial \rho e_o}{\partial t} + \frac{\partial \rho u_j h_o}{\partial x_j} = \frac{\partial u_i \tau_{ji}}{\partial x_j} - \frac{\partial q_j}{\partial x_j} \tag{12}$$

The momentum equations in Eq. (11) are the Navier-Stokes equations although the term is generally used to refer to all three equations listed above.

Thermodynamic Relations

In order to complete the above set of equations thermodynamic quantities are related using the perfect gas law and an additional thermodynamic state relation.

$$p = \rho R T \tag{13}$$

$$e = e\left(T, p\right) \tag{14}$$

For a calorically perfect gas, the specific internal energy, e , is

$$e = c_v T \tag{15}$$

The stagnation internal energy is defined as

$$e_o = e + \frac{1}{2} u_i u_i \tag{16}$$

And the stagnation enthalpy

$$h_o = e_o + \frac{p}{\rho} \tag{17}$$

Stress-Strain Rate Constitutive Relation and Heat Flux

The viscous stress tensor, $\mathbf{T}$, is given by

$$\mathbf{T} = \begin{bmatrix} \tau_{xx} & \tau_{xy} & \tau_{xz} \\ \tau_{yx} & \tau_{yy} & \tau_{yz} \\ \tau_{zx} & \tau_{zy} & \tau_{zz} \end{bmatrix} \tag{18}$$

For a Newtonian fluid, the stress-strain rate constitutive relation is

$$\tau_{ij} = 2\mu s_{ij} + \lambda \frac{\partial u_k}{\partial x_k} \delta_{ij} \tag{19}$$

where s_{ij} is the strain-rate tensor given by

$$s_{ij} = \frac{1}{2}\left(\frac{\partial u_i}{\partial x_j} + \frac{\partial u_j}{\partial x_i}\right) \tag{20}$$

The heat flux vector is obtained using Fouriers law.

$$q_j = -\kappa \frac{\partial T}{\partial x_j} \tag{21}$$

And for a calorically perfect gas, the heat flux vector can be written as

$$q_j = -\frac{\mu}{\mathrm{Pr}} \frac{\partial T}{\partial x_j} \tag{22}$$

Equations for Turbulent Flow Simulation

Turbulent fluid flow simulation is performed using an averaged form of the governing equations. Depending on whether density variations in the flow are significant either Reynolds averaging or Favre averaging techniques are used to obtain a new set of equations.

Reynolds and Favre Averaging

Reynolds averaging is the process of obtaining a mean value of any fluctuating flow quantity. Three different Reynolds averaging procedures are commonly used in studying turbulent flows: time averaging, spatial averaging and ensemble averaging. Only time averaging will be described here as it is the most relevant of the three techniques.

Any instantaneous flow quantity can be split into a mean value and a fluctuating value.

$$\phi = \bar{\phi} + \phi' \tag{23}$$

The instantaneous value ϕ and the fluctuation ϕ' are functions of the spatial coordinate and time while the mean value $\bar{\phi}$ is a function of only the spatial coordinate. The mean value $\bar{\phi}$ is obtained by time averaging the instantaneous flow quantity

$$\bar{\phi}\,(x, y, z) = \frac{1}{T} \int_{t}^{t+T} \phi(x, y, z, t) dt \tag{24}$$

The time average of the mean and the fluctuating components are the mean and zero respectively. The time over which averaging is performed is critical since it has to be larger than the period of the fluctuations of the flow quantity but smaller

than that of variations in the mean flow.

For flows with density fluctuations the above described averaging technique leads to additional terms in the governing equations including triple correlations. In order to avoid these complications a density weight averaging technique used by Favre is applied. This leads to a set of equations similar in form to those governing mean incompressible flows. The density weighed average of a flow quantity is defined as

$$\tilde{\phi} = \frac{\overline{\rho\phi}}{\bar{\rho}} \tag{25}$$

where the overbar indicates Reynolds averaging. We can also write equation 25 in terms of Reynolds averaging.

$$\bar{\rho}\tilde{\phi} = \overline{\rho\phi} = \bar{\rho}\bar{\phi} + \overline{\rho'\phi'} \tag{26}$$

Reynolds Averaged Equations for Incompressible Flow

Applying the Reynolds averaging procedure and using the following identities

$$\overline{\frac{\partial\phi}{\partial x}} = \frac{\partial\bar{\phi}}{\partial x} \tag{27}$$

$$\overline{\phi\varphi} = \overline{\left(\bar{\phi} + \phi'\right)\left(\bar{\varphi} + \varphi'\right)} = \overline{\phi\varphi + \phi\varphi' + \phi'\varphi + \phi'\varphi'} = \bar{\phi}\bar{\varphi} + \phi'\varphi' \tag{28}$$

we obtain the governing equations for mean incompressible turbulent flow.

$$\frac{\partial\bar{u}_i}{\partial x_i} = 0 \tag{29}$$

$$\rho\frac{\partial\bar{u}_i}{\partial t} + \rho\bar{u}_i\frac{\partial\bar{u}_i}{\partial x_j} = -\frac{\partial\bar{p}}{\partial x_i} + \frac{\partial}{\partial x_i}\left(\tau_{ij} - \rho\overline{u_i'u_j'}\right) \tag{30}$$

In the above equation an extra term, $\rho\overline{u_i' u_j'}$, is present when compared with the instantaneous equations. This is a symmetric tensor with six independent components and is usually referred to as the Reynolds stress tensor.

Favre Averaged Equations for Compressible Flow

The instantaneous flow variable is decomposed into a density weighted component and a fluctuating component.

$$\phi = \tilde{\phi} + \phi'' \tag{31}$$

Favre decomposition is applied to all flow variables except ρ , p and q_j, which are decomposed using the Reynolds technique. The resulting equations are averaged to obtain the density weighed mean flow equations.

$$\frac{\partial \bar{\rho}}{\partial t} + \frac{\partial \bar{\rho}\tilde{u}_i}{\partial x_i} = 0 \tag{32}$$

$$\frac{\partial \bar{\rho}\tilde{u}_i}{\partial t} + \frac{\partial \bar{\rho}\tilde{u}_j\tilde{u}_i}{\partial x_j} = -\frac{\partial \bar{p}}{\partial x_i} + \frac{\partial}{\partial x_j}\left[\bar{\tau}_{ij} - \bar{\rho}\widetilde{u_i'' u''}_j\right] \tag{33}$$

$$\frac{\partial \bar{\rho}\tilde{e}_o}{\partial t} + \frac{\partial}{\partial x_i}\left(\bar{\rho}\tilde{e}_o\tilde{u}_i + \overline{pu_i} + \bar{\rho}\widetilde{e_o'' u''}_i\right) = \frac{\partial}{\partial x_i}\left(\overline{\tau_{ij}u_j}\right) - \frac{\partial \bar{q}_i}{\partial x_i} \tag{34}$$

Boussinesq Approximation

Simulating turbulent flows is a challenging task because of numerous factors. Turbulent flows are characterized by a fluid motion over a wide range of spatial and temporal scales. The range of scales is dependent on the Reynolds number of the flow. In order to completely capture all spatial structures in the flow the grid used should be of the order of $\mathrm{Re}^{9/4}$. Thus for a flow with Reynolds number of 1.0E+06, total number of grid points should be around 31.0E+12. Apart from the grid size

constraint, the time step used in the simulation should be small enough to capture the smallest of eddies in the flow. Clearly, grids of this size cannot be accommodated using commonly available computer technology where memory is usually limited to a few hundred gigabytes in the best of cases.

The process of simulating the complete flow field without the use of any averaging technique is called Direct Numerical Simulation (DNS). As discussed previously, DNS is not a viable option for flows with high Reynolds numbers but is nonetheless a valuable tool since DNS results for low Reynolds number turbulent flows can be used to fine tune turbulence models.

Large Eddy Simulation (LES) is a technique where only the dissipative scales are modeled while all other scales are resolved. This is still an expensive technique since the range of large scale structures increases with increase in Reynolds number. However, LES been applied successfully to a wide range of flows. The current standard for simulating turbulent flows is the using first-order, two-equation models such as $k - \varepsilon$ or $k - \omega$.[29] Second-order models[32] involving equations for the transport of Reynolds stress terms, adding an additional seven equations to the five mean flow equations, are becoming more popular with increasing availability of faster computers. Hybrid techniques such as Detached Eddy Simulation (DES)[33] where flow closer to solid walls is simulated using one- or two-equation models while that in the freestream is resolved using LES like methods. This has the advantage of lowering the grid point requirement near walls while providing better results in the freestream. In this work, two equation models and their DES variants are used. The details regarding these will be presented in appropriate sections in this chapter.

In two-equation turbulence models, the Reynolds stress term in Eq. (33) is modeled using the Boussinesq approximation which hypothesizes that this term is

generated due to effects of a turbulent viscosity, analogues to molecular viscosity. The approximation for the Reynolds stress term is written as:

$$-\bar{\rho}\widetilde{u_i''u_j''} = \mu_t\left(\frac{\partial u_i}{\partial x_j} + \frac{\partial u_j}{\partial x_i}\right) - \frac{2}{3}\delta_{ij}\left(\mu_t\frac{\partial \tilde{u}_k}{\partial x_k} + \bar{\rho}K\right) \tag{35}$$

where K is the turbulent kinetic energy defined as

$$K = \frac{1}{2}\widetilde{u_i''u_i''} = \frac{1}{2}\frac{\overline{\rho u_i''u_i''}}{\bar{\rho}} \tag{36}$$

and μ_t is the turbulent viscosity that has to be modeled. In two-equation models, the turbulent viscosity is evaluated as:

$$\mu_t = \frac{C_\mu \rho K}{\omega} \tag{37}$$

where ω is the turbulence frequency. Using the value of μ_t from Eq. (37), the turbulent stresses are evaluated using Eq. (35). The equations for K and ω are presented in a later section.

GASP

Aerosofts General Aerodynamics Simulation Program (GASP) was used for all two-equation structured grid simulations related to this work. GASP is an advanced CFD solver that has been in development over a number of years. Over that time, it has been show to reliably simulate a wide variety of flows including jet interaction flows which is the topic of this work.

GASP has the ability to simulate the Favre averaged equations governing unsteady, compressible and viscous flows. The effect of turbulence can be simulated

using models of varying degrees of fidelity including algebraic equations, one-equation, two-equation and seven-equation second-order models. GASP can also simulate subsets of the Navier-Stokes equations like the Thin-Layer equations, the Parabolized Navier-Stokes equations and the inviscid Euler equations. Flows that can be simulated with GASP include those with thermo-chemical non-equilibrium and speeds ranging from low subsonic to hypersonic Mach numbers.

All of the simulations in GASP were performed using the two-equation $k-\omega$ model. The seven equation second-order model was incorporated towards the end of this work and hence was not used to perform any simulations. Algorithmic details for various options used in this work is presented in the following sections.

Inviscid Terms

Inviscid fluxes at the cell interfaces are evaluated using Roe's approximate solver. This is flux difference splitting scheme and involves solving the local Riemann problem at each cell interface. This is done using Roe's approximate Riemann solver[34] implemented in GASP. Roe's solver is used because of its high accuracy in resolving shock and boundary layers. The following is an algorithm to compute the intercell flux using Roe's method.

- Calculate Roe average values.

$$\tilde{u} = \frac{\sqrt{\rho_L}u_L + \sqrt{\rho_R}u_R}{\sqrt{\rho_L} + \sqrt{\rho_R}} \tag{38}$$

$$\tilde{v} = \frac{\sqrt{\rho_L}v_L + \sqrt{\rho_R}v_R}{\sqrt{\rho_L} + \sqrt{\rho_R}} \tag{39}$$

$$\tilde{w} = \frac{\sqrt{\rho_L}w_L + \sqrt{\rho_R}w_R}{\sqrt{\rho_L} + \sqrt{\rho_R}} \tag{40}$$

$$\tilde{H} = \frac{\sqrt{\rho_L}H_L + \sqrt{\rho_R}H_R}{\sqrt{\rho_L} + \sqrt{\rho_R}} \tag{41}$$

$$\tilde{a} = (\gamma - 1)\left[\tilde{H} - \frac{1}{2}\tilde{\mathbf{V}}^{\mathbf{2}}\right]^{\frac{1}{2}} \tag{42}$$

where $\tilde{\mathbf{V}} = \tilde{u}^2 + \tilde{v}^2 + \tilde{w}^2$.

- Calculate averaged eigenvalues.

$$\tilde{\lambda}_1 = \tilde{u} - \tilde{a} \tag{43}$$

$$\tilde{\lambda}_2 = \tilde{\lambda}_3 = \tilde{\lambda}_4 = \tilde{u} \tag{44}$$

$$\tilde{\lambda}_5 = \tilde{u} + \tilde{a} \tag{45}$$

- Calculate averaged right eigenvectors.

$$\tilde{\mathbf{K}}^{(1)} = \begin{bmatrix} 1 \\ \tilde{u} - \tilde{a} \\ \tilde{v} \\ \tilde{w} \\ \tilde{H} - \tilde{u}\tilde{a} \end{bmatrix} \tag{46}$$

$$\tilde{\mathbf{K}}^{(2)} = \begin{bmatrix} 1 \\ \tilde{u} \\ \tilde{v} \\ \tilde{w} \\ \frac{1}{2}\tilde{V}^2 \end{bmatrix} \tag{47}$$

$$\tilde{\mathbf{K}}^{(3)} = \begin{bmatrix} 0 \\ 0 \\ 1 \\ 0 \\ \tilde{v} \end{bmatrix} \tag{48}$$

$$\tilde{\mathbf{K}}^{(4)} = \begin{bmatrix} 0 \\ 0 \\ 0 \\ 1 \\ \tilde{w} \end{bmatrix} \tag{49}$$

$$\tilde{\mathbf{K}}^{(5)} = \begin{bmatrix} 1 \\ \tilde{u} + \tilde{a} \\ \tilde{v} \\ \tilde{w} \\ \tilde{H} + \tilde{u}\tilde{a} \end{bmatrix} \tag{50}$$

- Calculate wave strengths.

$$\tilde{\alpha}_1 = \frac{1}{2\tilde{a}} \left[\Delta u_1 \left(\tilde{u} + \tilde{a} \right) - \Delta u_2 - \tilde{a}\tilde{\alpha}_2 \right] \tag{51}$$

$$\tilde{\alpha}_2 = \frac{(\gamma - 1)}{\tilde{a}^2} \left[\Delta u_1 \left(\tilde{H} - \tilde{u}^2 \right) - \tilde{u}\Delta u_2 - \overline{\Delta \tilde{u}_5} \right] \tag{52}$$

$$\tilde{\alpha}_3 = \Delta u_3 - \tilde{v}\Delta u_1 \tag{53}$$

$$\tilde{\alpha}_4 = \Delta u_4 - \tilde{w}\Delta u_1 \tag{54}$$

$$\tilde{\alpha}_5 = \Delta u_1 - (\tilde{\alpha}_1 + \tilde{\alpha}_2) \tag{55}$$

where $\overline{\Delta u_5} = \Delta u_5 - (\Delta u_3 - \tilde{v}\Delta u_1)\,\tilde{v} - (\Delta u_4 - \tilde{w}\Delta u_1)\,\tilde{w}$.

- Calculate $\mathbf{F}_{i+\frac{1}{2}}$.

$$\mathbf{F}_{i+\frac{1}{2}} = \frac{1}{2}\left(\mathbf{F}_L + \mathbf{F}_R\right) - \frac{1}{2}\sum_{i=1}^{m} \tilde{\alpha}_i \left|\tilde{\lambda}_i\right| \tilde{\mathbf{K}}^{(i)} \tag{56}$$

Entropy Fix

The eigenvalues of the Roe matrix are modified according to Harten and Hyman[35] as

$$\tilde{u} \pm \tilde{a} = \begin{cases} |\tilde{u} \pm \tilde{a}| & \text{for } |\tilde{u} \pm \tilde{a}| > \varepsilon \\ \\ \dfrac{(\tilde{u} \pm \tilde{a}) + \varepsilon^2}{2\varepsilon} & \text{for } |\tilde{u} \pm \tilde{a}| \leq \varepsilon \end{cases} \tag{57}$$

where ε is a small positive number.

Cobalt

The Cobalt flow solver is used to perform simulations using DES turbulence models. Cobalt is a derivative of Cobalt$_{60}$[36] developed at AFRL. The commercial version of Cobalt used in this work has undergone numerous changes as compared to the original Cobalt$_{60}$.

The integral form of the Navier-Stokes equations used in Cobalt is given by

$$\frac{\partial}{\partial t}\iiint_V \mathbf{Q} dV + \iint_S \left(\mathbf{f}\hat{i} + \mathbf{g}\hat{j} + \mathbf{h}\hat{k}\right) \cdot \hat{n} dS = \iint_S \left(\mathbf{r}\hat{i} + \mathbf{s}\hat{j} + \mathbf{t}\hat{k}\right) \cdot \hat{n} dS \tag{58}$$

where

$$\mathbf{Q} = \begin{bmatrix} \rho \\ \rho u \\ \rho v \\ \rho w \\ \rho e \end{bmatrix} \tag{59}$$

$$\mathbf{f} = \begin{bmatrix} \rho u \\ \rho u^2 + p \\ \rho uv \\ \rho uw \\ u\left(\rho e + p\right) \end{bmatrix} \tag{60}$$

$$\mathbf{g} = \begin{bmatrix} \rho u \\ \rho uv \\ \rho v^2 + p \\ \rho vw \\ v\left(\rho e + p\right) \end{bmatrix} \tag{61}$$

$$\mathbf{h} = \begin{bmatrix} \rho u \\ \rho uw \\ \rho vw \\ \rho w^2 + p \\ w\left(\rho e + p\right) \end{bmatrix} \tag{62}$$

$$\mathbf{r} = \begin{bmatrix} 0 \\ \tau_{xx} \\ \tau_{xy} \\ \tau_{xz} \\ u\tau_{xx} + v\tau_{xy} + w\tau_{xz} + kT_x \end{bmatrix} \tag{63}$$

$$\mathbf{s} = \begin{bmatrix} 0 \\ \tau_{xy} \\ \tau_{yy} \\ \tau_{yz} \\ u\tau_{xy} + v\tau_{yy} + w\tau_{yz} + kT_y \end{bmatrix} \tag{64}$$

$$\mathbf{t} = \begin{bmatrix} 0 \\ \tau_{xz} \\ \tau_{yz} \\ \tau_{zz} \\ u\tau_{xz} + v\tau_{yz} + w\tau_{zz} + kT_z \end{bmatrix} \tag{65}$$

The semi-discrete form of the equations that Cobalt solves is

$$V_i \frac{d\mathbf{Q}_i}{dt} + \sum_{M=1}^{N_i} \left(\mathbf{f}^M \hat{i} + \mathbf{g}^M \hat{j} + \mathbf{h}^M \hat{k} \right) \cdot \hat{n}^M S^M = \sum_{M=1}^{N_i} \left(\mathbf{r}^M \hat{i} + \mathbf{s}^M \hat{j} + \mathbf{t}^M \hat{k} \right) \cdot \hat{n}^M S^M \tag{66}$$

where i represents any cell with N_i faces. Refer to the work cited for additional details of the flow solver.

The inviscid fluxes are obtained using the exact Riemann solver of Gottlieb and Groth.[37] The solution to the Riemann problem is formulated in terms of the

intermediate flow velocity (u^*). A different implicit equation is obtained for each of the four physically viable wave patterns which are dependent on the left and right states of the cell interface. The solution to these equations provides the necessary intermediate states.

The turbulence model used for the purpose of this work is that of Menter.[38] Menter's SST model is a combination of $k-\epsilon$ and $k-\omega$ models. It takes advantage of the near wall behavior of $k-\omega$ and the freestream behavior of $k-\epsilon$. The combined equations[39] are given by

$$\frac{D}{Dt}(\rho k) = \tau_{ij}\frac{\partial u_i}{\partial x_j} - \beta^*\rho\omega k + \frac{\partial}{\partial x_j}\left[(\mu + \sigma_k\mu_t)\frac{\partial k}{\partial x_j}\right] \tag{67}$$

$$\frac{D}{Dt}(\rho\omega) = \frac{\gamma\rho}{\mu_t}\tau_{ij}\frac{\partial u_i}{\partial x_j} - \beta\rho\omega^2 + \frac{\partial}{\partial x_j}\left[(\mu + \sigma_{\omega 1}\mu_t)\frac{\partial \omega}{\partial x_j}\right] + 2\rho(1-F_1)\sigma_{\omega 2}\frac{1}{\omega}\frac{\partial k}{\partial x_j}\frac{\partial \omega}{\partial x_j} \tag{68}$$

The switching function F_1 is evaluated as

$$\begin{aligned} \arg 1 &= \min\left[\max\left(\frac{\sqrt{k}}{0.09\omega y}; \frac{500\mu}{\rho\omega y^2}\right); \frac{4\rho\sigma_{\omega 2}k}{CD_{k\omega}y^2}\right] \\ CD_{k\omega} &= \max\left[2\rho\sigma_{\omega 2}\frac{1}{\omega}\frac{\partial k}{\partial x_i}\frac{\partial \omega}{\partial x_i}; 10^{-20}\right] \\ F_1 &= \tanh\left(\arg_1^4\right) \end{aligned} \tag{69}$$

The model constants for the above mentioned equations are obtained using the blending function

$$\phi = F_1\phi_1 + (1-F_1)\phi_2 \tag{70}$$

where ϕ_1 is the model constant in the $k-\omega$ equation and ϕ_2 is the model constant

in the $k-\epsilon$ equation. The turbulent viscosity is given by

$$\mu_t = \frac{\rho a_1 k}{\max\left(a_1\omega; \Omega F_2\right)} \tag{71}$$

Ω is the absolute value of vorticity. The function F_2 is included to prevent singular behavior in the freestream where Ω goes to zero. F_2 is evaluated as

$$F_2 = \tanh\left(\arg_2^2\right)$$
$$\arg_2 = \max\left(2\frac{\sqrt{k}}{0.09\omega y}; \frac{400\nu}{y^2\omega}\right)$$

The model constants for the $k-\omega$ equations are

$$\sigma_{k1} = 0.85$$
$$\sigma_{\omega 1} = 0.5$$
$$\beta_1 = 0.075$$
$$\beta^* = 0.09$$
$$\kappa = 0.41$$
$$\gamma_1 = \frac{\beta_1}{\beta^*} - \frac{\sigma_{\omega 1}\kappa^2}{\sqrt{\beta^*}}$$

and for $k-\epsilon$

$$\sigma_{k2} = 1.0$$
$$\sigma_{\omega 2} = 0.5$$
$$\beta_2 = 0.0828$$
$$\beta^* = 0.09$$
$$\kappa = 0.41$$
$$\gamma_2 = \frac{\beta_2}{\beta^*} - \frac{\sigma_{\omega 2}\kappa^2}{\sqrt{\beta^*}}$$

Using compressibility corrections (compressible dissipation and pressure dilata-

tion) suggested by Suzen and Hoffmann[40] to the $k-\epsilon$ portion of Menter's equations, we get

$$\frac{D}{Dt}(\rho k) = \tau_{ij}\frac{\partial u_i}{\partial x_j} + (1-F_1)\,\overline{p''d''} - \beta^*\rho\omega k\left(1+\alpha_1 M_t^2\,(1-F_1)\right) + \frac{\partial}{\partial x_j}\left[(\mu+\sigma_k\mu_t)\,\frac{\partial k}{\partial x_j}\right] \tag{72}$$

$$\frac{D}{Dt}(\rho\omega) = \frac{\gamma\rho}{\mu_t}\tau_{ij}\frac{\partial u_i}{\partial x_j} + (1-F_1)\,\beta^*\alpha_1 M_t^2\rho\omega^2 - \beta\rho\omega^2 + \frac{\partial}{\partial x_j}\left[(\mu+\sigma_{\omega 1}\mu_t)\,\frac{\partial \omega}{\partial x_j}\right] + 2\rho\,(1-F_1)\,\sigma_{\omega 2}\frac{1}{\omega}\frac{\partial k}{\partial x_j}\frac{\partial \omega}{\partial x_j} - (1-F_1)\,\frac{\overline{p''d''}}{\nu_t} \tag{73}$$

CHAPTER IV

GRID GENERATION AND PROCEDURE

Introduction

Grid generation is the process of discretization of a flow domain into an addressable set of smaller regions. It is a significant step in obtaining numerical solutions to flowfields using the Navier-Stokes equations. Grid generation is a time consuming process. For certain simulations wherein the domain is complex, it is possible for the grid generation process to be more time intensive than the flow solver time. The solution obtained is significantly influenced by the size and quality of grid used in the simulation. Grid convergence studies are conducted to eliminate the dependence of solutions on the grids. This involves increasing the number of grid points (discretized volumes) in the flow domain and resolving the governing equations for the new grid. This process is repeated until there is negligible change in integral quantities like lift and drag coefficients. Since this idealized grid convergence study is sometimes very computationally demanding, usually three or four successively refined grids are used to demonstrate grid convergence. Refinement is accomplished in different ways depending on the type of grid and will be presented in relevant sections in this chapter. The following sections of this chapter will discuss the types of grids used in this work and the methods of their generation and refinement.

Structured Grids

Structured grids are composed of logical cubes having constant I, J and K lines. Each individual cell in a 3D structured grid is a hexahedron. The procedure for

generating structured generally involves specifying the distribution of points on the boundaries of the logical cube. The points on the interior are then generated using transfinite interpolation techniques. The geometry of the domain dictates the quality of the cells generated through interpolation. Elliptic relaxation techniques can be used to smooth the distribution of grid points if skewed cells are present in the grid obtained through interpolation. Multiple blocks of structured grids can be assembled to fit complex flow domains.

Advantages and Disadvantages of Structured Grids

The early adoption of structured grids for CFD simulations has had the consequence of development of algorithms that perform with greater efficiency and accuracy on structured grids. These algorithms cannot be used with other grid types without losing their benefits. In addition, many of these algorithms have the added advantage of efficient memory utilization. Thus, computers with small memory capacity are able to execute simulations that would normally require larger amounts of memory. Also, the long development history of structured grid CFD has led to as mature set of tools that are available for any new code development. In recent years, the use of multiple CPUs for code execution has come into vogue. The development of language extensions such as OpenMP and HPC FORTRAN as well as communication libraries like MPI and PVM has enabled CFD codes to utilize multiple CPUs. Structured grids lend themselves easily to partitioning into numerous blocks, each of which is treated as an independent domain by the CPU on which it is executed. Boundary information for all blocks is updated at each iteration step. Good scaling in multiprocessor performance has been obtained in codes using these techniques to accelerate execution time.

One of the areas where structured grids have some disadvantages is grid refinement. Adding additional grids points in regions of high gradients of flow quantities and areas of interest usually leads to increase in grid points in other areas. Thus memory and computational time requirements are increased without any added benefit. Recent research in structured grid refinement techniques such as r-refinement has shown promise in the ability of structured grids to adapt to solution gradients without additional point insertion.

GRIDGEN

All structured grids used in the current work were generated using GRIDGEN, a general-purpose grid generator developed by Pointwise, Inc. GRIDGEN has the capability of generating structured, unstructured and hybrid grids. Since GRIDGEN has been used generate structured grids for this study, only details pertaining to structured grid generation will be presented. The Database section of GRIDGEN is designed to either import geometry from an external CAD program or build one using primitives and operations such as lines, surfaces, extrusions, intersections, etc. Once a geometry is created using these primitives, grid point density on the geometry edges are defined using Connectors. The total number of grid points in the domain is determined the number of points on the connectors. The grid point distribution on the connector can be varied to affect grid density in different sections of the domain. Numerous distribution functions are available in GRIDGEN including hyperbolic tangent and MRQS.[41]

After connectors are formed on the edges defining the geometry, Domains or surfaces are created to form the bounding faces of the flow region. Each domain has to form a logical rectangle with matching number of grid points on oppo-

site sides. The interior points of the domain are determined using interpolation. If necessary, surface grids can be smoothed using the elliptic solver available in GRIDGEN. The behavior of the elliptic solver may be controlled by specifying the following parameters.

- Relaxation parameter: Controls the convergence of the elliptic solver.
- Control functions: Background control functions influence grid point distribution in the interior of the domain whereas foreground control functions influence grid point distribution near the boundaries.
- Solver boundary conditions: Grid point movement on the boundaries is controlled by selecting solver boundary conditions.

The surface grids are then assembled to create a logical cube forming a volume grid. Each of the six surfaces of the cube may be composed of one or more domains. The interior points of the block are determined by interpolation similar to interior points of domains. If necessary, the elliptic solver may be used to improve the quality of the initial interpolated grid. Multiple blocks can be built to encompass the entire flow domain with the only requirement being that grid points on the block interfaces are coincident.

Structured Grids for RANS Simulations

In this section a description of the geometry of the flow domains is presented along with details regarding structured grids and their generation.

Shown in Fig. 5 is an illustration of the coordinate system and test section for injection through diamond jets. The domain used in the simulation is that of experiments conducted by Bowersox et al[28]. The origin is located is at the center of

the jet exit which is flush with the tunnel floor. The positive x-coordinate is in the freestream flow direction, positive y-coordinate is normal to the tunnel wall into the domain and the z-coordinate completes the right-handed coordinate system. The inlet of the domain is located at a distance of 15.75 d_{eff} from the center of the jet and the outlet is at 23 d_{eff}. Prior CFD simulations of transverse jet injection into supersonic flowfields using RANS models[2] provides the basis for simulating only one half of the domain with the symmetry plane located along the $x - y$ surface. The outer wall of the domain at z_{max} and the top surface of the domain at y_{max} are located at a distance of 7.8 d_{eff}. Only one-half of the total height of the tunnel is simulated since all flow features of interest are located within this region. This numerical test section is shown in red in Fig. 5.

A schematic of the diamond injector is shown in Fig. 6. The length of the injector is 11.86 mm. The half angle of the diamond injector is 15 degrees. The half angle was arbitrarily chosen with the goals of (1) weak leading edge shock and (2) minimization of tunnel wall reflections. The injection angle is the angle formed in the counter-clockwise direction between the tunnel floor and the axis of the jet. The five different injection angles investigated for diamond injectors were $10°$, $27.5°$, $45°$, $90°$ and $135°$. Each of the injection angle cases were simulated with three different jet total pressures. The $90°$ and $45°$ cases are shown in Fig. 7. Circular injector geometry was also investigated with a diameter equal to 4.89 mm and two different jet total pressures. For all cases the injector port was modeled to include the effects of losses accrued in the port. The height of the injector port is 5.08 mm. Details regarding boundary conditions for the simulations will be presented in a later section in this chapter.

The discretization of the geometry was performed through an iterative process. Initial simulations were performed without modeling the injector port geometry

and by using a single block H-type structured grid. The injector exit on the tunnel floor was modeled by selecting strips of cells to approximate the injector cross-section. In the next iteration the geometry was modified to represent the injector exit cross-section accurately. A multi-block grid was generated for this purpose. A top-hat velocity profile was provided as the input at the jet exit. Results obtained from these simulations indicated that higher penetration was being predicted because the simulation did not account for losses in the injector port. In order to compensate for the losses in the injector, the injector port geometry was added to the grid used in the previous iteration. Satisfactory results were obtained from this grid. The next step was to refine the grid i.e. cluster cells in regions of high flow gradients. Initial attempts at refinement concentrated on regions around the main interaction shock. Interior blocks were curved to match the curvature of the interaction shock. The process of manually adapting the grid to the flowfield for seventeen distinct cases proved to be tedious and the resulting grids were not satisfactory. One of the stumbling blocks in the refinement process was the three-dimensionality of shocks in these flowfields. The final grids used for these simulations consisted of only two blocks, one each for the tunnel and the injector port. Grid points are densely clustered around the injector exit since this is the main interaction region that leads to other flowfield features. It was reasoned that once the flow physics in this region was captured adequately the development of the flow downstream of the injector would be more accurate. A description of the grid for the 90° injector is presented below.

The x_{max}, y_{min}, and z_{min} planes of the tunnel grid for the 90° injector geometry are shown in Fig. 8. The hyperbolic tangent stretching function is used to cluster grid points near the wall. The boundary layer grid at the inlet of the geometry is gradually stretched in the positive y-axis direction in order to adequately capture

the recirculation region ahead of the jet. Surrounding the injector exit is a subset of the larger grid, Fig. 9, in which grid points are densely packed in order to better capture the physics of the interaction between the jet and the freestream. The size of the box is approximately 4 d_{eff} x 2 d_{eff} x 2 d_{eff} for cases with low jet total pressures while the box is enlarged to 4 d_{eff} x 3 d_{eff} x 2 d_{eff} for the high jet total pressure cases. This is done in order to capture the entire barrel shock within the box. Downstream of the box surrounding the injector, grids are clustered in a trapezoidal region to capture the jet wake and the counter rotating vortex pair. This is shown in Fig. 10.

The structured grid for the injector port is shown in Fig. 11. Since a symmetry plane is assumed, only one half of the diamond is modeled. Grid points are clustered close to the two walls of the injector port to capture the viscous effects. Grid for the circular injector geometry is shown in Fig. 12. The total number of grid points for the tunnel in the ξ, η, and ζ directions are 321, 129 and 129. For the injector port it is 65, 33 and 33 respectively. The total number of grid points in the entire domain is approximately 5.4 million with approximately 5.3 million cells. Of these, roughly a million cells lie in the immediate vicinity of the injector exit. Additional details are available in Table 4.2.1.

Unstructured Grids

Unstructured grids by definition lack the structure i.e. constant I, J and K lines that characterize structured grids. The data structures used for storing unstructured grid are complex since numerous bits of information have to be stored for each grid point such as neighbor points, cell information etc. Due to the complex nature of the data structures, algorithms used for structured grids are usually not applica-

ble in unstructured grid solvers. This increases solution time which has been one of the negative aspects of unstructured grids. However, unstructured grids have become popular in recent years with the developments in computing technology which has led to fast multiprocessor computers with large memory capacities. Data interpolation which affects solution quality is also a cause for concern in unstructured grids.

Even with the negative aspects mentioned previously, unstructured grids have certain advantages over structured grids. Generating structured grids for complex flow domains is tedious and time consuming since grid points on opposing surfaces and block interfaces have to coincide. With unstructured grids, this process is simplified to a large extent allowing more time for simulation and analysis of results. Another advantage of unstructured grids is in grid refinement. Since there is no definite structure grid points can be added in regions of high flow gradients without adding unnecessary points in other regions. These features have increased the appeal of unstructured grids.

GridTool and VGRIDns

Unstructured grids for DES were generated using the GridTool and VGRIDns[42] combination package. These were developed at NASA Langley Research Center (LARC). GridTool is a CAD program with grid generation capabilities. VGRIDns is a tetrahedral unstructured grid generator. In this section, details of generating a grid using these tools will be outlined.The first step in generating an unstructured grid using the GridTool/VGRIDns combination is to define the flow geometry in GridTool. A convenient way of doing this is to import an IGES or PLOT3D surface file into GridTool. CAD tools are also available in GridTool to define the geometry.

If a geometry file is imported, then an additional step has to be performed where edges are created on surfaces that are imported. Edges are then connected to form patches. For non-coplanar patches the number of edges defining the patch cannot exceed four. Boundary condition identifiers are then applied to the patches. The only boundary identifier of importance is the viscous wall identifier. Viscous grids on walls are enabled by turning on the viscous grid switch. Additional information required for viscous grids are the total number of layers, the thickness of the first layer and stretching parameters. Grid point distribution in the domain is controlled by specifying sources at various points. The four different types of sources available in GridTool are point, line, triangle and tetrahedral. Source parameters that can be controlled include the size of the source, stretching, strength as well as orientation. The file is then exported to VGRIDns where a surface grid is created on all the patches. The results are saved and the generated grid surfaces are projected on the geometric surfaces. Next, viscous grid layers are generated on all no-slip walls. VGRIDns employs an advancing layers algorithm to generate viscous grid layers. Inviscid cells are then generated using the advancing fronts algorithm. The final output from VGRIDns is a grid with viscous and inviscid cells and a few incomplete pockets. PostGrid, a tool that is part of the VGRIDns package, is used to complete the grid as well as smooth sections of the grid that are skewed.

Unstructured Grids for Detached Eddy Simulation

The procedure for generating an unstructured grid for the 90 circular injector geometry will be presented in this section.Since the geometry was already available in GRIDGEN, a PLOT3D file of all the surfaces in the domain was created and imported into GridTool. A screenshot of GridTool with the imported domain is dis-

played in Fig. 13. The domain is designated as a set of CAD surfaces. Also, the existence of an X-Y symmetry plane is not assumed since DES simulations are time accurate. The next step is to create curves on the borders of the imported surfaces as shown in Fig. 14. One of the curves is highlighted showing a series of points. These points do not represent grid spacing but are helpful in partitioning curves, if required. A patch that is created on one of the surfaces of the domain is indicated in Fig. 15. It is made up of a set of curves enclosing an area. For coplanar patches any number of curves can be used to form a patch. The direction of the arrow is into the domain in which grid cells are to be generated. For each patch created, a specific boundary identifier is assigned. Similar boundary surfaces were grouped under a single family name so that changes could be applied to all of the surfaces in the family at the same time.Once the creation of the patches is complete, the next step is to create grid sources. Distribution of grid sources is a process that is time consuming in the initial stages of grid generation for a new domain. This process has to has to go though numerous iterations in order to obtain a satisfactory grid. Knowledge of the flowfield a priori provides some advantage since grid sources can be placed to adequately capture known flowfield features. The flow domail with grid sources is displayed in Fig. 16. Point and line grid sources are used for grid distribution. The size of grid sources in the figure gives an indication of the size of cells propagated by the sources. Propagation occurs in a spherical front from point sources while it is cylindrical for line sources. The corners of the top surface of the domain are populated with large point sources since the flow is inviscid and uniform in those regions. On the tunnel floor, slightly smaller sources are used. These sources affect only the size of the grid in the axial and the lateral directions. The size of the grid cells in the wall normal direction is controlled by stretching parameters used for viscous grid spacing. Line sources that propagate larger cells are

also used on the tunnel side walls to reduce the grid points in that region. Sources with the smallest cells are used around the jet and the wake region. This can be observed in Fig. 17 showing the source distribution near the jet exit. A series of line sources are used to approximate the circumference of the circle in order to obtain good grid distribution. A line source is also placed along the approximate axis of the barrel shock and along the axis of each of the axial counter rotating vortices in the wake. The total number of viscous layers desired along with the thickness of the first cell and the cell distribution parameters for the viscous layers are provided. The final step in GridTool is to output a .d3m file for VGRIDns.A screenshot of VGRIDns is shown in Fig. 18, displaying the imported domain with resulting grid point distribution based on sources placed in GridTool. The surfaces of the domain are then triangulated to create the initial front for the viscous grid generation. Grid point distribution on the surface of the entire domain can be seen in Fig. 19 (a). Darker regions around the jet and in the wake region indicate higher grid point density. Figure 19 (b) is a close-up showing grid points around the jet exit and also in the viscous region. The surface front is saved and projected onto the actual CAD surfaces in GridTool to ensure that the grid lies on the domain surface. The output is saved and imported back into VGRIDns. Viscous grid layers are then generated on all no-slip surfaces of the domain. On average about 25 viscous layers are present for all unstructured grids generated. The viscous layers generated in the domain can be seen in Fig. 20. The last step in VGRIDns is to generate inviscid grid cells inside the domain. A snapshot of the inviscid grid cells being generated in the wake region is shown in Fig. 21. A few pockets of empty space exist at the end of the grid generation process. These pockets are filled using the Postgrid program module. The final grid is then saved in double precision binary format.

Simulation Procedure

The procedure for RANS simulations using GASP and DES using Cobalt are presented outlined below.

RANS Simulations on Structured Grids

The first step in performing RANS simulations is to import the grid in double-precision PLOT3D format into GASP. Since the grid has more than one block, block interfaces are determined within the solver interface by using an automated process. The resulting pairs of matching interfaces are stored in a separate surfaces folder. For the current domain a single pair of matching surfaces i.e. the exit of the injector port and part of the tunnel floor surface, are stored. Six different folders namely Inlet, Extrapolation, Adiabatic Wall, Symmetry X-Y, Tangency and Jet Inlet, each representing a specific boundary condition, are created and surfaces from the imported grid are places in appropriate folders. Two additional grids are created within the GASP interface by utilizing its grid sequencing capabilities resulting in a total of three grid sequences: fine, medium and coarse. The medium and coarse grids contain exactly one-half and one-fourth the total number of cells in the fine grid.

Freestream and jet inlet conditions are created in the QSpec section. The angle of attack for the jet inlet was dictated by the injection angle being simulated. Inlet boundary condition was imported from a text file specifying primitive variables density, velocity components, pressure, TKE and rate of dissipation per unit TKE (ω). Appropriate boundary conditions, as described in a previous section, were set for each of the six folders. Inviscid flow solver properties such as solver scheme, accuracy, limiters and viscous properties such as turbulence models, viscosity law

etc were then chosen.

Run steps are then setup for each of the three grids. For each grid at least two steps are utilized. The first step ramps the local CFL number for the solution from a value of 0.01 to 1 over a certain number of iterations. Additional steps are then used with a constant global CFL of 1 until solution convergence. Results from coarser grids are interpolated automatically to finer grids within GASP to speed up solution convergence. The run steps are repeated for medium and fine grids. Only the coarse grid solution is initialized using freestream conditions. Solution initialization for medium and fine grids happens through solution interpolation from coarse and medium grids respectively. For all grids, the solution is monitored along the tunnel floor centerline. Various flow properties are output every 100th iteration for all grid sequences.RANS simulations were performed on a wide range of computers. Initial simulations were performed on dual processor Alpha workstations (GASP v3.2). With increase in grid size and availability of GASP v4.0 with the capability of using multiple processors distributed over several machines, a 24-node Beowulf class computing cluster was built to perform these simulations. The last set of results were obtained by using Air Force supercomputers (SGI Origin, MIPS) as well as IBM p690 (Power 4) and SGI Altrix (Itanium 2) machines located at Texas A&M University. A RANS solution was obtained in approximately 2-3 days of wall time, executing on 16 Itanium 2 processors i.e. about 800-1200 hours of CPU time. The list of all RANS simulation test cases are presented in Table 1.

Detached Eddy Simulations on Unstructured Grids

The grid generated in VGRID was imported into Blacksmith, the preprocessor provided with Cobalt. The tetrahedral cells in the boundary layer are merged to form

prisms to reduce total cell count and hence execution time. The grid is then converted to the Cobalt format and used with the flow solver.

Boundary and initial conditions are set in the input deck for the flow solver. The conditions used are the same as those in the RANS simulations with the exception of the symmetry plane, which is not used in this case as the complete lateral cross section of the domain is modeled.

Initial iterations were executed using the laminar form of the Navier-Stokes equations. The solution was then restarted with Menter's SST turbulence model. After convergence of the two equation model, the solution was restarted again with the DES version of Menter's SST model. Initial DES iterations were executed without any averaging in order to avoid transient flow features. Time averaging was then enabled and the solution continued until there was negligible change in averaged results. Grid convergence studies were conducted using four different grids. The criteria used for grid convergence were wall pressure and percentage of resolved turbulent kinetic energy. Accuracy of the time step used was validated by using two different time steps. Table 2 lists details of the calculation including iterations, models and time steps used for the DES simulations. The simulations were executed on supercomputers at Aeronautical Systems Center (ASC), one of the Major Shared Resource Centers (MSRC).

Grid and Solution Convergence

Demonstration of grid convergence is an important step in performing reliable numerical simulations. The accepted method of achieving grid convergence in structured grids is to first obtain a solution on a coarse grid. The next step is to refine the grid by a factor of 2 in all directions and rerun the simulation. Results from this

first step refinement are compared to the results from the coarse grid for quantities line coefficient of pressure, drag etc. This procedure is repeated by successively refining the grid by a factor of 2 until changes in results obtained are negligible. In this work grid convergence study has been performed by utilizing the sequencing feature available in GASP. A fine grid is generated and input into GASP where the grid is reduced (sequenced) by a factor of 2 in every step to obtain coarser grids. Thus 3 grid levels were achieved in GASP. The solver is then run on the coarse grid to obtain a solution which is interpolated to the medium grid to reduce the number of iterations for the medium grid solution to converge. This medium grid solution is then interpolated to the fine grid and the solution restarted. Normalized surface pressure from the tunnel floor centerline for three cases is plotted. This is shown in Fig. 22. The plot shows a trend towards convergence with increasing grid refinement. The results from the medium and fine grids are almost identical with the only discrepancy being in the region immediately downstream of the injector exit.Solution convergence is demonstrated in Fig. 23 which shows the normalized surface pressure along the tunnel floor centerline at three successive iterations levels separated by a hundred iteration steps for the fine grid. The plots align with each other indicating that the solution has not changed over 200 iterations. Figure 24 is a plot of the normalized residual versus iteration number. The residual decreases by five orders of magnitude for the first 600 iterations and then oscillates around a mean value. Although it is more important to monitor solution variables such as pressure and density to determine solution convergence, residual monitoring can indicate the approximate time of solution convergence in terms of CPU time thus helping to estimate turn around time for a simulation.

Grid convergence of the DES simulations was monitored using the ratio of the resolved TKE and the total TKE. The resolved TKE is evaluated from the averages

of the solution. The total TKE is the sum of the resolved TKE and the modeled TKE. A plot of this ratio is shown in Fig. 25. It is observed that this ratio is over 90 percent in the region of interest that is downstream of the injector orifice. Solution convergence was monitored by noting the change in turbulent statistics. The solution was deemed converged when the statistics stopped changing by over 2 percent.

CHAPTER V

COMPARISON WITH EXPERIMENTAL RESULTS

Results from simulations using GASP and Cobalt are compared to experimental results in this chapter. Qualitative comparison of CFD results with experimentally obtained shadowgraphs and surface oil flow images are performed. Mach number, total pressure ratio and normalized surface pressure results are also compared. The 90-degree injection angle is defined as the baseline case. Hence in all further discussions, this case is presented first followed by results from other injection angles. Results from higher momentum ratio and the circular injector configurations are presented in appendix B.

Comparison with RANS Results from GASP

Shadowgraphs

Experimental shadowgraph pictures were obtained using a continuous light source and a mirror to direct parallel rays into the test section. The shadowgraph image is projected on a screen and captured using a high resolution digital camera.[28] Numerical shadowgraphs were obtained along the tunnel center plane by computing the laplacian of density. Resulting values are plotted using a grayscale color map. The comparison is tenuous since the experimental results of shadowgraph represent the summation over the entire cross section of the tunnel whereas the numerical results are for the tunnel center plane.

Numerical and experimental shadowgraphs for the 90-degree J_1 case are shown in Fig. 26. Blue lines on the shadowgraph obtained from CFD simulations indicate primary shock structures. The red lines are used for alignment of injector exits in

the two images and also indicate leading and trailing corners of the injector exit. Effort has been made to show images on the same length scale. Freestream flow is from right to left in all shadowgraph images. The interaction shock generated upstream of the injector is clearly seen in both images. The blue lines show initial and eventual shock angles. The angle of this shock is approximately the same in both images. The interaction shock is blurred away from the wall in the CFD shadowgraph due to inadequate grid resolution. The barrel shock structure is seen immediately behind the interaction shock. The height of the barrel shock as predicted by GASP is larger than that seen in the experimental image. The barrel shock is a little blurred in the experimental image due to the effects of image resolution and distortion due to the boundary layer. The reattachment shock along with the shear layer is also seen in the CFD shadowgraph while the above mentioned reasons may explain their absence in the experimental image. A very weak lambda shock is also seen just ahead of the interaction shock. This is due to the separation region that exists in front of the injector exit. The weak shock is also an indication that the separation region is small. The lambda shock is not observed in the experimental shadowgraph. Additional shocks seen above the interaction shock in the experimental shadowgraph are those due to the interaction of freestream flow with the test section leading edge.

Results for the 10, 27.5, 45 and 135 degree J_1 cases are presented in Figs. 27, 28, 29, and 30 respectively. The 10-degree injection case shows an interaction shock with smaller angle as compared to the 90 degree J_1 case. The barrel shock height is also smaller and it is swept back in the freestream flow direction due to the inclination of the injector. This is unobservable in the experimental shadowgraph due to the presence of the boundary layer. The 27.5-degree interaction shock angle is slightly larger. The barrel shock shape is similar to that of the 10-

degree case with the trailing edge at a slightly steeper inclination than that in the 10-degree case. This injector exit trailing edge angle is indicative of the cross flow jet injection angle. The 45-degree injection angle follows the trend of the 10 and 27.5 degree cases with larger interaction shock angle and larger barrel shock with steeper trailing edge shock. The angle of the barrel shock trailing edge increases with increasing injection angle as seen in the shadowgraphs. Experimental shadowgraph results were not available for the 135-degree injection cases. Numerical shadowgraph for the 135-degree J_1 case indicates a shock structure that is somewhat different than the other cases. The difference is the structure of the Mach disk. In cases where the injector is aligned in the down stream direction, i.e., injection angle is less than 90 degrees; the Mach disk is a narrow surface formed at the intersection of the leading and trailing edge shock surfaces of the barrel shock. For the 135-degree case the larger distance between the leading and trailing edge shocks leads to a larger Mach disk. The main interaction shock structure is unchanged except near the injector exit where the angle is nearly perpendicular to the tunnel floor.

Surface Oil Flow

Numerical and experimental results for surface oil flow visualization of the 90-degree J_1 diamond injector are shown in Fig. 31. The experimental result is annotated indicating salient flow features. The freestream flow is from left to right. The shock induced separation region is the lighter region ahead of the interaction shock. This is similar to that seen in results obtained from GASP. The horseshoe vortex can be observed in the images as it wraps around the injector. The distance separating the two arms of the vortex is correctly predicted by the RANS model.

Starting at the trailing edge of the injector port is a pair of wake vortices clearly seen in experimental results. Although not clearly visible in numerical oil flow results, the presence of these wake vortices can be observed in the streamlines and cross sectional velocity vectors as discussed in chapter VI. The dark region between the wake vortices close to the injector is the location of the peak pressure point discussed in the previous section.

Results for the 10-degree J_1 case shows little effect of the interaction shock on the surface streamlines. This is also reflected in the experimental results as shown in Fig. 32. An increase in the injection angle to 27.5 degrees leads to the formation of features seen in the normal injection case. The numerical results showing the horse shoe vortex and the small separation region mirrors the experimental results (see Fig. 33). A stronger shock is seen in the 45-degree injection case as shown in Fig. 34. The change in the direction of streamlines due to the action of the interaction shock is clearly seen in the numerical results. This streamline curvature region corresponds to the region of oil accumulation as the shock wraps around the injector.

The 135-degree injection angle results are shown in Fig. 35. The stronger interaction shock and larger seperation region leads to early curvature of the surface lines. The numerical results predicts a slightly larger separation region as compared to experiments. This is due to shock-boundary layer interaction which is not adequately captured by the model. Apart from this discrepancy the remaining aspects of the flow are captured adequately by the simulation.

Pitot Pressure and Mach Number

Pitot pressure and Mach number comparisons for planes x/d_{eff} = 8 and x/d_{eff} = 23 are performed in this section. A comparison of pitot pressure and Mach number contours obtained from RANS simulations and experiments for the 90-degree J_1 case is shown in Fig. 36 . The plane of data shown is at a distance of x/d_{eff} = 8 from the *leading edge of the injector exit*. The distance from the leading edge is used instead of the center of the injector exit because the experimental coordinate system for this measurement started from the injector leading edge. The extent of the data shown in the y and z directions are 0.0 to 7.0 and -4.0 to 4.0. The freestream flow is directed into the page. The numerical results are mirrored across the symmetry plane and the experimental data is overlaid on the numerical results for better comparison.

The Mach number is measured in experiments using a five-hole probe. The holes are arranged on the conical surface at the tip of the probe with one of the holes at the apex and the other four on the lateral surface. The port at the apex of the cone measures the stagnation pressure (p_{02}) behind the normal shock ahead of the probe. If the local Mach number at the probe location is less than 1.0, the local stagnation pressure is measured. The combination of local static and stagnation pressures are used to evaluate the Mach number at the probe location.

Centered around z/d_{eff} = 0.0 near y/d_{eff} = 0.0 is a bell shaped structure that is the wake. The wake region is characterized by low Mach numbers and total pressures and this is represented by blue regions in Fig. 36. The width of wake region varies from 0.5 z/d_{eff} to 2.0 z/d_{eff} and the height of the wake region is approximately 1.8 y/d_{eff}. The boundary layer is thinner around the wake region. This is due to the action of the counter rotating vortex pair capturing and lifting the

surrounding boundary layer fluid. Comparing this with experimentally measured pitot pressure, it was found that the width of the wake region is more or less constant at approximately 1.25 z/d_{eff}. The height of the wake region is approximately 1.8 y/d_{eff} indicating that CFD predictions match experimental results. Boundary layer thinning around the wake is observed in experimental and numerical results. Above the wake region is the jet plume where the injectant fluid interacts with the freestream forming a shear layer. At first glance, the height of the shear layer seems to be under predicted in the CFD simulation. The outer boundary of the shear layer is represented by yellow contours at Mach 4.4 - 4.6. This outer edge height of the shear layer, at approximately 3.0 y/d_{eff}, is correctly predicted by the CFD solver. Just beyond the shear layer is the inviscid region. The Mach numbers in this region as measured in experiments is higher than those in CFD results. The interaction shock wave is the last dominant feature in Fig. 36. It is represented by the arch extending across the entire measurement plane with the peak located at y/d_{eff} 5.0 and centered at z/d_{eff} = 0.0. Moving along the positive and negative z-axis direction, the height of the shock wave decreases and at z/d_{eff} = $\pm$4.0 it is y/d_{eff} = 3.0. These values correspond to those measured in experiments.

As mentioned in chapter I, experimental parametric studies with high resolution are expensive and time consuming and this is one of the primary motivations for performing CFD simulations. Having this information in consideration, some of the discrepancies seen the comparison could be attributed to certain experimental and numerical uncertainties. The probe resolution in the z-axis direction is considerably lower as compared to that in the y-axis direction. This could possibly explain the absence of certain flow features in experimental results that are captured by simulations. Also, it was not possible to measure quantities close to the floor in experiments due to the finite probe thickness. It is possible that the experi-

mental measurement of static pressure was affected by the change in flow angle of the freestream as it passes through the interaction shock. The change in flow angle leads to the formation of a shock wave ahead of one of the static pressure ports and an expansion near the port on the opposite side. This leads to erroneous measurement of static pressure and hence Mach number. The vertical traversal speed of the probe also affects the measured quantities. Numerical uncertainities include the effect of the turbulence model. From the results seen in the above comparison, the turbulence model seems to under predict the diffusion in the plume region. Disabling the compressibility corrections to the turbulence model produced better results in other studies[43].

Comparison plots for the angled injection cases are presented in Figs. 37 - 40. Numerical and experimental Mach number contours for the 45-degree J_1 case at plane x/d_{eff} = 8 are plotted in Figs. 39. The flow structure is similar to that of the 90-degree described before. Close to y/d_{eff} = 0.0, a pair of wake vortices can be clearly seen in Fig. 39(a). Located above that is a pair of axial counter rotating vortices observed in supersonic jet interaction flows. Experimental data is not available in the region of the wake vortices for reasons cited previously. The axial counter rotating vortex pair is not observed in the experimental Mach number plot since this location is below the probe traversal limit. The width of the wake region is correctly predicted at z/d_{eff} = $\pm$ 1.0, while the height is slightly higher in CFD results. The dog eared structures located in the CFD results at y/d_{eff} = 0.8 and z/d_{eff} = $\pm$1.5 is not observed in experimental results. The prior explanation regarding the resolution of experimental measurement may explain the absence of these structures. The inviscid region width is approximately z/d_{eff} = $\pm$3.0 in both experimental and CFD results. The Mach number in the inviscid region is higher in experiments. This trend was also observed in the 90-degree case. The peak of

the jet interaction shock is correctly predicted at approximately y/d_{eff} = 4.0. This is lower than that in the 90-degree case. The 27.5-degree J_1 case results from CFD and experiments are shown in Figs. 38. The structure of this flow is very similar to the 45-degree case. Features such as the "dog eared" structures, wake vortices are seen in this case albeit with reduced dimensions. The height of the wake is again slightly over predicted by approximately y/d_{eff} = 0.2 in CFD results. Boundary layer thinning around the wake region is observed in this case similar to the 45 and 90-degree cases. Higher Mach numbers are measured in experiments in the inviscid region between the shear layer and the interaction shock. The height of the interaction shock is approximately 3.6 D at z/d_{eff} = 0.0. The 10-degree J_1 case results are shown in Fig. 37. The wake and the interaction shock heights are over predicted by the simulations. The wake vortices are buried in the boundary layer and are not as predominant in this case. Boundary layer thinning is also observed around the wake region. CFD results for the 135-degree J_1 case is shown in Fig. 40. Experimental results for the 135-degree cases were not obtained due to possible errors induced by large flow angles. The separation between the wake vortices along the floor is larger than that in the lower injection angle cases. The largest width of the wake is approximately 1.5 D centered at z/d_{eff} = 0.0. The core of the counter rotating vortex pair is also larger as compared to the lower injection angle cases. The inviscid region is flat in this case. The peak of the interaction shock is slightly higher than the 90-degree case at y/d_{eff} = 5.2.The primary difference as compared to the 27.5 and 45-degree cases is the absence of the "dog eared" structures associated with the axial transverse counter rotating vortex pair.

Pitot pressure and Mach number plot at location x/d_{eff} = 23.0 are included in the plots refering to those at $x/d_{eff} = 8.0$. Fig. 36 shows pitot pressure and Mach number contours as obtained from CFD and experiments for the 90-degree

J_1 case. The wake exhibits a mushroom shaped structure in this farfield region. A pair of kidney bean shaped structures is clearly visible within the wake in Fig. 36(c). These structures are not resolved in experimental measurements. The outer edge of the wake is over predicted by about 30 percent. The extent of the high momentum fluid surrounding the wake is correctly predicted by the numerical simulation. A band of high Mach number fluid is also observed over a range of y/d_{eff} = 4.0 6.0 and across the entire plane. Results for the angled injection cases are compared at x/d_{eff} = 23 showing trends similar to that seen in the normal injection case. In the 10-degree case, the mushroom shaped plume is barely visible and is overwhelmed by the high momentum fluid reorganized into a boundary layer like structure. This is similar to the structure observed in experiments. The behavior can also be seen in the 27.5 and 45-degree cases. The mushroom like plume becomes more predominant with increasing injection angle. Although the height of the reorganized boundary layer like structure is correctly predicted, the penetration height of the wake is over predicted by the CFD simulations. This follows the trend observed at location x/d_{eff} = 8. The alternating bands of high and low speed fluid at the top of the images are also consistent with experimental results. The location however is lower in the CFD simulation results. The width of the wakes is approximately the same as that in experiments. This also follows the trend at location x/d_{eff} = 8. In the 135-degree case the reorganization of the boundary layer structure is not consistent with that found in the lower injection angle cases. Also, the base of the wake region is larger than that in the lower injection angle cases. Results for the high momentum ratio cases and circular injector geometries are presented in appendix B.

Surface Pressure

Experimental measurement of static pressure along the tunnel floor was performed using the Pressure Sensitive Paint (PSP) Uni-FIB provided by ISSI Inc. The paint contains an oxygen permeable binder and an oxygen sensitive probe molecule. The paint is applied to the floor of the tunnel using an airbrush. The paint was cured at 65° C for 30 minutes to reduce temperature sensitivity. With the tunnel in operation, the floor was illuminated with two blue light emitting diode sources. The wavelength of the incident light was 464 nm while that of the emitted light was 650 nm. The emitted light was captured by a Pixelvision Spectra Video 16-bit CCD camera. The image was post-processed for static pressure on the surface. Additional information about the experimental procedure and post-processing may be obtained from Bowersox et al.[28] Measurement using the PSP is a complicated and tedious process in the best of cases. For these experiments, the process was exacerbated by the presence of temperature gradients that exist in the tunnel due to the heating of stagnation air to avoid liquefaction as it expands across the nozzle. The test section was removed from the setup during the heating process to reduce the effect of temperature gradients on the PSP. Uncertainties may exist in the PSP measurements even with all the precautions that were taken.

Comparisons of surface pressure between CFD and experiments follow the outline of the Mach number and total pressure ratio comparisons. Static pressure obtained from both experiments and CFD was normalized by the freestream pressure. The resulting contours plots from CFD and experiments for the 90-degree J_1 case is shown in Fig. 41. The top half of the image is the result from CFD and the bottom half from experiments. The freestream flow is from left to right in the image. Moving from left to right, the increase in pressure across the interaction

shock is seen in both sections around $x/d_{eff} = -2.0$. The CFD result shows pressure changes even a little further ahead of this location. The sensitivity of PSP and the application of paint on the surface may explain this discrepancy. Close to the injector exit, near the leading edge, the pressure is highest on the tunnel floor. The injector exit itself is colored in red indicating that the pressure in the injector is higher than the surface pressure in the tunnel. Experimental values of peak pressure are higher than that obtained by CFD simulations. However, the structure of the shock is similar in both section of the image with the termination occurring near $z/d_{eff} = \pm 4.0$ and $x/d_{eff} = +1.5$. Around the trailing edge of the jet, the flow undergoes expansion leading to lower pressures. This low pressure region is observed in experiments and CFD. The angle of the outer boundary of this region is approximately the same for both cases. The length of this region is slightly larger in the CFD as compared to experiments. The size of the inner core of the low-pressure region is nearly identical for both cases. Beyond the area of low pressure is a narrow region of high pressure around the tunnel centerline. Experimental values for this region are higher than the CFD values indicating a trend similar to that observed near the interaction shock region. Downstream, after x/d_{eff} = 6.0, starts a region where the pressure is close to the freestream pressure. This region expands in the shape of a "V" with the tip located on the centerline of the tunnel.

The 10-degree J_1 case is shown in Fig. 42. The prediction of surface pressure by the numerical simulation follows the trend outlined above for the 90-degree J_1 case. The shape of the shock is similar in both CFD and experiments. The pressure rise across the shock is less than that in the 90-degree J_1 case. The injector exit shows higher pressure in experiments. This is due to the fact that the injector exit is a hole in the floor in the experimental setup and there is no PSP present in this region whereas in the simulation the exit contours show static pressure of the

injected fluid. The low-pressure region near the injector port trailing edge extends all the way to the end of the plotted domain. This region is smaller in experiments. Further downstream, around $x/d_{eff} = 10$, the predicted and measured pressure values are similar.

Figures 43 and 44 show surface pressure contours from CFD and experiments for the 27.5 and 45-degree J_1 cases. Pressure rise across the interaction shock is clearly visible as a region of high pressure wrapping around the jet. The low-pressure wake region is again smaller in area in experiments as compared to CFD. The high-pressure region near the end of the plotted domain in CFD is also observed in experimental results. Results for the 135-degree J_1 case is shown in Fig. 45. The pressure rise across the interaction shock is higher than any of the lower injection angles. This is due to the increased shock strength. The low-pressure wake region area is smaller as compared to other injection angle cases.

Comparison with DES Results from Cobalt

Instantaneous and time-averaged DES results from Cobalt are compared to experimentally obtained results in this section.

Shadowgraph images from DES results are shown in Fig. 46. The interaction shock angle in both the instantaneous and time-averaged results correspond well with the experimental and RANS results shown in Fig. 26. Large scale structures are seen in the plume region indicating a shear layer. The shock waves generated by these structures merge with the recompression shock causing the unsteady behavior of he recompression shock in the instantaneous DES result as seen in the plot. The time-averaged result however has no indication of this behavior and agrees well with the RANS result. Also, no change in the shape of the barrel

shock is observed. The instantaneous oilflow result is compared with experimental data in 47(a). The upstream separation region is over predicted by the DES model as compared to RANS and experiments. The shock boundary layer interaction phenomenon along with the turbulence model switching is responsible for this discrepancy in prediction. Apart from the leading edge separation, all other flow features are adequately captured by the DES model. The time-averaged results indicate behavior similar to the instantaneous results. Additional flow features are seen in the separation region and are discussed in more detail in chapter VI. Pitot pressure and Mach number comparisons between DES and experiments are shown in Figs. 48 and 49. The numerical domain has no symmetry plane and therefore the experimenal domain is not overlaid on the numerical results in order to avoid masking any asymmetry in the flow. The instantaneous and time-averaged results show better agreement with experiments in the plume region as compared to RANS results. The interaction shock heights at different in the $y-z$ plane agree with experimental observations as well as RANS results. The width of the plume in the time-averaged far field is in better agreement with experimental results. The surface pressure contours (see Fig. 49) reflect the observations made in the surface oil flow plots. The pressure rise upstream of the injector in the separation region is seen at $x/d_{eff} = -4.0$ where as it is located at $x/d_{eff} = -2.5$ in RANS results. The size of the low pressure region downstream of the injector is larger than that seen in experiments and is similar to RANS results. There is little difference between the instantaneous and time-averaged DES solutions. The high pressure point just downstream of the low pressure region is also seen in DES results indicating that the structures producing this feature is present in RANS and DES. The high pressure point is a little upstream as compared to the RANS result.

In summary, the simulations indicate that two-equation and DES turbulence

models perform adequately in predicting high-speed jet interaction flows. DES models provide better results in the plume region than RANS models. Surface oil flow visualisation shows that the DES model predicts larger separation region as compared to experiments and RANS results. Surface pressure predictions follow the trend of the oil flow visualisation results. The shock angles obtained from RANS and DES models show good agreement with experiments.

Additional images comparing experimental results to RANS and DES solutions are presented in appendix B.

CHAPTER VI

FLOW STRUCTURE AND TURBULENCE

The flow structure generated by transverse injection into a high-speed cross-flow is highly complex due to the presence multiple shocks, vortex pairs, shear layers and recirculation regions. Additional challenges are introduced in the analysis of these flow fields due to the coupling of these structures to the turbulent transport properties of the flow. A detailed study of the predominant flow structures and there coupling to the flow field turbulence is presented in the following sections.

Results for the 90-degree J_1 case are presented and discussed in detail while discussion of other cases is limited to comparing and contrasting with the 90-degree J_1 case. Understanding three-dimensional flow by observing images on two-dimensional paper is a difficult task. The reader is therefore oriented to the flow field before starting the discussion of the relevant flow structures. The dataset is mirrored across the *x-y* plane in order to give a view of the complete flow field cross section. An isometric view of the overall flow field is shown in Figure 50. Annotations indicate the direction of the freestream flow and the transverse jet. No structures are shown in this figure. Contours on the tunnel floor are that of normalized static pressure. The outer boundary of the domain is also shown in the figure.

Shock Structures

Transverse injection into supersonic flows is characterized by numerous shock structures as discussed previously. Shocks that are of interest are the interaction or bow shock generated due to the obstruction of the freestream flow by the injector

fluid, the recompression shock generated as the freestream flow encounters the shear layer and the barrel shock formed as by the expansion of the underexpanded jet fluid. A lambda shock is also formed upstream of the injector port due to the presence of a separation region created by the interaction shock. The following is a discussion of these shock structures.

Interaction and Recompression Shocks

The presence of objects obstructing the flow in supersonic flows creates disturbances leading to the formation of shock waves. A classic example is the formation of a bow shaped shock upstream of a blunt body in a supersonic flow. The same phenomena leads to the formation of a bow shaped shock, also called as interaction shock, upstream of the injector exit. This shock surface is shown in Fig. 51. The interaction shock surface is obtained using Fieldview's Shock Finder function. As seen in the figure, the shock surface starts just upstream of the injector orifice. The interaction shock is indicated by the black outline on the red shock isosurface. The outline of the mirrored domain is shown to indicate the extent of the shock. The angle of the shock surface along the tunnel centerline decreases with increasing distance from the tunnel floor. This is due to the effect of lower Mach numbers in the incoming freestream boundary layer. An estimate of the shock angle at different y locations is shown in Fig. 52. Globally, the interaction shock structure is reminiscent of a shock produced due to a conical object in supersonic flow.

The recompression shock is created when the freestream flow passes through the interaction shock and encounters the jet plume as it turns in the freestream direction. A contour plot of Mach number on the $x - y$ surface along the tunnel centerline is shown in Fig. 53. The interaction and recompression shock lines are

indicated. The leading edge of the recompression shock is located just downstream of the injector exit, at y/d_{eff} = 1.6 from the tunnel floor. Pressure rise across the recompression shock in the indicated region (green line) is approximately 0.2 p/p_{inf}. This is considerably lower than the pressure jump across the interaction shock, which is 2.5 p/p_{inf}, at the same height from the tunnel floor. The angle of this shock, along the tunnel centerline is indicated in Fig. 53.

Visualizing the recompression shock surface is more difficult since the interaction shock surface obstructs the view. A different orientation, with a view of the recompression shock is shown in Fig. 54. A clear picture of the origin of this shock surface is not available in this view. The lateral extent of this shock is smaller as compared to that of the interaction shock.

An additional shock is generated in the interaction region between the jet and freestream under conditions where δ/d_{eff} is $O(1)$. Since this is the case in the present flow, an additional shock, called the lambda shock is generated in the region ahead of the injector port. This shock is created due to the formation of a separation region ahead of the injector. Contours of pressure on the tunnel center plane are seen in Figure 55. The increase in pressure due to the presence of the lambda shock is indicated at a location upstream of the injector exit. The lambda shock merges with the interaction shock. The distance the lambda shock has to travel before merging with the interaction shock is shortest along the tunnel centerline. Away from the tunnel centerline, it was found that the lambda shock/interaction shock merging location moves further downstream. The shocks do not merge at locations close to tunnel side walls. Isosurfaces of the lambda and interaction shock are shown in Fig. 56. The interaction region is indicated by a green line. Mach number contours are also shown on a lateral plane to indicate the effects of the lambda shock. The separation distance between the interaction

shock and the lambda shock on the tunnel floor increases with increasing lateral distance from the tunnel centerline.

Barrel Shock

The injector fluid static pressure is an order of magnitude higher than that of the freestream fluid. This causes the injector fluid to expand as it enters the tunnel. The expansion of the injector fluid terminates in a shock called the barrel shock. The barrel shock is named for the shape of the shock that is produced when the injector orifice is circular and the ambient fluid is quiescent. As discussed below, the shape of the barrel shock produced in the case of diamond shaped orifices does not resemble the shock produced by circular orifices.

Mach number contours on the tunnel centerline in the region surrounding the injector exit are shown in Fig. 57. The outline of the barrel shock is shown by a black line. The expansion of the injector fluid is indicated by increase in Mach number within the barrel shock. The highest values of Mach number within the barrel shock are around 4.0 and are observed near the trailing edge of the shock. The barrel shock terminates in the jet stream direction through a shock structure called as the Mach disk. This is denoted by the black line in Fig. 58. A plot of Mach number along the green line in Fig. 58 is shown in Fig. 59. It indicates that the flow becomes subsonic as it passes through the Mach disk.

A more thorough study of the structure of the barrel shock is necessary in order to understand the flow around the injector orifice. This is achieved by using numerical schlieren (density gradient magnitude) plots and also an entropy iso-surface to highlight the shock. A series of numerical schlieren plots showing the barrel shock at different x locations are displayed in Fig. 60. It is observed that the

barrel shock starts as a point at the tip of the injector exit upstream of the origin. At location x/d_{eff} = -0.5, shown in Fig. 60 (b), the top surface of the barrel shock is approximately parallel to the tunnel floor. On the plane passing through the origin, Fig. 60(c), the top surface is curved. The lateral edges of the shock top surface have less curvature as compared to the center of the surface. Further downstream, at x/d_{eff} = 0.5, the lateral edges of the top surface are almost parallel to the floor whereas the center of the surface is still curved. The last image is at location x/d_{eff} = 1.0. It shows the trailing edge of the barrel shock. Approximately half of the top surface of the barrel shock at this location is parallel to the tunnel floor. The trailing surface of the shock is shape like a ”V”. This is more clearly shown in Fig. 61 using an entropy isosurface. The isosurface colors show contours of Mach number. As mentioned before, the Mach numbers on the isosurface at the leading edge of the jet are lower as compared to that at the trailing edge. The change in curvature of the top surface at the lateral edges can also be seen in Fig. 61. The leeward surface of the barrel shock is shown in Fig. 62. The shape clearly resembles a ”V” with an included angle of 90 degrees. The fan angle and inclination of this surface are favorable for the formation of interesting vortex structures. The barrel shock also exhibits ”axis-switching”[44], i.e., it expands more in the lateral direction than in the freestream direction. This behavior is also observed in transverse injection with elliptic ports.

Vortex Structures

As mentioned earlier, strong rotating secondary flow is a defining characteristic of JI flows. The salient vortex motions are described in this section. An effective way of analyzing flow structures is to use streamlines. Streamlines are lines in space

that are tangent to the local velocity vector at all points. Streamlines have to be seeded at proper locations in order to highlight different structures in the flow. A good indicator of locations suitable for seeding streamlines is the vortex core. Vortex cores indicate the presence of vortices in the flow field. The post-processing software Fieldview facilitates the extraction of vortex cores using eigenmode analysis. The extracted vortex cores for the 90-degree J_1 case can be seen in Fig. 63. The vortex cores are colored in red. The tunnel floor contours are that of normalized surface pressure. The relevant flow structures are analyzed separately in the next few sections.

Horseshoe Vortex

A vortex is formed upstream of the injector exit due to the obstruction of the freestream flow by the exiting injector fluid. The incoming freestream boundary layer has negative z-vorticity as shown in Fig. 64. Also shown is the injector port with positive z-vorticity at the leading edge. The high pressure due to the injector fluid causes the incoming boundary layer to separate. The prevalent negative z-vorticity leads to the formation of the horseshoe vortex. This vortex is shown in Fig. 65. A close-up of the formation of the horseshoe vortex near the injector leading edge is shown in Fig. 66. Moving away from the tunnel centerline towards the sidewalls, it was found that the horseshoe vortex wraps around the injector exit. The negative z-vorticity is changed to negative x-vorticity on the positive z-axis side and positive x-vorticity on the negative z-axis side. The positive z-axis side is shown in Fig. 67. The core of the horseshoe vortex is composed of fluid from the inner region of the boundary layer as observed in Fig. 66. Additional freestream boundary layer fluid is trapped by this vortex as it wraps around the injector exit.

This is shown in Fig. 68. The separation distance between the arms of this vortex increases as the flow moves downstream.

Leading Edge Mixing Vortex

A pair of vortex cores is present at the leading edge of the injector exit as shown in Fig. 69. This could be an extension of the vortices produced in the injector port boundary layer as illustrated in Fig. 70. Supporting evidence for this can be found at the trailing edge of the injector exit where an additional pair of vortex cores is present as indicated in Fig. 71. An isometric view of the leading edge vortices are shown in Fig. 72. The two vortices undergo lateral separation as the fluid travels downstream. This is due to the expansion of the injector fluid in the lateral direction and is discussed in detail in the relevant section. The maximum separation between the vortices occurs close to the trailing edge of the injector port and is approximately 2.0 d_{eff}. The interaction between the freestream boundary layer fluid and the injector fluid may also be a contributing factor for the formation of this vortex pair. It is observed that this vortex pair entrains fluid from the outer regions of the freestream boundary layer, i.e., the region away from the wall, as well as from the injector as shown in Fig. 72. Thus, this vortex pair could induce enhanced mixing of freestream and injector fluids.

The leading edge vortices colored by the normalized values of the magnitude of vorticity are displayed in Fig. 73. The colors indicate peak values of vorticity near the interaction region between the freestream and the jet. The vorticity levels drop significantly by the time the lateral separation between the vortices reaches a maximum near the injector trailing edge.

Wake Vortex Pair

A pair of vortices is formed on either side of the tunnel centerline near the injector trailing edge as shown in Fig. 74. Fluid from the outer regions of the freestream boundary layer and off the tunnel centerline move over the horseshoe vortex and down into the region on either side of the injector port as shown in Fig. 75. Part of this fluid moves towards the tunnel centerline. This is due to the lower static pressure in the region as it is on the leeward side of the barrel shock. The flow sweeping into this region from either side interacts and gives rise to the wake vortex pair.

The wake vortices form a coherent pair around x/d_{eff} = 3.0. Immediately downstream of this location the wake vortices start to lift off of the tunnel floor due to the action of the CVP. This is discussed elsewhere in this section. The local reduction in area created in the region between this vortex pair causes the supersonic flow to decelerate and leads to the spot with increased pressure as seen in the surface pressure plots discussed previously. This can be observed in Fig. 76.

Further downstream, it was found that the wake vortex lifts completely off of the tunnel floor and merges with the CVP (described in the next section). An end view indicating this is shown in Fig. 77. The increase in lateral separation between the vortices and their curvature indicates that the merging process is completed close to the end of the domain i.e., after x/d_{eff} = 20.0. Mach number contours on the end plane of the domain are shown to indicate the position of the CVP.

Axial Counter-rotating Vortex Pair

The primary mechanism for the mixing of freestream and injector fluid is the CVP. The composition of this vortex pair can be observed in Fig. 78. The interaction

between the injector fluid and the freestream boundary layer is the source of the formation of this vortex pair. Further analysis requires the dissection of this interaction. The leading edge mixing mechanism, formed due to this interaction, eventually forms the axial CVP. The axial ejection mechanism of the lateral counter-rotating vortex (LCVP) pair (described in the next section) also contributes to the formation of this vortex pair. The leading edge vortex and the axial ejection of the LCVP are shown as red and blue streamlines respectively in Fig. 78.

Apart from the mechanisms mentioned above, two other sources contribute to the CVP. These are the lateral ejection mechanism from the LCVP and the wake vortex mechanism describe previously. Of all these vortex pairs, the wake vortices are the only ones with vorticity opposite to that of the CVP.

A study of the layers within the CVP reveals interesting details about the origin of the streamlines. Layers with the core are identified using values of axial vorticity. Streamlines passing through the core of the CVP structures are seen in Fig. 79. The lateral plane is colored using values of axial vorticity. The core is essentially made up of injector fluid. Specifically, fluid from the injector port boundary layer, a little downstream of the injector leading edge, is transported to the core of the CVP. Streamlines in the next layer are those originating from the leading edge mixing vortices as shown in Fig. 80. The next layer of streamlines, seen in Fig. 81 mostly originates from the leeward side of the injector port with little content from the windward side or the freestream boundary layer. The last layer of streamlines, shown in Fig. 82, indicates the presence of freestream boundary layer as well as injector fluid.

Lateral Counter-rotating Vortex Pair

A new vortex pair has been identified in this flow. The axes of this vortex pair are oriented in the z-axis direction. The cores of this vortex pair are shown in Fig. 83. This new structure is particularly interesting since it has the potential to serve as a gasdynamically induced flame holder. An attempt has been made to explain the formation of this vortex pair in the following paragraph.

After analyzing the flow structures in detail, it was found that the LCVP formations is closely coupled to the barrel shock shape. The barrel shock shape is described in section 6.1.2. The shape of the barrel shock is significantly different for the diamond injector configuration as compared to that generated by a circular orifice. The barrel shock structure generated by the 90-degree diamond injector is shown in Fig. 84. The leeward side of the barrel shock for the 90-degree J_1 case is a surface normal to the freestream direction as indicated in Fig. 84. The formation of this shock surface is analogous to a Japanese "sensu" fan, i.e., the shock seems to expand in the lateral direction as the fluid exits the injector port and forms a shape similar to a "V". This shock shape facilitates the formation of the LCVP. The low pressures generated on the leeward side of the barrel shock causes part of the incoming freestream boundary layer fluid to lift off of the tunnel floor. This fluid interacts with the injector fluid that is turning in the freestream direction. A recirculation region is set in motion due to this interaction. This recirculation region contains a pair of vortices with axes in the z-direction. The top vortex rotates in the clockwise direction and the bottom vortex in the anti-clockwise direction forming an "8" shaped structure as observed from the positive z-axis. The structure of this vortex pair is shown in Fig. 85.

Further analysis of this vortex pair reveals interesting features. A pair of cone

shaped structures is formed at the downstream edge of this vortex pair. This is displayed in Fig. 86. Part of the fluid rotating in the top vortex is captured in the cone shaped structures. At the tip of these cones, the fluid splits into two channels. One of the channels is ejected in the downstream direction while the other channel is ejected upstream. The channel that is ejected upstream is engulfed by the top vortex. Another ejection mechanism is the capture and transport of fluid in the LCVP by the axial CVP as it moves past the barrel shock. This is shown in Fig. 87.

It is observed that the LCVP entrains fluid from the injector. This enables the vortex pair to act as a potential flame holder in scramjet engines. The advantages of using this structure for flame holding as compared to cavity flame holders include reduced heat transfer to the wall since the vortices are not in contact with the tunnel floor and elimination of instabilities induced in the flow due to the presence of cavities. Another important requirement for this structure to act as a flame holder is the residence time of the fluid passing through this vortex pair. The average residence time of streamlines passing through this vortex pair is then compared to that of a streamline in the freestream. Using the duration output of streamlines in Fieldview the average residence time of streamlines passing through the LCVP is estimated as 2 ms while that of the streamline in the freestream is 0.2 ms. In order to perform a more meaningful comparison a streamline was tagged in the boundary layer at approximately the same height as that of the streamlines passing through the LCVP. The duration of this streamline is found to be 0.4 ms as it travels through the domain. The flame holding properties of the LCVP are enhanced because the residence times of the streamlines passing through the LCVP are approximately an order of magnitude higher that that of streamlines in the freestream.

Injector Fluid Plume Structure

As mentioned before, one of the primary applications of transverse jet injection is in scramjets for fuel injection. The combustion characteristics of fuel injected through the orifice are affected to a certain extent by the structure of the plume. It is therefore essential to understand the structure of the jet plume.

The injector fluid plume structure is strongly coupled with the vortices discussed in the previous section. Because of this there are areas of overlap between the previous section and this discussion. Following the trend in the previous section, the jet plume structure is analyzed by observing fluid from different regions of the injector exit. These regions are illustrated in Fig. 88. Streamlines from the injector boundary layer upstream of the origin, which is located at the center of the injector exit orifice and is denoted by region 1 in Fig. 88, are shown in Fig. 89. The view is from the negative x-axis. It is observed that the injector boundary layer fluid interacts strongly with the freestream, leading to the formation of the leading edge mixing vortices. This can be clearly seen in Fig. 89. The barrel shock is also shown to put the size of these structures in perspective. The cross-sectional area of the vortices formed by these streamlines experiences at least two jumps as the streamlines travel downstream. The first of these jumps occurs at $x/d_{eff} = 0.5$ corresponding to the peak pressure behind the interaction shock on either side of the injector and is shown in Fig. 90. The second jump is a little more gradual and starts at the termination of the barrel shock. Streamlines originating in the injector boundary layer downstream of the origin (region 2) are shown in Fig. 91. It is observed that most of these streamlines are engulfed in the CVP. However, fluid at the trailing edge of the jet orifice is captured by the LCVP. This was also observed in the LCVP structure discussed previously. The entrainment of the jet fluid in the

LCVP is shown in Fig. 92.

Streamlines from the core of the injector orifice denoted by region 3 can be seen in Fig. 93. The abrupt change in direction of the streamlines as they pass through the barrel shock is observed. The barrel shock is partially transparent in the figure. in order to show streamlines inside the shock. Fluid on either side of the x-y plane in the jet core is not entrained in the CVP as see in Fig. 94 while streamlines closer to the x-y plane moves up and over the LCVP and come up between the CVP cores from underneath. The red and blue streamlines in Fig. 94 are from the injector boundary layer.

Streamlines from regions 4 and 5 are shown in Fig. 95. It was observed in a previous section that the core of the CVP has streamlines originating from a region close to the leading edge of the injector. However, streamlines from region 4 (red), which is close to the leading edge of the injector, are shown to form one of the outer layers of the CVP and are wrapped around the streamlines originating from region 5. The end view is shown in Fig. 96 shows a clear picture of these streamlines as they are entrained in the CVP.

Velocity/Vorticity Analysis

Further analysis of freestream and injector fluid interaction is performed using two-dimensional velocity vectors in x and y planes and corresponding components of vorticity. In the images displayed, the left half of the displayed plane is populated by planar velocity vectors while the right half has contours of the corresponding vorticity component.

The initial interaction region between the freestream and the jet is seen in Fig. 97. The location of the plane is x/d_{eff} = -1.0. The vorticity is normalized by

V/d_{eff} and the displayed contour scale is from -1.0 (blue) to +1.0 (red). The positive x- vorticity at the leading edge is due to the shearing action between the injection and freestream fluid. The $y - z$ velocity vectors on the left indicate a vortex formation close to the tunnel floor at this x/d_{eff} location. This is the initial section of the leading edge vortex discussed previously. The vectors also show that the interaction shock height at this location is about y/d_{eff} = 1.0. The incoming boundary layer is displaced in the lateral direction and can be observed in both the vorticity and velocity plots. At x/d_{eff} = -0.5 the size of the leading edge vortex region, indicated by a blue line, is bigger as observed in Fig. 98. The lateral expansion of the jet is also apparent from this image. The height of the interaction shock is 1.5 y/d_{eff}. The thickness of the lateral boundary layer is also larger at this location. Further downstream, at x/d_{eff} = +1.0, the leading edge vortex has moved away from the tunnel floor and the core is at location z/d_{eff} = 0.8. The lateral boundary layer is no longer visible in the domain plotted in Fig. 99. The interaction shock height is approximately 2.2 y/d_{eff} while the width is greater than 1.5 z/d_{eff}. The "V" shape of the trailing edge of the barrel shock is seen at location x/ deff = +1.0 as shown in Fig. 100. The leading edge vortex pair has moved further away from the wall and the core is at location z/d_{eff} = 1.0 and y/d_{eff} = 0.6. A new region of vorticity is also seen at the lateral ends of the barrel shock. This can be attributed to the action of the leading edge vortex on the fluid passing over the flat section of the barrel shock. Beyond the trailing edge of the barrel shock, at x/d_{eff} = +1.5, the leading edge vortex is carried downstream and leads to the vorticity of the opposite sign on the inside part of the "V" region. This is seen in Fig. 101. The additional region of vorticity seen in the previous image is detached from the main structure. The axial vortex pair resulting from the LCVP is seen at location y/d_{eff} = 1.0 and z/d_{eff} = 0.1. The boundaries of the interaction

shock are beyond that of the domain plotted. Further evolution of these vortices can be seen in the sequence of images plotted in Fig. 102. They show the formation of the wake vortex at x/d_{eff} = +2.0. The additional vorticity of opposite sign on the inside part of the "V" region starts to dissipate at x/d_{eff} = +3.0. At x/d_{eff} = +4.0 only three dominant structures left in the flow field. These eventually merge to form the CVP structure.

Velocity vectors and vorticity contours are plotted on y planes in Fig. 103. At y/d_{eff} = 0.25 the wrapping of freestream fluid around the injector is evident by the existence of vorticity around the injector port. The change in direction of the freestream fluid towards the side walls is observed around the leading edge of the injector port. The vectors change direction again, this time towards the tunnel centerline, downstream of the origin. This is indicated in Fig. 103 (a). Downstream of the injector, the accelerating fluid creates a region of alternating vorticity. A vortex is observed immediately downstream of the injector port in Figs. 103 (b) and (c) showing planes at y/d_{eff} = 0.50 and 0.75. These vortices are the downward pointing arms of the top vortex in the LCVP. The leading edge of the interaction shock, which causes the freestream fluid to change direction, is indicated in Fig. 103 (d). At y/d_{eff} = 1.5, there is comparatively little interaction between the two different streams as seen in Fig. 103 (e).

Shear Layers

This flowfield is characterized by two shear layers of note, one of which plays a significant role in injector and freestream fluid mixing. The first shear layer is formed at the leading edge of the injector as the freestream fluid impinges on the injector fluid, forcing it to turn downstream. As the injector fluid turns downstream,

the freestream engulfs the injector fluid creating an interaction region around the injector port exit. This interaction is illustrated in Fig. 104. The interaction between the freestream and injector fluids along the $z/d_{eff} = 0.0$ plane and around in injector port is indicated. On the same image, another shear layer is indicated. This second and dominant shear layer is downstream of the injector exit wherein the freestream flow nearly surrounds the jet plume. The velocity magnitude at $x/d_{eff} = 15.0$ and $z/d_{eff} = 0.0$ is plotted in Fig. 105 and indicates that there exists a velocity difference of approximately 300 m/s between the plume and the freestream.

Low Pressure Angled Injection

The advantages provided by using diamond shaped injectors are enhanced in certain cases by injecting at angles other then 90-degrees. For example, the interaction shock angle reduces with decrease in injection angle. This leads to lower total pressure loss across the shock and hence lower drag, which is ideal for scramjet applications. Injection angles over 90-degrees increase the lateral penetration of injector fluid into the freestream.

Interaction Shock

The effect of angled injection on the interaction shock is to increase or decrease its inclination angle. For the low pressure cases simulated in this work, the interaction shocks are shown in Fig. 106. As expected, lower injection angles lead to lower interaction shock angles. The 135-degree injection case differs from this trend in that the initial shock angle seems to be lower than that for the 90-degree case. However, upon closer inspection, a bump is observed at the location where

the injector fluid impinges on the interaction shock. Downstream of this bump, the inclination increases again as a weak shock wave originating from the inlet of the domain merges with the interaction shock. The weak shock wave is due the perturbation of the upstream boundary layer by the large separation region induced due to the strong interaction shock.

Vortex Cores

Vortex cores for the 10-degree J_1 case are plotted in Fig. 107. It is observed that the leading edge mixing vortex core extends into the CVP core without any discontinuities. This supports the conclusion previously drawn about the contribution of the leading edge vortex to the formation of the CVP. The cores of the wake vortices along the floor indicate that there is no movement away from the tunnel floor. Absence of a vortex core around the injector indicates that that horseshoe vortex is weak compared to that in the 90-degree J_1 case.

The leading edge mixing vortex core in the 27.5-degree J_1 case, seen in Fig. 108, has more penetration in the transverse direction. There is a clear discontinuity in the cores as they transition into the CVP. The wake vortices follow the tunnel floor as seen in the 10-degree J_1 case while the horseshoe vortex is more pronounced. This same trend is observed for the 45-degree J_1 case as seen in Fig. 109. Vortex cores for the 135-degree J_1 case are more disorganized than the lower injection angle cases. Additional cores are seen around the injector port leading edge. There is also evidence of a LCVP like structure behind the barrel shock as indicated in Fig. 110

Barrel Shock

Numerical schlieren images of the barrel shock are shown for the angled injection cases in Figs. 111 - 114. The views also show the interaction shock shape. The magnitude of the density gradient indicates the strength of the shock which increases with increasing injection angle. The formation of the leading edge vortex can be clearly seen in the schlieren images. The shear layer formed near the injector is also indicated. The barrel shock extend downstream of the injector trailing edge for lower injection angles. The top surface of the barrel shock is parallel to the tunnel floor around z/d_{eff} = 0.0. Downstream of the injector, two distinct shock arms are seen on the top surface of the barrel shock. This is seen in both the 27.5 and 45-degree cases. The vortices generated are seen wrapped around the top arm of barrel shock. The barrel shock for the 135-degree J_1 case shows that the shock is much stronger upstream of the origin. The top surface of the shock is similar that in the normal injection case.

Injector Streamlines

Injector fluid streamlines for the low pressure angled injection cases are shown in Figs. 115 - 130 Region 1 streamlines give a good indication about the lateral penetration of the injector fluid for different injection angles. For the 10-degree case, shown in Fig. 115, it is observed that streamlines from region 1 are restricted to approximately the width of the injector port. The CVP structure downstream of the injector does not exhibit the large scale rotating motion that is present in the normal injection case. Increase in injection angle to 27.5 and 45-degrees leads to the development of these large rotating structures in the CVP. The barrel shocks are also shown along with the region 1 stream lines for the 27.5 and 45-degree

cases in Figs. 119 and 123. The large scale rotation may be caused due to the pronounced axis switching exhibited by the barrel shocks. The larger lateral separation of the injector fluid in these cases helps amplify the large scale rotation immediately downstream of the barrel shock. The upstream inclination of the injector fluid in the 135-degree case, Fig. 127, creates a strong interaction with the freestream fluid leading to a relatively disorganized CVP structure as compared to other injection angle cases.

Turbulence - RANS

The Reynolds shear stress values are extracted from the TKE and eddy viscosity results output from GASP. This was done using the Boussinesq approximation given by

$$\bar{\rho}\tau_{ij} \equiv \overline{-\rho u_i'' u_j''} = 2\mu_t \left(S_{ij} - \frac{1}{3}\frac{\partial u_k}{\partial x_k}\delta_{ij} \right) - \frac{2}{3}\bar{\rho}k\delta_{ij} \tag{74}$$

The values are scaled by the local mean density values. This is done in order to ease the comparison of RANS and DES results which are presented later in this chapter.

The axial stresses (τ_{11}, τ_{22} and τ_{33}) at location $x/d_{eff} = 8.0$, obtained using the Boussinesq relation, are plotted as contours in Figs. 131, 132 and 133. The left half of the images have contours of TKE for comparison. The span wise extents are from $z/d_{eff} = -4.0$ to $z/d_{eff} = +4.0$ while the height is from $y/d_{eff} = 0.0$ to $y/d_{eff} = 7.0$. From Fig. 131, it is seen that the values of τ_{11} are higher around the top edge of the injector fluid plume. Higher values are also observed within the wake vortices which are off the tunnel floor at this x/d_{eff} location. These two locations constitute the largest regions of peak τ_{11}. A smaller τ_{11} peak is also

observed in the region of one of the vortex pairs that contribute to the axial CVP. A lower TKE and τ_{11} region is observed just underneath the top edge of the injector fluid plume. Contours of τ_{22}, shown in Fig. 132, indicate higher values near the peak of the injector plume, similar to τ_{11}. However, this is this only location with such high values. A band of moderately high values are observed near the span wise outer boundary of the plume region and also in the wake vortices. The plots of τ_{33} are similar to the τ_{11} plots in that higher values are observed in the wake vortices. The plume peak region observed in τ_{11} and τ_{22} are non-existent. However, there is a region of moderately high τ_{33} near the span wise edge of the plume peak. The low values observed inside the plume peak in similar to that seen in plots of τ_{11}. There is also region of relatively low axial stresses just outside the plume region. This feature is noticed in all three plots.

At $x/d_{eff} = 23.0$, the plume region has a more circular structure as seen in Figs. 134, 135 and 136. The band of high TKE stretches across the entire outer edge of the plume with the ends of the band curving in towards the centers of the CVP. The highest values of t11 are again observed near the peak of the plume region, similar to location $x/d_{eff} = 8.0$. The low values observed within the two cores are approximately collocated with the centers of the CVP. A tear drop shaped region of low τ_{11} is observed around the center of the plume. The contours of τ_{22} clearly indicate a kidney-bean shaped region within the CVP. A larger area of moderately high values are observed near the bottom edge of the plume while the highest values are observed near the peak of the plume. The peak values of τ_{33} occur around the span wise boundary of the plume. This is similar to the contours at location $x/d_{eff} = 8.0$. Low values are observed near the centers of the CVP.

Contour plots of the turbulence shear stress, at location $x/d_{eff} = 8.0$, are shown in Figs. 137, 138 and 139. The entire cross-sectional plane is colored by the same

variable. The scales are changed as compared to the axial stress plots in order to provide a better view of the flow features. Also, since the RANS simulations were performed using a symmetry plane, the data on the left half of the images were mirrored from the right half. The mirrored data were modified based on the variables and the symmetry plane i.e., stresses involving fluctuations in the z direction were scaled with -1.

The τ_{12} contour plots show a big band of high negative values around the top part of the plume region and including the recompression shock. High positive values are observed just underneath the wake vortices and also in the upwash region of the CVP and the boundary layer. Contours of τ_{23} show high positive and negative values all around the periphery of the plume and within the wake vortices. Regions of slightly lower values are observed outside of the plume region. The τ_{31} plot has high values only near the top edge of the plume and within the wake vortices.

The plots of shear stresses at $x/d_{eff} = 23.0$ are shown in Figs. 140, 141 and 142. The τ_{12} contours show peak values near the bottom edge and the top arch of the plume. Results for τ_{23} do not show the banded region observed in plots of τ_{12}. The regions are more localized with some activity at the span wise extents of the plume. The plot of τ_{31} gives a clearer picture of the flow structure by highlighting the CVP as well as the wake vortices that are moving between the CVP.

In all these contours plots, the regions of high values are clustered around the wake region boundary and the downstream vortices. The different peak locations of the various variables may be explained by considering the shearing action of the freestream fluid and the injector plume. For example, shear stresses with the z component tend to exhibit high values near the span wise extent of the plume. This is the location where the fluid in the plume interacts with the freestream fluid

in the next z location.

Reynolds stress plots on the $z/d_{eff} = 0.0$ plane are shown in Figs. 143 - 148. The plots exhibit higher levels of turbulence along the peak of the plume. The LCVP location is highlighted by stresses with the z component of the fluctuations. A distinctive feature observed in all of these plots is the increased level of stresses at the location of the merging of the wake vortices.

Turbulence DES

Time-averaged axial turbulent stresses and the corresponding turbulent kinetic energy are plotted in Figs. 149 - 151. The x/d_{eff} location of these planes is 8.0. The left half of the image has contours of TKE while the right half is that of the axial stresses. The turbulent stresses are those that are resolved by the DES model. The Boussinesq approximation is not used in this case. The results are normalized by the square of the freestream velocity. Results indicate that the levels of TKE and the axial turbulent stresses are relatively lower near the outer edge of the plume when compared to RANS results. However, levels within the wake vortex are in good agreement between the two models. The vertical extent of the plume is lower as compared to the RANS model results. This was also observed in the experimental comparisons made in chapter V.

The comparison at location $x/d_{eff} = 23.0$ (see Figs. 152 - 154) of the axial stresses shows that the vertical location of the TKE peak is in relatively good agreement between RANS and DES. The TKE spread area is larger than the corresponding RANS result. Also, the structure of the plume is not as defined in DES as it is in RANS. The τ_{33} stress values are somewhat similar in the fact that the peak values occur at the span wise extent of the plume. The values are however slightly

larger in the RANS results.

The shear stresses at locations $x/d_{eff} = 8.0$ and $x/d_{eff} = 23.0$ are plotted in Figs. 155 - 160. The near-field structure of τ_{12} is more disorganized in the DES results. This is in contrast to the τ_{23} which exhibits a structure somewhat similar to that in the RANS result. The values of τ_{31} at the peak of the plume shown similar structure in both models. Within the plume, the structure is more disorganized. The far-field structure of τ_{12} is strikingly similar in DES and RANS. A large band of high negative values at the top of the plume is offset by two distinct high positive values near the bottom of the plume. The RANS plots of τ_{23} in the far-field have a dumb-bell shaped structure and is smaller than the similar structure found in DES plots. Results for τ_{31} follow the trend of τ_{12}

Plots of DES turbulent stresses along the tunnel center plane ($z/d_{eff} = 0.0$, see Figs 161 - 166) consistently show a larger shear layer at the top of the plume in the far-field region. The interaction of the wake vortices are highlighted by the DES results similar to RANS.

CHAPTER VII

VORTICITY TRANSPORT ANALYSIS

The datasets obtained from numerical simulations of transverse jet injection into high speed crossflows are subjected to vorticity transport analysis in order to estimate the effects of different mechanisms on vortex structures. Specifically, the effects of baroclinic torque, compressibility and vortex stretching mechanisms on the LCVP are investigated.

Governing Equation

The compressible form of the vorticity transport equation is derived by using the curl operator on the non-conservation form of the Favre averaged equations. The resulting equation is given below.

$$\frac{D\omega}{Dt} = -\omega\left(\nabla.\mathbf{V}\right) + \left(\omega.\nabla\right)\mathbf{V} - \nabla\times\left(\frac{1}{\rho}\nabla p\right) + \frac{1}{\rho}\nabla\times\left(\nabla.\mathbf{\Pi}\right) + \nabla\left(\frac{1}{\rho}\right)\times\left(\nabla.\mathbf{\Pi}\right) \quad (75)$$

The terms in equation 75 are grouped using braces. The term on the left hand side of equation 75 represents vorticity convection. The first term on the right had side is the compressibility term since this would be zero in incompressible flows. The second and third terms denote three-dimensional vortex stretching and baroclinic torque. The fourth term is the anisotropic torque while the fifth term represents stress torque.

The above equation is modified using the following vector identities.

$$\nabla\times\left(\phi\Phi\right) = \phi\nabla\times\Phi + \nabla\phi\times\Phi \quad (76)$$

$$\nabla \times \nabla\phi = 0 \tag{77}$$

$$\nabla\left(\frac{1}{\phi}\right) = -\frac{1}{\phi^2}\nabla\phi \tag{78}$$

In the above equations, ϕ is a scalar and Φ is a vector variable. The modified equation is given as

$$\begin{aligned}\frac{D\omega}{Dt} = -\omega\left(\nabla.\mathbf{V}\right) + \left(\omega.\nabla\right)\mathbf{V} + \left(\frac{\left(\nabla\rho\right)\times\left(\nabla p\right)}{\rho^2}\right) \\ +\frac{1}{\rho}\nabla\times\left(\nabla.\mathbf{\Pi}\right) - \left(\frac{\left(\nabla\rho\right)\times\left(\nabla.\mathbf{\Pi}\right)}{\rho^2}\right)\end{aligned} \tag{79}$$

In the above equation the quantity Π is a tensor. The divergence of this tensor can be evaluated using the following relation.

$$\left(\nabla.\mathbf{\Pi}\right)_i = \sum_j \left(\partial\mathbf{\Pi}_{ji}/\partial x_j\right) \tag{80}$$

The equation shown in 79 is a vector equation with three components, one each for the x, y and z vorticities. Assuming steady state conditions, the full form of the three transport equations are given below.

x-vorticity:

$$\begin{aligned}\mathbf{V}_x\frac{\partial\omega_x}{\partial x} + \mathbf{V}_y\frac{\partial\omega_x}{\partial y} + \mathbf{V}_z\frac{\partial\omega_x}{\partial z} = -\omega_x\frac{\partial\mathbf{V}_x}{\partial x} - \omega_x\frac{\partial\mathbf{V}_y}{\partial y} - \omega_x\frac{\partial\mathbf{V}_z}{\partial z} \\ +\omega_x\frac{\partial\mathbf{V}_x}{\partial x} + \omega_y\frac{\partial\mathbf{V}_x}{\partial y} + \omega_z\frac{\partial\mathbf{V}_x}{\partial z} \\ +\frac{1}{\rho^2}\left[\frac{\partial\rho}{\partial y}\frac{\partial p}{\partial z} - \frac{\partial\rho}{\partial z}\frac{\partial p}{\partial y}\right] \\ +\frac{1}{\rho}\left[\frac{\partial T_3^L}{\partial y} - \frac{\partial T_2^L}{\partial z}\right] + \frac{1}{\rho}\left[\frac{\partial T_3^T}{\partial y} - \frac{\partial T_2^T}{\partial z}\right] \\ -\frac{1}{\rho^2}\left[T_3^L\frac{\partial\rho}{\partial y} - T_2^L\frac{\partial\rho}{\partial z}\right] - \frac{1}{\rho^2}\left[T_3^T\frac{\partial\rho}{\partial y} - T_2^T\frac{\partial\rho}{\partial z}\right]\end{aligned} \tag{81}$$

y-vorticity:

$$\begin{aligned}\mathbf{V}_x\frac{\partial\omega_y}{\partial x}+\mathbf{V}_y\frac{\partial\omega_y}{\partial y}+\mathbf{V}_z\frac{\partial\omega_y}{\partial z}=&-\omega_y\frac{\partial\mathbf{V}_x}{\partial x}-\omega_y\frac{\partial\mathbf{V}_y}{\partial y}-\omega_y\frac{\partial\mathbf{V}_z}{\partial z}\\&+\omega_x\frac{\partial\mathbf{V}_y}{\partial x}+\omega_y\frac{\partial\mathbf{V}_y}{\partial y}+\omega_z\frac{\partial\mathbf{V}_y}{\partial z}\\&+\frac{1}{\rho^2}\left[\frac{\partial\rho}{\partial z}\frac{\partial p}{\partial x}-\frac{\partial\rho}{\partial x}\frac{\partial p}{\partial z}\right]\\&+\frac{1}{\rho}\left[\frac{\partial T_1^L}{\partial z}-\frac{\partial T_3^L}{\partial x}\right]+\frac{1}{\rho}\left[\frac{\partial T_1^T}{\partial z}-\frac{\partial T_3^T}{\partial x}\right]\\&-\frac{1}{\rho^2}\left[T_1^L\frac{\partial\rho}{\partial z}-T_3^L\frac{\partial\rho}{\partial x}\right]-\frac{1}{\rho^2}\left[T_1^T\frac{\partial\rho}{\partial z}-T_3^T\frac{\partial\rho}{\partial x}\right]\end{aligned}\tag{82}$$

and z-vorticity:

$$\begin{aligned}\mathbf{V}_x\frac{\partial\omega_z}{\partial x}+\mathbf{V}_y\frac{\partial\omega_z}{\partial y}+\mathbf{V}_z\frac{\partial\omega_z}{\partial z}=&-\omega_z\frac{\partial\mathbf{V}_x}{\partial x}-\omega_z\frac{\partial\mathbf{V}_y}{\partial y}-\omega_z\frac{\partial\mathbf{V}_z}{\partial z}\\&+\omega_x\frac{\partial\mathbf{V}_z}{\partial x}+\omega_y\frac{\partial\mathbf{V}_z}{\partial y}+\omega_z\frac{\partial\mathbf{V}_z}{\partial z}\\&+\frac{1}{\rho^2}\left[\frac{\partial\rho}{\partial x}\frac{\partial p}{\partial y}-\frac{\partial\rho}{\partial y}\frac{\partial p}{\partial x}\right]\\&+\frac{1}{\rho}\left[\frac{\partial T_2^L}{\partial x}-\frac{\partial T_1^L}{\partial y}\right]+\frac{1}{\rho}\left[\frac{\partial T_2^T}{\partial x}-\frac{\partial T_1^T}{\partial y}\right]\\&-\frac{1}{\rho^2}\left[T_2^L\frac{\partial\rho}{\partial x}-T_1^L\frac{\partial\rho}{\partial y}\right]-\frac{1}{\rho^2}\left[T_2^T\frac{\partial\rho}{\partial x}-T_1^T\frac{\partial\rho}{\partial y}\right]\end{aligned}\tag{83}$$

where

$$\mathbf{\Pi}=\mathbf{\Pi}_{ij}^L+\mathbf{\Pi}_{ij}^T$$

$$\mathbf{\Pi}_{ij}^L=\mu\left(\frac{\partial u_i}{\partial x_j}+\frac{\partial u_j}{\partial x_i}\right)+\lambda\delta_{ij}\nabla.\mathbf{V}$$

$$\mathbf{\Pi}_{ij}^T=2\mu_T\left(S_{ij}-\frac{1}{3}\frac{\partial\bar{u}_k}{\partial x_k}\delta_{ij}\right)-\frac{2}{3}\bar{\rho}k\delta_{ij}$$

$$S_{ij}=\frac{1}{2}\left(\frac{\partial u_i}{\partial x_j}+\frac{\partial u_j}{\partial x_i}\right)$$

$$\mathbf{\Pi}_{xx} = 2\mu\frac{\partial u}{\partial x} + \lambda\frac{\partial u_i}{\partial x_i} + 2\mu_T\left(\frac{\partial u}{\partial x} - \frac{1}{3}\frac{\partial u_i}{\partial x_i}\right) - \frac{2}{3}\bar{\rho}k$$

$$\mathbf{\Pi}_{yy} = 2\mu\frac{\partial v}{\partial y} + \lambda\frac{\partial u_i}{\partial x_i} + 2\mu_T\left(\frac{\partial v}{\partial y} - \frac{1}{3}\frac{\partial u_i}{\partial x_i}\right) - \frac{2}{3}\bar{\rho}k$$

$$\mathbf{\Pi}_{zz} = 2\mu\frac{\partial w}{\partial z} + \lambda\frac{\partial u_i}{\partial x_i} + 2\mu_T\left(\frac{\partial w}{\partial z} - \frac{1}{3}\frac{\partial u_i}{\partial x_i}\right) - \frac{2}{3}\bar{\rho}k$$

$$\mathbf{\Pi}_{xy} = \mathbf{\Pi}_{yx} = \left(\frac{\partial u}{\partial y} + \frac{\partial v}{\partial x}\right)(\mu + \mu_T)$$

$$\mathbf{\Pi}_{yz} = \mathbf{\Pi}_{zy} = \left(\frac{\partial v}{\partial z} + \frac{\partial w}{\partial y}\right)(\mu + \mu_T)$$

$$\mathbf{\Pi}_{zx} = \mathbf{\Pi}_{xz} = \left(\frac{\partial w}{\partial x} + \frac{\partial u}{\partial z}\right)(\mu + \mu_T)$$

$$T_1^L = \frac{\partial \mathbf{\Pi}_{xx}^L}{\partial x} + \frac{\partial \mathbf{\Pi}_{yx}^L}{\partial y} + \frac{\partial \mathbf{\Pi}_{zx}^L}{\partial z}$$
$$T_2^L = \frac{\partial \mathbf{\Pi}_{xy}^L}{\partial x} + \frac{\partial \mathbf{\Pi}_{yy}^L}{\partial y} + \frac{\partial \mathbf{\Pi}_{zy}^L}{\partial z}$$
$$T_3^L = \frac{\partial \mathbf{\Pi}_{xz}^L}{\partial x} + \frac{\partial \mathbf{\Pi}_{yz}^L}{\partial y} + \frac{\partial \mathbf{\Pi}_{zz}^L}{\partial z}$$

$$T_1^T = \frac{\partial \mathbf{\Pi}_{xx}^T}{\partial x} + \frac{\partial \mathbf{\Pi}_{yx}^T}{\partial y} + \frac{\partial \mathbf{\Pi}_{zx}^T}{\partial z}$$
$$T_2^T = \frac{\partial \mathbf{\Pi}_{xy}^T}{\partial x} + \frac{\partial \mathbf{\Pi}_{yy}^T}{\partial y} + \frac{\partial \mathbf{\Pi}_{zy}^T}{\partial z}$$
$$T_3^T = \frac{\partial \mathbf{\Pi}_{xz}^T}{\partial x} + \frac{\partial \mathbf{\Pi}_{yz}^T}{\partial y} + \frac{\partial \mathbf{\Pi}_{zz}^T}{\partial z}$$

Algorithm and Procedure

The terms in equations 81, 82, and 83 are evaluated using two FORTRAN programs, one each for the structured and unstructured grids. The inputs for the program are the grid file and steady state RANS solution and the time averaged DES solution output. The following variables are used in the program; (a) density, (b) velocity components, (c) pressure, and (d) Reynolds stress tensor components.

Solution results are stored at grid points within the domain. Time averaged temperature is calculated using the ideal gas relation and dynamic viscosity is calculated using Sutherlands law.

Structured Grids

For the structured grid analysis, the first step is to read the nodal coordinates of the grid and also the average data for each cell in the domain. These results are obtained from GASP. Using the nodal coordinates, the normal vectors of the cell faces are evaluated along with cell face areas and cell volumes. The gradient theorem is then used to form the necessary derivatives of the variables. These derivatives are then used in calculating the terms in the vorticity transport equation.

The surface area of a cell face is evaluated using the relation. See Fig. 167 for the node references.

$$\mathbf{S}_{ABCD} = \frac{1}{2}\left(\mathbf{r}_{AC} \times \mathbf{r}_{BD}\right) \tag{84}$$

Each hexahedron in the structured grid is divided into three pyramids as shown in Fig. 168. The total volume of the hexahedron is the sum of the volumes of these pyramids.

$$V_{hex} = V_{CBFEA} + V_{CFGHE} + V_{CAEHD} \tag{85}$$

The volume of a pyramid is calculated using the relation.

$$V_{CBFEA} = \frac{1}{24}\left(\mathbf{r}_{CB} + \mathbf{r}_{CF} + \mathbf{r}_{CE} + \mathbf{r}_{CA}\right) \cdot \left(\mathbf{r}_{BE} \times \mathbf{r}_{FA}\right) \tag{86}$$

The gradient theorem, used to evaluate the required derivatives, is given below.

$$\frac{1}{V}\iiint_V \nabla\phi dV = \frac{1}{V}\iint_A \phi\hat{n}dA \tag{87}$$

For example, the x-derivative of the variable ϕ is given by

$$\frac{1}{V}\iiint_V \frac{\partial \phi}{\partial x} dV = \frac{1}{V}\iint_A \phi \hat{n}_x dA \tag{88}$$

The RHS of the above equation is evaluated as

$$\begin{aligned}\frac{1}{V}\iint_A \phi \hat{n}_x dA = \Bigg[& \frac{(\phi_{i-1}+\phi_i)}{2}\hat{n}_{x_{i-1/2}} A_{i-1/2} + \frac{(\phi_i+\phi_{i+1})}{2}\hat{n}_{x_{i+1/2}} A_{i+1/2} \\ & + \frac{(\phi_{j-1}+\phi_j)}{2}\hat{n}_{x_{j-1/2}} A_{j-1/2} + \frac{(\phi_j+\phi_{j+1})}{2}\hat{n}_{x_{j-1/2}} A_{j+1/2} \\ & + \frac{(\phi_{k-1}+\phi_k)}{2}\hat{n}_{x_{k-1/2}} A_{k-1/2} + \frac{(\phi_k+\phi_{k+1})}{2}\hat{n}_{x_{k-1/2}} A_{k+1/2} \Bigg] \\ & /V_{ijk}\end{aligned} \tag{89}$$

Similarly, the cell average values of the y and z derivatives are given by

$$\begin{aligned}\frac{1}{V}\iint_A \phi \hat{n}_y dA = \Bigg[& \frac{(\phi_{i-1}+\phi_i)}{2}\hat{n}_{y_{i-1/2}} A_{i-1/2} + \frac{(\phi_i+\phi_{i+1})}{2}\hat{n}_{y_{i+1/2}} A_{i+1/2} \\ & + \frac{(\phi_{j-1}+\phi_j)}{2}\hat{n}_{y_{j-1/2}} A_{j-1/2} + \frac{(\phi_j+\phi_{j+1})}{2}\hat{n}_{y_{j-1/2}} A_{j+1/2} + \\ & \frac{(\phi_{k-1}+\phi_k)}{2}\hat{n}_{y_{k-1/2}} A_{k-1/2} + \frac{(\phi_k+\phi_{k+1})}{2}\hat{n}_{y_{k-1/2}} A_{k+1/2} \Bigg] \\ & /V_{ijk}\end{aligned} \tag{90}$$

$$\frac{1}{V}\iint_A \phi\hat{n}_z dA = \Bigg[\frac{(\phi_{i-1}+\phi_i)}{2}\hat{n}_{z_{i-1/2}}A_{i-1/2} + \frac{(\phi_i+\phi_{i+1})}{2}\hat{n}_{z_{i+1/2}}A_{i+1/2} + \frac{(\phi_{j-1}+\phi_j)}{2}\hat{n}_{z_{j-1/2}}A_{j-1/2} + \frac{(\phi_j+\phi_{j+1})}{2}\hat{n}_{z_{j-1/2}}A_{j+1/2} + \frac{(\phi_{k-1}+\phi_k)}{2}\hat{n}_{z_{k-1/2}}A_{k-1/2} + \frac{(\phi_k+\phi_{k+1})}{2}\hat{n}_{z_{k-1/2}}A_{k+1/2}\Bigg] /V_{ijk} \quad (91)$$

Results

The primitive variable output from the GASP flow solver was processed using the procedure detailed in the structured grids section in this chapter. The terms on the LHS of equations 81, 82, and 83 were recombined into vectors whose magnitudes were used in this analysis. Only the 90-degree J_1 case is analyzed since this is the only test case in which the LCVP structure is present.

Compressibility

The magnitude contours of the compressibility term in the vorticity transport equation are plotted in Fig. 170 along with velocity vectors. In the plot 170(a), for the axial location $x/d_{eff} = -1.0$, the effects of compressibility are apparent around the barrel shock centered on $z/d_{eff} = 0.0$ and extending to $y/d_{eff} = 0.25$. The effects of compressibility can also be seen around the interaction shock extending from $z/d_{eff} = +0.8$ to $z/d_{eff} = -0.8$ and with a maximum height of $y/d_{eff} = 0.9$. At location $x/d_{eff} = +1.0$, the edges of the barrel shock is indicated by peak values of compressibility. Higher values are also observed in the region around the vortex structure generated by the barrel shock. This can be seen in Fig. 170(b). The outline of the LCVP structure can be observed by noting the peak values at location

$x/d_{eff} = 2.0$. The axial ejection mechanism of the LCVP can be seen at $z/d_{eff} = 0.0$ and $y/d_{eff} = +1.0$ along with the corresponding raise in compressibility magnitude in Fig. 170(c). The peak values at this axial location occur near the CVP structure positioned at approximately $z/d_{eff} = \pm 1.2$ and $y/d_{eff} = +0.7$. Peak values are also observed near $z/d_{eff} = 0.0$ and $y/d_{eff} = +0.2$ and 0.4. The peak value close to the wall is also observed at location $x/d_{eff} = +3.0$ in Fig. 170(d). This corresponds to the location of the high pressure spot observed in the surface pressure plots. A triangular outline of high compressibility is present in the interaction region between the large CVP vortex and the smaller wake vortices. The z/d_{eff} and y/d_{eff} coordinates of the triangle corners are $(\pm 1.0, 0.0)$, $(\pm 0.5, +0.4)$, and $(\pm 0.2, +0.2)$. The effect of the recompression shock can be seen at location $y/d_{eff} = +1.4$ in Fig. 170(d). At locations $x/d_{eff} = +8.0$ and $+15.0$, the peak values in the plume are about an order of magnitude lower than those seen in the near field.

The velocity vector lengths at location $x/d_{eff} = +1.0$ seem to indicate that that surface of the barrel shock is at a different location as compared to the location indicated by compressibility results. This is because of the positioning of the tails of the velocity vectors at the grid point locations.

Vortex Stretching

The axial planes displayed in the Fig. 171 are repeated with contours of the vortex stretching term. The contours at location x/d_{eff} = +1.0 show the effects of vortex stretching around the lateral edge of the barrel shock. This interaction was also observed in the schlieren images shown in Fig. 60. The primary areas of vortex stretching can be seen in Fig. 171(c) at location $x/d_{eff} = +2.0$. The axial ejection mechanism of the LCVP pushing fluid downstream and upstream with the cone

shaped structures contributes to the large magnitudes of vortex stretching. The lateral ejection and merging of the LCVP fluid with the CVP can also be observed. The stretching of the wake vortex is seen around $z/d_{eff} = 0.0$ and $y/d_{eff} = 0.0$ in Figs. 171(c) and (d). At $x/d_{eff} = +3.0$, the wake vortex has the highest vortex stretching values followed by the components of the CVP. The high vortex stretching values persist as the wake vortices lift off the floor and begin to merge with the CVP. This can be seen in the plot at location $x/d_{eff} = +8.0$ as shown in Fig. 171(e).

The physical effects of compressibility and vortex stretching are contradictory. The compressibility or dilatational term tends to expand a given region of fluid while the effect of vortex stretching is to reduce the volume. Thus these the interaction of these two terms has considerable bearing on the evolution of the vorticity in the flow field. Further investigation is required in order to gain insight into this interaction.

Baroclinic Torque

Baroclinic torque is generated by the misalignment of the density and pressure gradient vectors. The magnitude of the baroclinic torque vector at different axial locations are plotted in Fig. 172. The misalignment of the density and pressure gradient vectors caused due to the barrel and the interaction shocks can be seen in Fig. 172(a) showing contours at location $x/d_{eff} = -1.0$. The effect is stronger at the barrel shock as compared to the interaction shock. This is similar to the trend observed in the case of compressibility effects. Near the trailing edge of the injector, at $x/d_{eff} = +1.0$, the interaction shock peak is at location $y/d_{eff} = +2.6$ and is represented by contours which indicate that the baroclinic torque magni-

tude is approximately an order of magnitude smaller than that at the barrel shock. Large magnitudes are also observed near the core of the initial leading edge mixing vortex as seen in Fig. 172(b). At $x/d_{eff} = +2.0$ the peak values around the CVP vortex, near the periphery of the plotted domain in Fig. 172(c), is lower by an order of magnitude as compared to the magnitudes of compressibility and vortex stretching. This is also the trend within the LCVP structure, where the baroclinic torque magnitude is about two orders of magnitude lower than vortex stretching. The interaction region between the CVP and the wake vortex is highlighted as seen in Fig. 172(d). The recompression shock can also be seen at location $y/d_{eff} = +1.4$. There is comparatively little effect of this torque at downstream locations of $x/d_{eff} = +8.0$ and $x/d_{eff} = +15.0$. A plot of the compressibility, vortex stretching and baroclinic torques contours around the injector in the x-y plane is shown in Fig. 173. In the region just downstream of the barrel shock it is observed that compressibility and vortex stretching terms dominate over the effects of the baroclinic torque. As discussed before, the axial and lateral ejection mechanisms within the LCVP contribute to the large magnitudes of the vortex stretching term.

Laminar and Turbulent Diffusion Terms

The laminar and turbulent diffusion magnitudes are plotted in Fig. 174 and 175. The initial plots around the injector leading and trailing edges are significantly different for the laminar and turbulent contours. The turbulent diffusion magnitude is approximately four orders of magnitude higher than the laminar diffusion in the entire region between the barrel shock and the interaction shock. This is possibly due the shear interaction between the injector and freestream fluids. Higher turbulent diffusion values are also observed near the top surface of the barrel shock

at $x/d_{eff} = +1.0$. Downstream of $x/d_{eff} = +1.0$, the relative values of the laminar and turbulent terms are more comparable with the turbulent terms being an order of magnitude higher. The peak values observed in both cases generally coincide with the vortex cores that constitute the CVP. The anisosteric laminar and turbulent terms plotted in Fig. 176 and 177 show that their effect on the vorticity production is relatively low as compared to the other terms in the transport equation. This is particularly true when compared to the compressibility, vortex stretching, and baroclinic torque.

Vorticity Components vs. Production and Transport

Following the example of Lee, Kim and Mitani[45], the individual components of vorticity are integrated over several cross sectional planes of the domain and the results are plotted in Fig. 178. The center of the injector is indicated by a vertical line in the plot. It is seen that the x and y components of vorticity are essentially zero upto the leading edge of the injector whereas the z component is non-zero due to vorticity present in the freestream boundary layer. At the leading edge of the injector there is an increase in the x-vorticity followed by an increase in the y-component a little downstream of the leading edge of the injector. It is noted plot denoting the rise in x-vorticity across the injector is similar to the shape of the barrel shock. This rise is due to the formation of the leading edge vortices. An abrupt reduction in x-vorticity is seen at the trailing edge of the injector where the barrel shock terminates. The increase in the y-vorticity levels is higher than the x-vorticity levels. This increase reflects the vertical portion of the LCVPs top vortex and the corner vortices exiting the injector (see Fig. 63). The large increase in z-vorticity near the trailing edge is due to the flow structures associated with

LCVP. At 4 d_{eff} downstream of the injector, the z-vorticity reduces to the original freestream values.

A line plot similar to that in Fig. 178 is shown in Fig. 179 for the RHS terms in the compressible vorticity transport equation. All the terms in the plot show peak values around the trailing edge of the injector following the trend of the vorticity plots. The largest increase (about four orders of magnitude) is seen in the vortex stretching term, which also has the highest peak value of any other term except laminar diffusion. The peak values of compressibility coincide with those of vortex stretching. A steep rise in the baroclinic term is also seen but the peak value is lower as compared to the first two terms. Of the first three terms, it is noted that the increase in vortex stretching persists over a longer time within the domain. The laminar diffusion term has the highest overall value but it is confined to the boundary layer. This is also seen in the contour plots discussed previously. The turbulent diffusion term increases at the leading edge of the injector and has a local minima at the injector trailing edge after which it has a peak at the LCVP location. Finally, both the anisosteric laminar and diffusion terms follow similar trends peaking at the LCVP location and gradually returning to their freestream values at the end of the domain.

A similar analysis was performed using the results from the Cobalt solver. However, the results obtained are not presented since errors introduced in the analysis are large. This is because of the storage of the solver results at nodal locations instead of cell centers in the visualisation output files. The solver output conforms to the Fieldview file specifications, which requires results at nodal locations.

CHAPTER VIII

CONCLUSIONS AND RECOMMENDATIONS

A set of detailed numerical simulations were performed to characterize the flow and turbulence generated by sonic injection through diamond orifices into a Mach 5.0 freestream flow. The focus areas of this study were; (a) the evaluation of two-equation and DES models for this flow field. This was done by comparing numerical results to experimental data from Bowersox et al. (b) gain an in-depth understanding of the flow field using results from the simulations and visualization tools, (c) obtain information on the terms that significantly impact the near-field vorticity, (d) from the analysis performed, identify controllable flow features. In order to answer these questions, a total of nineteen complete simulations were performed. The details are outlined and the results are summarized below.

Simulations were performed using the GASP flow solver from AeroSoft Inc. and the Cobalt flow solver from Cobalt LLC. Structured grids, generated using Gridgen, were used for simulations with GASP. The structured grid simulations utilized a symmetry plane boundary condition since the steady state RANS simulations were considered to be symmetric at $z/d_{eff} = 0.0$. The total number of grid points in the structured domain was approximately 5.4 million. The grid was clustered near areas of high gradients such as the nozzle exit and the downstream plume region. Clustering was also performed closed to the wall to maintain a y+ value of less than one. Grid convergence was demonstrated by obtaining a solution on a medium and coarse grid for which the grid points were reduced by a factor of 2 in each direction and plotting the surface pressure along the tunnel centerline. The solution was interpolated from the coarse to the medium and from medium

to the fine grid to speed up solution convergence. Flow structures for the different grids were also inspected to confirm grid convergence. Solution convergence was demonstrated by plotting the surface pressure along the tunnel centerline at every 100th iteration step. The solution was deemed converged when the change in pressure and also the residual were deemed negligible. Unstructured grids were used for Cobalt simulations. The combination of GridTool/VGRID was used to generate unstructured grids. The complete span wise extent of the experimental domain was modeled for DES simulations using Cobalt. The total number of grid points for the finest grid was approximately 6.0 million. As in the structured grid, clustering was performed around the injector exit and the plume region downstream of the injector. Grid convergence was demonstrated by evaluating the percentage of resolved TKE in comparison to the total TKE. An initial RANS solution was obtained after which the DES model was turned on. The DES simulation was executed at a constant time step for 6000 iterations. The average of the velocity fluctuations was performed over these 6000 iterations to obtain turbulent stresses.

A total of fifteen RANS simulations and one DES simulation were performed for the diamond injector configuration. The fifteen RANS simulations included five different injection angles are three different jet total pressures. The DES simulation was performed for the 90-degree injection angle and at the lowest jet total pressure (J_1).

Experimental comparison was performed for the low pressure injection cases involving five RANS and one DES simulation and included shadowgraphs, surface oil flow, pitot pressure and Mach number and surface pressure. It was concluded that both models perform adequately in predicting high-speed jet interaction flows. Surface oil flow results from RANS were in better agreement with experiments upstream of the injector exit while DES results indicated a larger separation region.

Surface pressure comparisons are similar to oil flow results. The downstream region prediction is quite similar for both RANS and DES. The shock angles predicted by DES and RANS compare favorably with experimental values.

The 90-degree J_1 case was chosen for the flow structure and turbulence analysis. A study of the shocks generated by the flow revealed an interesting barrel shock structure around the injector exit. The shape of the injector leads to the formation of a vertical shock surface on the downstream side of the shock. The presence of this surface leads to the formation of a pair of vortices called as the Lateral Counter-rotating Vortex Pair (LCVP). This vortex pair is formed due to the action of the injector fluid turning downstream and in the process interacting with the boundary layer fluid moving up into the low pressure region behind the shock. This trapped vortex pair has fluid entering from both the freestream and the injector and has the potential to act as a gas dynamic flame holder in scramjet applications. The residence time of the fluid within this vortex was found to be an order of magnitude higher than that of fluid in the freestream. This structure was found in RANS results as well as time-averaged and instantaneous DES results. Another feature discovered in these simulations is the presence of a leading edge mixing mechanism upstream of the injector. This mixing mechanism originates due to the action of the freestream fluid on the exiting injector fluid and also from the corner vortices within the injector. This vortex pair has significant contributions from both the freestream as well as the injector. The leading edge mixing vortex eventually leads to the formation of the axial CVP. Thus, higher mixing rates near the leading edge leads to more uniform mixing downstream in the plume region.

Vorticity transport analysis was performed to obtain an understanding of the effect of the different terms in the compressible form of the transport equation of vorticity. A FORTRAN program was written to analyze the RANS result for

the 90-degree J_1 case and evaluate all the terms in the transport equation. The results reveal that the effect on the vorticity is mostly limited to the compressibility, vortex stretching and baroclinic torque terms. Integrating the quantities along axial planes reveals that the largest increase is in the vortex stretching term and occurs near the jet exit.

This study can be extended to investigate the effects of the half-angle of the diamond injector. A wide range of freestream Mach numbers should be tested in order to verify the existence of the LCVP structure. Also, different turbulence models should be employed to investigate the effect on the flow field. Experimental verification of the LCVP structure would be an important step in its utilization as a flame holder. Mixing studies of the angled and hybrid injectors could possibly lead to further improvements in the characteristics of the flow field. Detached-eddy simulations of the high pressure cases may give an further insight into the structure of the downstream shear layer. Another area of investigation is the check for the existence of periodicity in the structure of the shear layer in DES runs.

REFERENCES

[1] Schetz, J. and Billig, F., "Penetration of Gaseous Jets Injected into a Supersonic Stream," *Journal of Spacecraft and Rockets*, Vol. 35, No. 11, 1966, pp. 1658–1665.

[2] Chenault, L., Beran, P., and Bowersox, R., "Numerical Investigation of Supersonic Injection Using a Reynolds-Stress Turbulence Model," *AIAA Journal*, Vol. 37, No. 10, 1999, pp. 1257–1269.

[3] McCann, G. and Bowersox, R., "Experimental Investigation of Supersonic Gaseous Injection into a Supersonic Freestream," *AIAA Journal*, Vol. 34, No. 2, 1996, pp. 317–323.

[4] Bowersox, R., Tucker, K., and Whitcomb, C., "Two-Dimensional Nonadiabatic Injection into a Supersonic Freestream," *Journal of Propulsion and Power*, Vol. 16, No. 2, March-April 2000, pp. 234–242.

[5] Gruber, M., Nejad, A., Chen, T., and Dutton, C., "Mixing and Penetration Studies of Sonic Jets in a Mach 2 Freestream," *Journal of Propulsion and Power*, Vol. 11, No. 2, 1995, pp. 315–323.

[6] Gruber, M. R., Nejad, A. S., Chen, T. H., and Dutton, J. C., "Bow Shock/Jet Interaction in Compressible Transverse Jet Injection Flowfield," *AIAA Journal*, Vol. 34, No. 10, 1996, pp. 2191–2193.

[7] McClinton, C., "The Effects of Injection Angle on the Interaction Between Sonic Secondary Jets and as Supersonic Freestream," Tech. Rep. TN D-6669, NASA, 1972.

[8] Heiser, W. and Pratt, D., *Hypersonic Airbreathing Propulsion*, AIAA Education Series, AIAA, Washington, DC, 1994.

[9] Auvity, B., Etz, M. R., and Smits, A. J., "Effect of Transverse Helium Injection on Hypersonic Boundary Layers," *Physics of Fluids*, Vol. 13, No. 10, 2001, pp. 3025–3032.

[10] Davis, D. L. and Bowersox, R. D. W., "Stirred reactor analysis of cavity flame holders for scramjets," AIAA Paper 1997-3274, 33rd AIAA/ASME/SAE/ASEE Joint Propulsion Conference and Exhibit, July 1997.

[11] Davis, D. L. and Bowersox, R. D. W., "Computational fluid dynamics analysis of cavity flame holders for scramjets," AIAA Paper 1997-3270, 33rd AIAA/ASME/SAE/ASEE Joint Propulsion Conference and Exhibit, July 1997.

[12] Kamotani, Y. and Gerber, I., "Experiments on a Turbulent Jet in a Cross-flow," *AIAA Journal*, Vol. 10, No. 11, 1972, pp. 1425–1429.

[13] Keuthe, A. M., "Investigation of the Turbulent Mixing Regions Formed by Jets," *Journal of Applied Mechanics*, 1935, pp. A–87–A–95.

[14] Margason, R. J., "Fifty Years of Jets in Cross-Flow Research," Tech. Rep., AGARD-CP-534, 1993.

[15] Fric, T. and Roshko, A., "Vortical Structure in the Wake of a Transverse Jet," *Journal of Fluid Mechanics*, Vol. 279, 1994, pp. 1–47.

[16] Lozano, A., Smith, S., Mungal, M., and Hanson, R., "Concentration Measurements in a Transverse Jet by Planar Laser Induced Fluorescence of Acetone," *AIAA Journal*, Vol. 32, 1994, pp. 218–221.

[17] Kelso, R., Delo, C., and Smits, A., "Unsteady Wake Structures in Transverse Jets," Tech. Rep., AGARD-CP-534, 1993.

[18] Hollo, S. D., McDaniel, J. C., and Harfield, R. J., "Quantitaive Investigation of Compressible Mixing: Staged Transverse Injection into a Mach 2 Flow," *AIAA Journal*, Vol. 32, No. 3, 1994, pp. 528–534.

[19] Grasso, F. Magi, V., "Simulation of Transverse Gas Injection in Turbulent Supersonic Air Flows," *AIAA Journal*, Vol. 33, No. 1, 1995, pp. 56–62.

[20] Andreopoulos, J. and Rodi, W., "Experimental Investigation of Jets in a Cross-flow," *Journal of Fluid Mechanics*, Vol. 138, 1984, pp. 93–127.

[21] Fric, T. F. and Roshko, A., "Structure in the Near Field of the Transverse Jet," *Proceeding of the Seventh Symposium on Turbulent Shear Flows*, Vol. 1 (A90-35176), August 1989, pp. 6.4.1–6.4.6.

[22] Bowersox, R., "Turbulent Flow Structure Characterization of Angled Injection into a Supersonic Cross-Flow," *Journal of Spacecraft and Rockets*, Vol. 34, No. 2, 1996, pp. 205–213.

[23] Chui, S., Karling, R., Margason, R., and Tso, J., "A Numerical Investigation of a Subsonic Jet into a Cross-flow," Tech. Rep., AGARD-CP-534, 1993.

[24] Alverez, J., Jones, W., and Seoud, R., "Predictions of Momentum and Scalar Fields in a Jet in a Cross-flow using First and Second Order Turbulence Closure," Tech. Rep., AGARD-CP-534, 1993.

[25] Barber, M., Schetz, J., and Roe, L., "Normal Sonic Helium Injection Thorough a Wedge Shaped Orifice into a Supersonic Flow," *Journal of Propulsion and Power*, Vol. 13, No. 2, 1997, pp. 257–263.

[26] Jacobsen, L. S., Gallimore, S. D., Schetz, J. A., Brien, W. F. O., and Goss, L. P., "Improved Aerodynamic-Ramp Injector in Supersonic Flow," *Journal of Propulsion and Power*, Vol. 19, 2003, pp. 663–673.

[27] Viti, V., Wallis, S., Schetz, J. A., Neel, R., and Bowersox, R. D. W., "Jet Interaction with a Primary Jet and an Array of Smaller Jets," *AIAA Journal*, Vol. 42, No. 7, July 2004, pp. 1358–1368.

[28] Bowersox, R., Fan, H., and Lee, D., "Sonic Injection into a Mach 5.0 Freestream Through Diamond Orifices," *Journal of Propulsion and Power*, Vol. 20, No. 2, 2004, pp. 280–287.

[29] Wilcox, D. C., *Turbulence Modeling for CFD*, DCW Industries, Inc., La Canada, CA, 1998.

[30] Yuan, L. L., Street, R. L., and Ferziger, J. H., "Large-eddy Simulations of a Round Jet in Crossflow," *Journal of Fluid Mechanics*, Vol. 379, 1999, pp. 71–104.

[31] Cortelezzi, L. and Karagozian, A. R., "On the formation of the counter-rotating vortex pair in transverse jets," *Journal of Fluid Mechanics*, Vol. 443, 2001, pp. 1–25.

[32] Pope, S. B., *Turbulent Flows*, Cambridge University Press, Cambridge, UK, 2000.

[33] Sparlat, P. R., Jou, W.-H., Strelets, M., and Allmaras, S. R., "Comments on the Feasibility of LES for Wings, and on a Hybrid RANS/LES Approach," Advances in DNS/LES, 1st AFOSR Int. Conf. on DNS/LES, August 1997.

[34] Roe, P. L., "Approximate Riemann Solvers, Parameter Vector, and Difference Schemes," *Journal of Computational Physics*, Vol. 43, No. 2, 1981, pp. 357–372.

[35] Harten, A. and Hyman, J. M., "Self adjusting grid methods for one-dimensional hyperbolic conservation laws," *Journal of Computational Physics*, Vol. 50, No. 2, 1983, pp. 235–269.

[36] Strang, W. Z., Tomaro, R. F., and Grismer, M. J., "The Defining Methods of Cobalt60: A Parallel, Implicit, Unstructured Euler/Navier-Stokes Flow Solver," AIAA Paper 1999-0786, Jan. 1999.

[37] Gottlieb, J. J. and Groth, C. P. T., "Assessment of Riemann Solvers for Unsteady One-Dimensional Inviscid Flows for Perfect Gases," *Journal of Computational Physics*, Vol. 78, 1988, pp. 437–458.

[38] Menter, F., "Two-Equation Eddy-Viscosity Turbulence Models for Engineering Applications," *AIAA Journal*, Vol. 32, No. 8, 1994, pp. 1598–1605.

[39] Forsythe, J. R., Hoffmann, K. A., and Squires, K. D., "Detached-Eddy Simulation with Compressibility Corrections Applied to a Supersonic Axisymmetric Base Flow," AIAA Paper 2002-0586, Jan. 2002.

[40] Suzen, Y. B. and Hoffmann, K. A., "Investigation of Supersonic Jet Exhaust Flow by One- and Two-Equation Turbulence Models," AIAA 98-0322, 1998.

[41] *Gridgen Users' Manual v 13.0*, Pointwise, Inc., Fort Worth, TX, 1999.

[42] Pirzadeh, S., "Three-Dimensional Unstructured Viscous Grids by the Advancing-Layers Method," *AIAA Journal*, Vol. 34, No. 1, January 1996, pp. 43–49.

[43] Ott, J. D., Kannepalli, C., Brinckman, K., and Dash, S. M., "Scramjet Propulsive Flowpath Prediction Improvements Using Recent Modeling Upgrades," AIAA Paper 2005-0432, Jan. 2005.

[44] Tomioka, S., Jacobsen, L., and Schetz, J., "Sonic Injection from Diamond-Shaped Orifices into a Supersonic Flow," *Journal of Propulsion and Power*, Vol. 19, No. 1, January-February 2003, pp. 104–114.

[45] Lee, S.-H., Kim, Y.-J., and Mitani, T., "Mixing Augmentation of Transverse Injection in Scramjet Combustor," AIAA Paper 2000-0090, Jan. 2000.

APPENDIX A

Tables and images referred to in the main body of the document are presented in this appendix. The tables are displayed first followed by the images.

Table 1 Simulation test cases

Case	Injection Angle	J	p_j (kPa)	ρ_j (kg/m^3)
1	10°	0.41	52.0	0.7771
2	27.5°	0.41	52.0	0.7771
3	45°	0.41	52.0	0.7771
4	90°	0.41	52.0	0.7771
5	135°	0.41	52.0	0.7771
6	10°	2.10	254.0	3.6856
7	27.5°	2.10	254.0	3.6856
8	45°	2.10	254.0	3.6856
9	90°	2.10	254.0	3.6856
10	135°	2.10	254.0	3.6856
11	10°	2.60	326.0	4.7432
12	27.5°	2.60	326.0	4.7432
13	45°	2.60	326.0	4.7432
14	90°	2.60	326.0	4.7432
15	135°	2.60	326.0	4.7432
16[a]	90°	0.41	52.0	0.7771
17[a]	90°	2.10	254.0	3.6856
18[b]	27°–90°	0.41	52.0	0.7771
19[b]	45°–90°	0.41	52.0	0.7771

[a] circular injectors,
[b] hybrid injectors.

Table 2 DES simulation details

Case	Model	Iterations	Timestep
Fan	Laminar	1000	CFL
	SST	2000	CFL
	DES-SST	3000	1E-6
	DES-SST-AVG	6000	1E-6

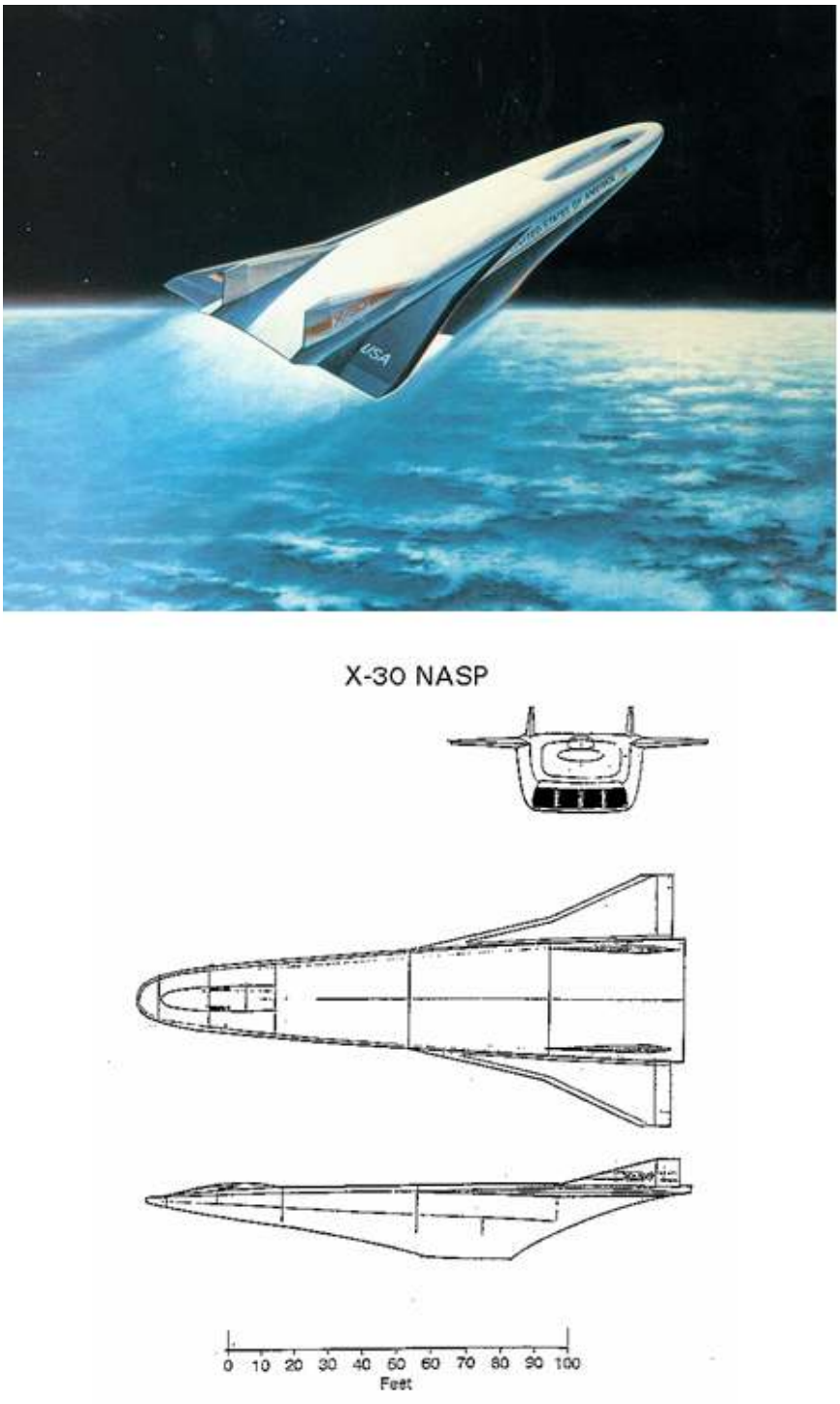

Fig. 1 X-30, NASP concept.

Fig. 2 X-43A concept and CFD result.

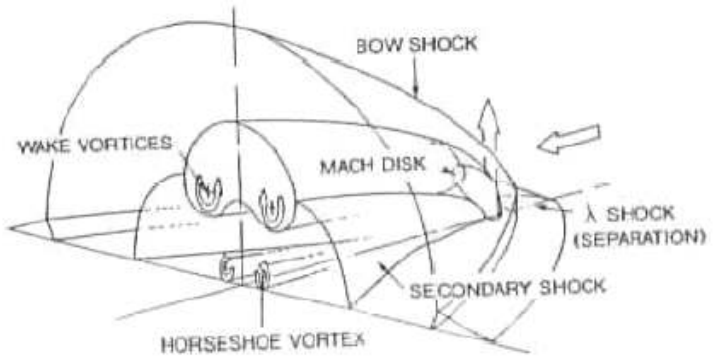

Fig. 3 Schematic of supersonic jet interaction flowfield.

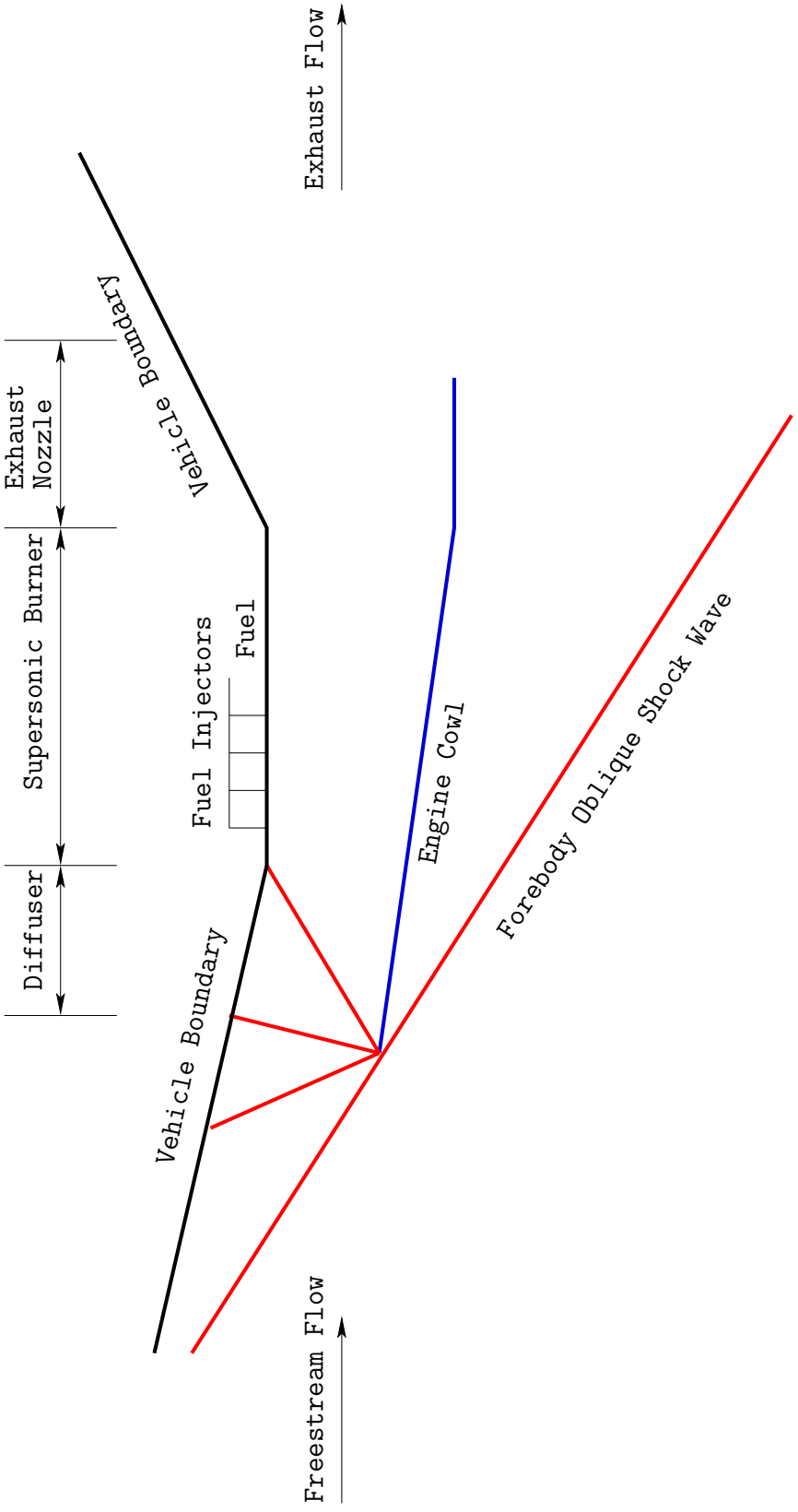

Fig. 4 Schematic of a scramjet engine.

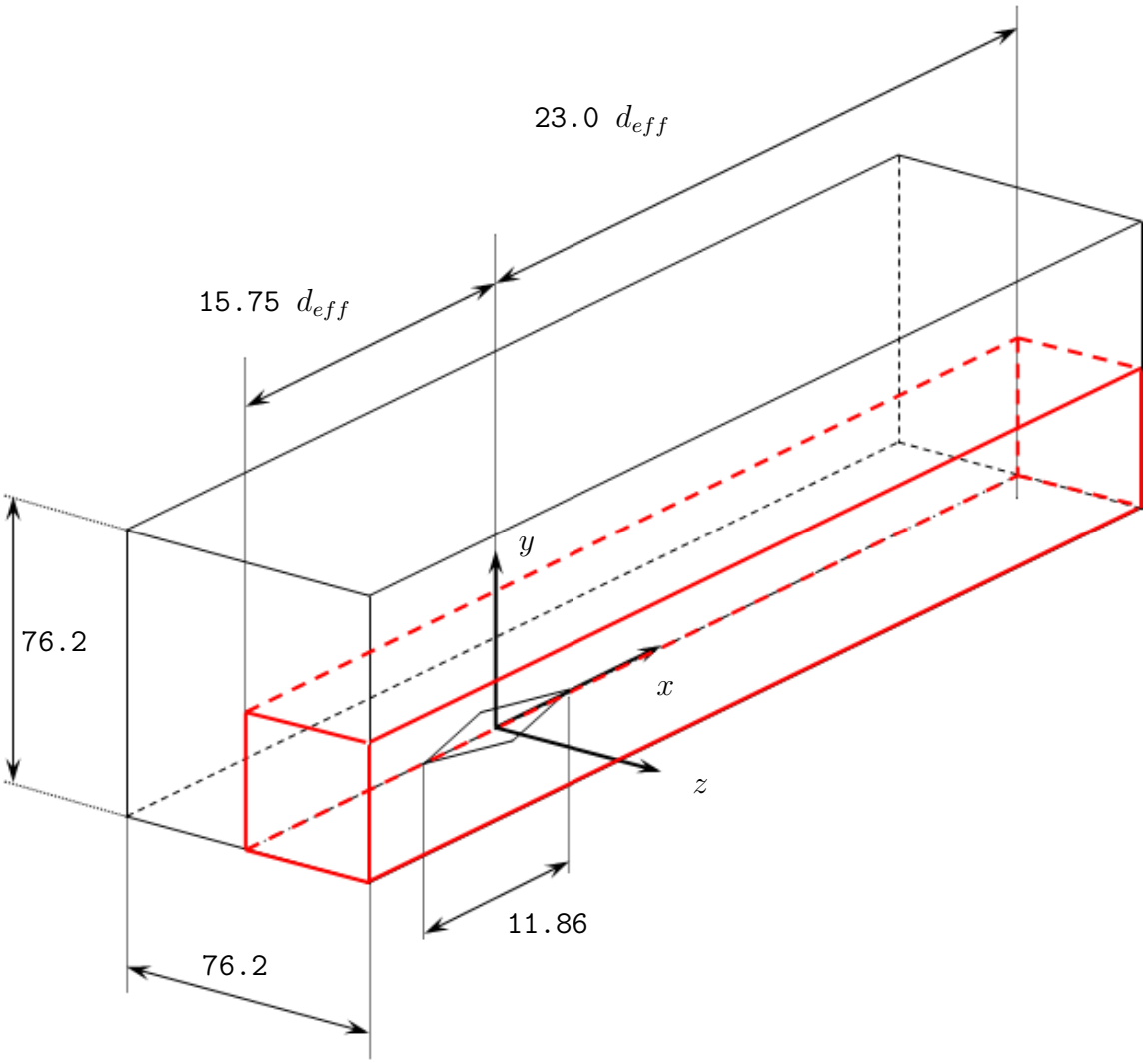

Fig. 5 Illustration of coordinate system and test section (mm).

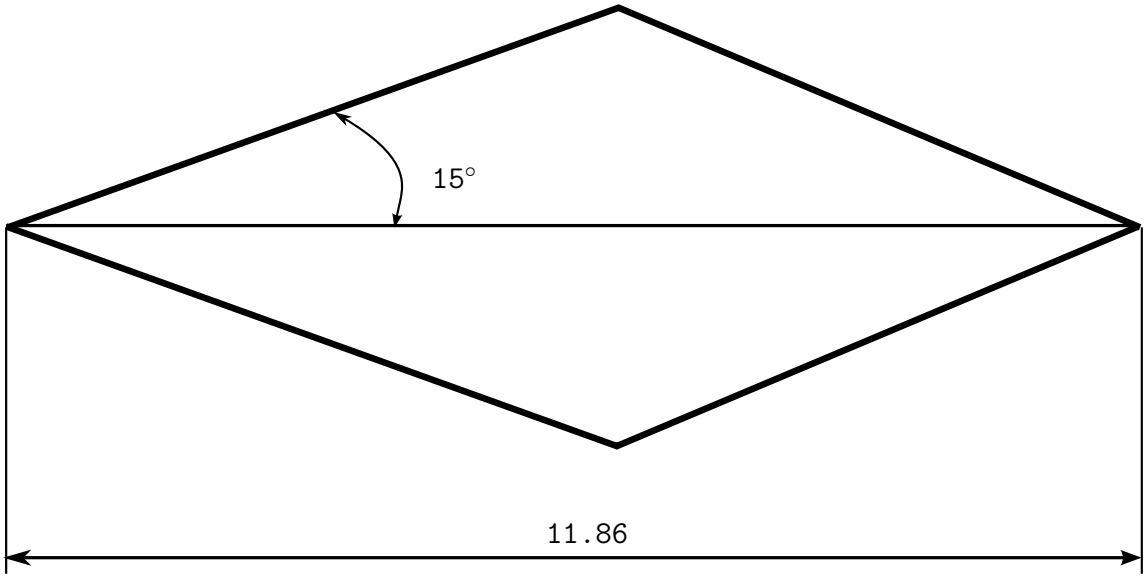

Fig. 6 Diamond jet cross section (mm).

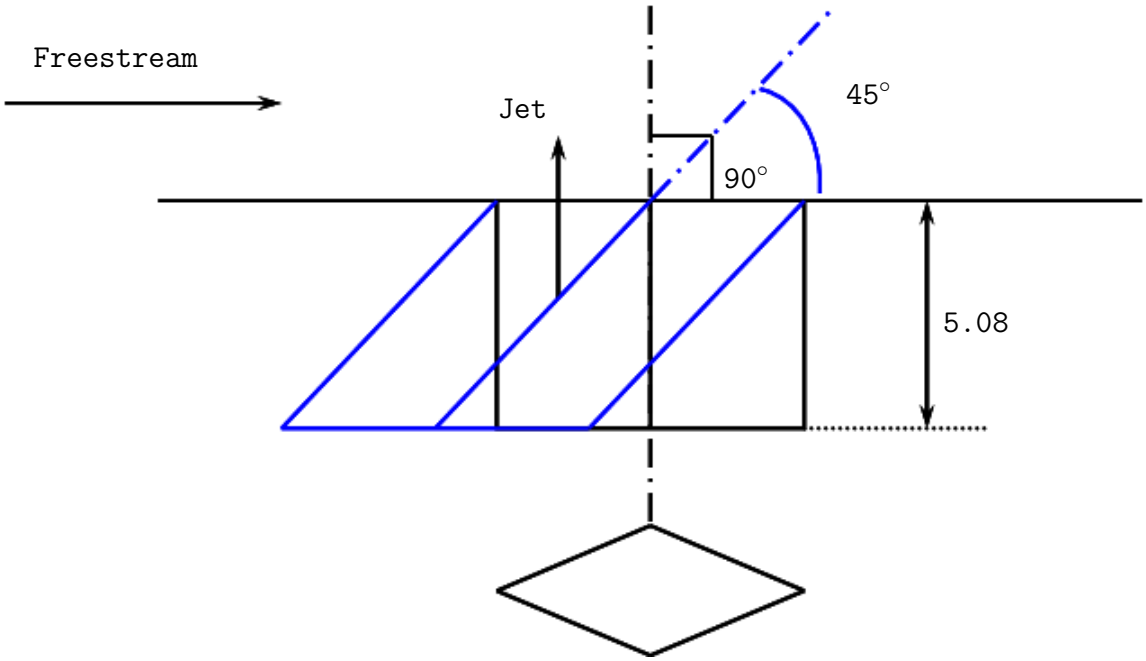

Fig. 7 Injection angle (mm).

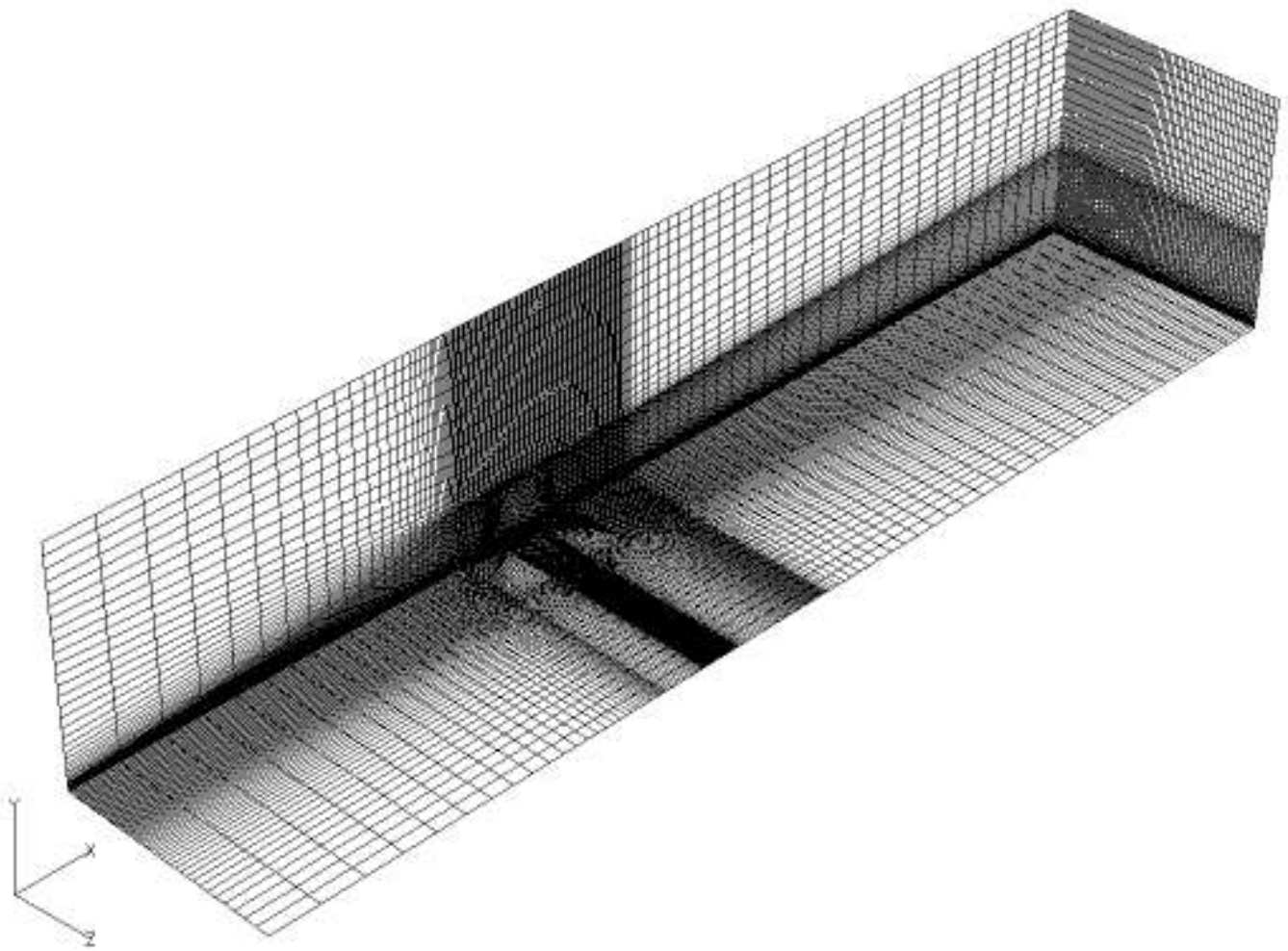

Fig. 8 ξ, η and ζ planes for 90-degree case.

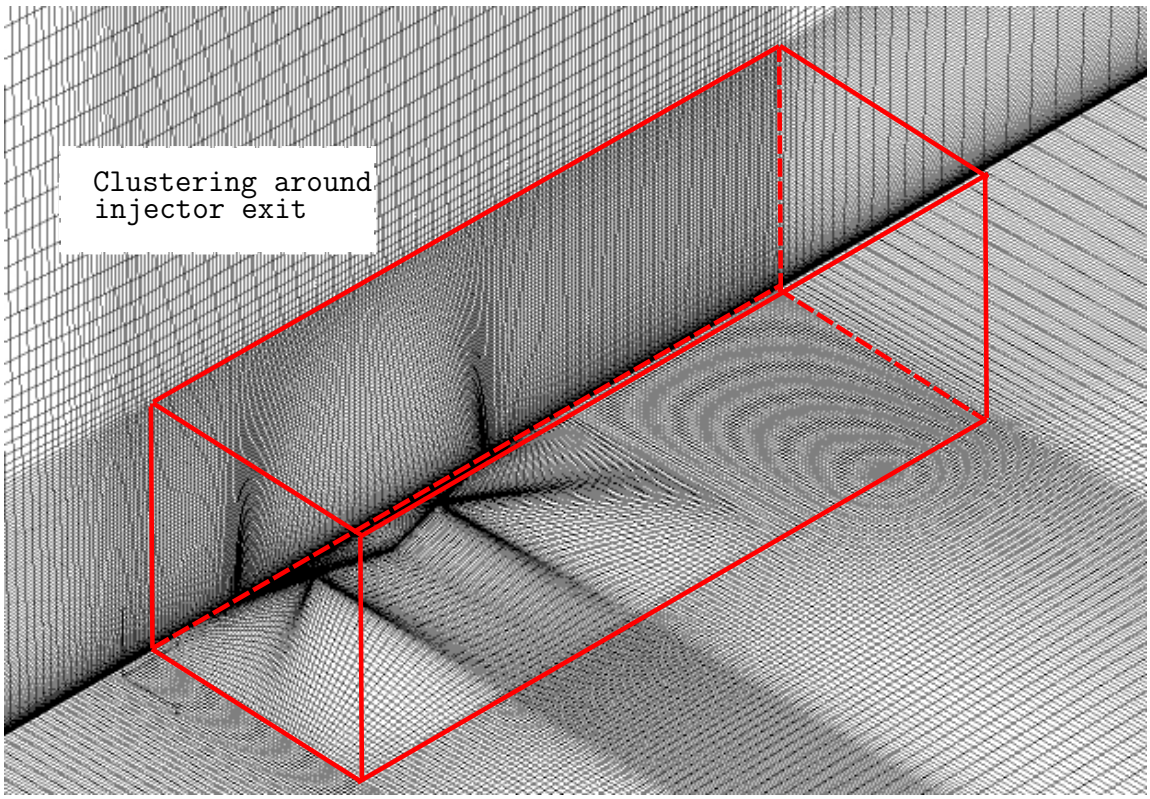

Fig. 9 Grid around injector exit for 90-degree case.

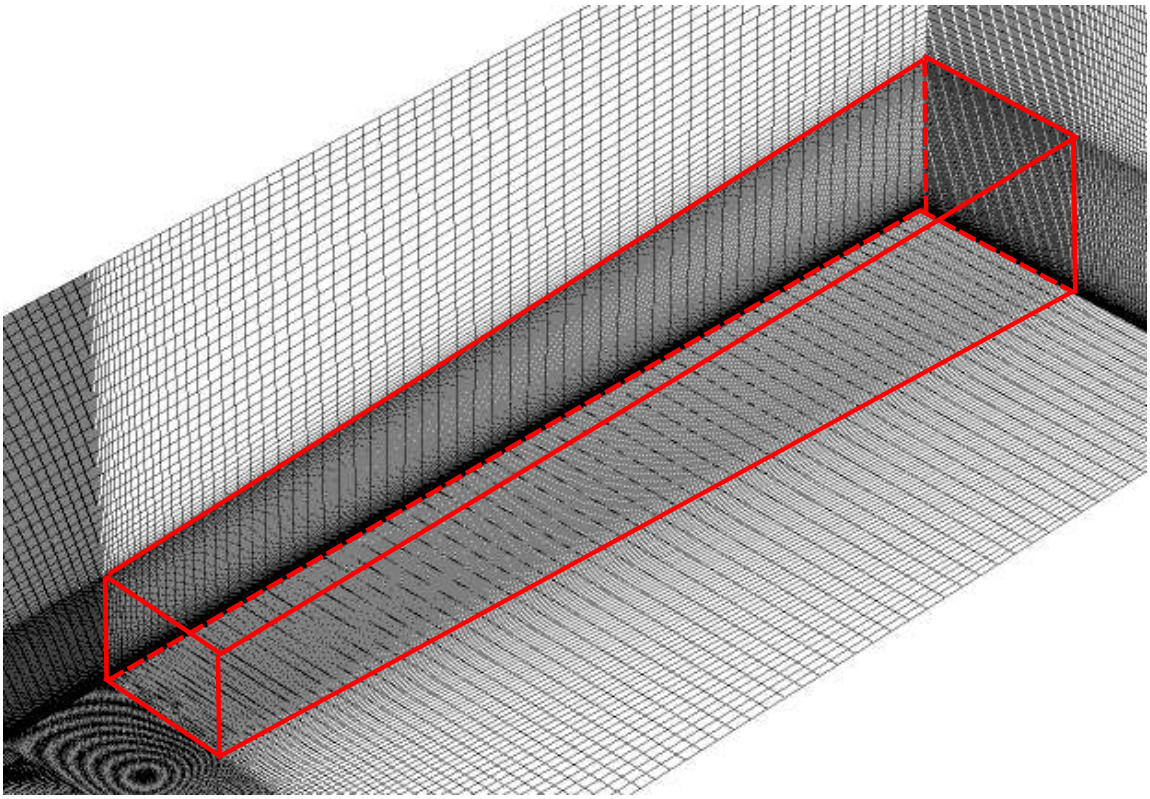

Fig. 10 Grid downstream of injector exit for 90-degree case.

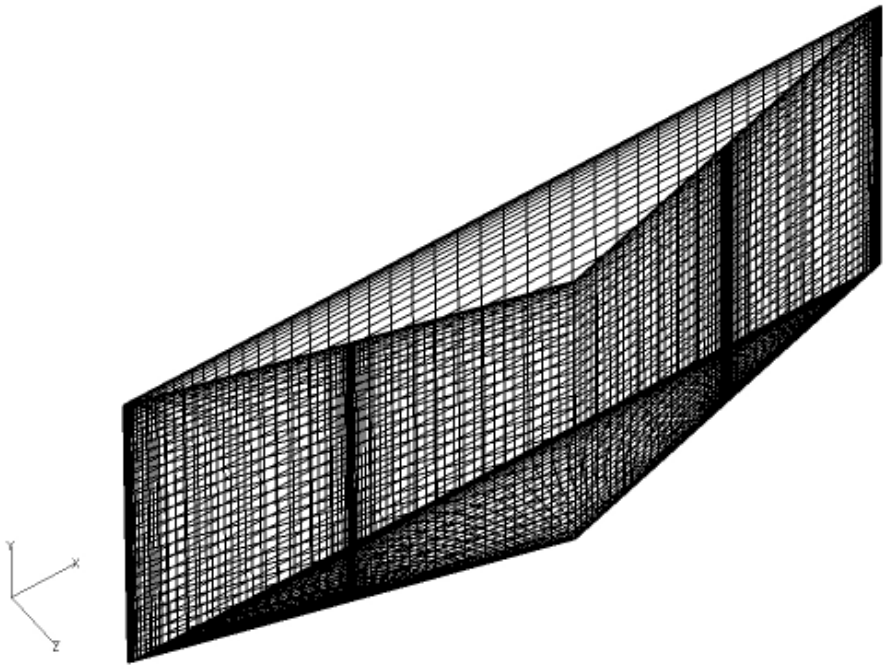

Fig. 11 Injector port grid for 90-degree case.

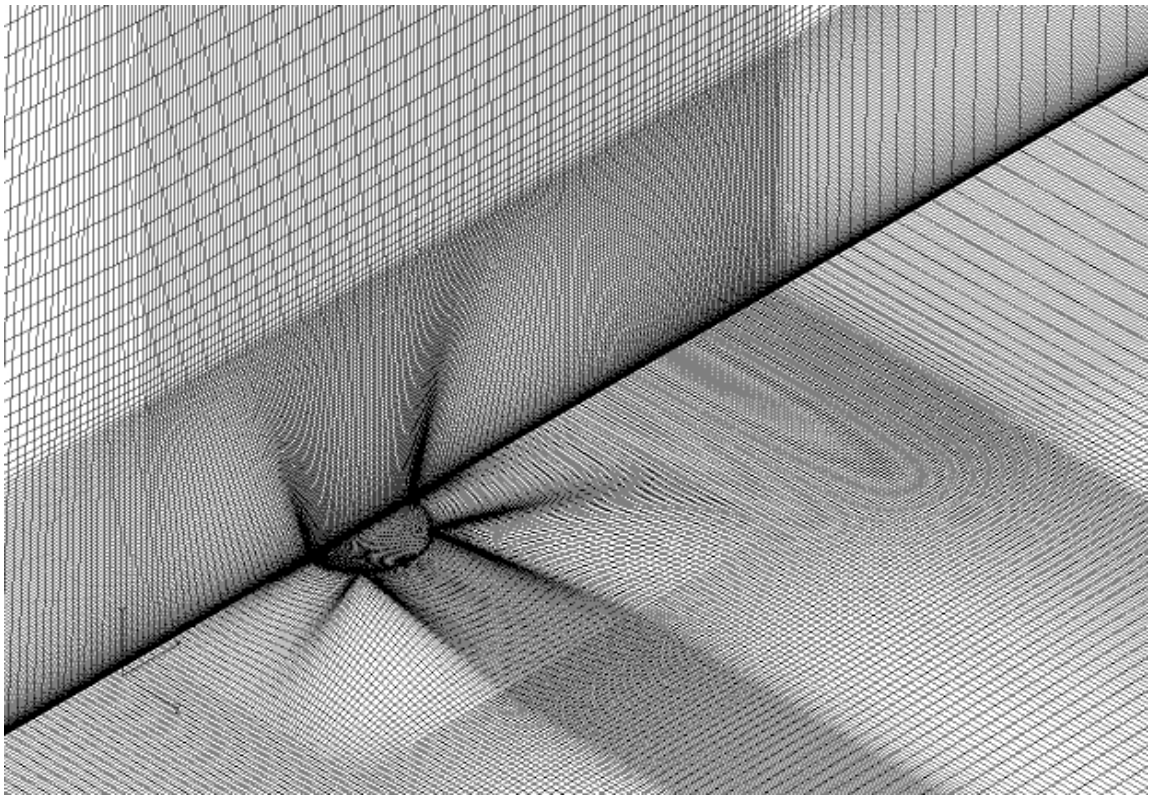

Fig. 12 Injector port grid for 90-degree case, circular.

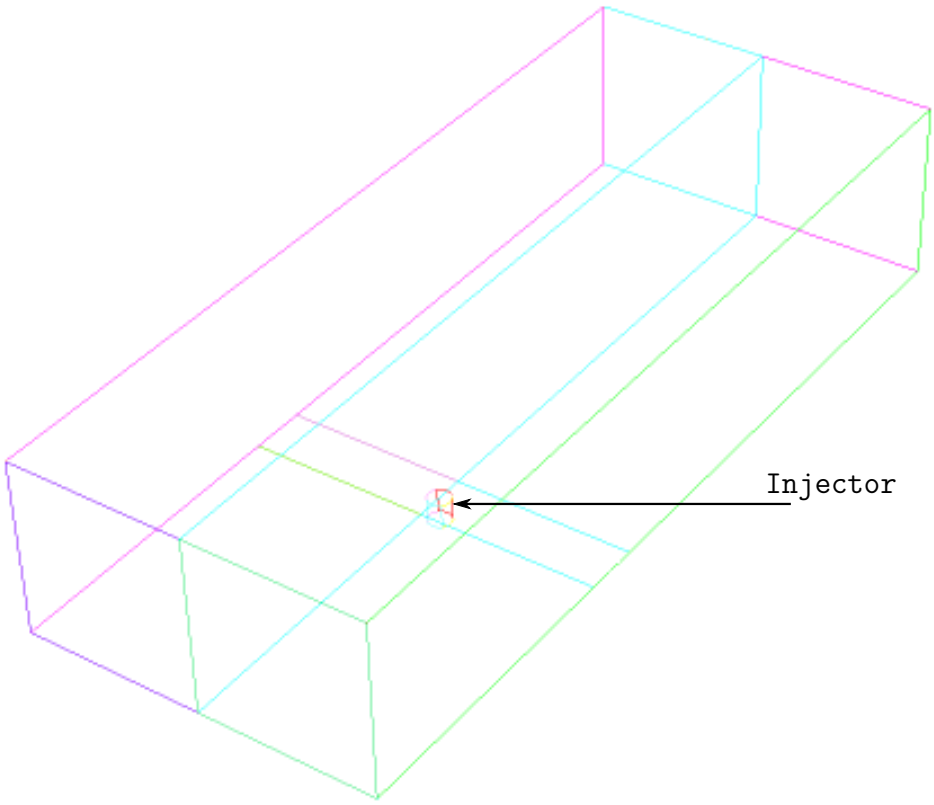

Fig. 13 Imported domain for 90-degree circular injector case.

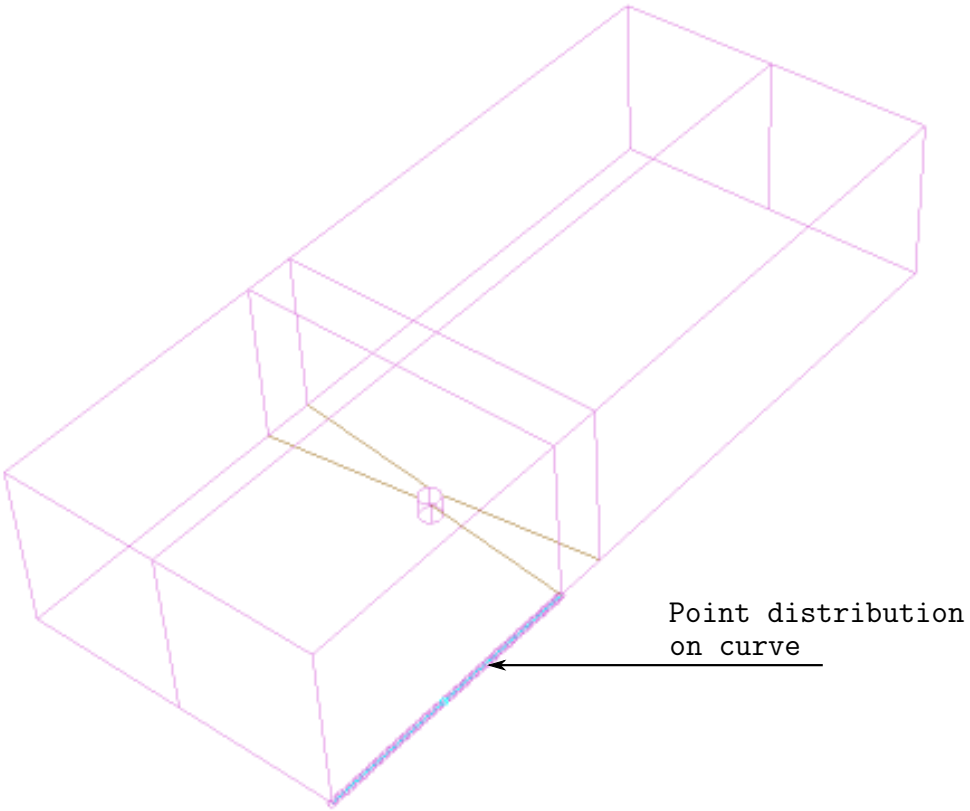

Fig. 14 Curves for 90-degree circular injector case.

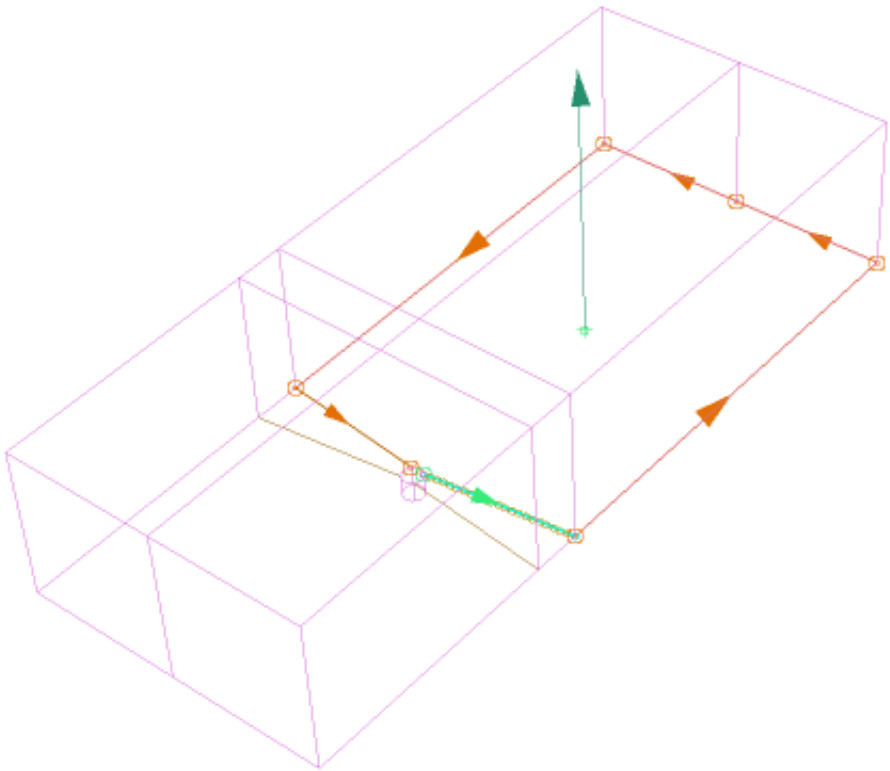

Fig. 15 Patches for 90-degree circular injector case.

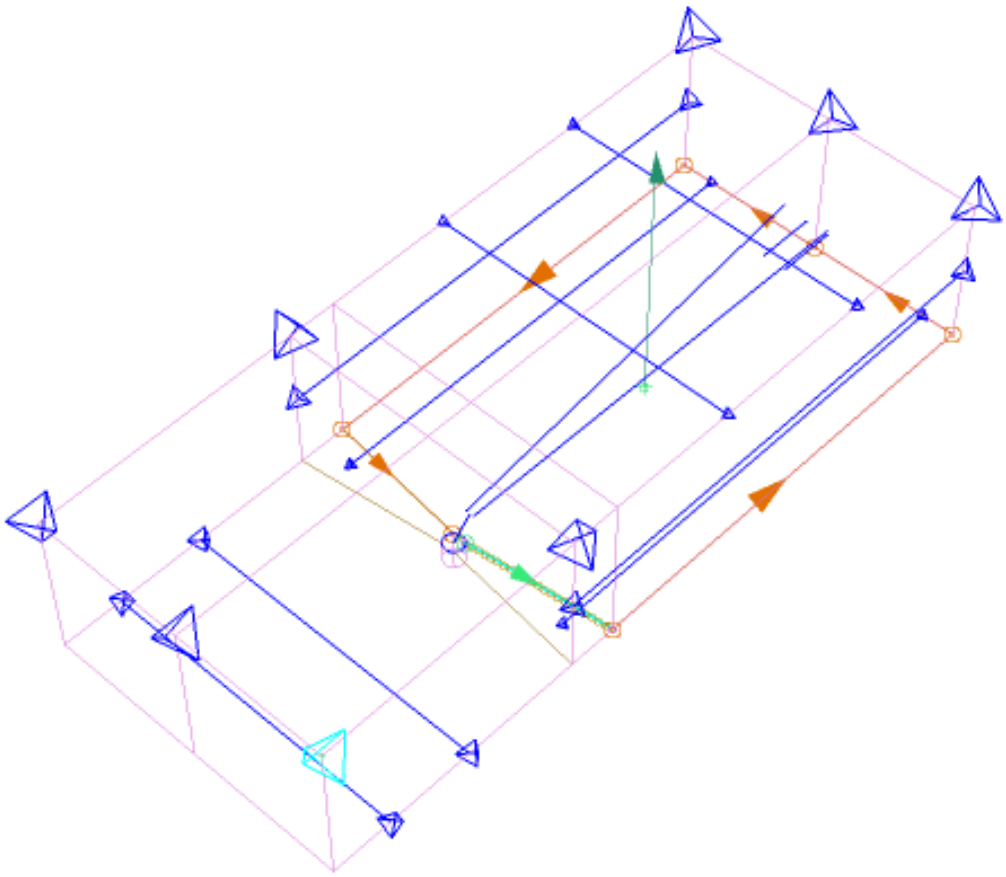

Fig. 16 Grid sources for 90-degree circular injector case.

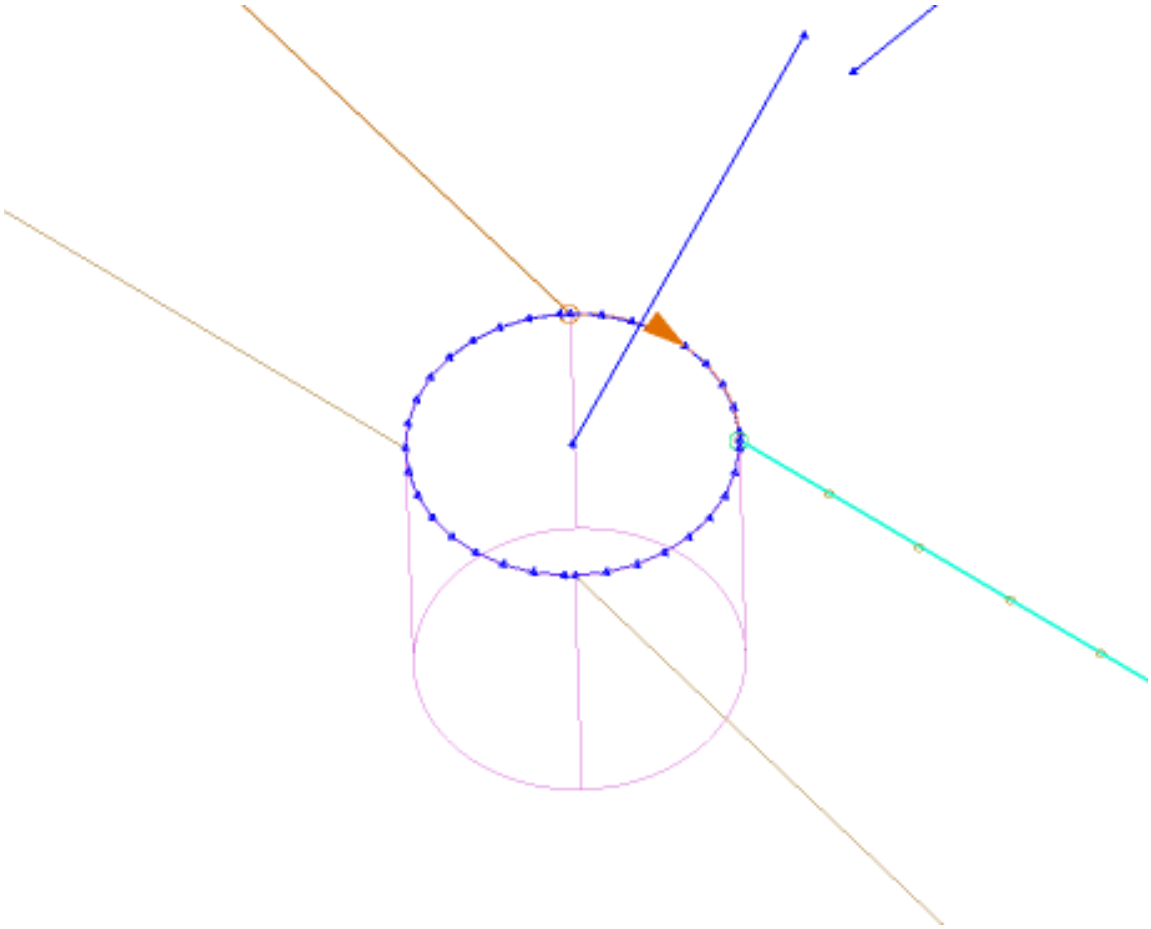

Fig. 17 Grid sources around injector exit for 90-degree circular injector case.

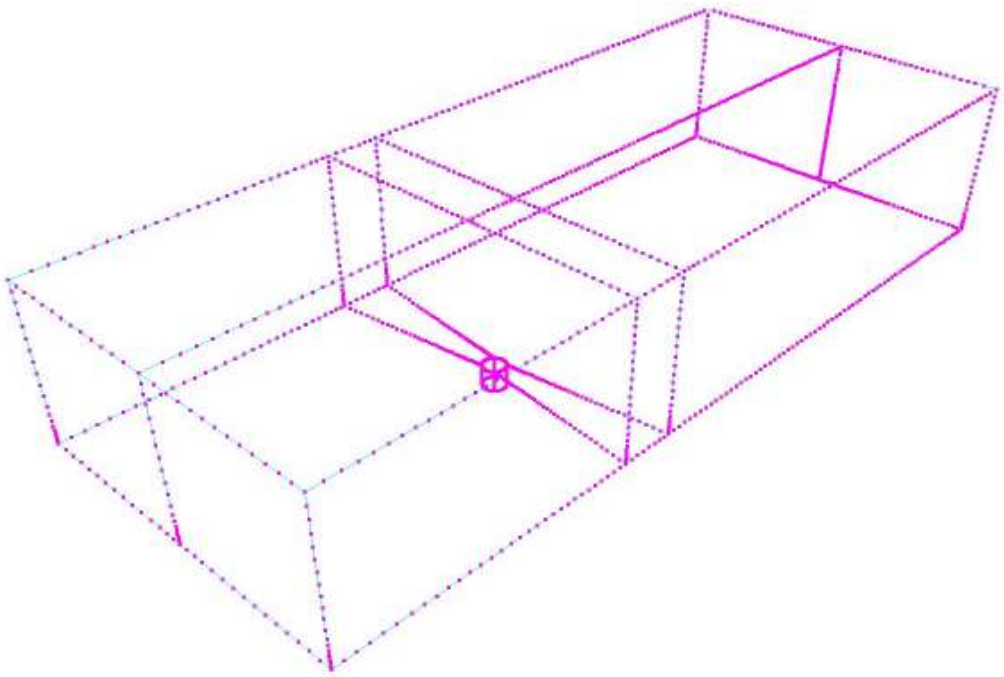

Fig. 18 Grid point distribution for 90-degree circular injector case.

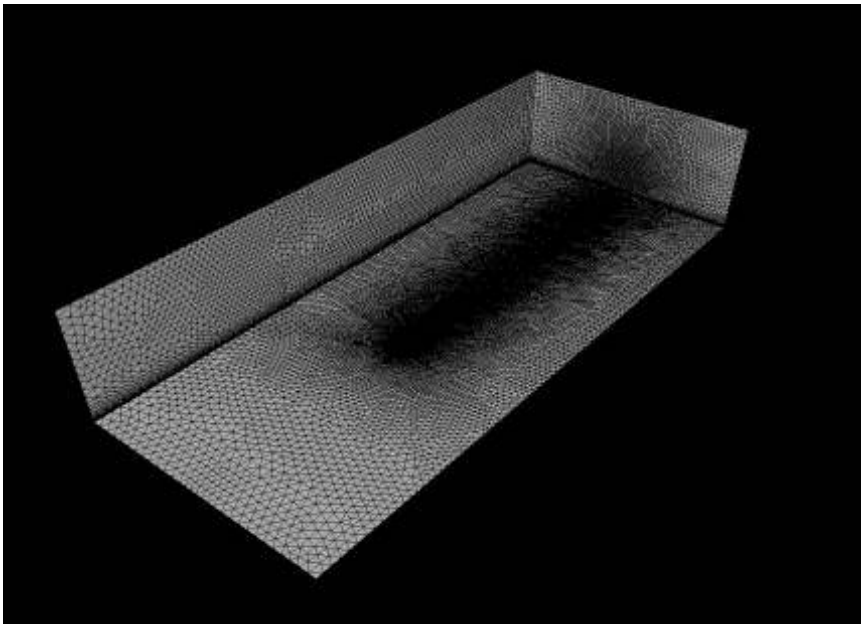

(a)

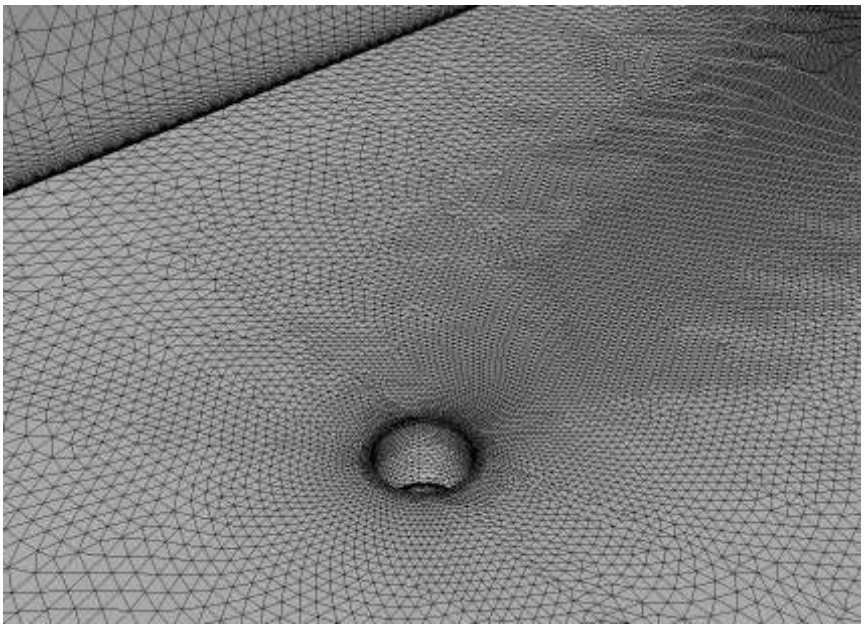

(b)

Fig. 19 Initial front for 90-degree circular injector case.

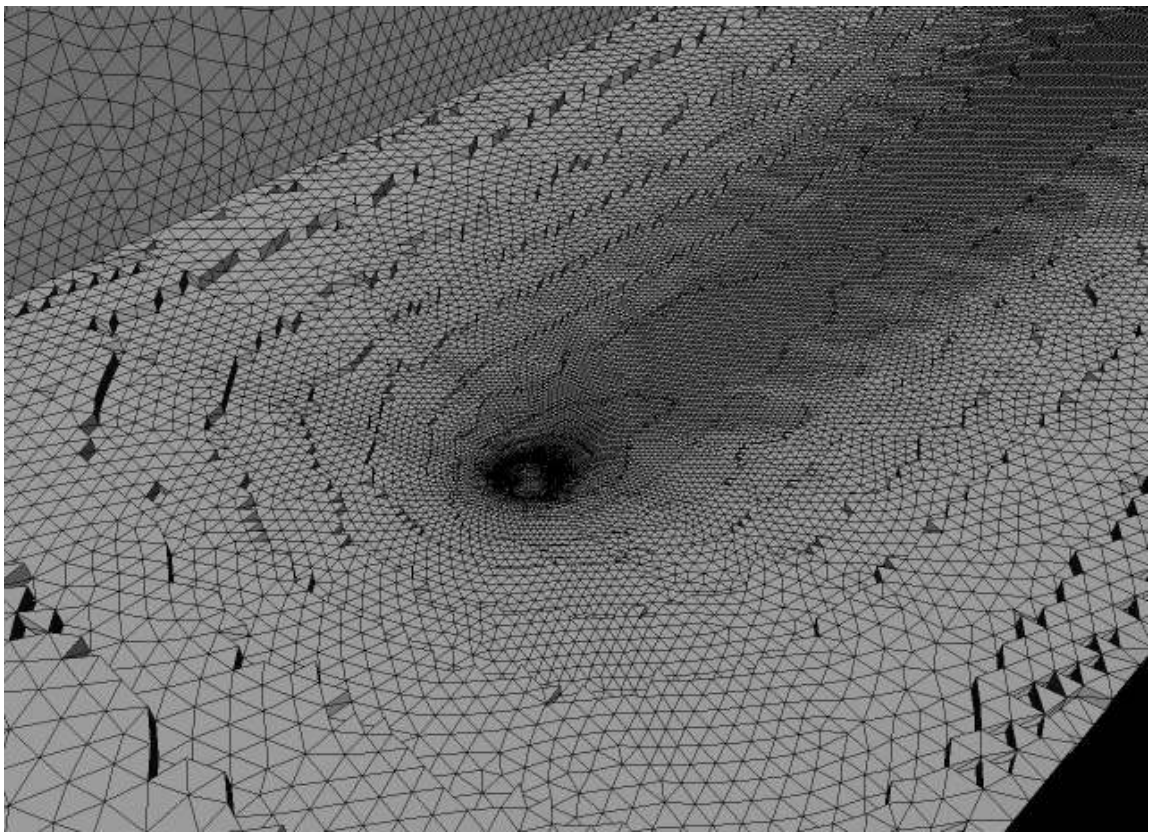

Fig. 20 Viscous grid layers 90-degree circular injector case.

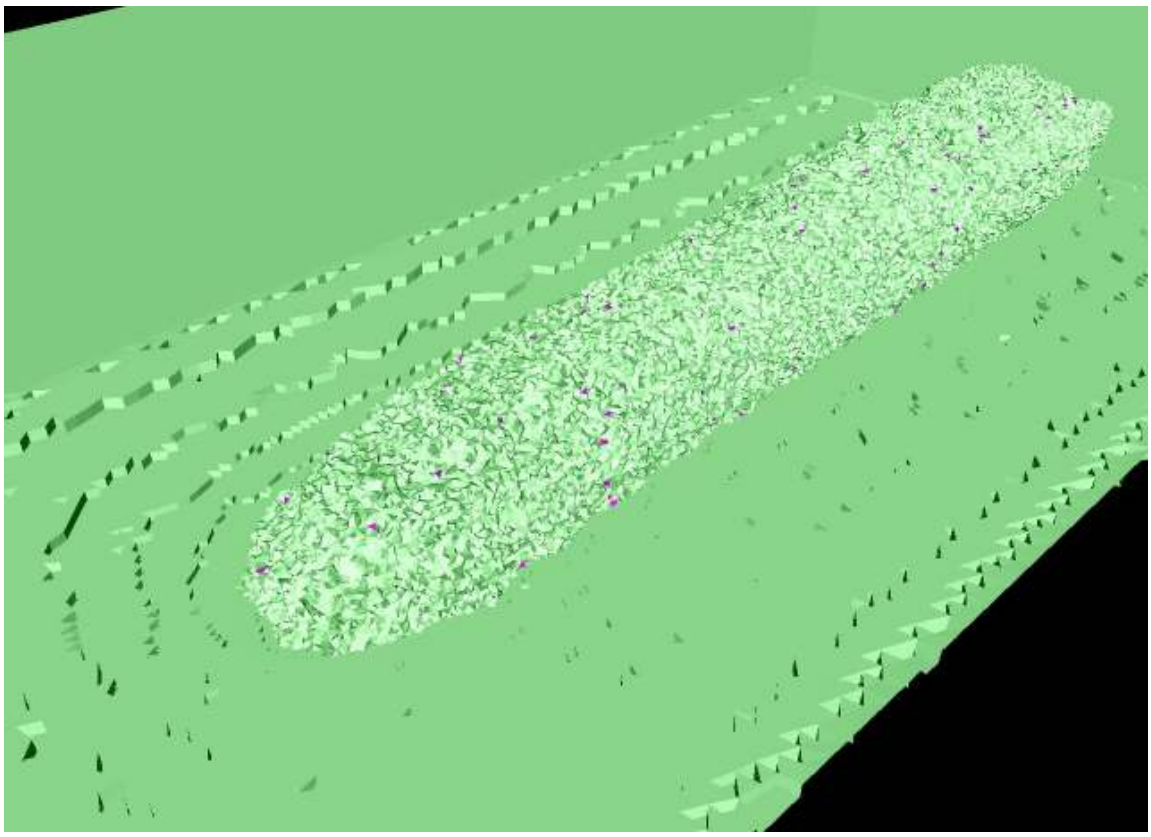

Fig. 21 Inviscid cells for 90-degree circular injector case.

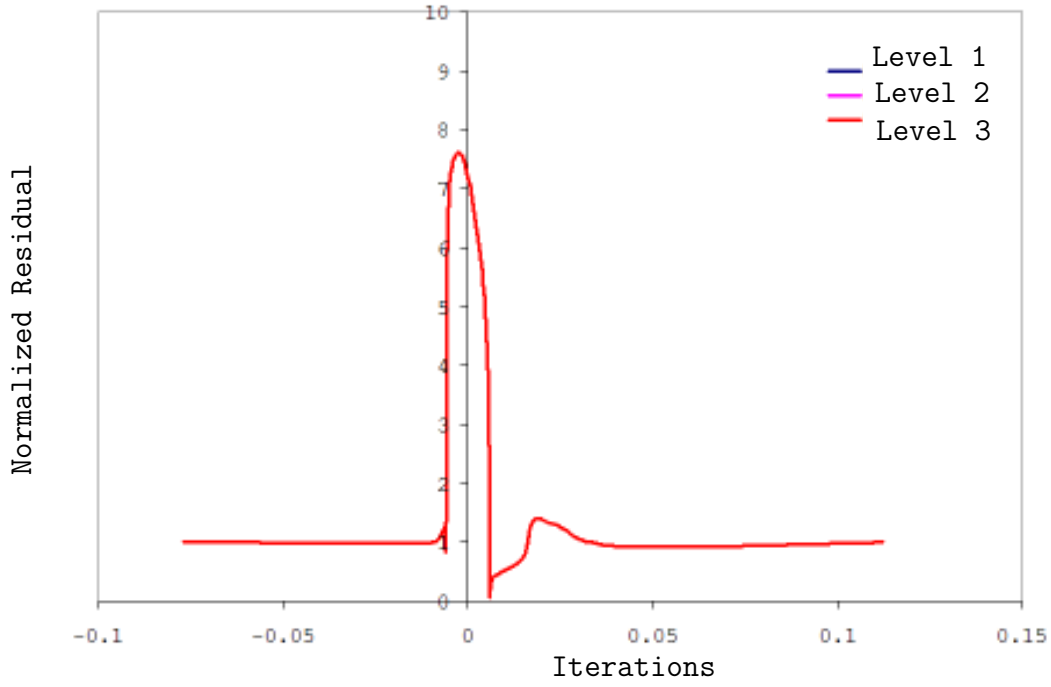

Fig. 22 Normalized tunnel floor centerline pressure solution convergence.

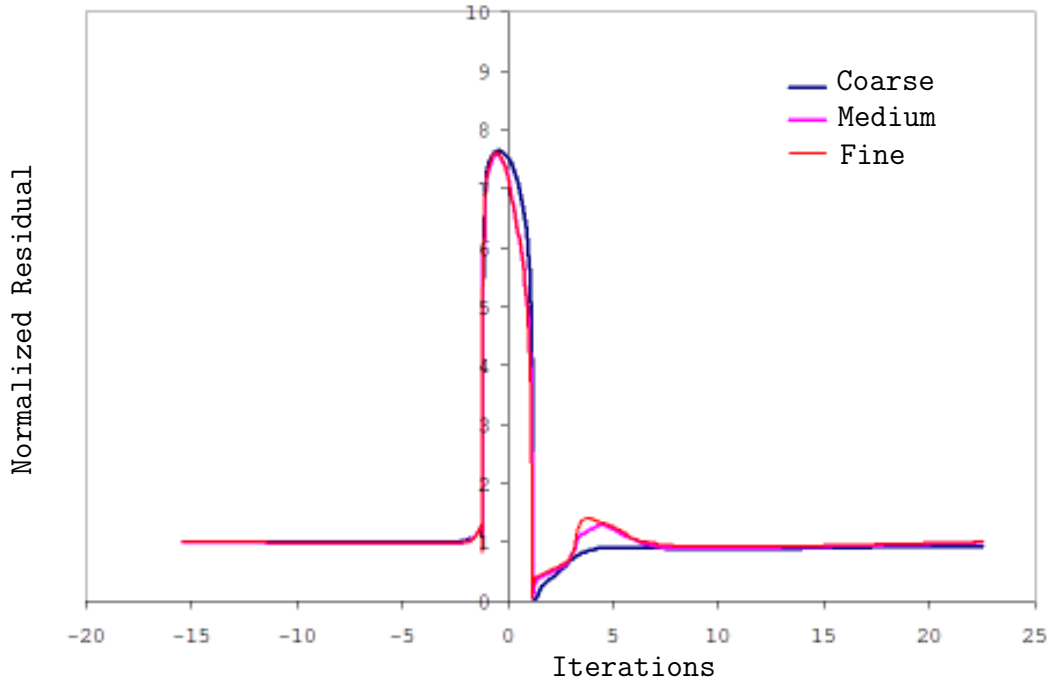

Fig. 23 Normalized tunnel floor centerline pressure grid convergence.

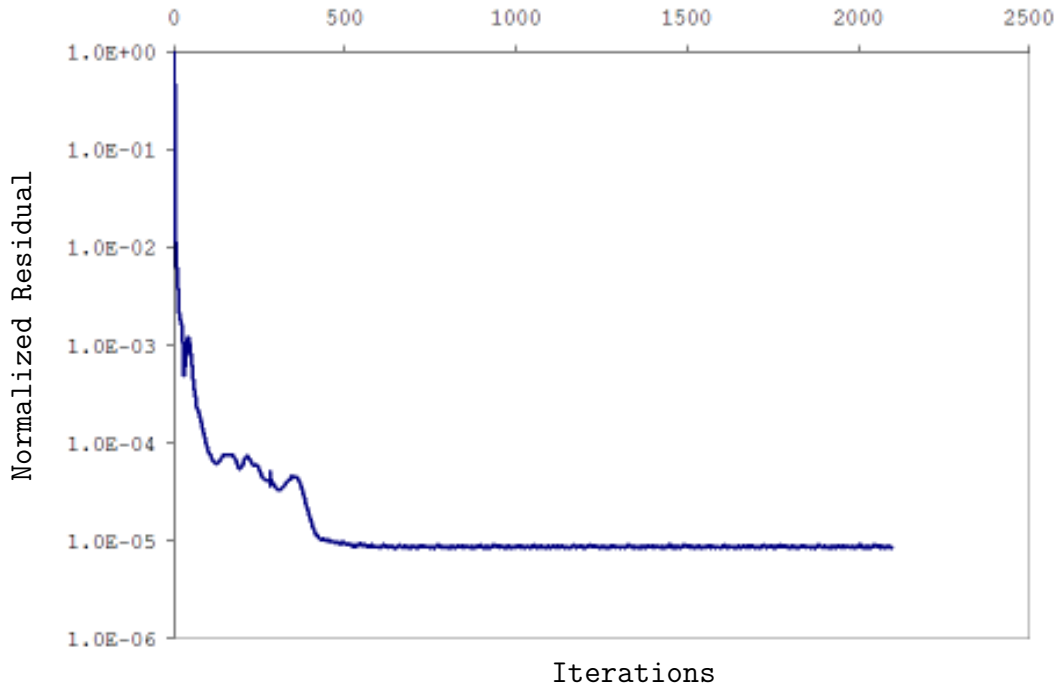

Fig. 24 Normalized residual.

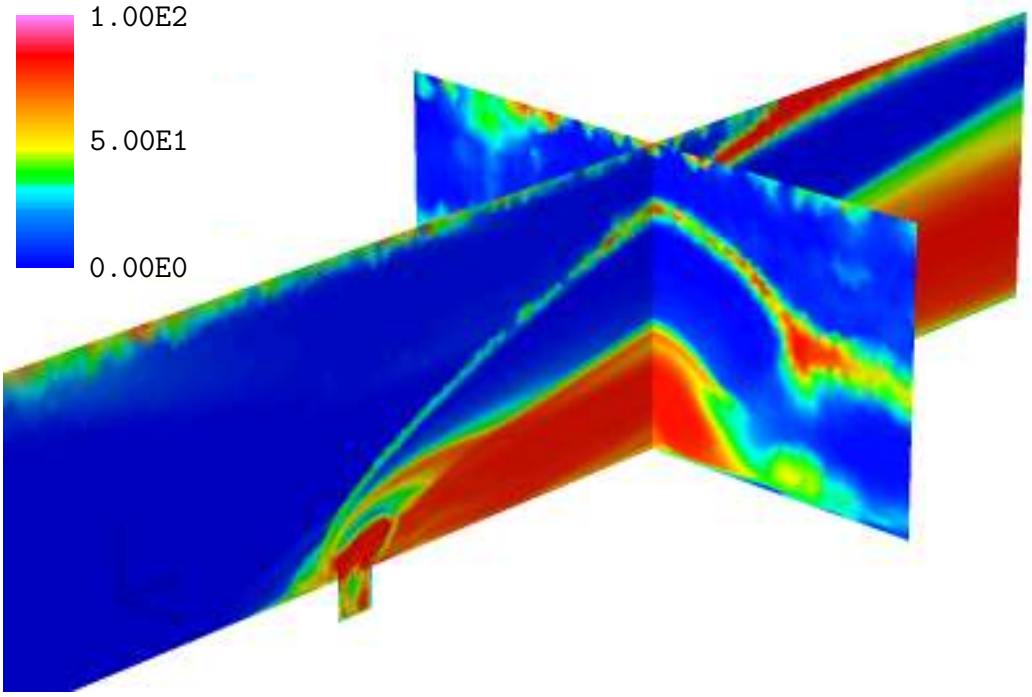

Fig. 25 Ratio of resolved TKE to total TKE for DES simulation.

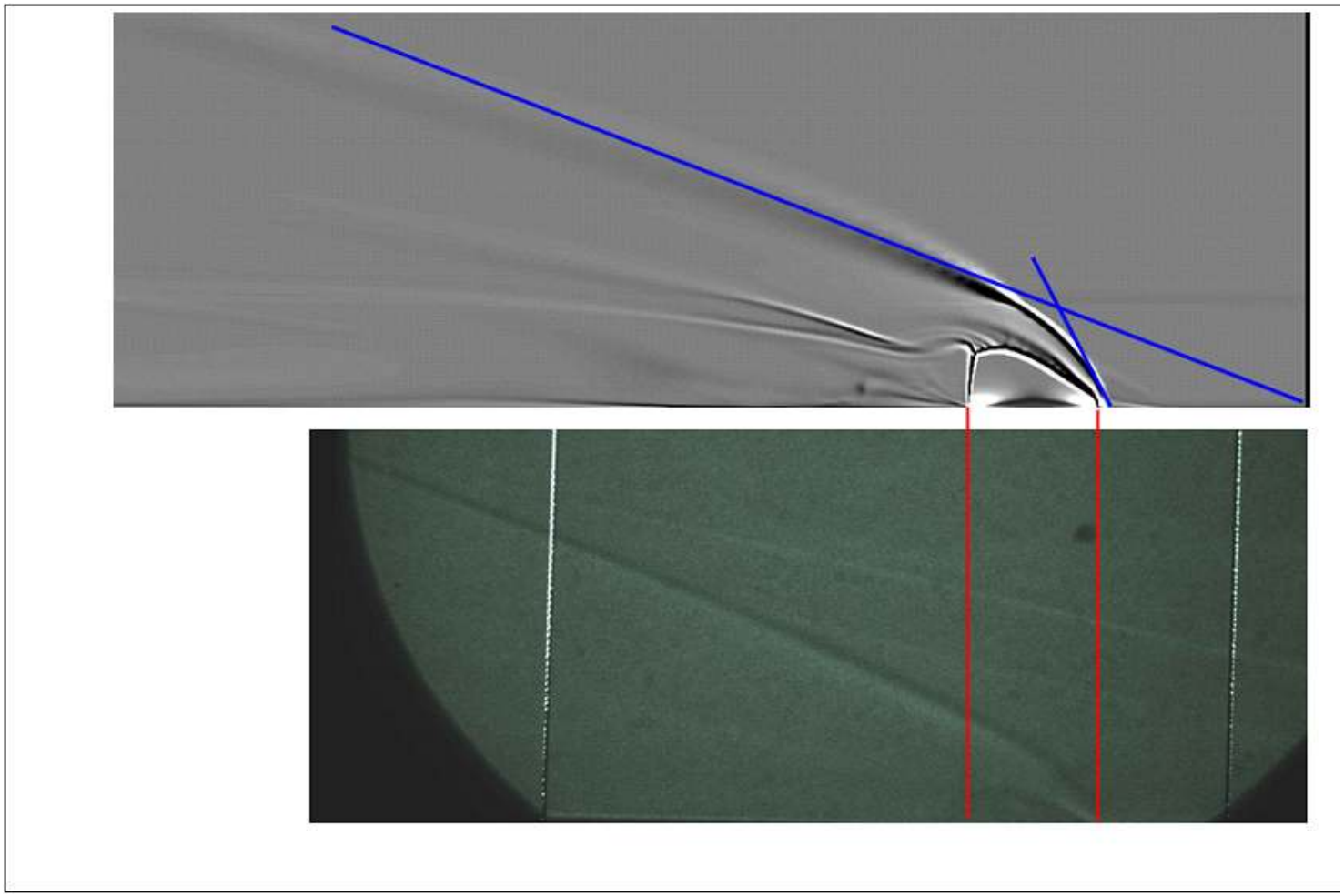

Fig. 26 Shadowgraph comparison of RANS results with experiments — 90-degree J_1.

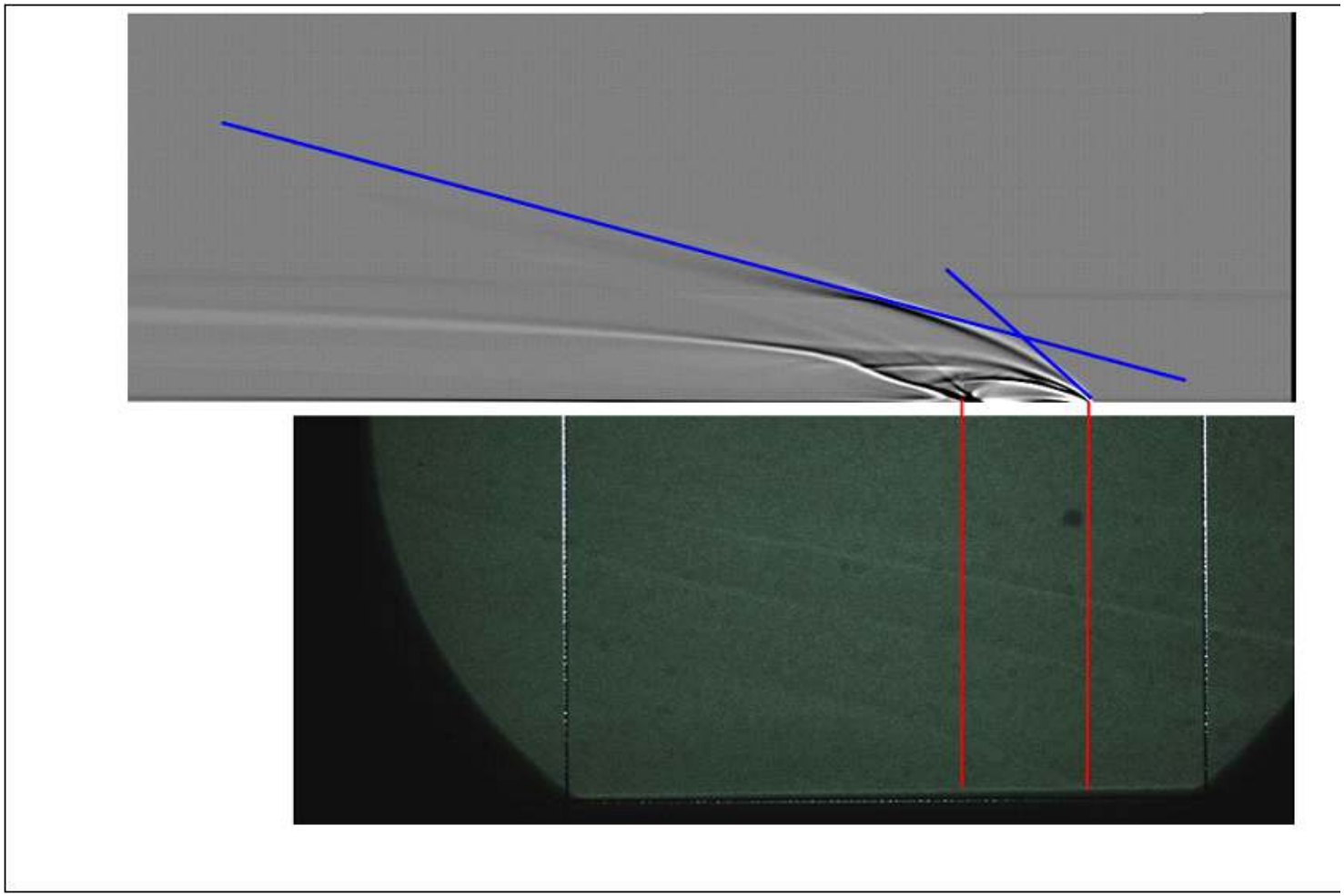

Fig. 27 Shadowgraph comparison of RANS results with experiments — 10-degree J_1.

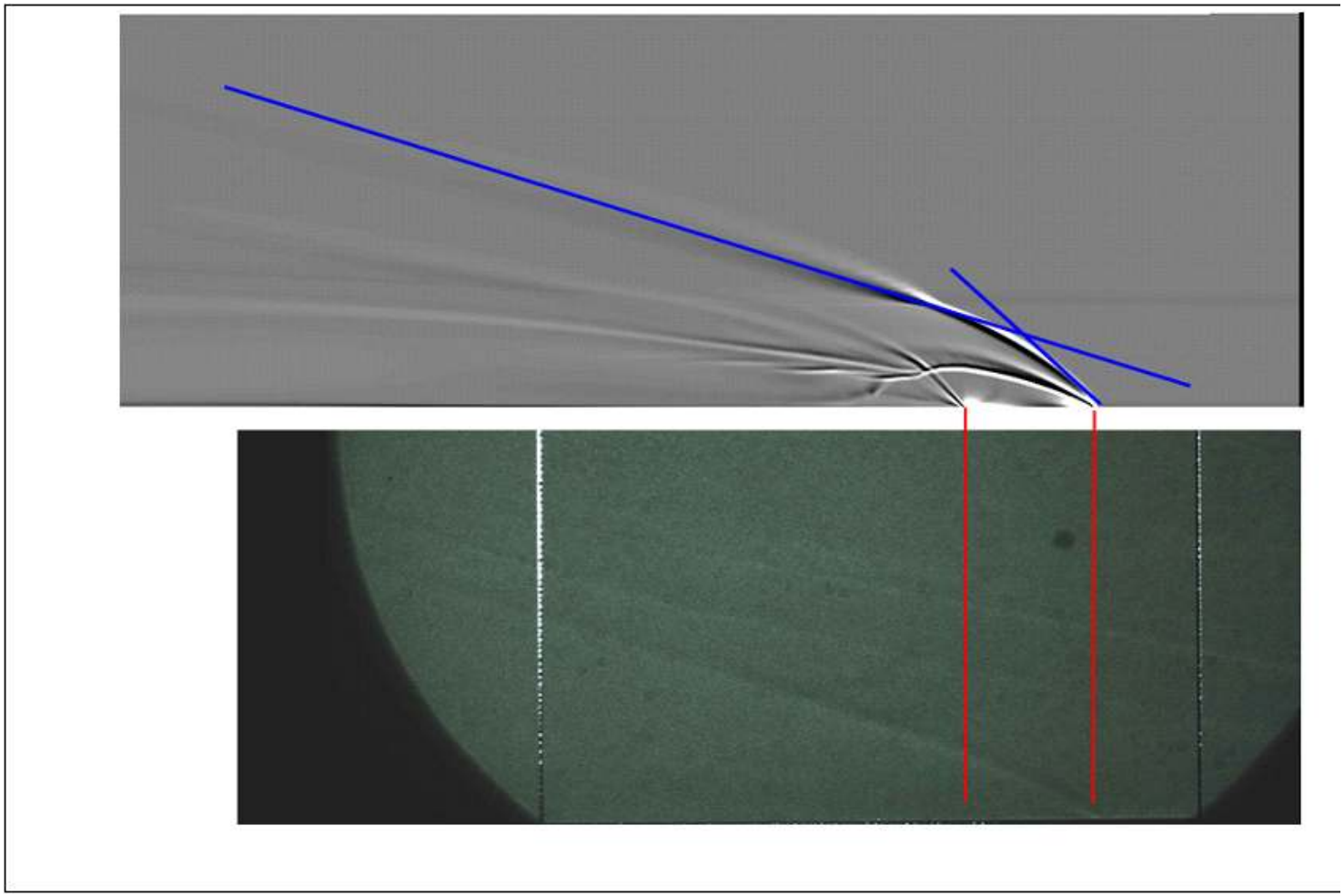

Fig. 28 Shadowgraph comparison of RANS results with experiments — 27.5-degree J_1.

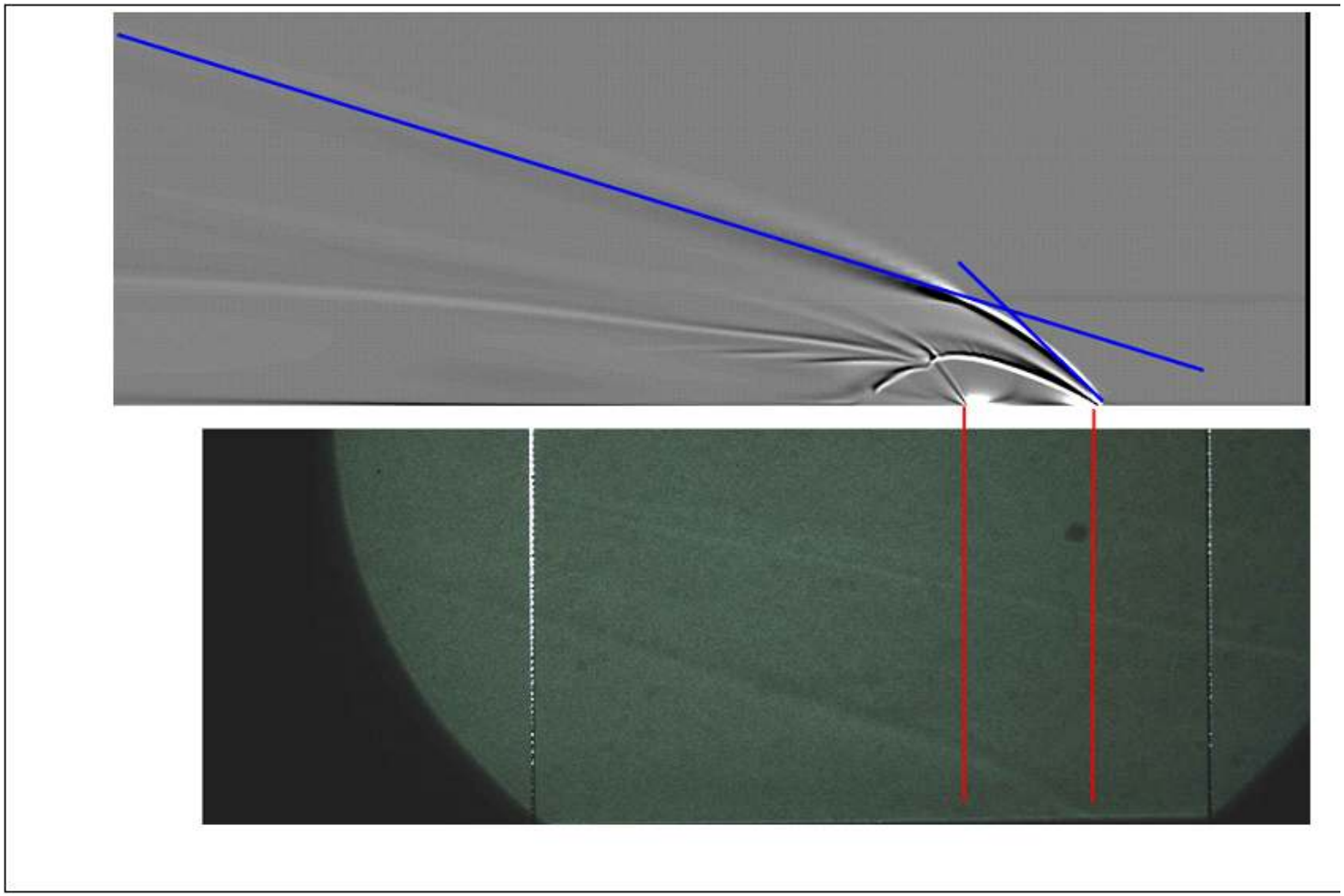

Fig. 29 Shadowgraph comparison of RANS results with experiments — 45-degree J_1.

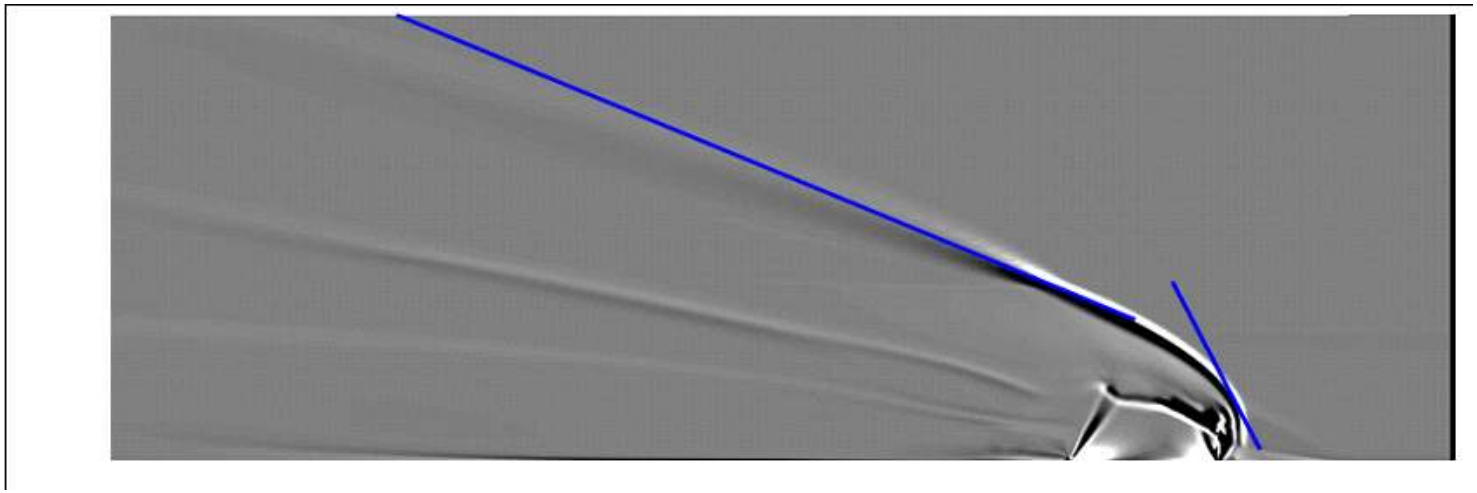

Fig. 30 Shadowgraph of RANS results — 135-degree J_1.

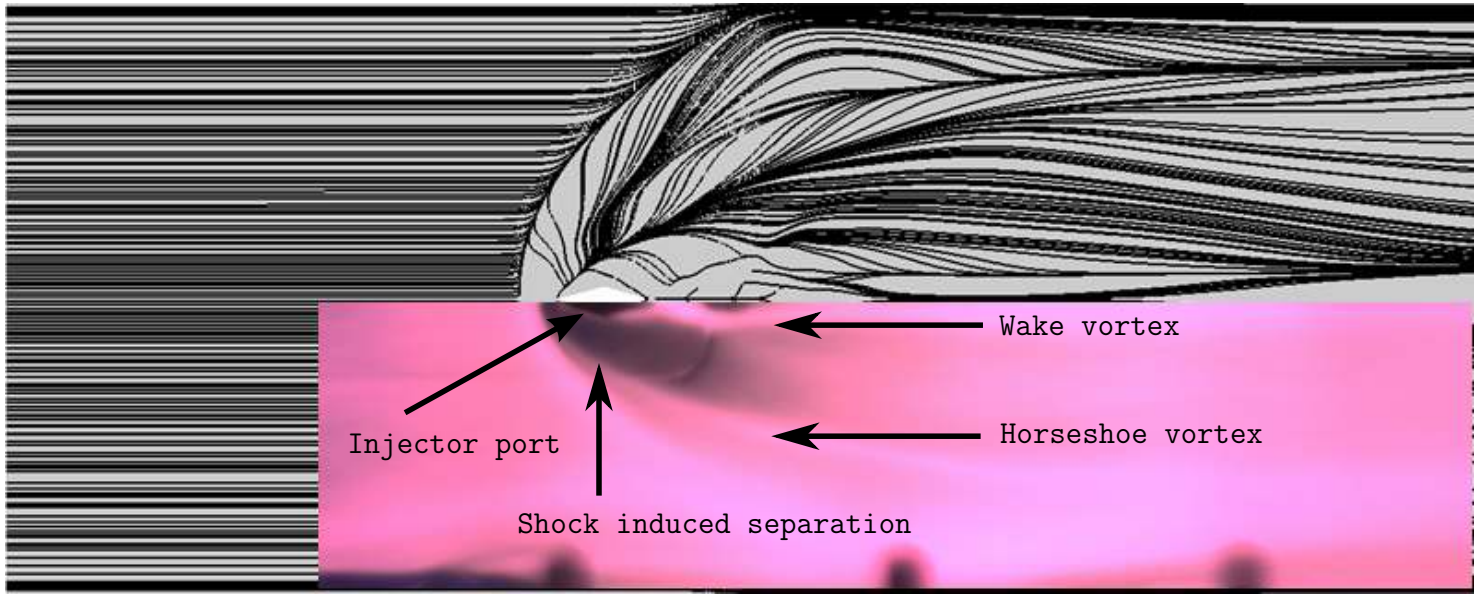

Fig. 31 Oil flow comparison of RANS results with experiments — 90-degree J_1.

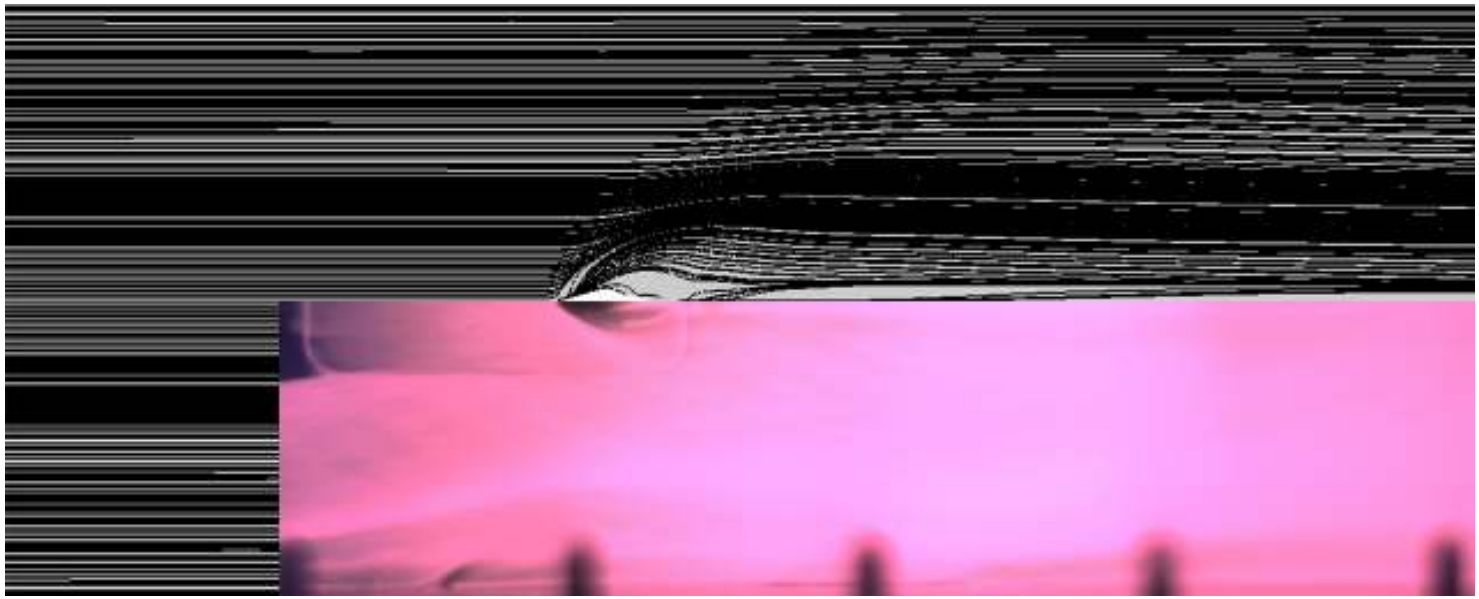

Fig. 32 Oil flow comparison of RANS results with experiments — 10-degree J_1.

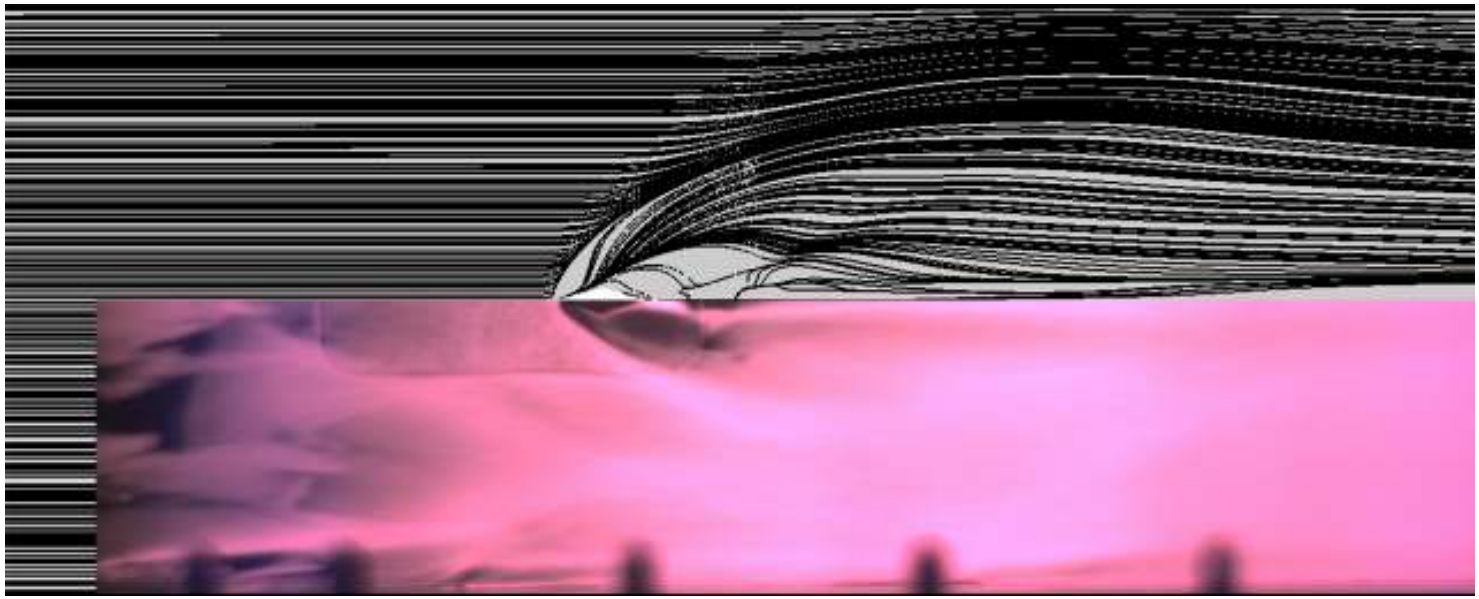

Fig. 33 Oil flow comparison of RANS results with experiments — 27.5-degree J_1.

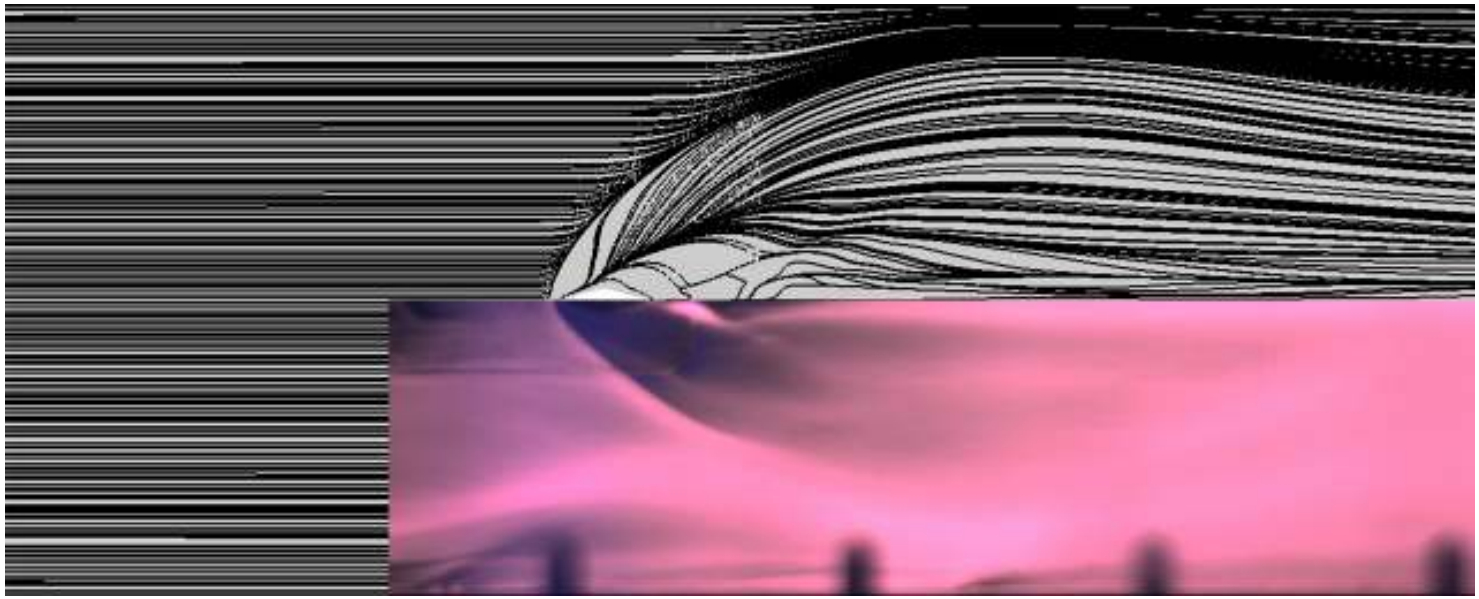

Fig. 34 Oil flow comparison of RANS results with experiments — 45-degree J_1.

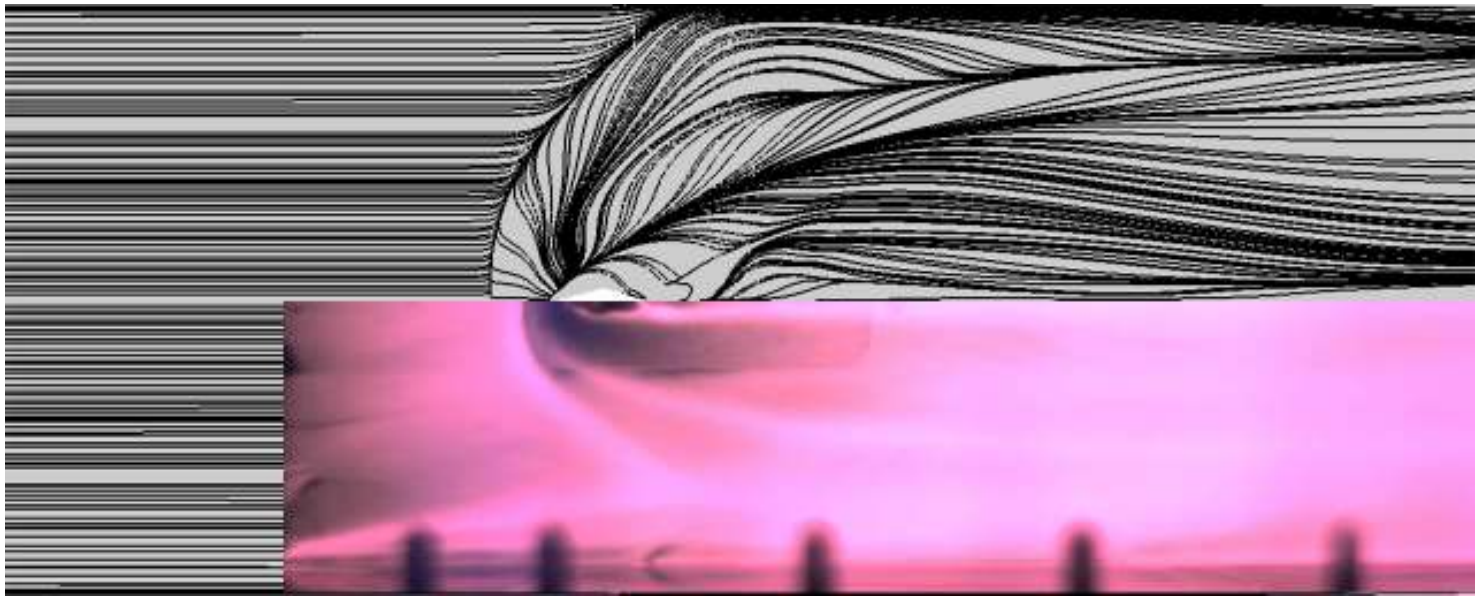

Fig. 35 Oil flow comparison of RANS results with experiments — 135-degree J_1.

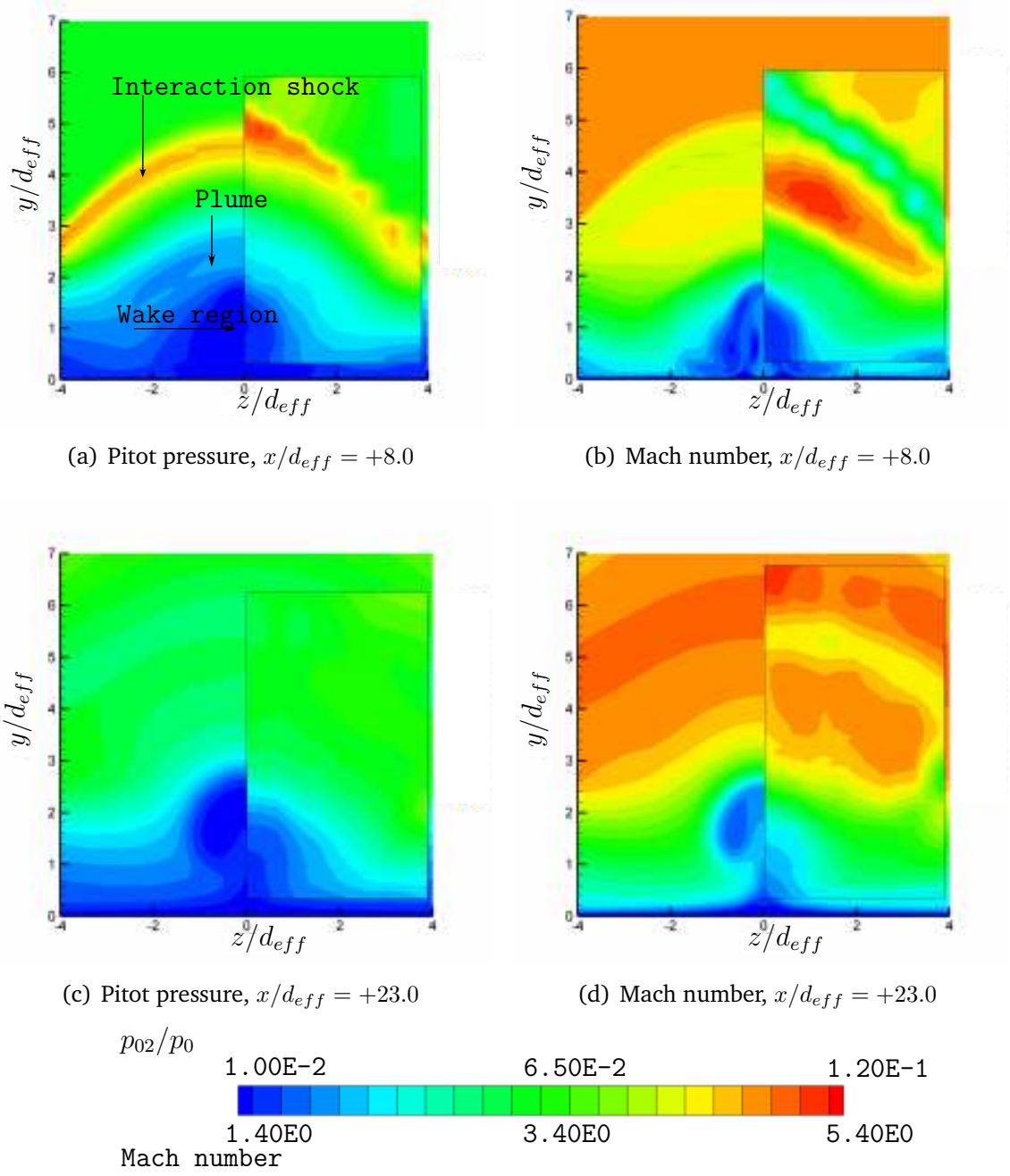

(a) Pitot pressure, $x/d_{eff} = +8.0$

(b) Mach number, $x/d_{eff} = +8.0$

(c) Pitot pressure, $x/d_{eff} = +23.0$

(d) Mach number, $x/d_{eff} = +23.0$

Fig. 36 Pitot pressure and Mach number contours at $x/d_{eff} = +8.0$ and $x/d_{eff} = +23.0$ — 90-degree J_1. The pitot pressure is normalized by the freestream total pressure. The axial locations x/d_{eff} are measured from the leading edge of the injector.

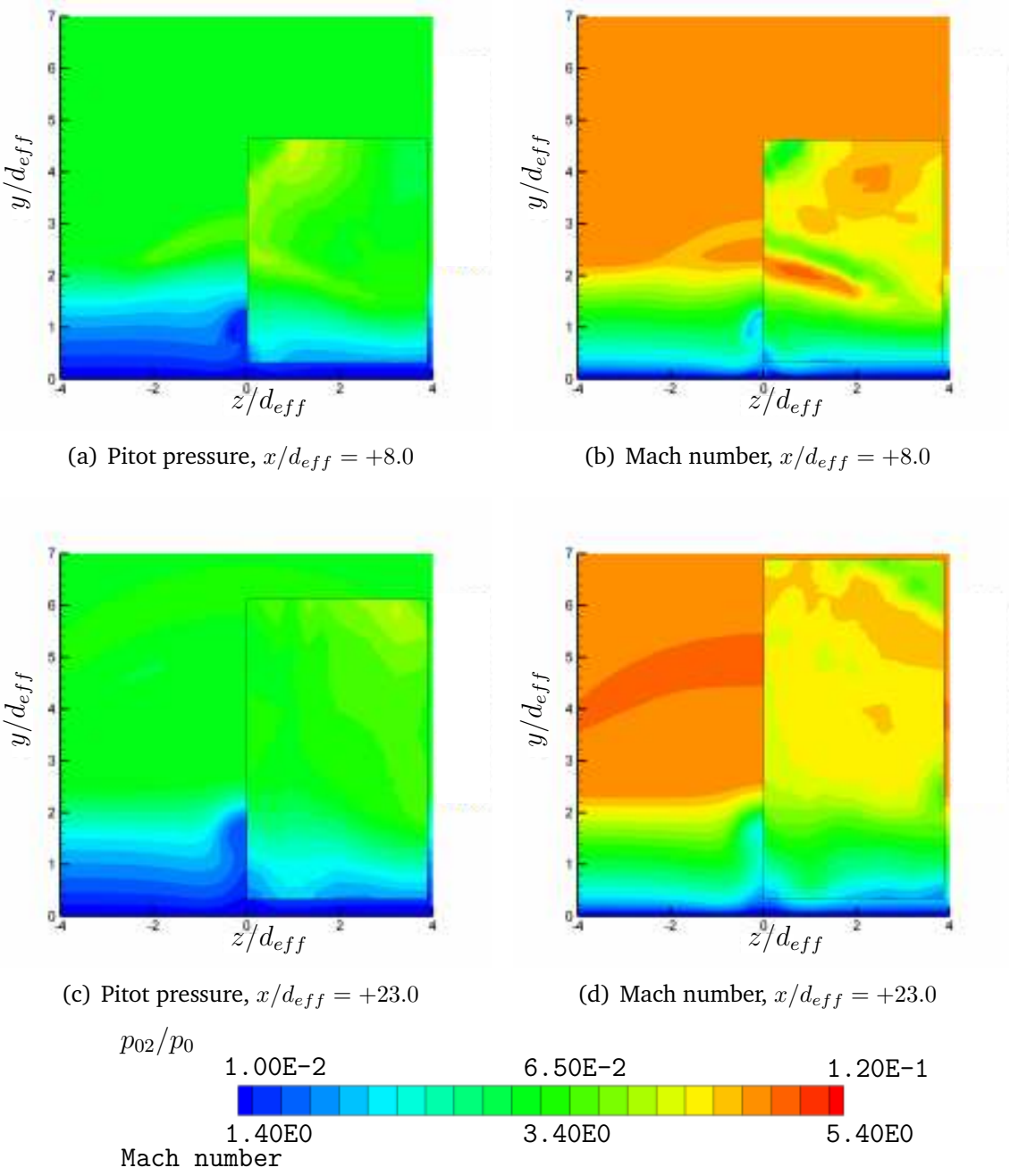

(a) Pitot pressure, $x/d_{eff} = +8.0$

(b) Mach number, $x/d_{eff} = +8.0$

(c) Pitot pressure, $x/d_{eff} = +23.0$

(d) Mach number, $x/d_{eff} = +23.0$

Fig. 37 Pitot pressure and Mach number contours at $x/d_{eff} = +8.0$ and $x/d_{eff} = +23.0$ — 10-degree J_1. The pitot pressure is normalized by the freestream total pressure. The axial locations x/d_{eff} are measured from the leading edge of the injector.

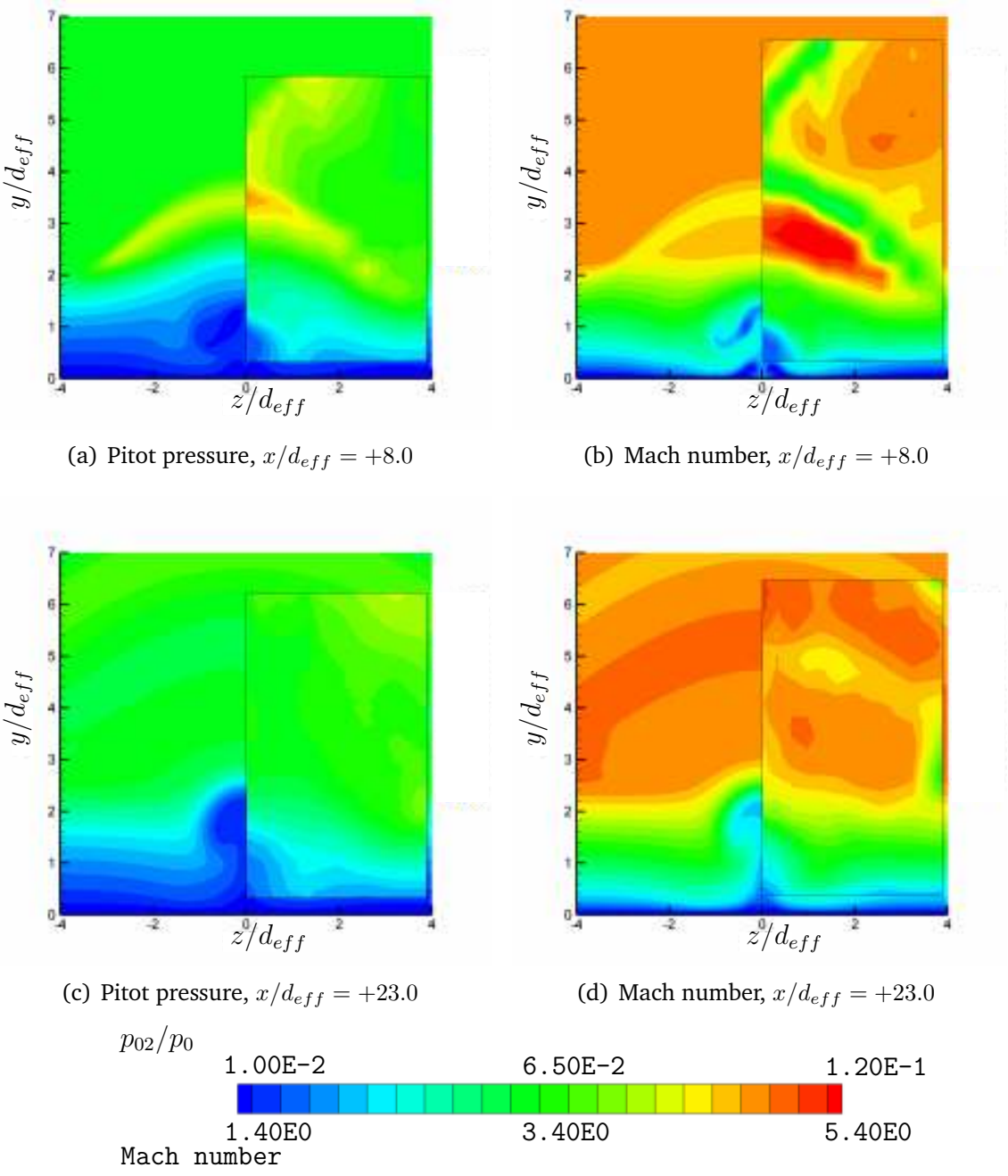

(a) Pitot pressure, $x/d_{eff} = +8.0$

(b) Mach number, $x/d_{eff} = +8.0$

(c) Pitot pressure, $x/d_{eff} = +23.0$

(d) Mach number, $x/d_{eff} = +23.0$

Fig. 38 Pitot pressure and Mach number contours at $x/d_{eff} = +8.0$ and $x/d_{eff} = +23.0$ — 27.5-degree J_1. The pitot pressure is normalized by the freestream total pressure. The axial locations x/d_{eff} are measured from the leading edge of the injector.

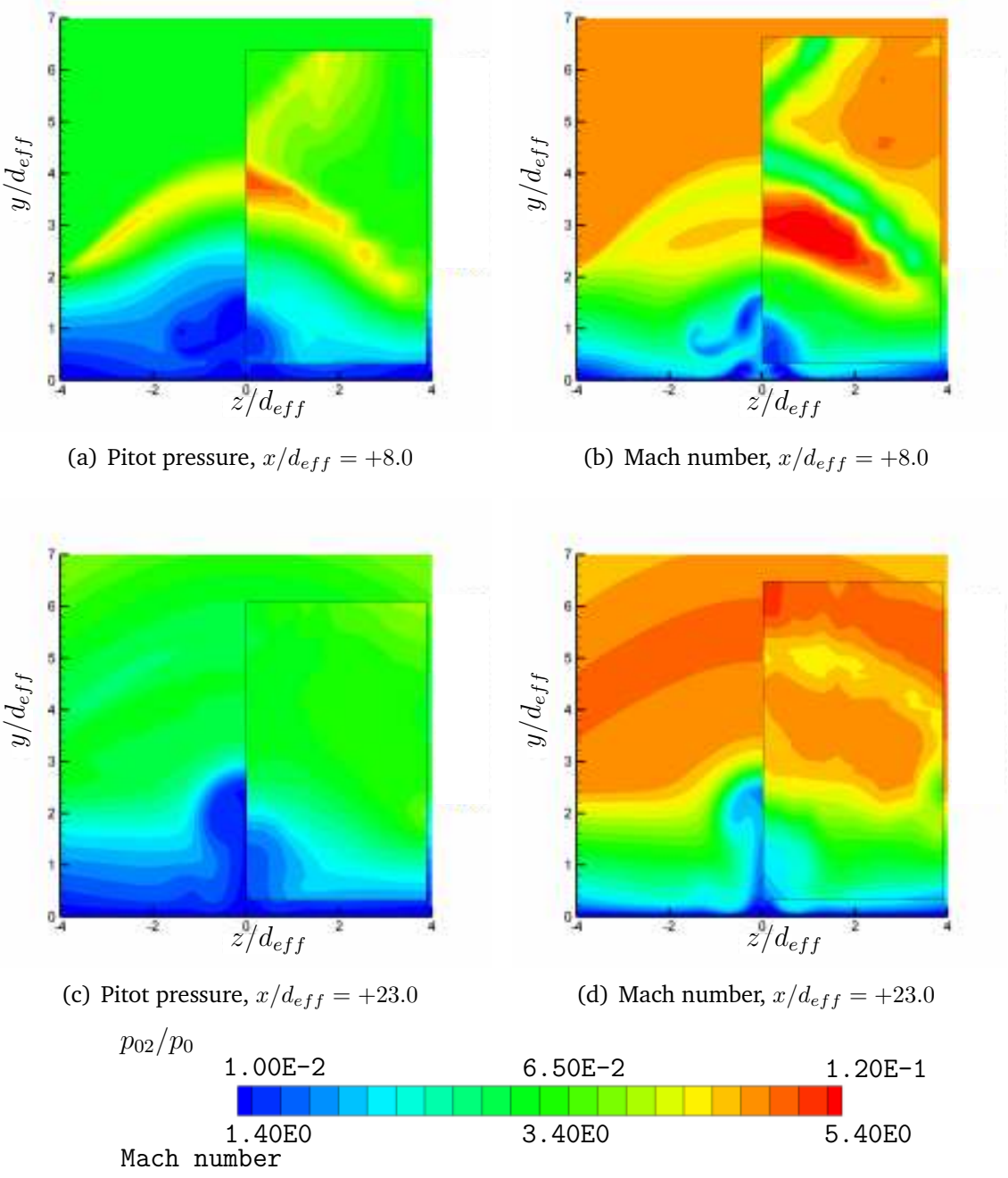

(a) Pitot pressure, $x/d_{eff} = +8.0$

(b) Mach number, $x/d_{eff} = +8.0$

(c) Pitot pressure, $x/d_{eff} = +23.0$

(d) Mach number, $x/d_{eff} = +23.0$

Fig. 39 Pitot pressure and Mach number contours at $x/d_{eff} = +8.0$ and $x/d_{eff} = +23.0$ — 45-degree J_1. The pitot pressure is normalized by the freestream total pressure. The axial locations x/d_{eff} are measured from the leading edge of the injector.

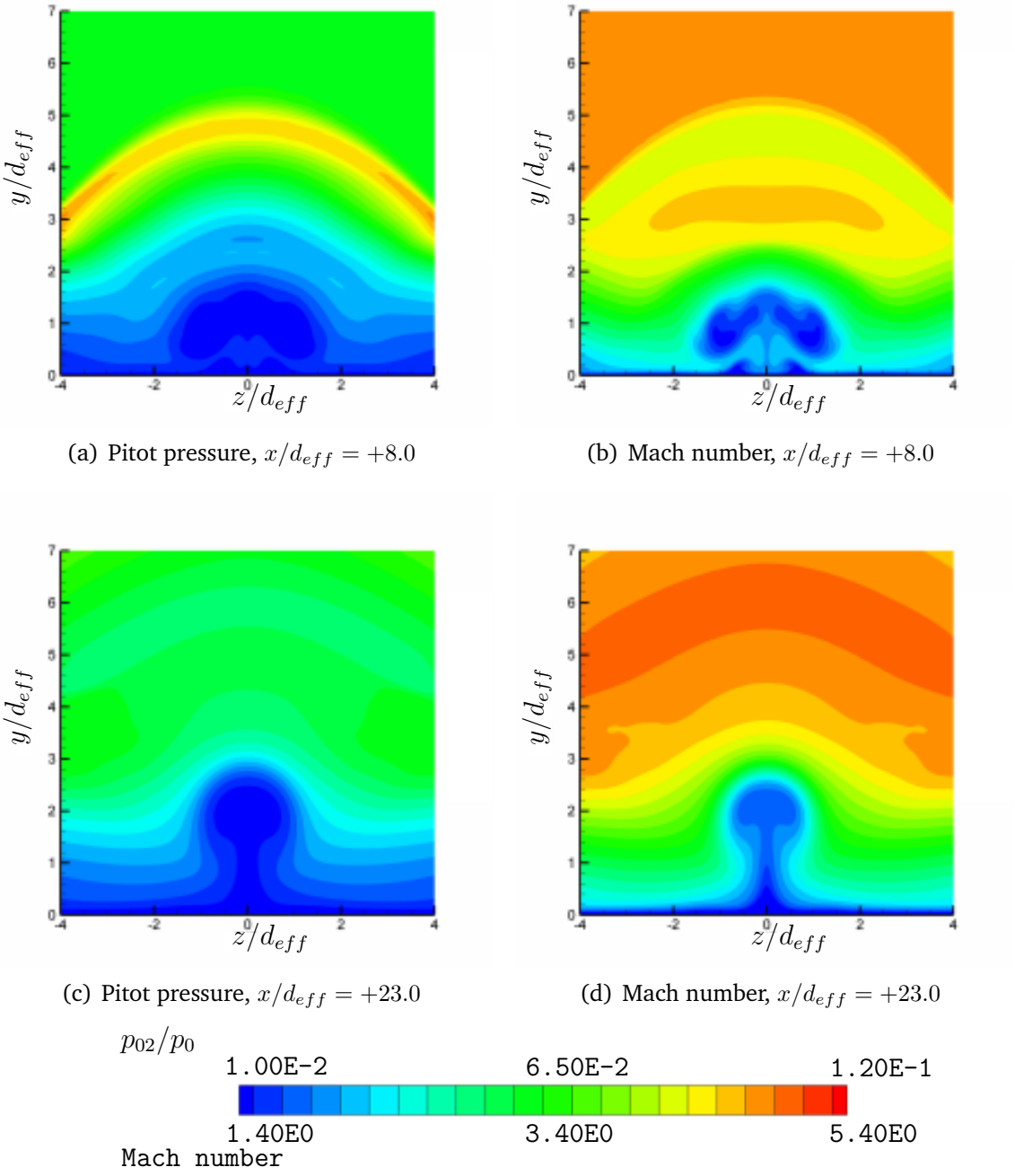

(a) Pitot pressure, $x/d_{eff} = +8.0$

(b) Mach number, $x/d_{eff} = +8.0$

(c) Pitot pressure, $x/d_{eff} = +23.0$

(d) Mach number, $x/d_{eff} = +23.0$

Fig. 40 Pitot pressure and Mach number contours at $x/d_{eff} = +8.0$ and $x/d_{eff} = +23.0$ — 135-degree J_1. The pitot pressure is normalized by the freestream total pressure. The axial locations x/d_{eff} are measured from the leading edge of the injector. Experimental results are not available for this case.

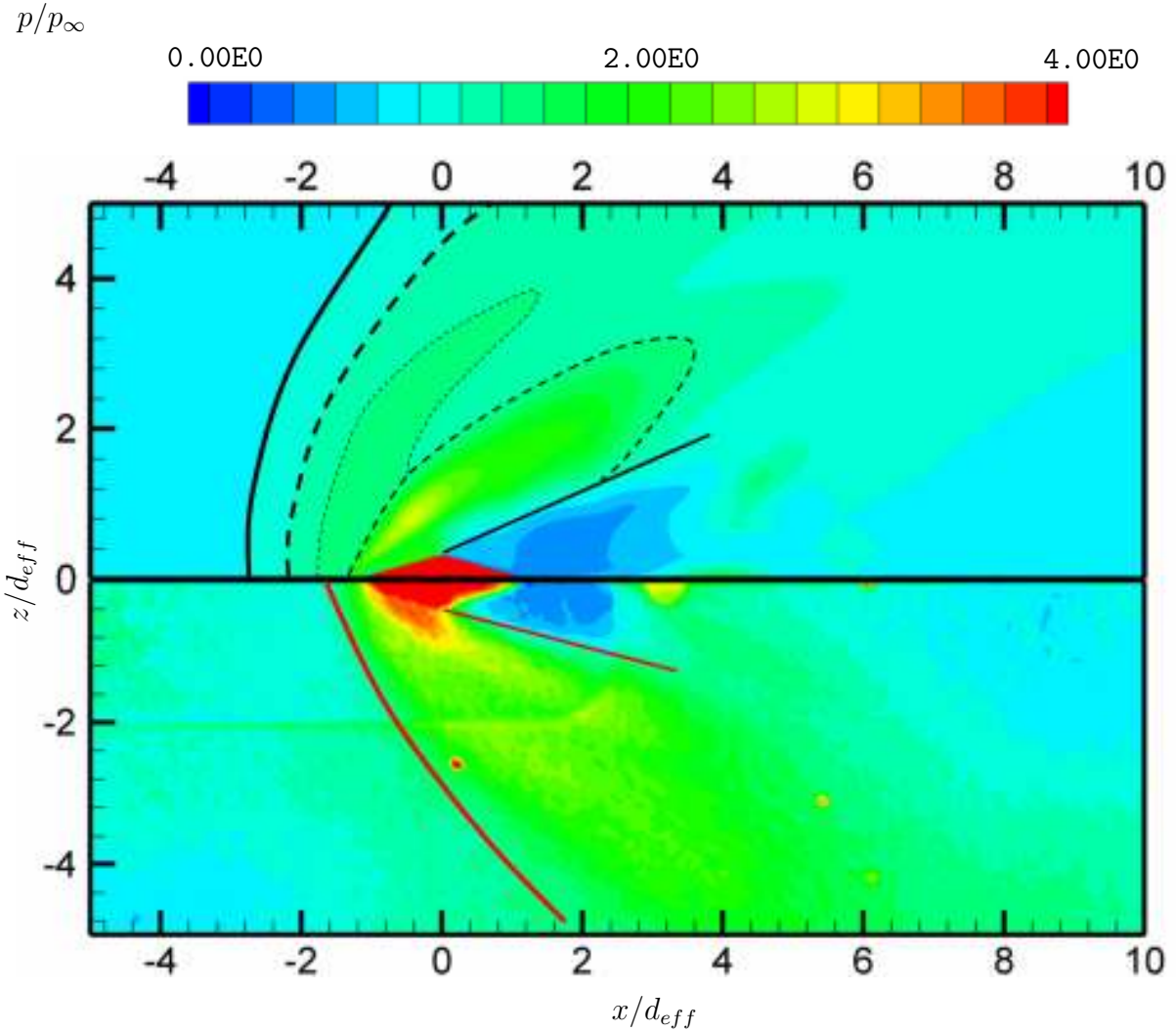

Fig. 41 Surface pressure comparison of RANS results with experiments — 90-degree J_1. The surface pressure is normalized by the freestream static pressure.

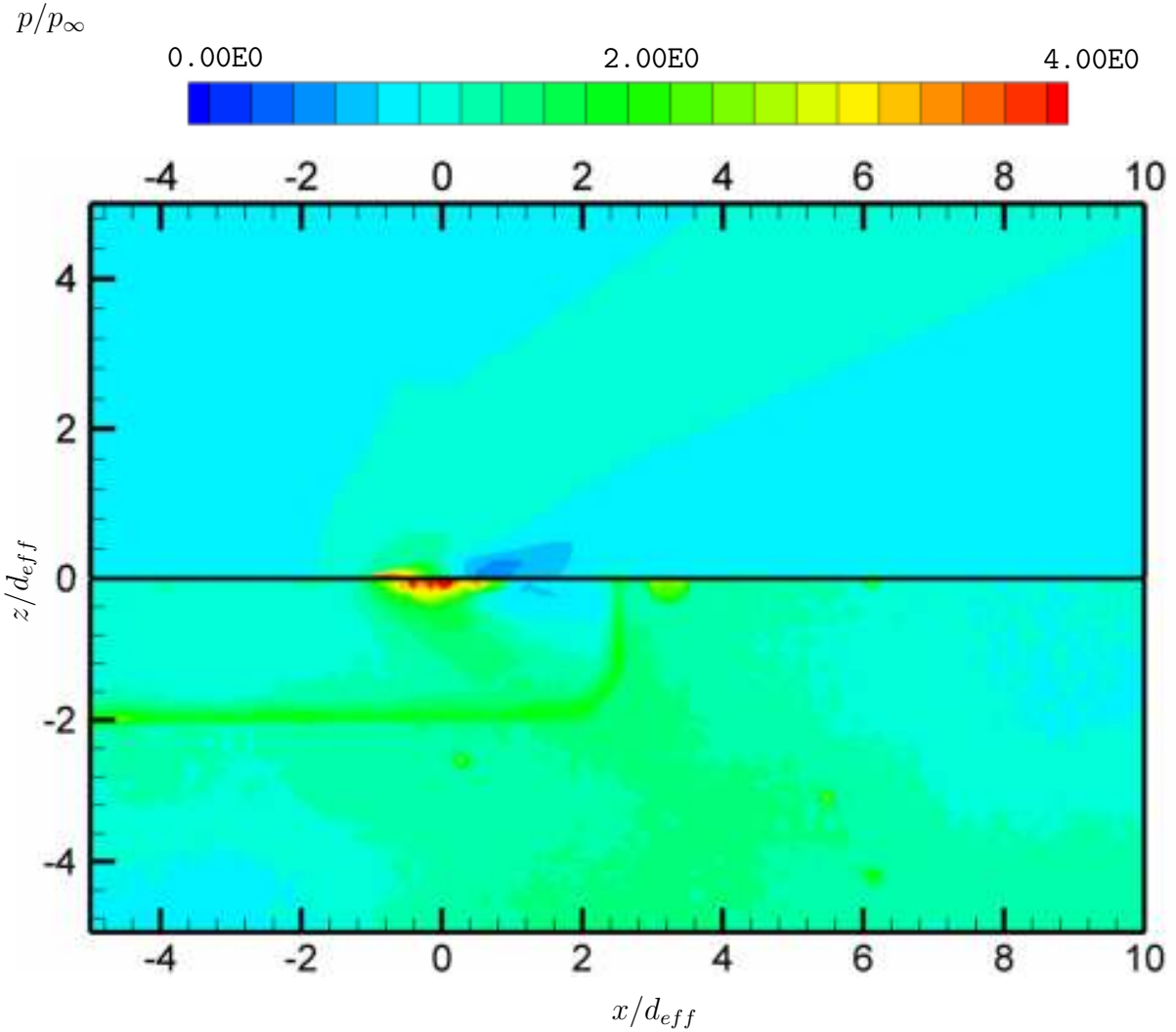

Fig. 42 Surface pressure comparison of RANS results with experiments — 10-degree J_1. The surface pressure is normalized by the freestream static pressure.

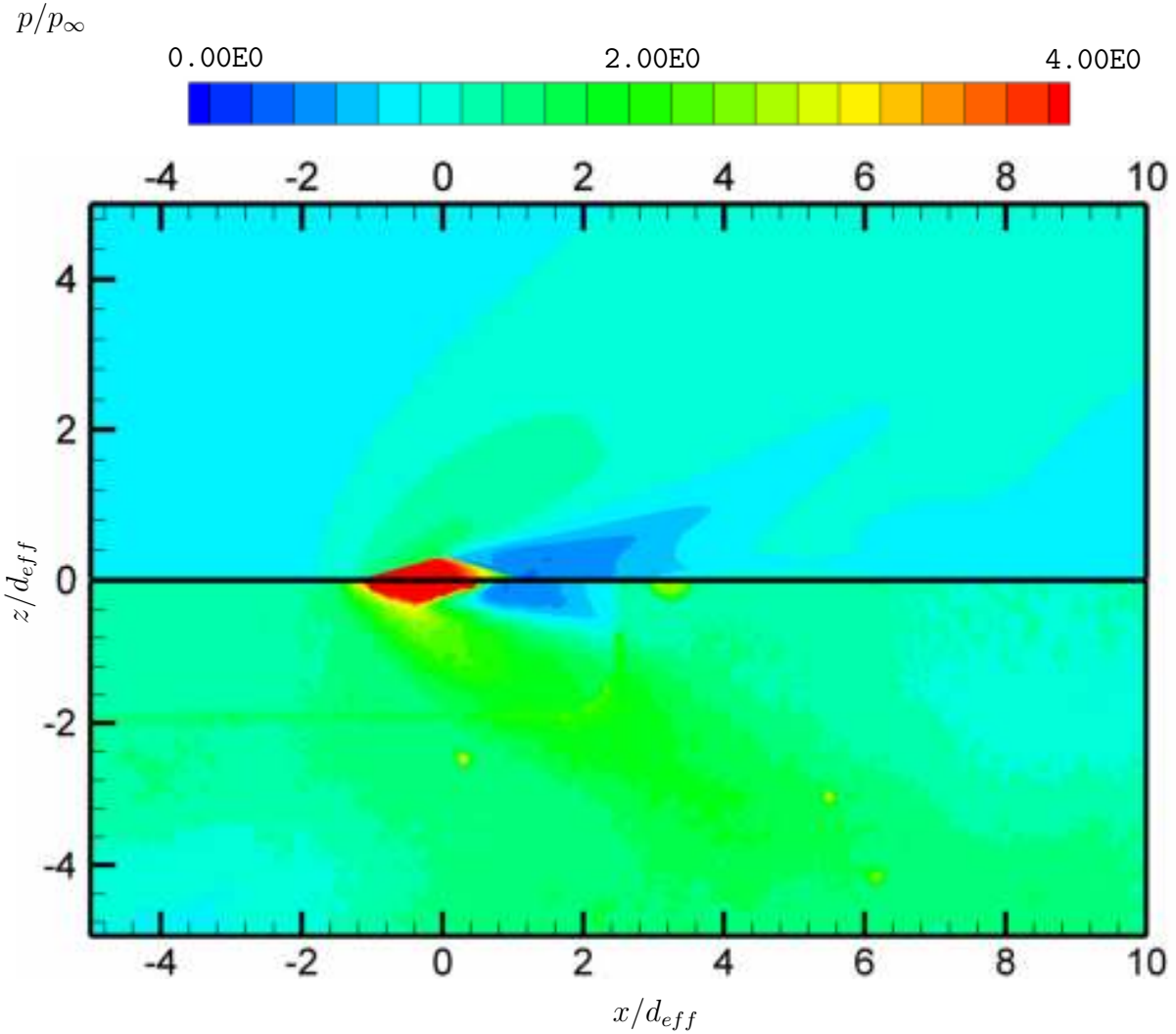

Fig. 43 Surface pressure comparison of RANS results with experiments — 27.5-degree J_1. The surface pressure is normalized by the freestream static pressure.

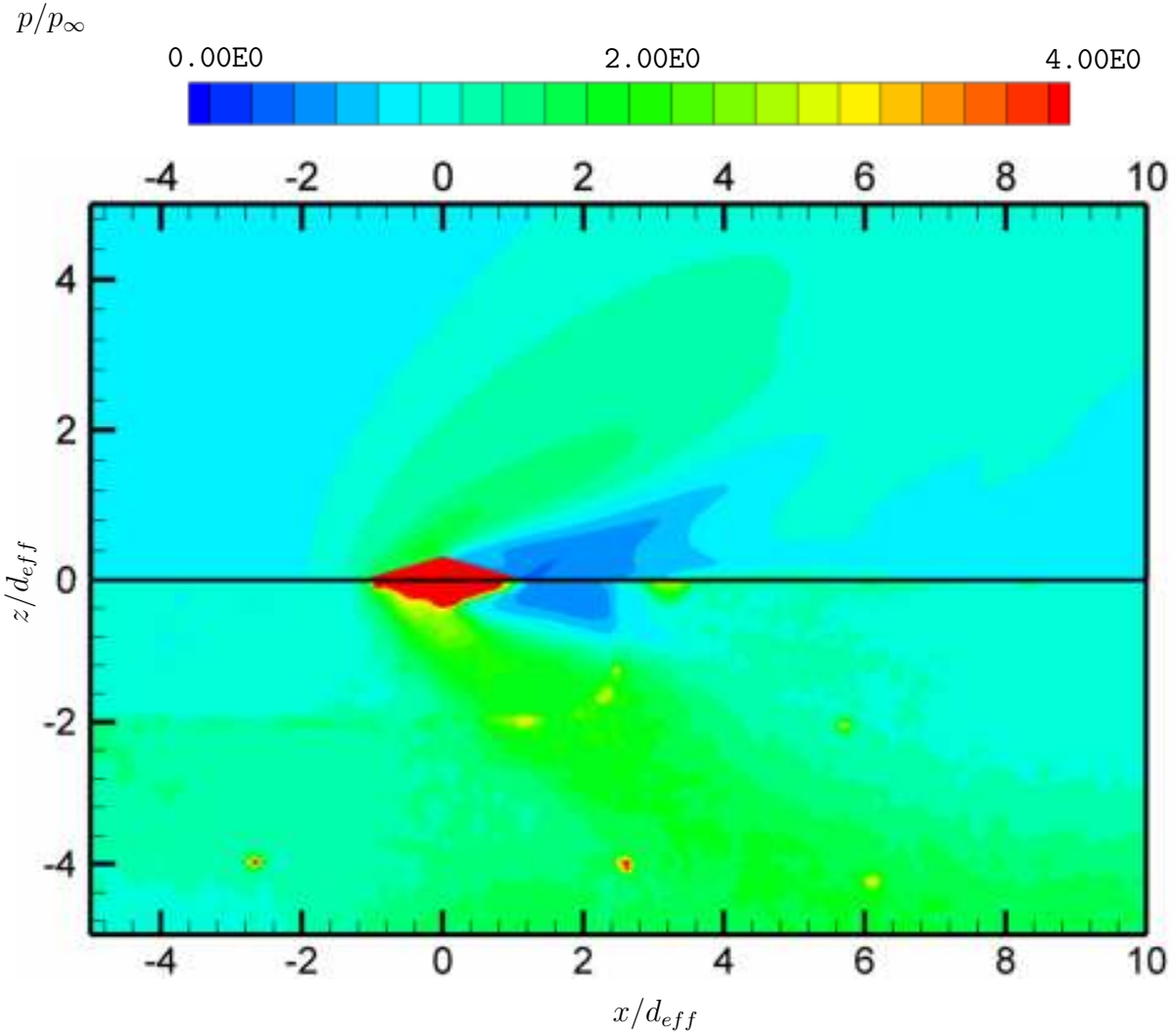

Fig. 44 Surface pressure comparison of RANS results with experiments — 45-degree J_1. The surface pressure is normalized by the freestream static pressure.

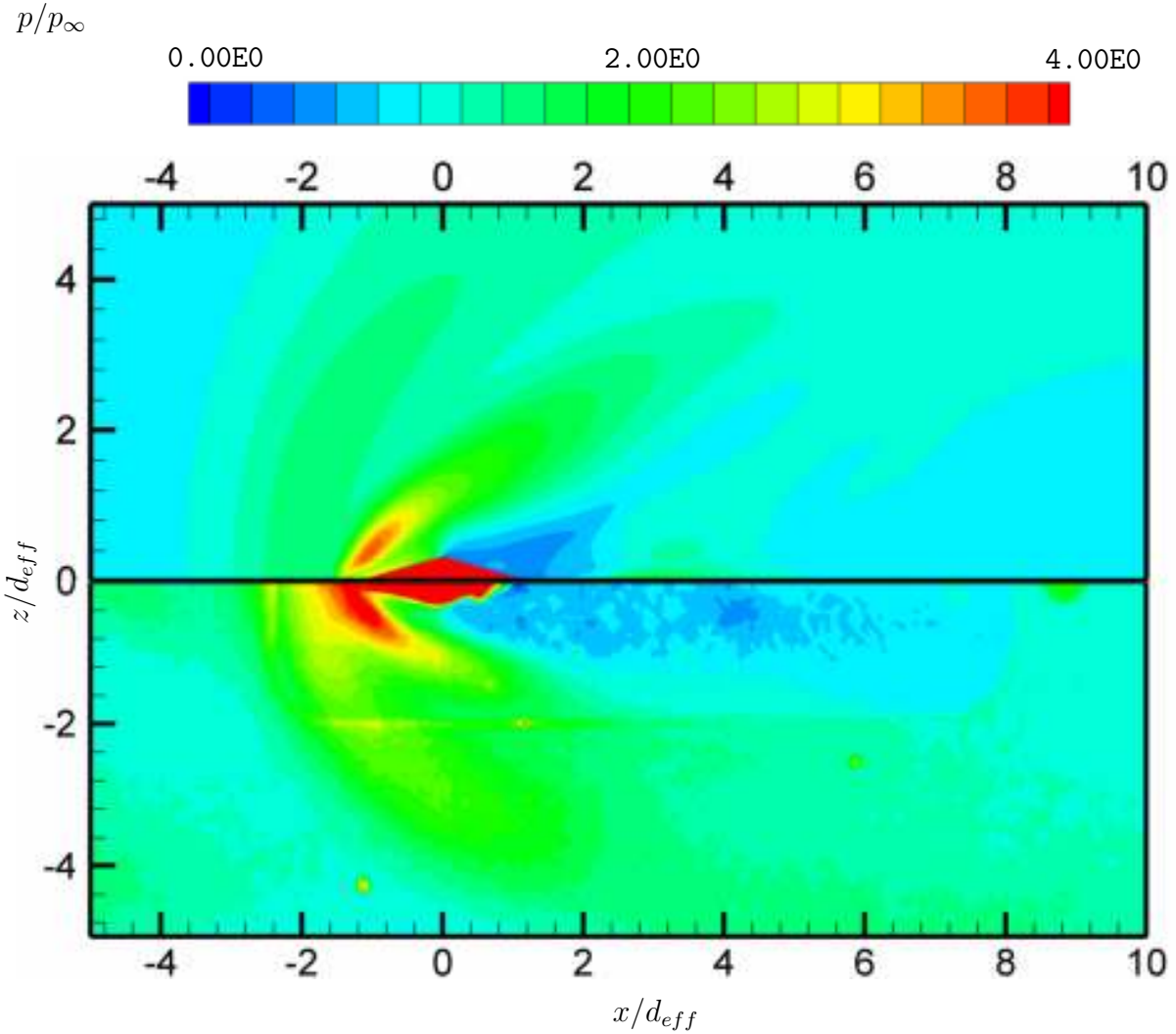

Fig. 45 Surface pressure comparison of RANS results with experiments — 135-degree J_1. The surface pressure is normalized by the freestream static pressure.

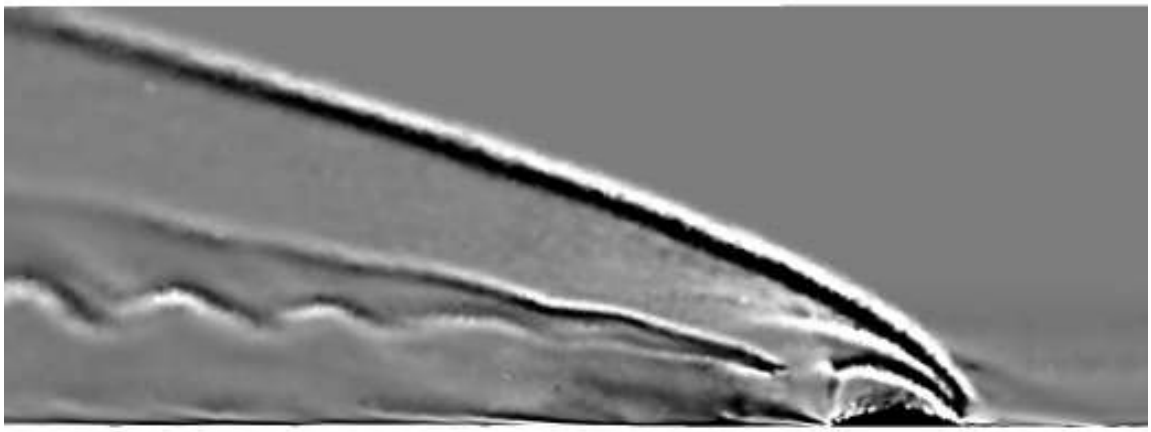

(a) Instantaneous

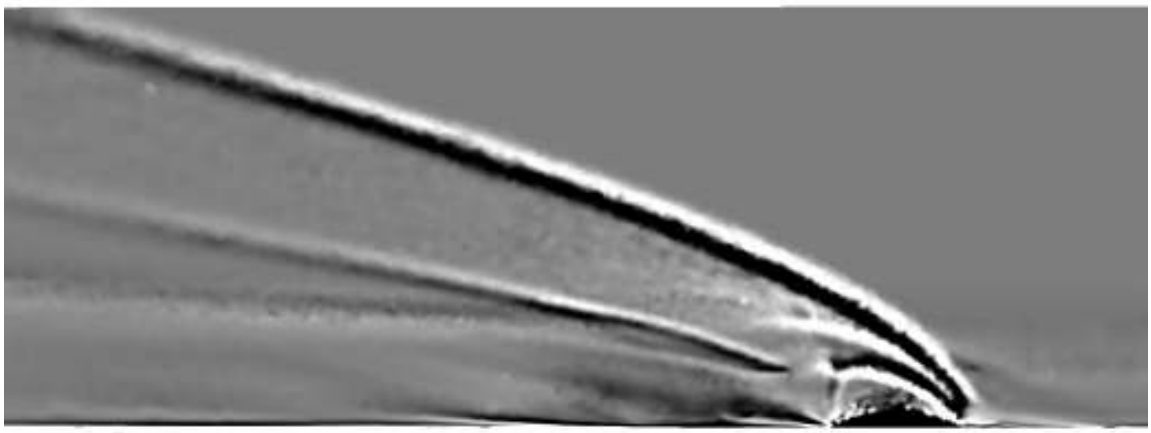

(b) Time-averaged

Fig. 46 Shadowgraph image of instantaneous and time-averaged DES solutions — 90-degree J_1

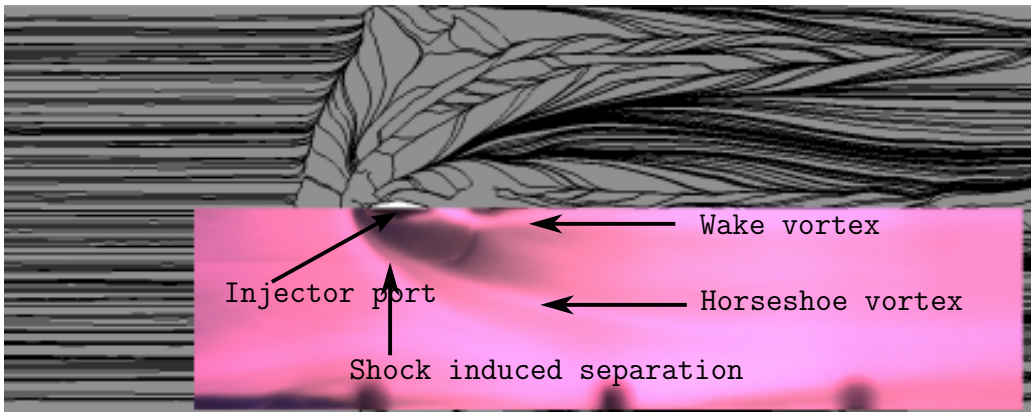

(a) Instantaneous

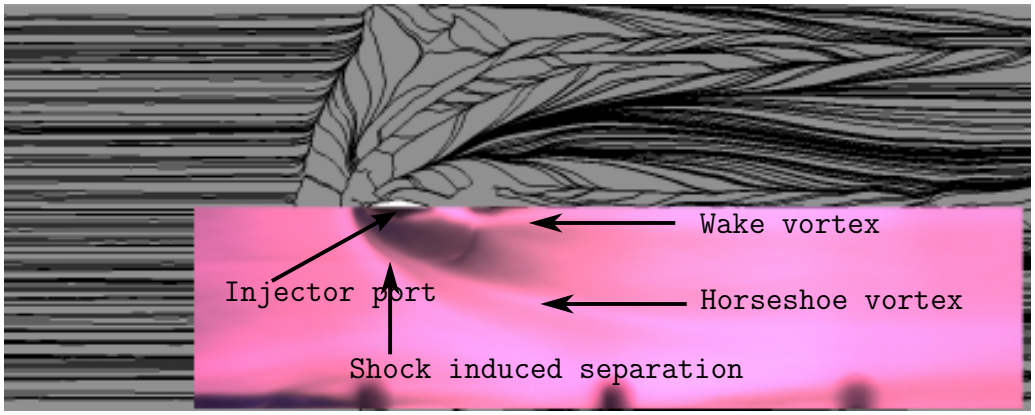

(b) Time-averaged

Fig. 47 Surface oil flow plot of instantaneous and time-averaged DES solutions — 90-degree J_1

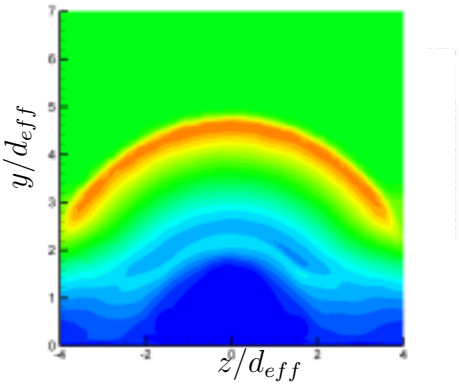

(a) Instantaneous pitot pressure.

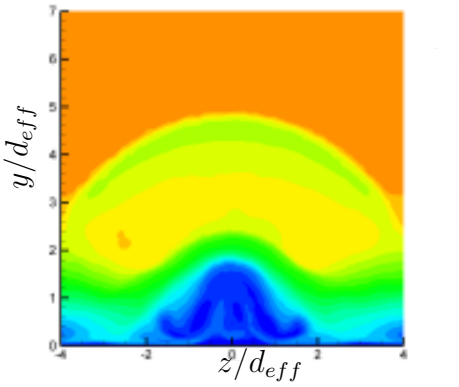

(b) Instantaneous Mach number.

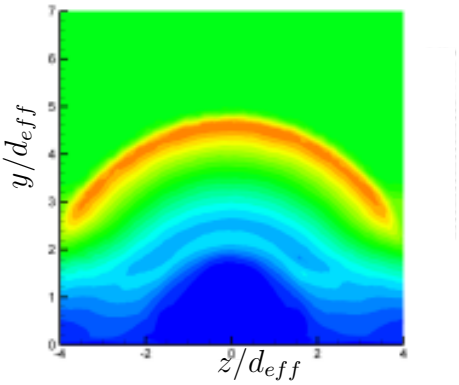

(c) Time-averaged pitot pressure.

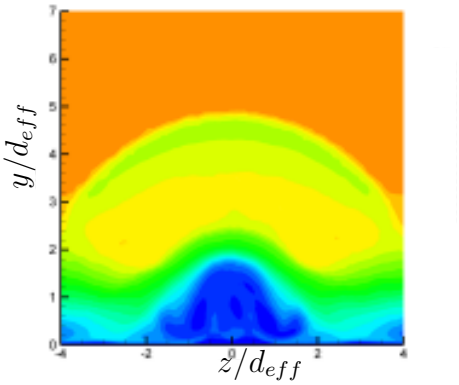

(d) Time-averaged Mach number.

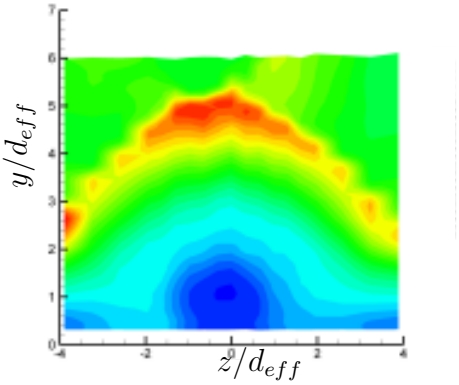

(e) Experimental pitot pressure.

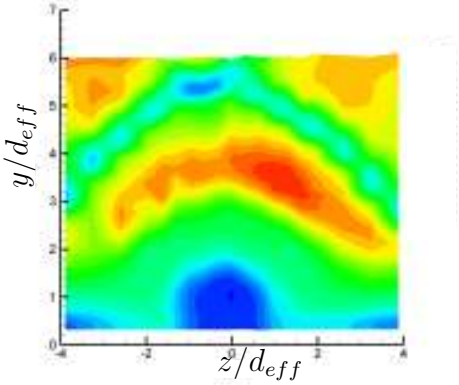

(f) Experimental Mach number.

Fig. 48 Pitot pressure and Mach number comparison of instantaneous and time-averaged DES solutions at $x/d_{eff} = +8.0$ to experiments — 90-degree J_1

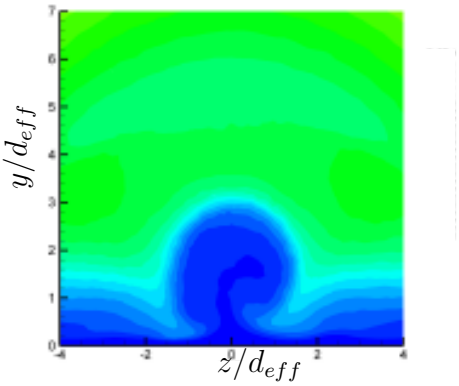

(a) Instantaneous pitot pressure.

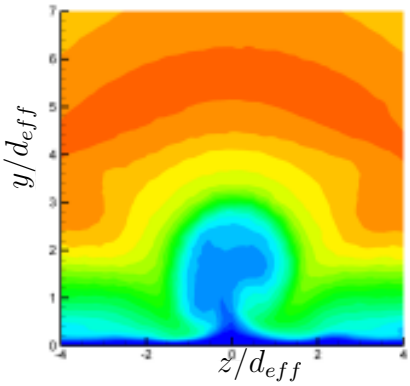

(b) Instantaneous Mach number.

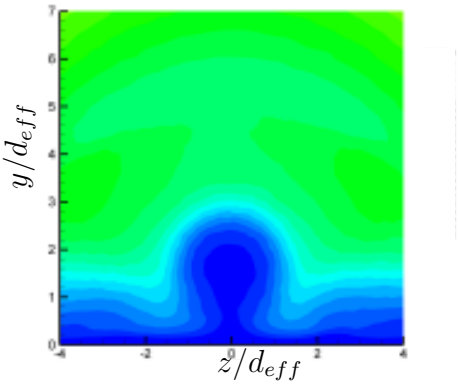

(c) Time-averaged pitot pressure.

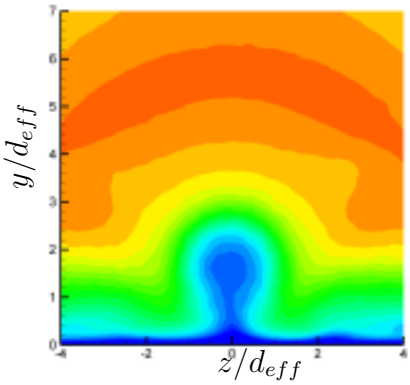

(d) Time-averaged Mach number.

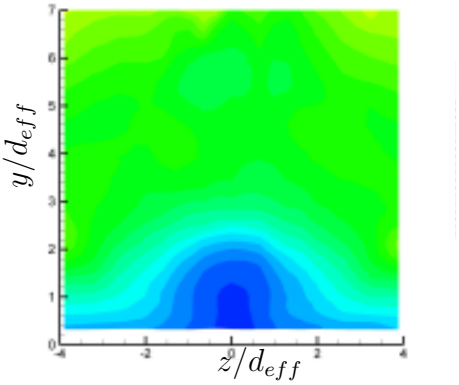

(e) Experimental pitot pressure.

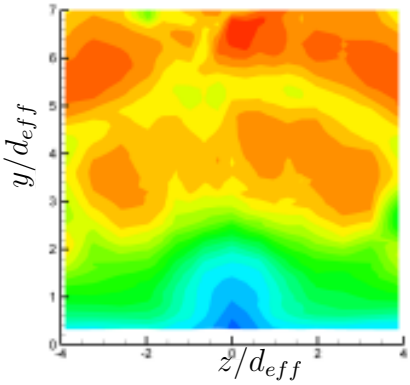

(f) Experimental Mach number.

Fig. 49 Pitot pressure and Mach number comparison of instantaneous and time-averaged DES solutions at $x/d_{eff} = +23.0$ to experiments — 90-degree J_1

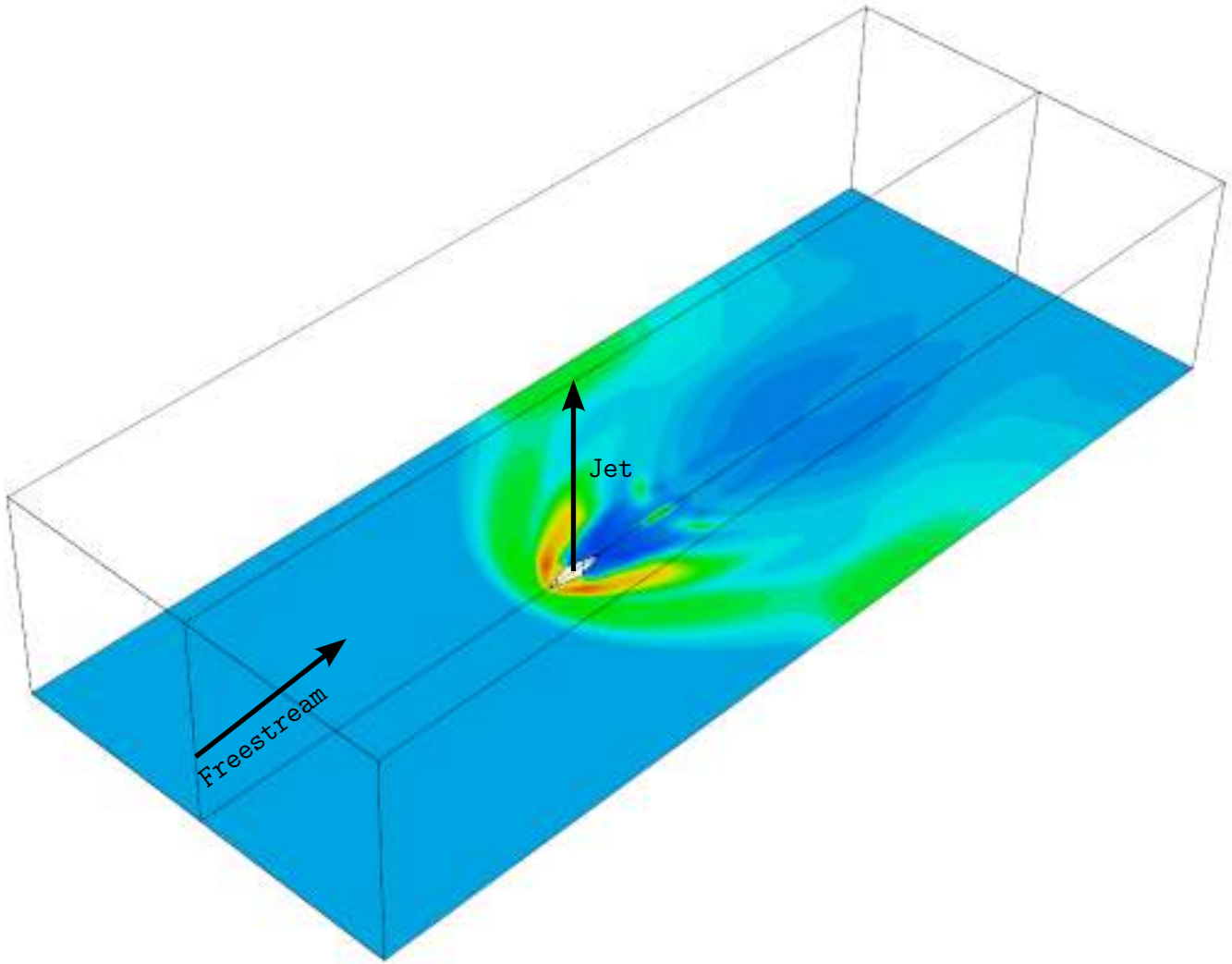

Fig. 50 Isometric view of the flow field — 90-degree J_1.

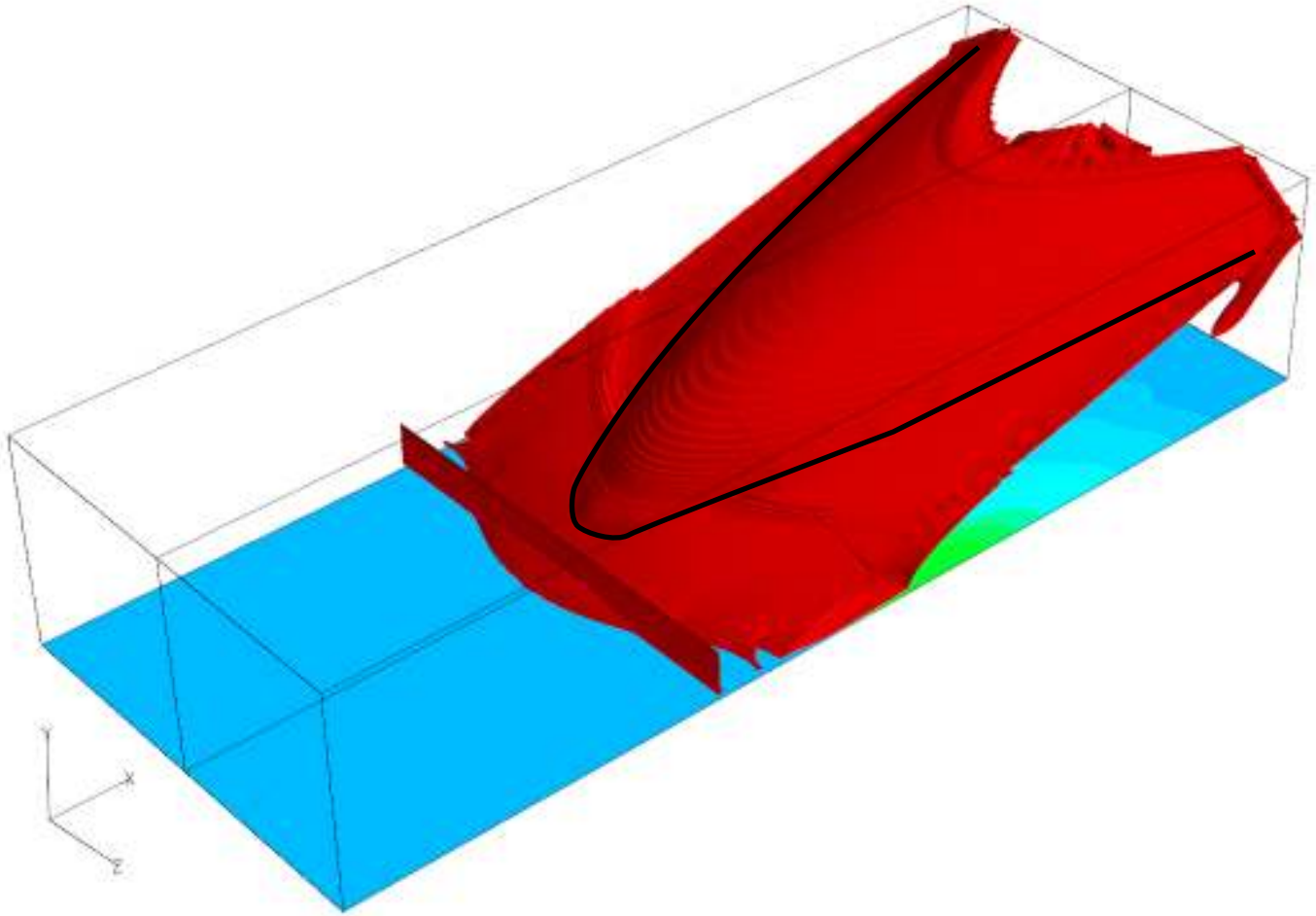

Fig. 51 Interaction shock surface.

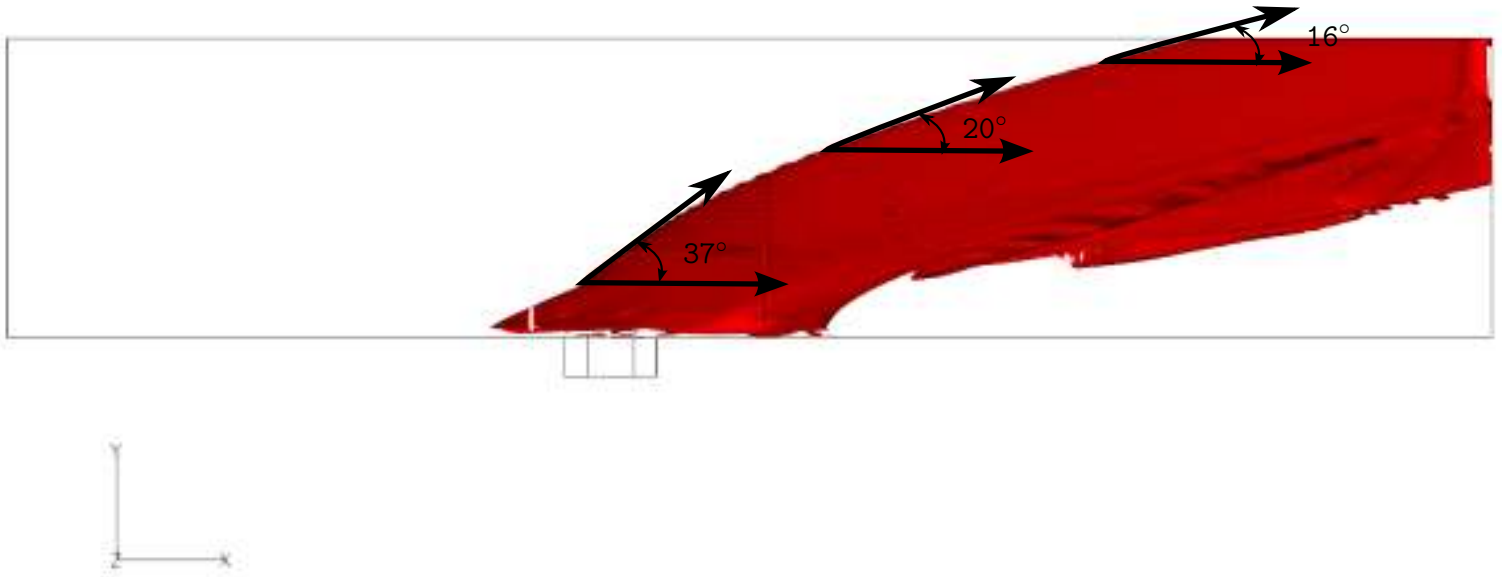

Fig. 52 Interaction shock surface angle.

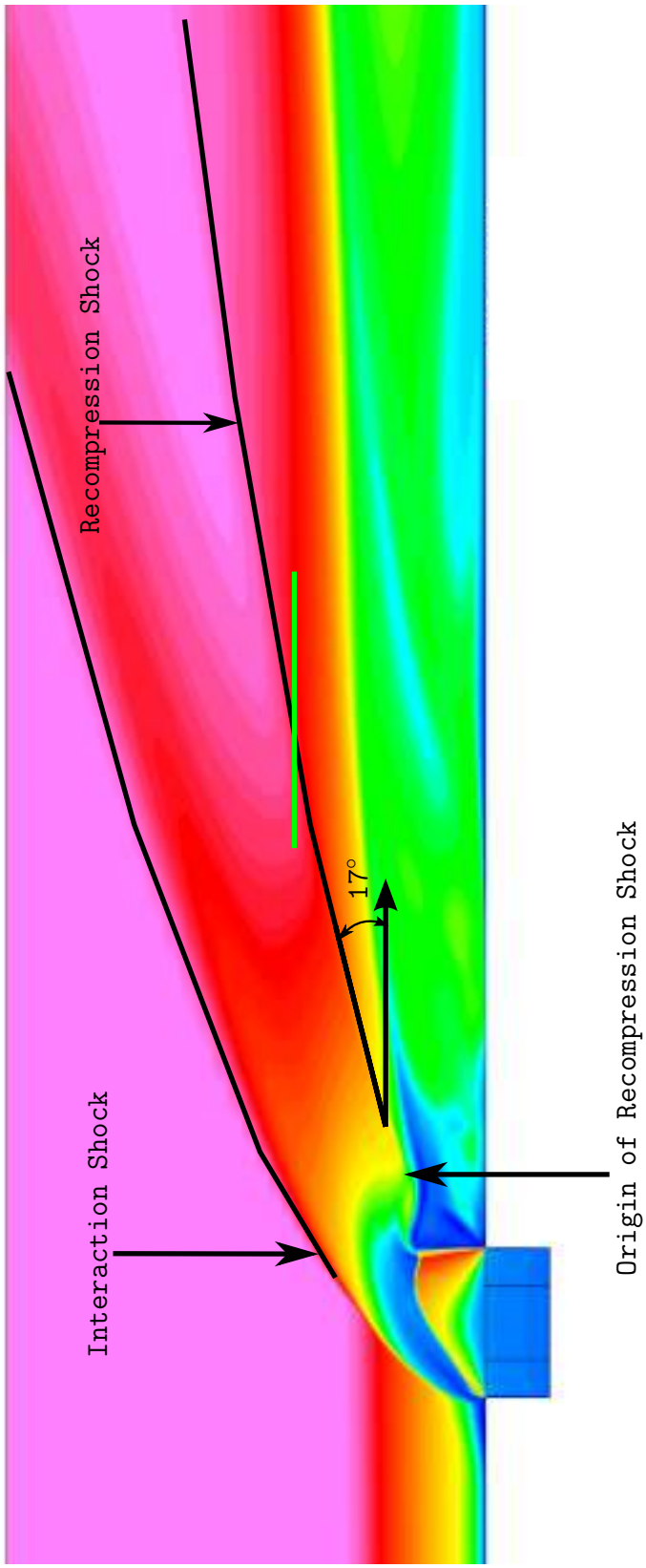

Fig. 53 Mach number contours along tunnel center plane.

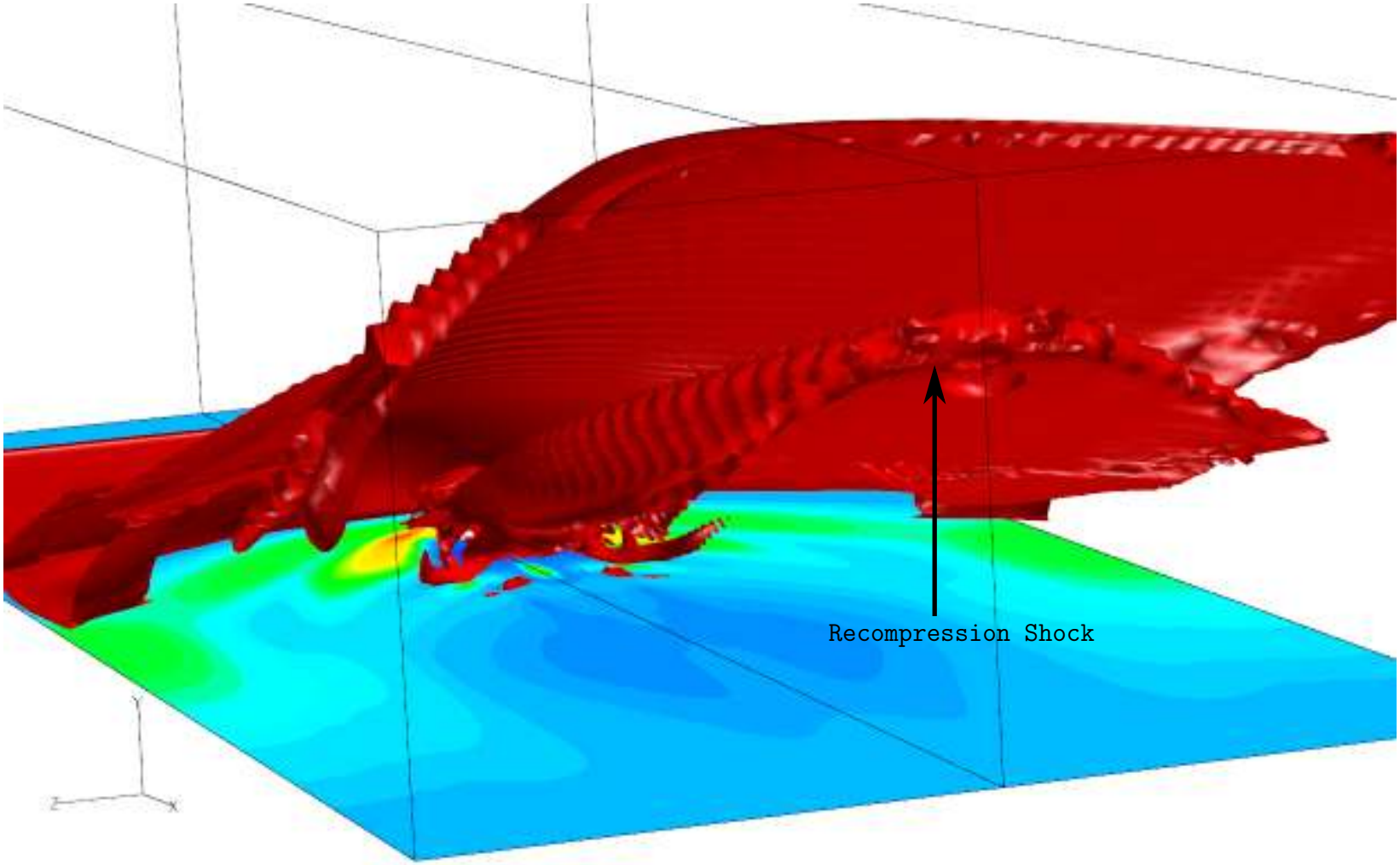

Fig. 54 Recompression shock surface.

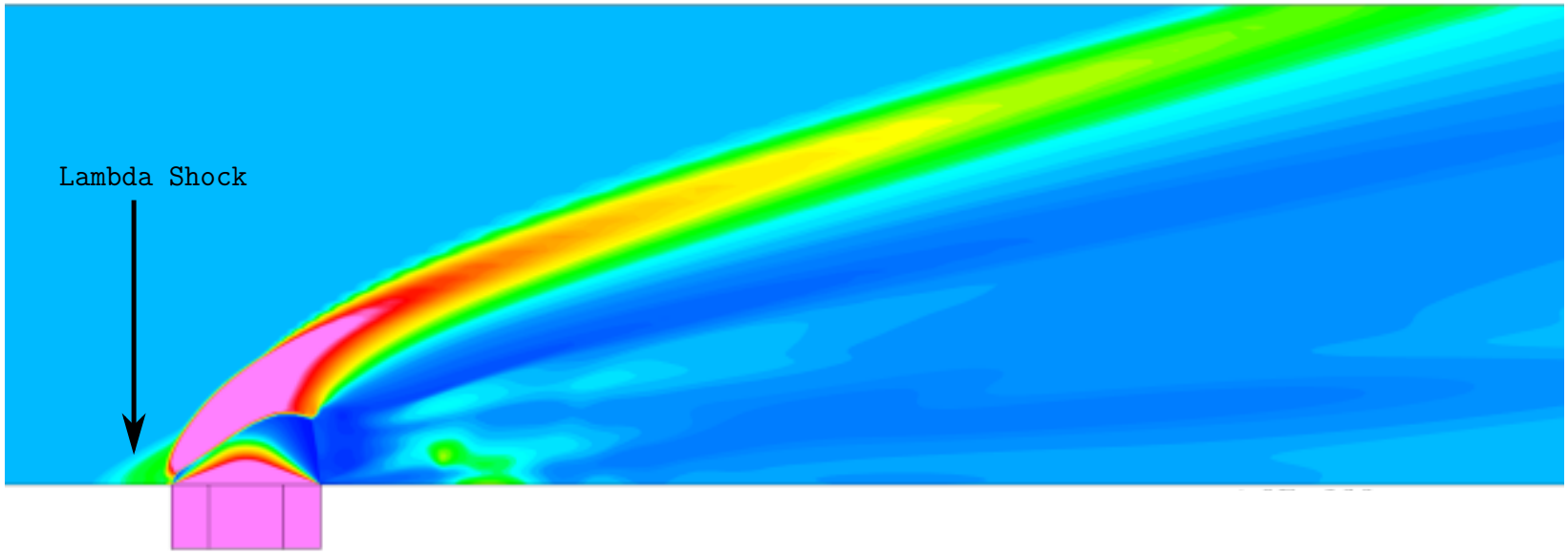

Fig. 55 Pressure contours$(/p_{inf})$.

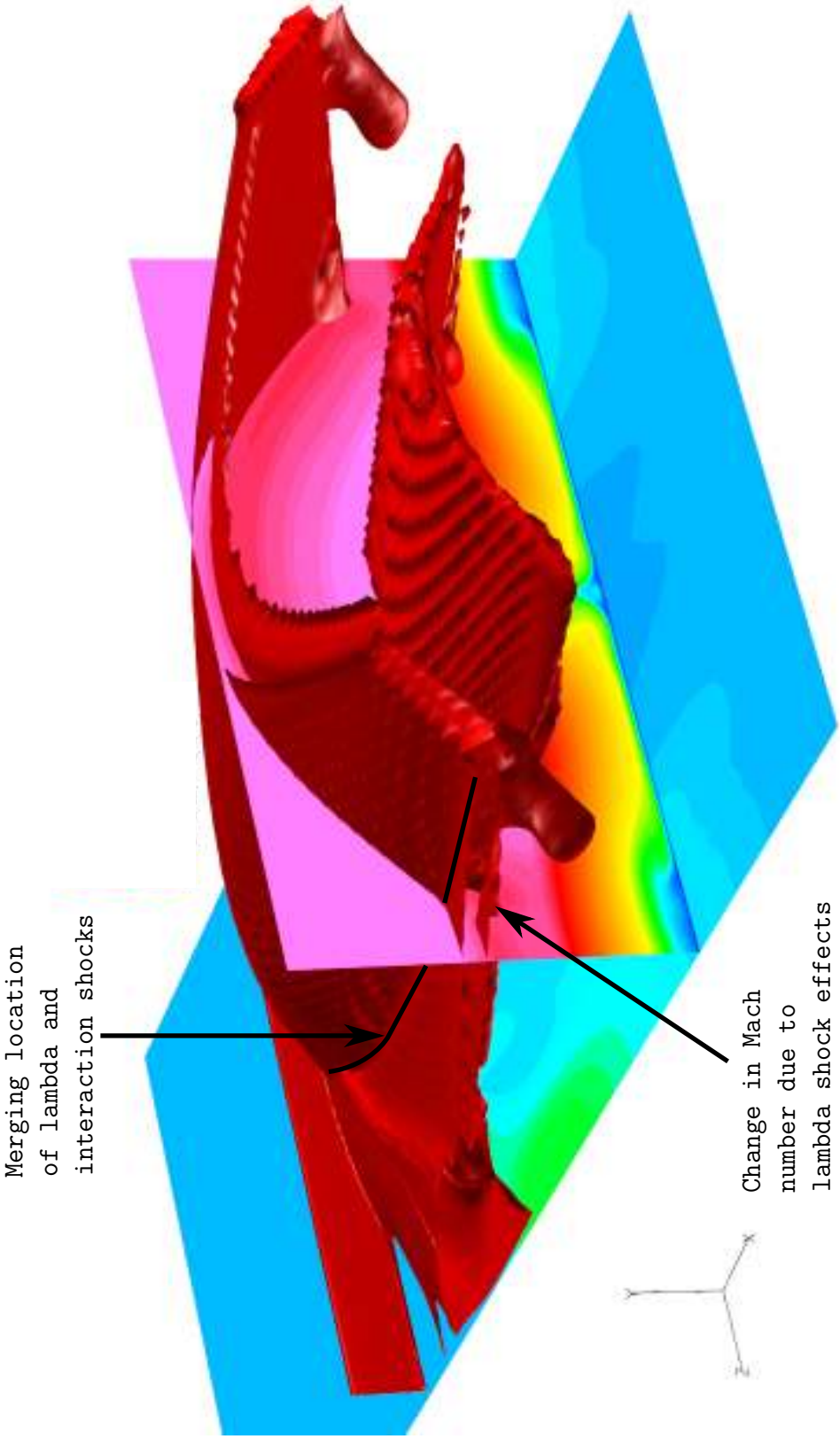

Fig. 56 Lambda/Interaction shock merging.

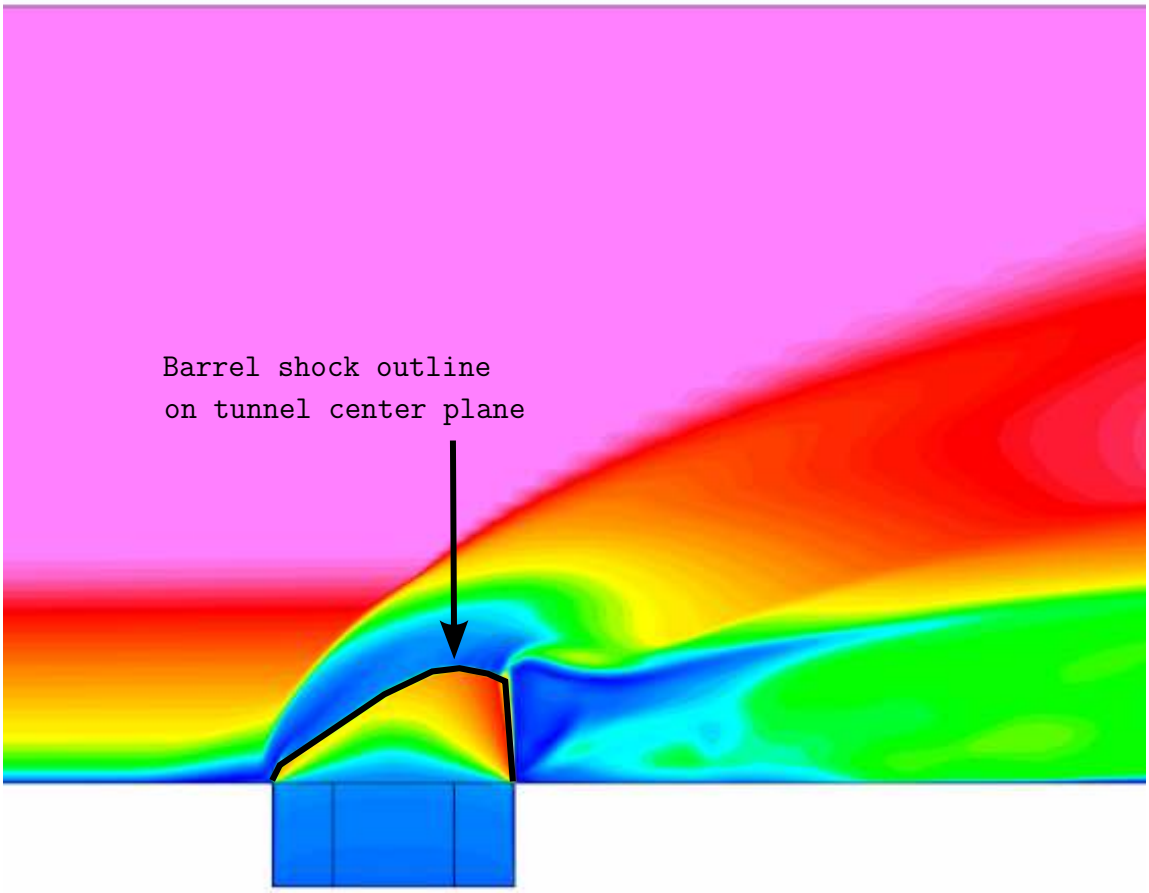

Fig. 57 Barrel shock Mach numbers.

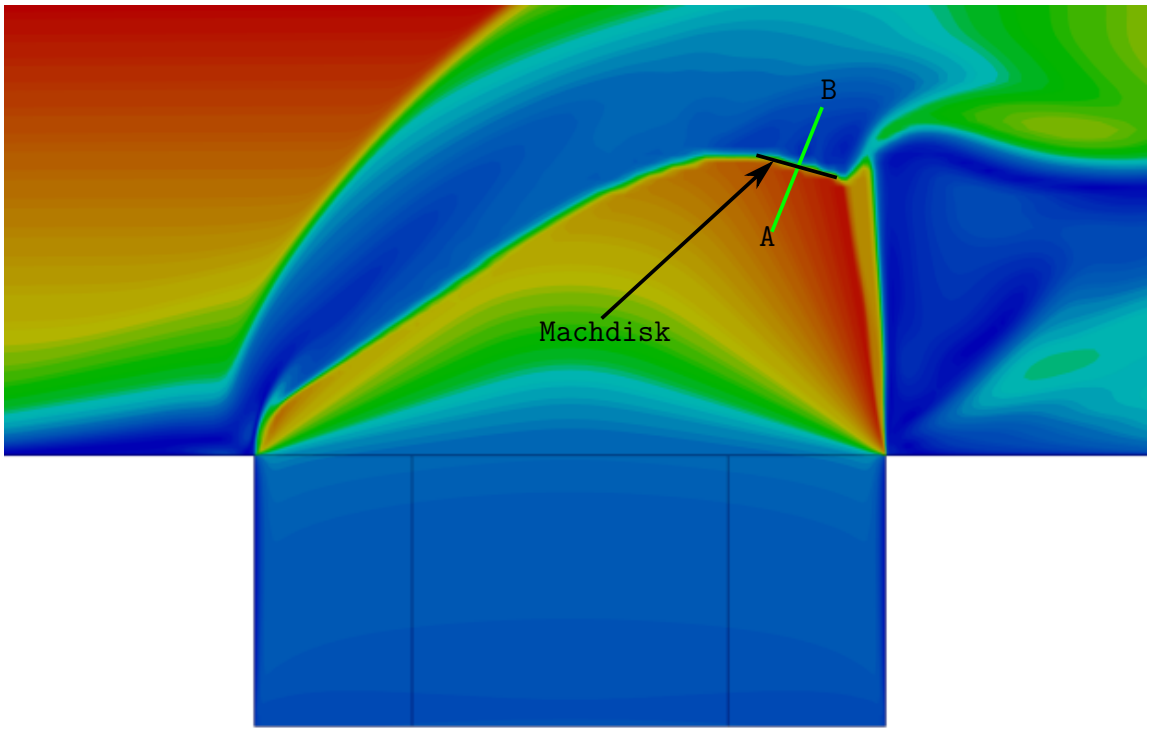

Fig. 58 Mach disk.

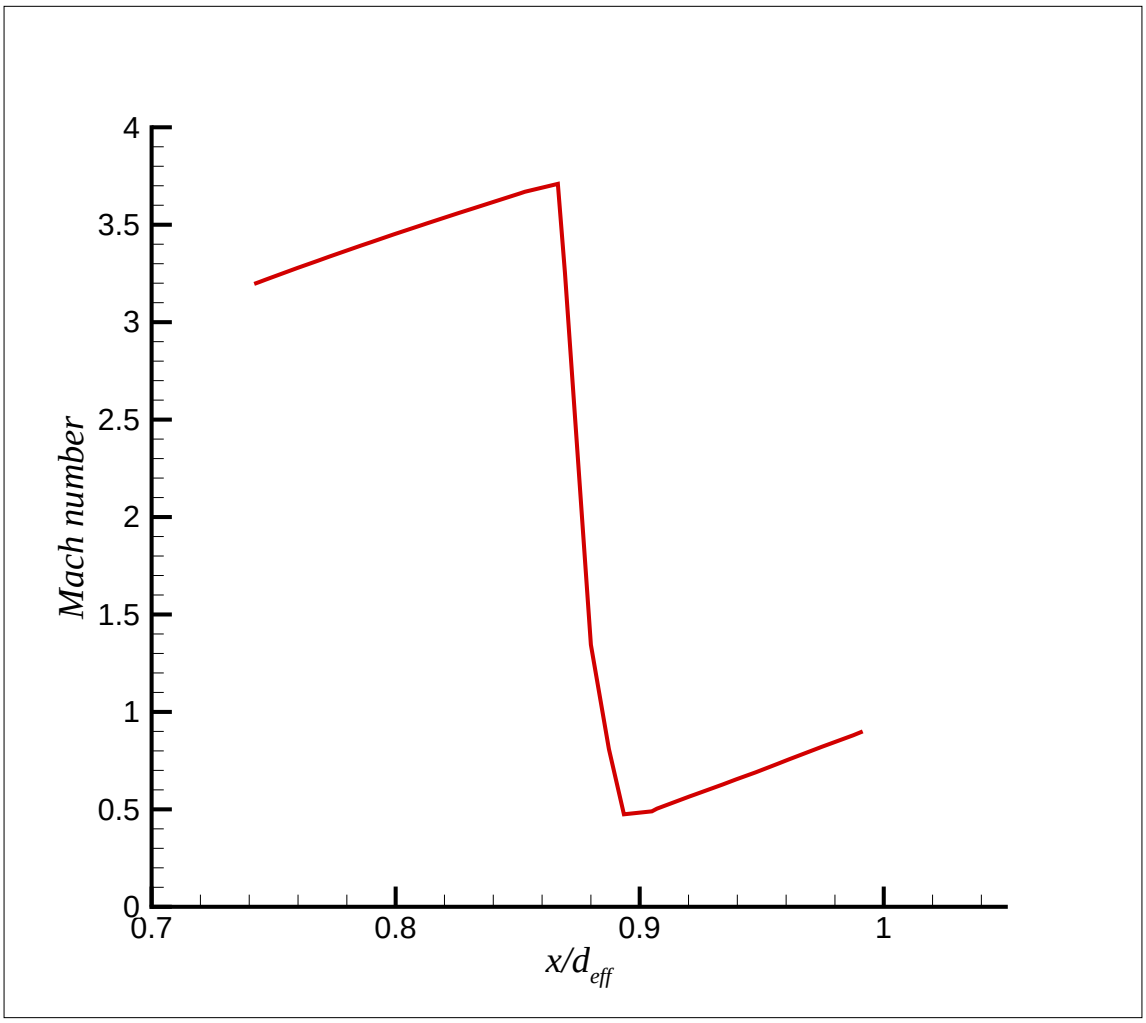

Fig. 59 Mach number across Mach disk.

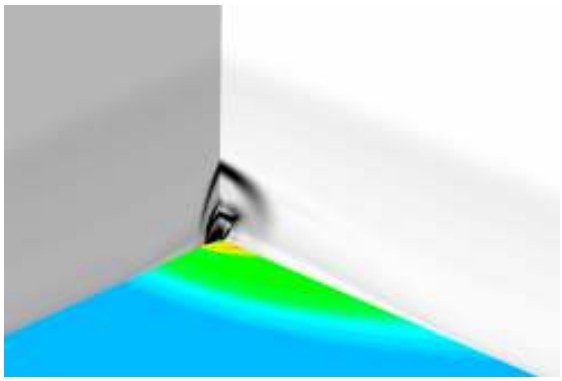

(a) $x/d_{eff} = -1.0$

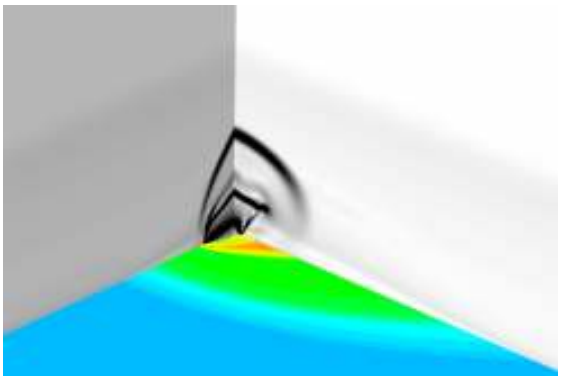

(b) $x/d_{eff} = -0.5$

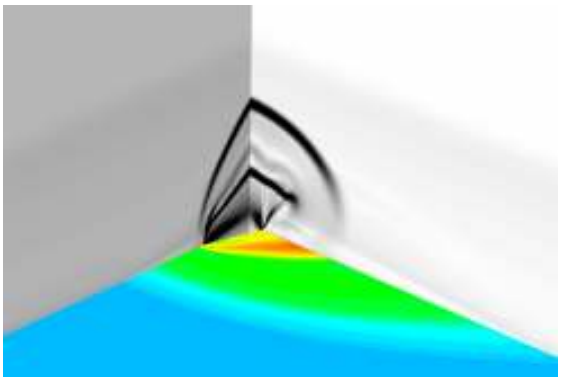

(c) $x/d_{eff} = 0.0$

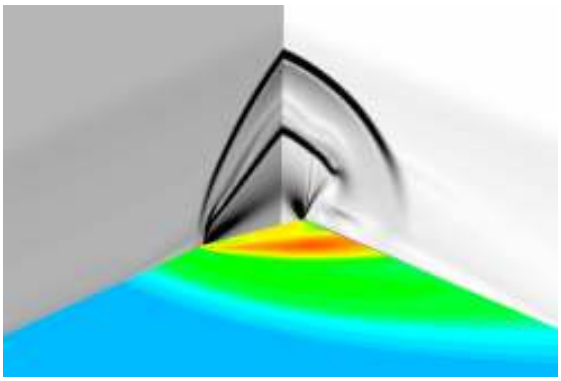

(d) $x/d_{eff} = +0.5$

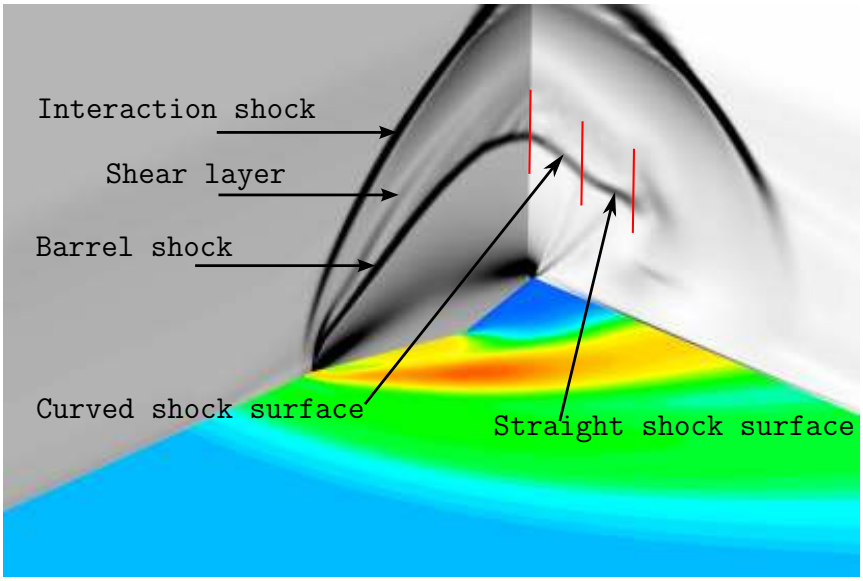

(e) $x/d_{eff} = +1.0$

Fig. 60 Numerical schlieren of barrel shock.

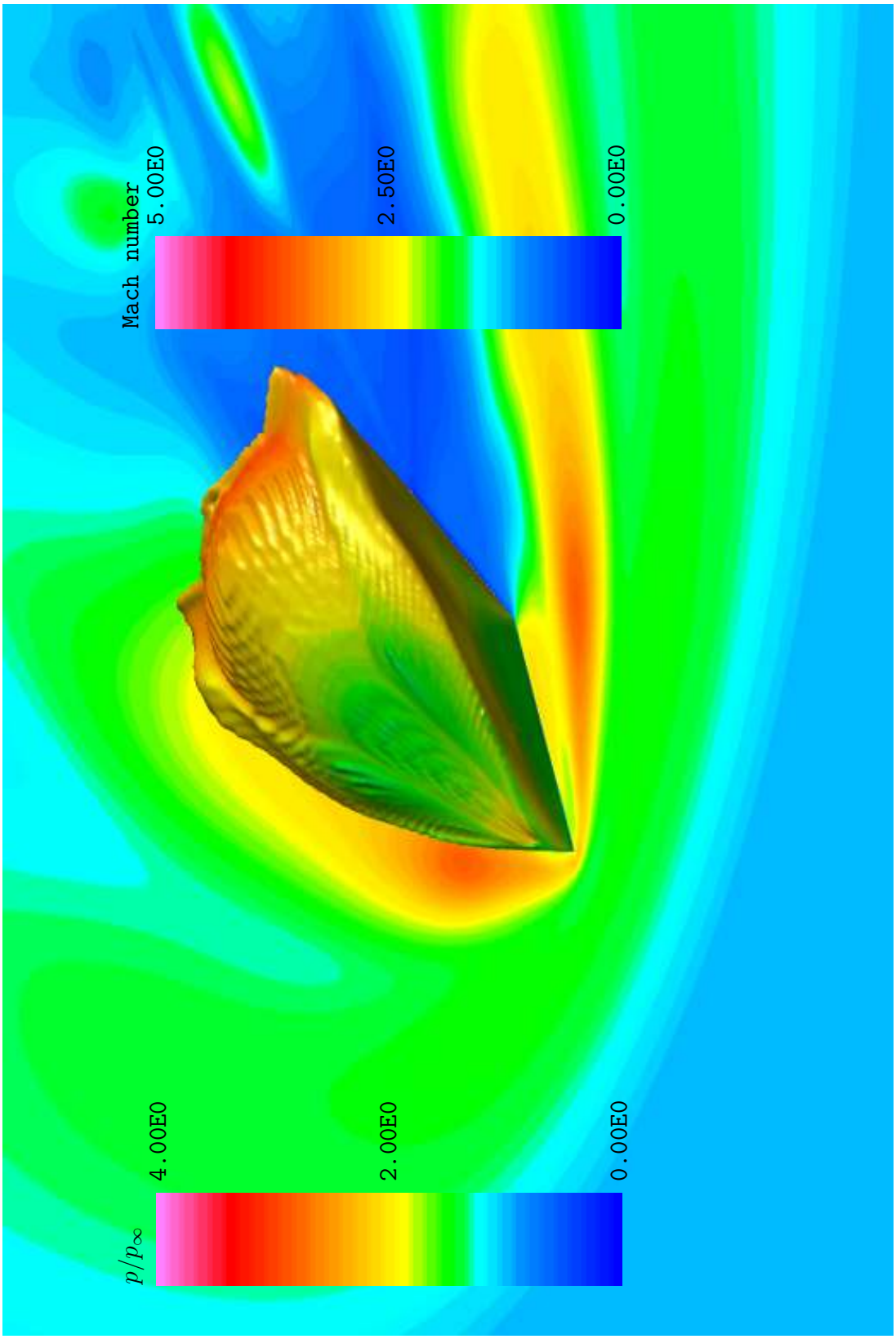

Fig. 61 Isosurface showing barrel shock.

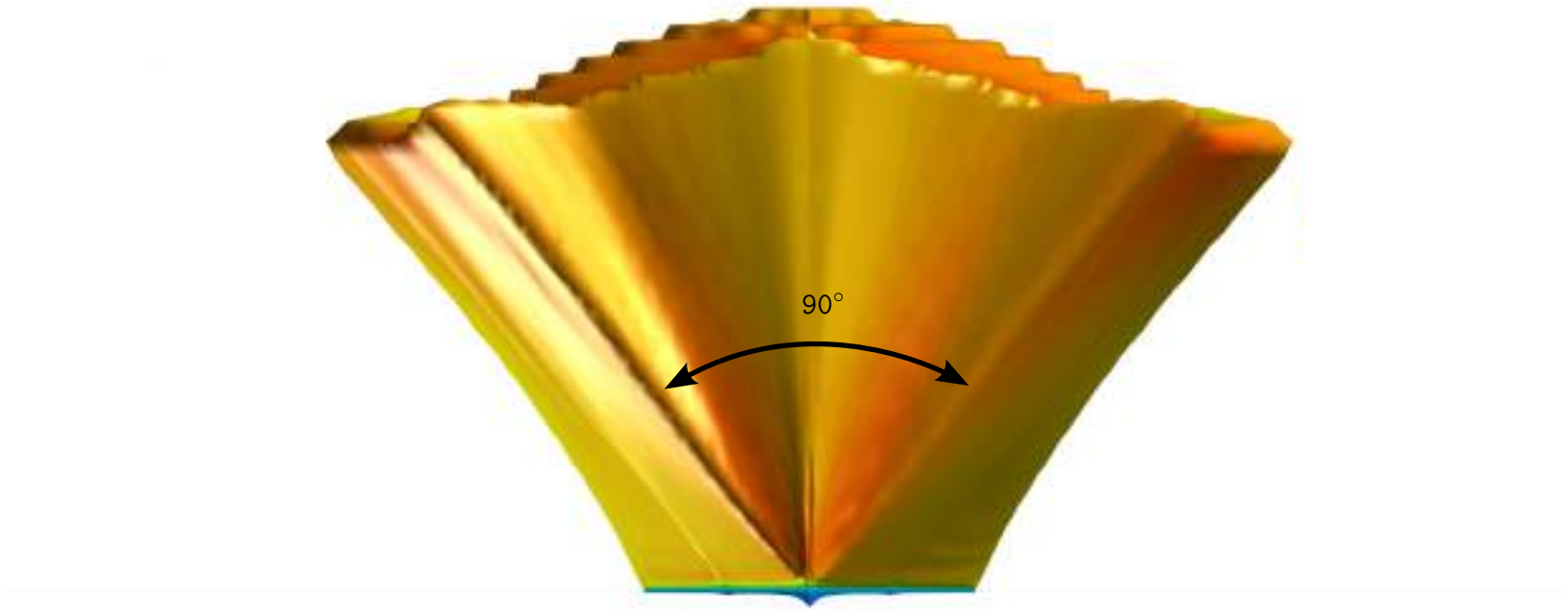

Fig. 62 Leeward surface of barrel shock.

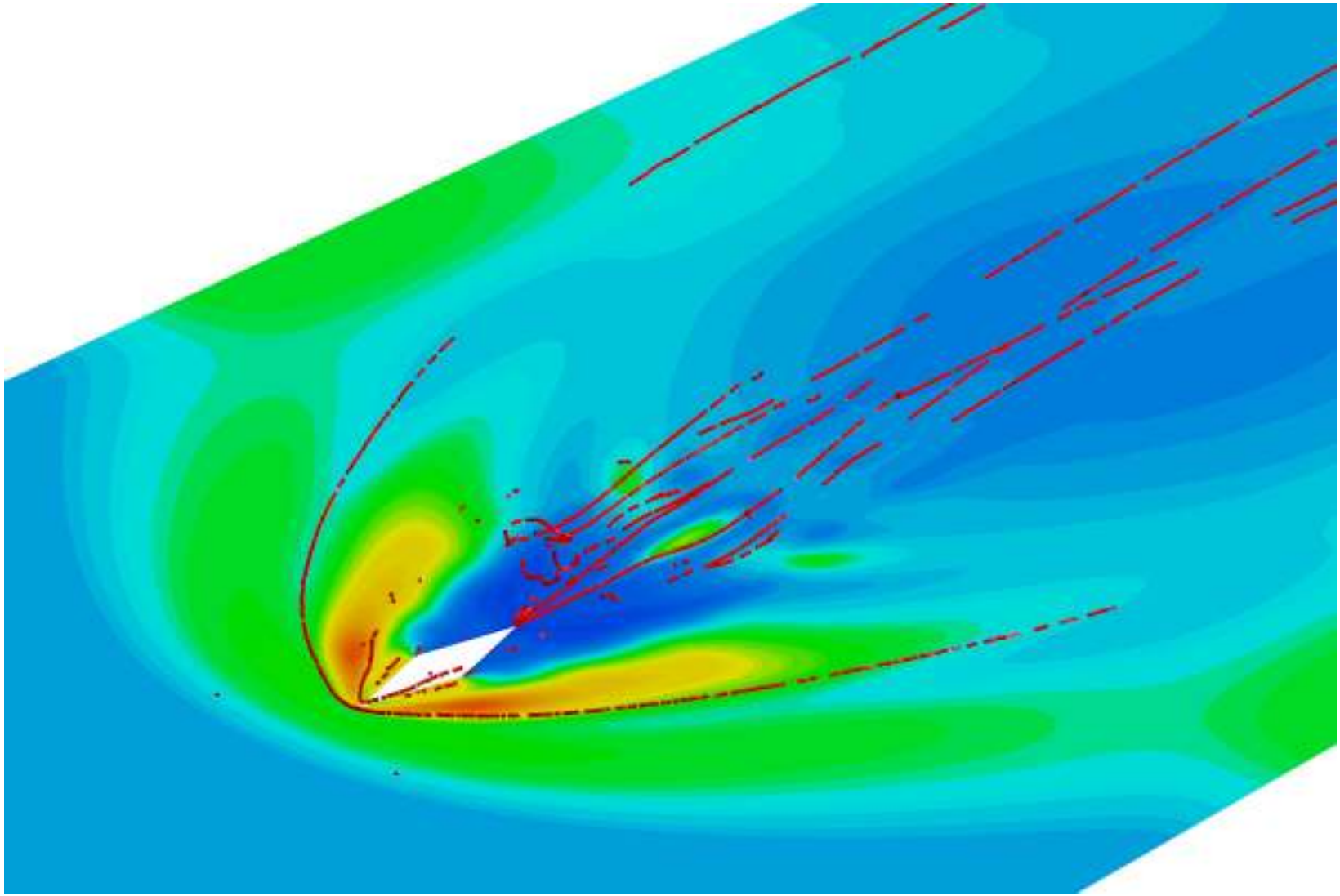

Fig. 63 Vortex cores extracted using Fieldview — 90-degree J_1.

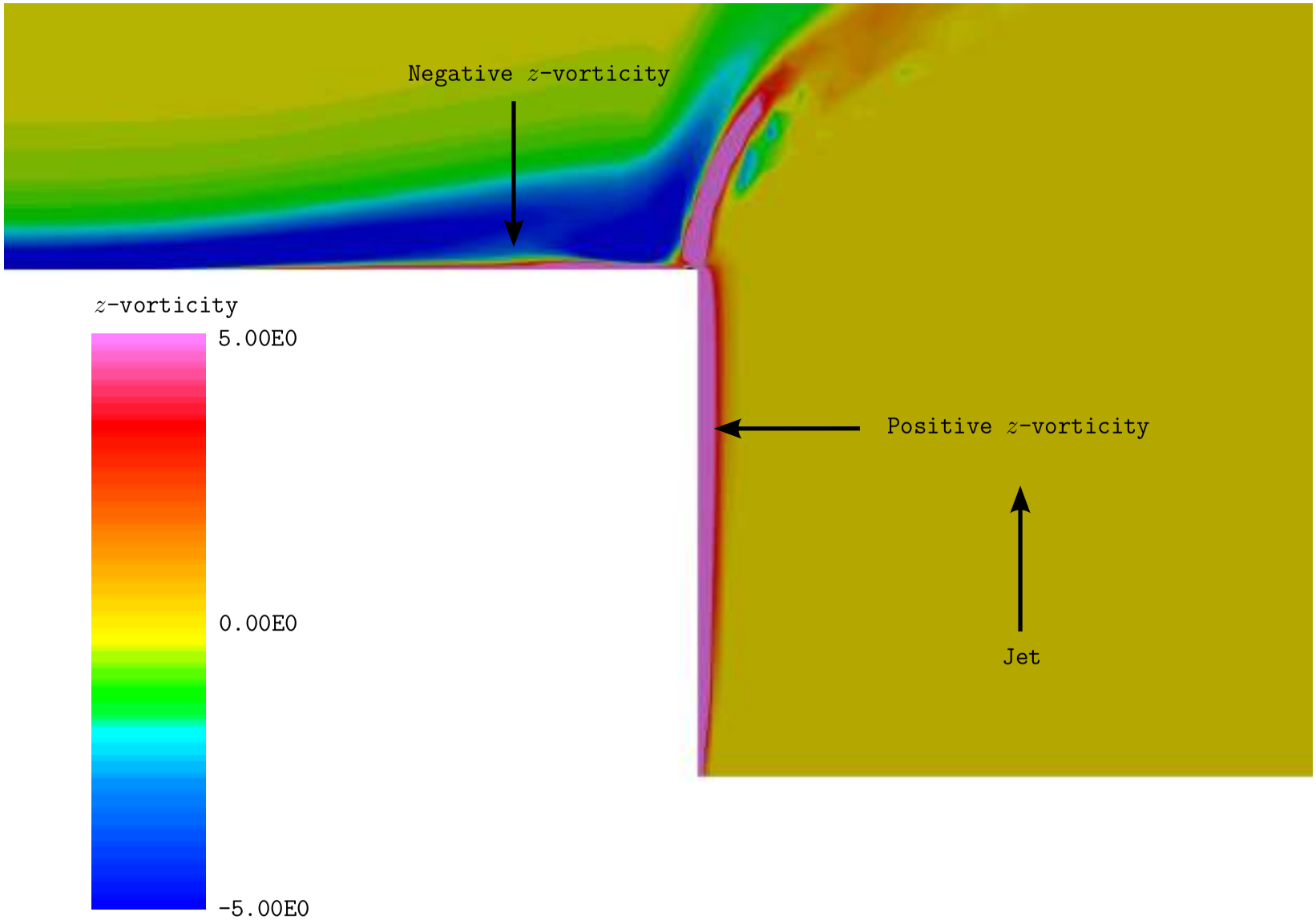

Fig. 64 Freestream boundary layer vorticity — 90-degree J_1.

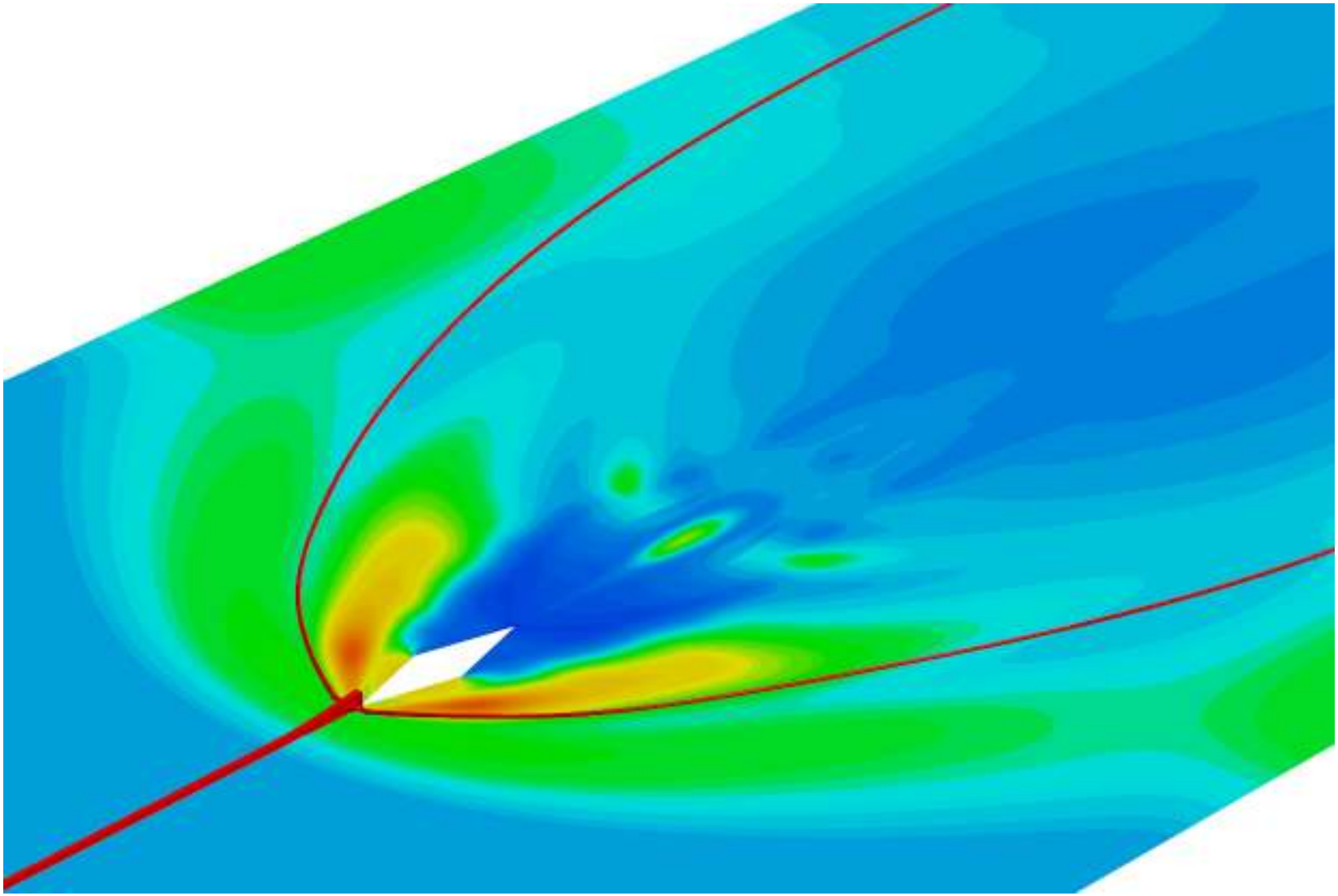

Fig. 65 Horseshoe vortex — 90-degree J_1.

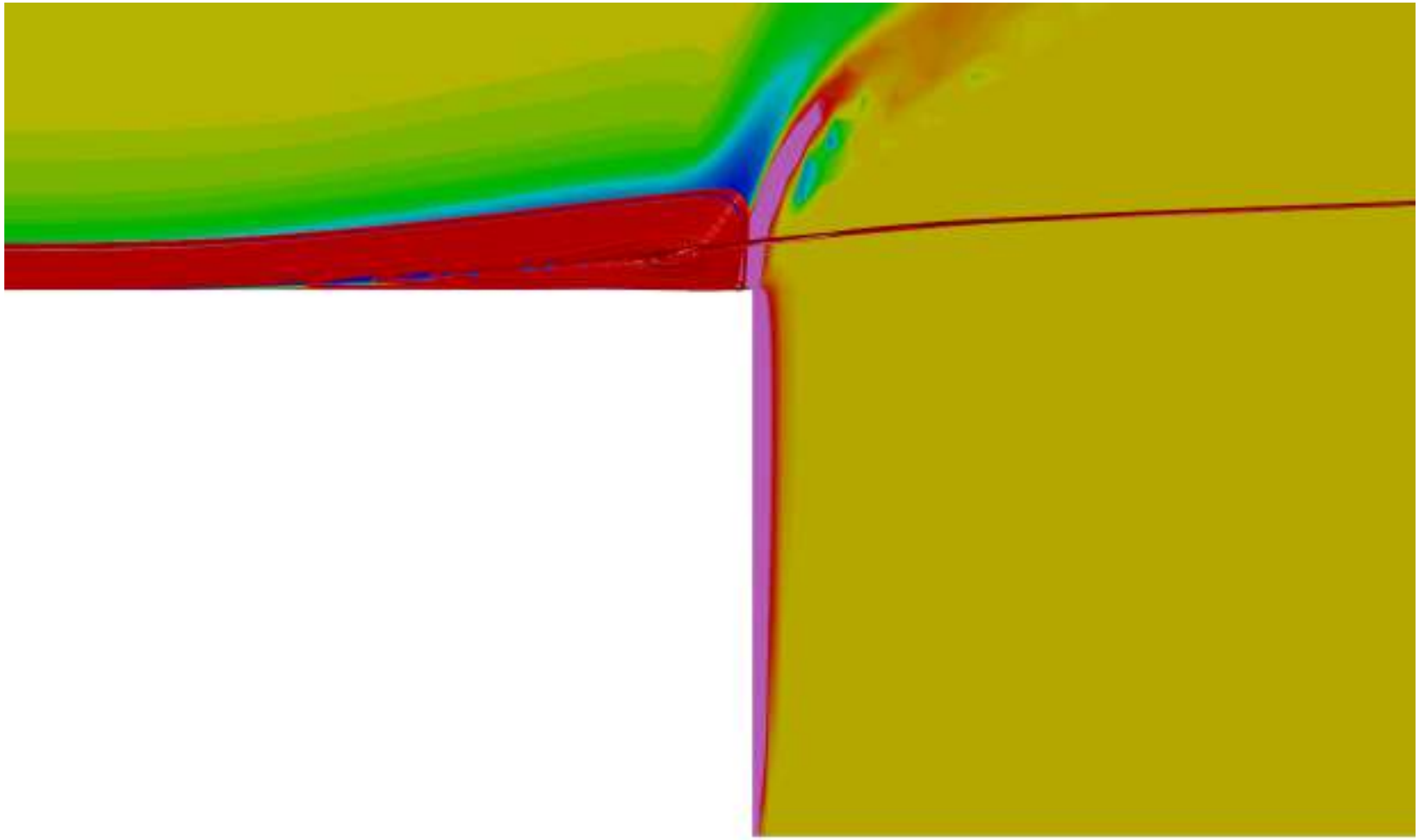

Fig. 66 Horseshoe vortex formation — 90-degree J_1.

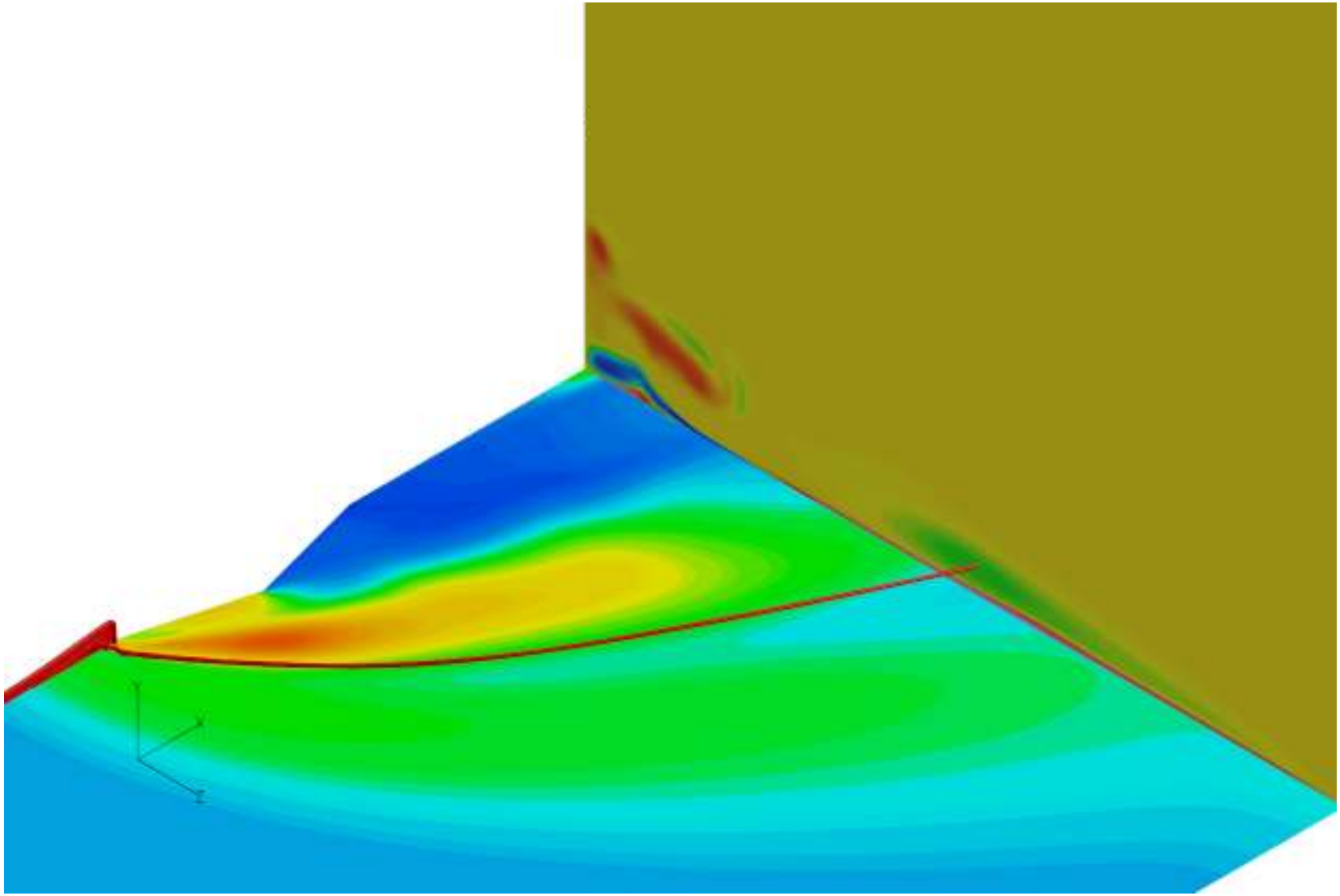

Fig. 67 Horseshoe vortex, change in vorticity — 90-degree J_1.

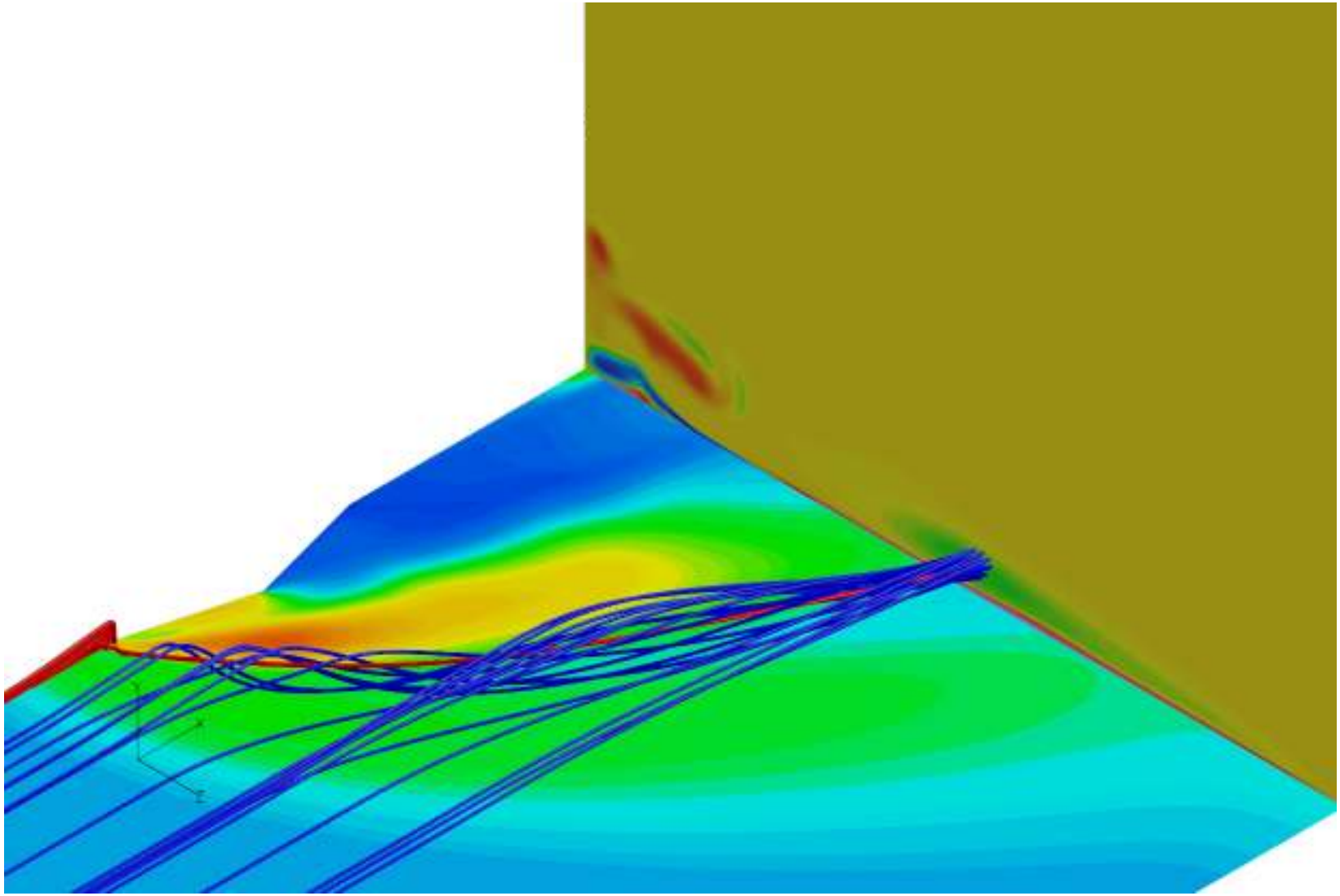

Fig. 68 Horseshoe vortex, change in vorticity — 90-degree J_1.

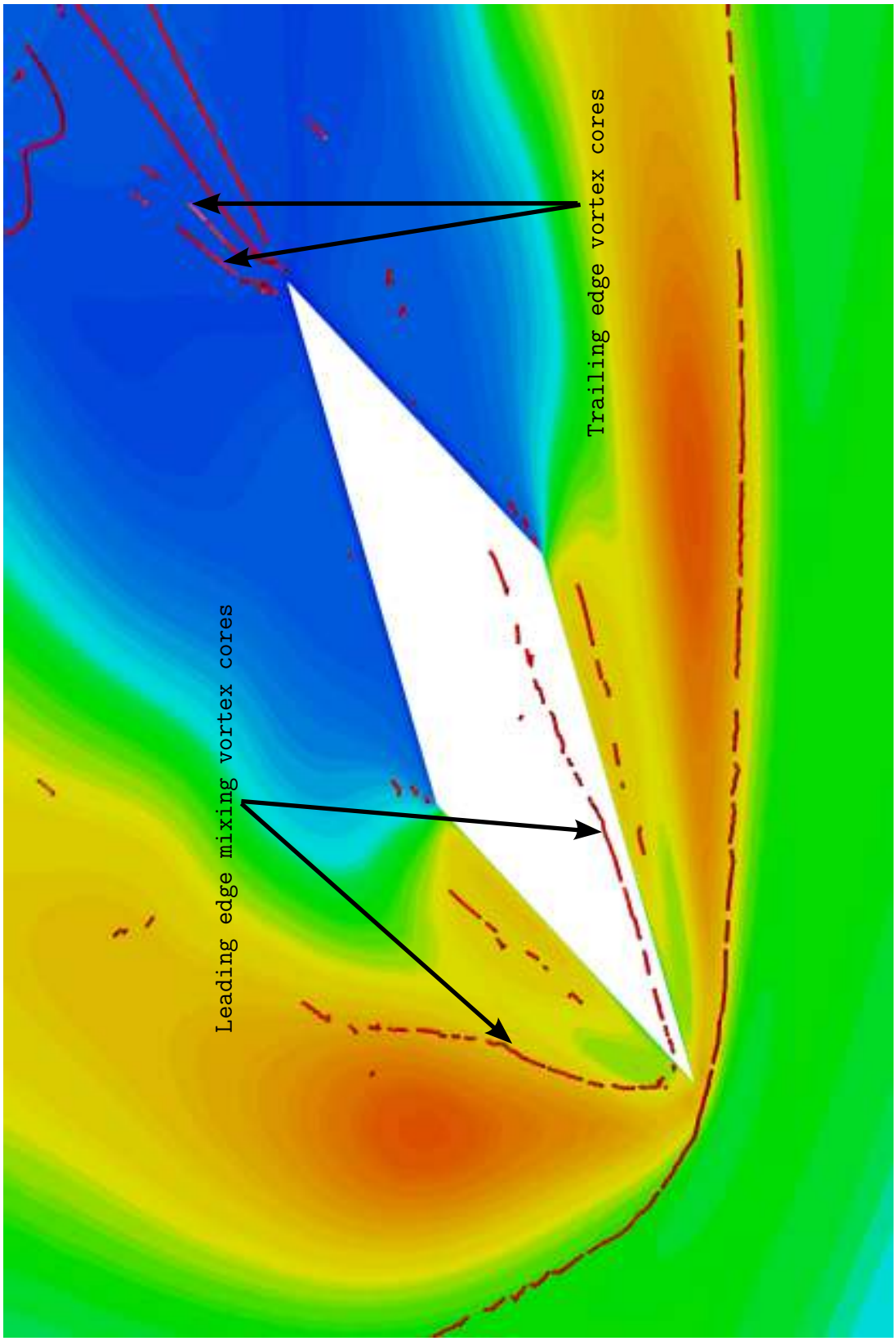

Fig. 69 Leading edge vortex cores — 90-degree J_1.

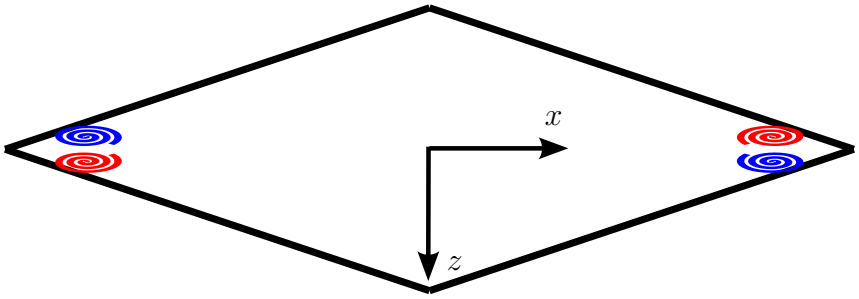

Fig. 70 Jet vortices — 90-degree J_1.

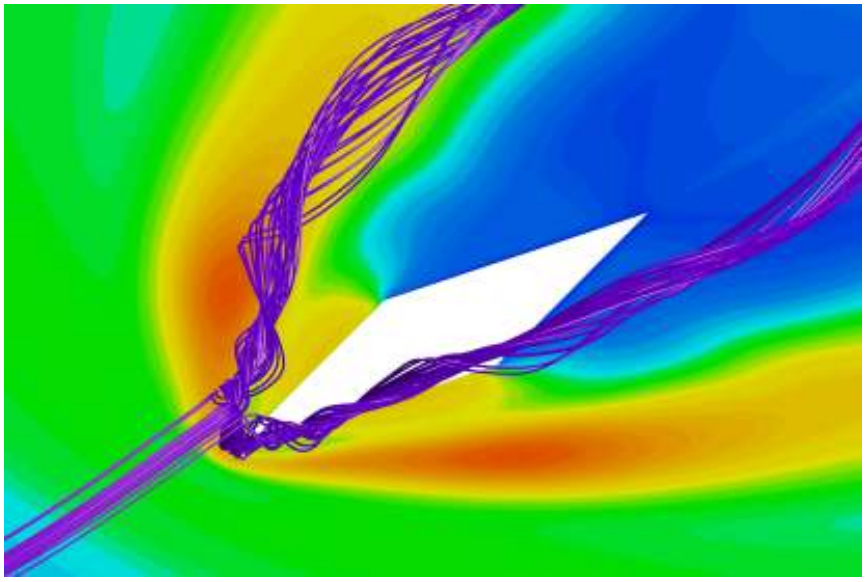

Fig. 71 Leading-edge vortices — 90-degree J_1.

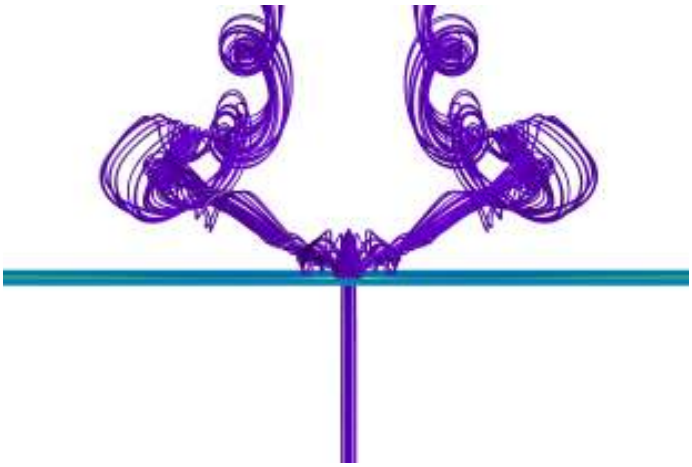

(a) $-^{ve}x$-axis

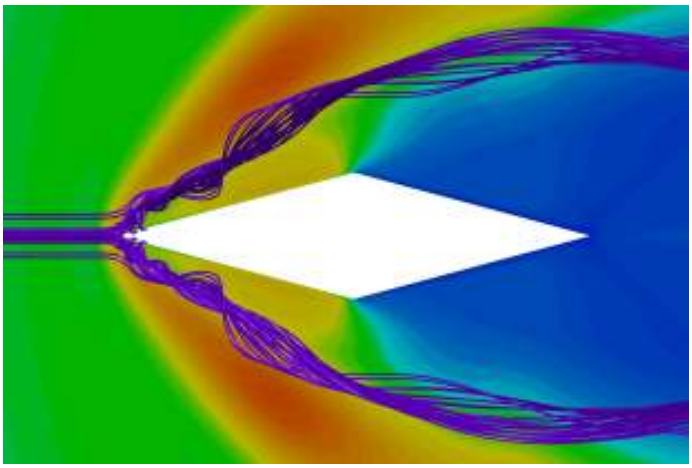

(b) $+^{ve}y$-axis

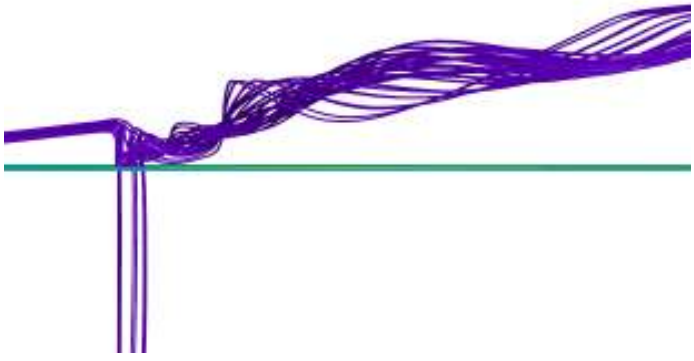

(c) $+^{ve}z$-axis

Fig. 72 Spread structure of leading-edge vortices — 90-degree J_1.

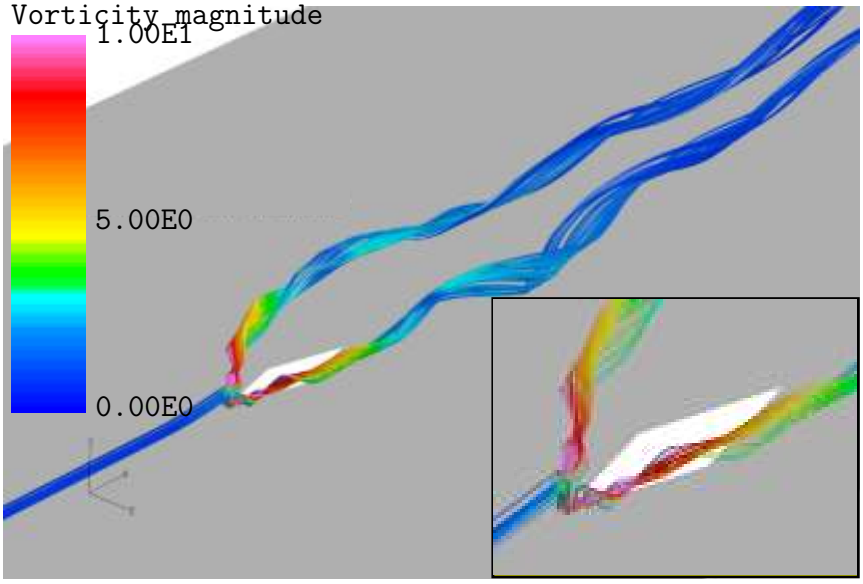

Fig. 73 Vorticity magnitude along leading-edge mixing vortex.

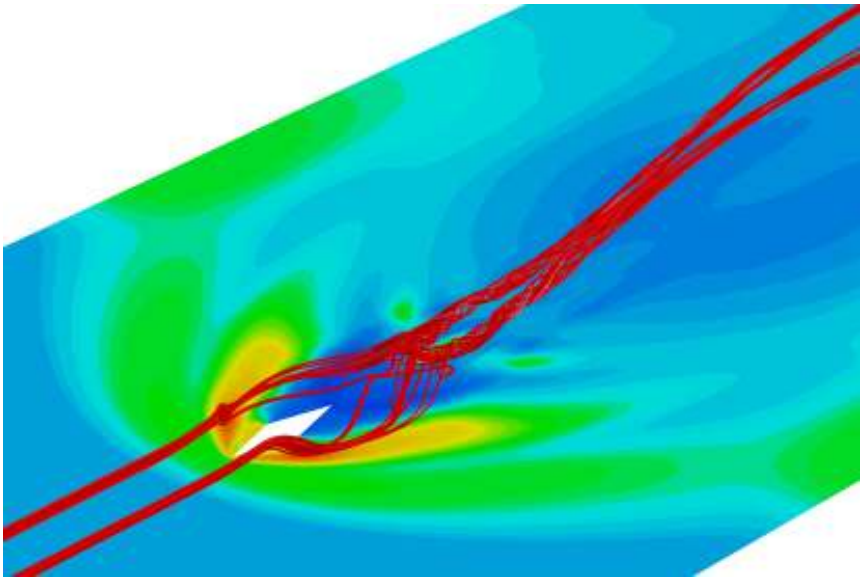

Fig. 74 Structure of wake vortices.

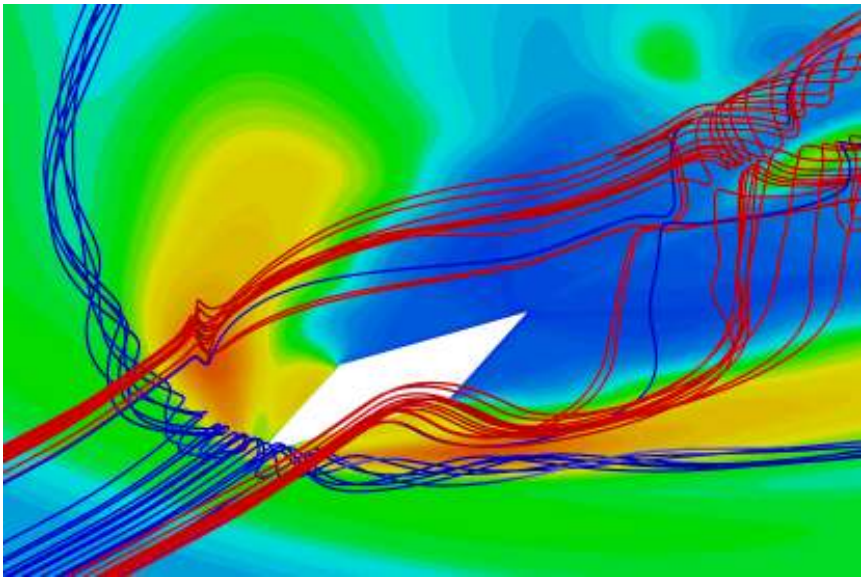

Fig. 75 Formation of wake vortices.

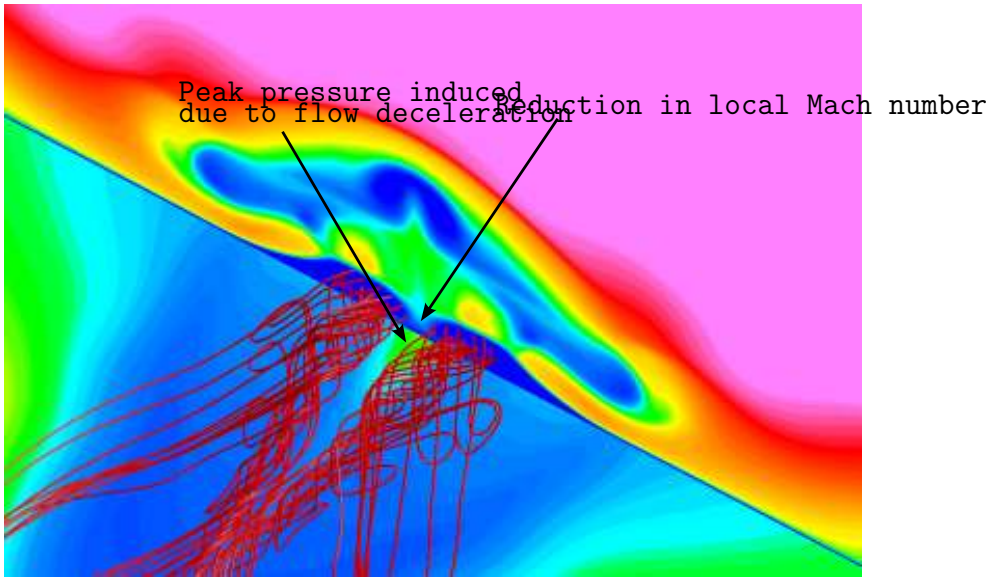

Fig. 76 Pressure peak due to wake vortices.

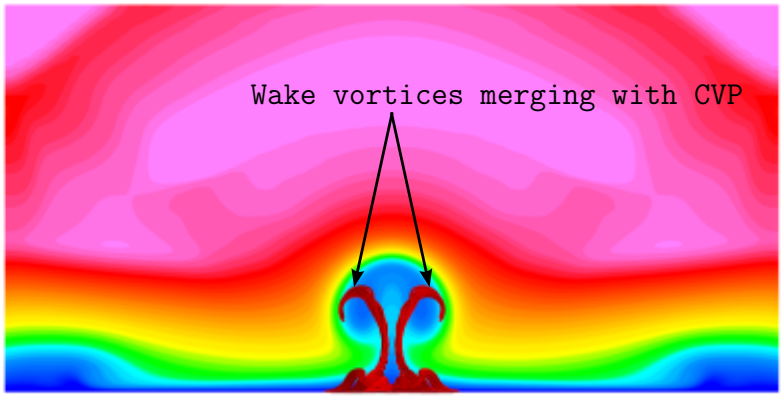

Fig. 77 Lift and merging of wake vortices.

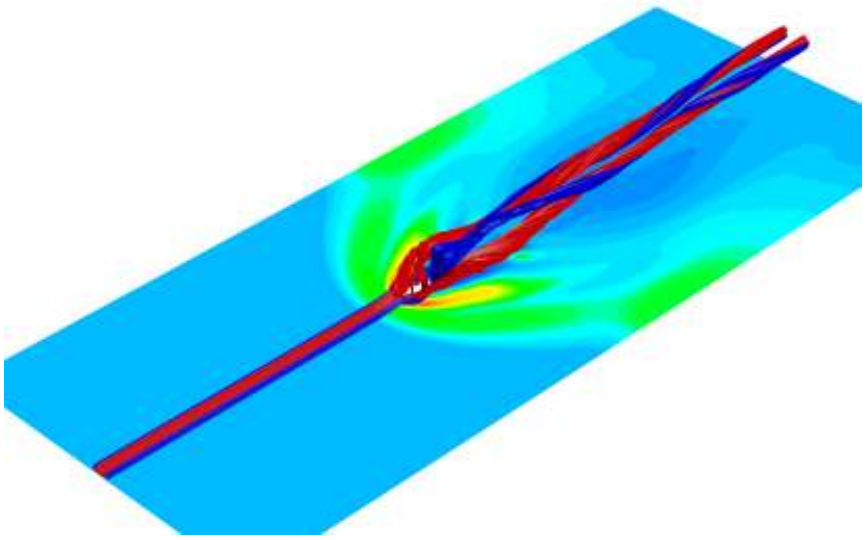

Fig. 78 Counter-rotating vortex pair.

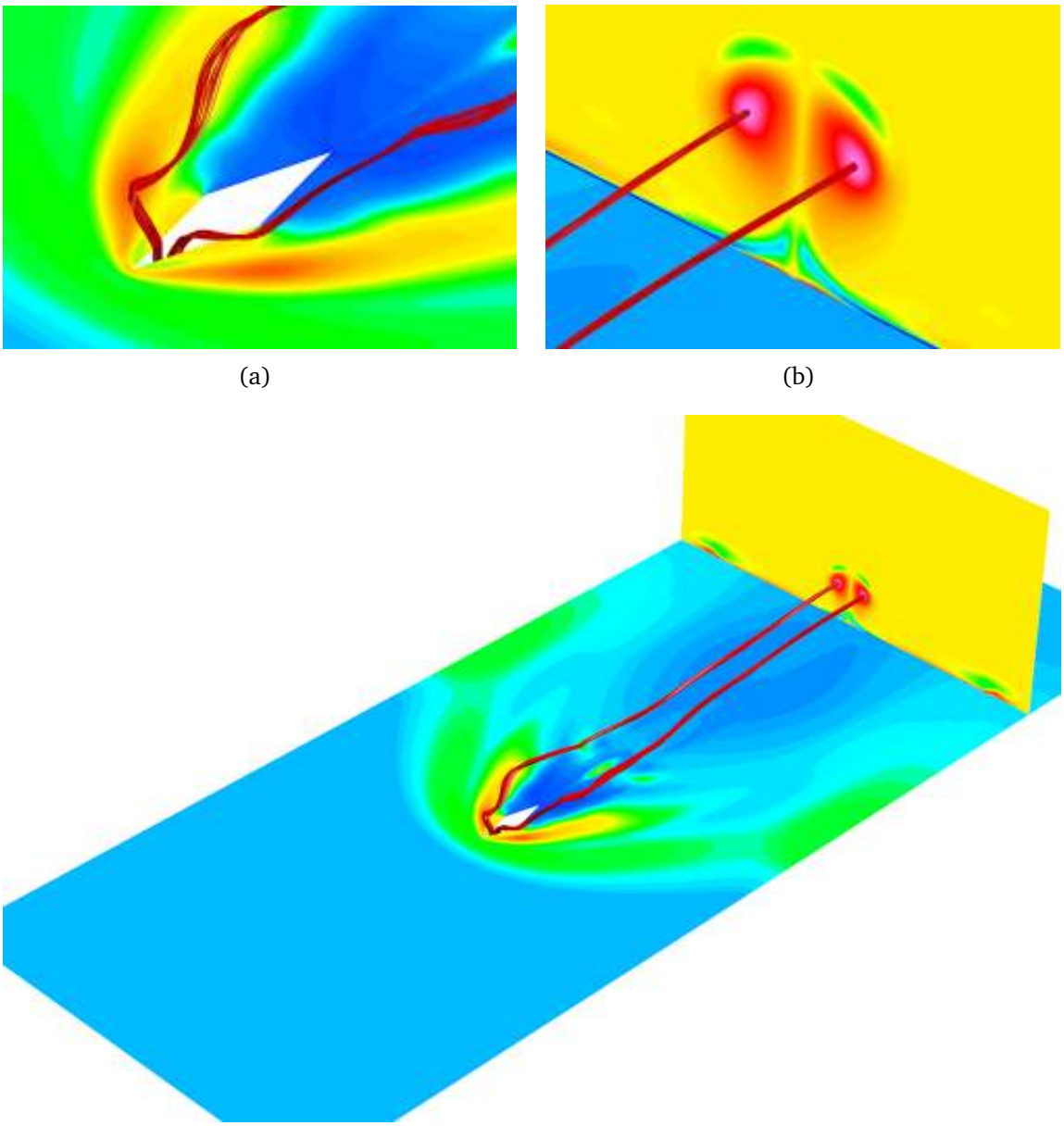

(a) (b)

(c)

Fig. 79 CVP, Layer 1 — Core.

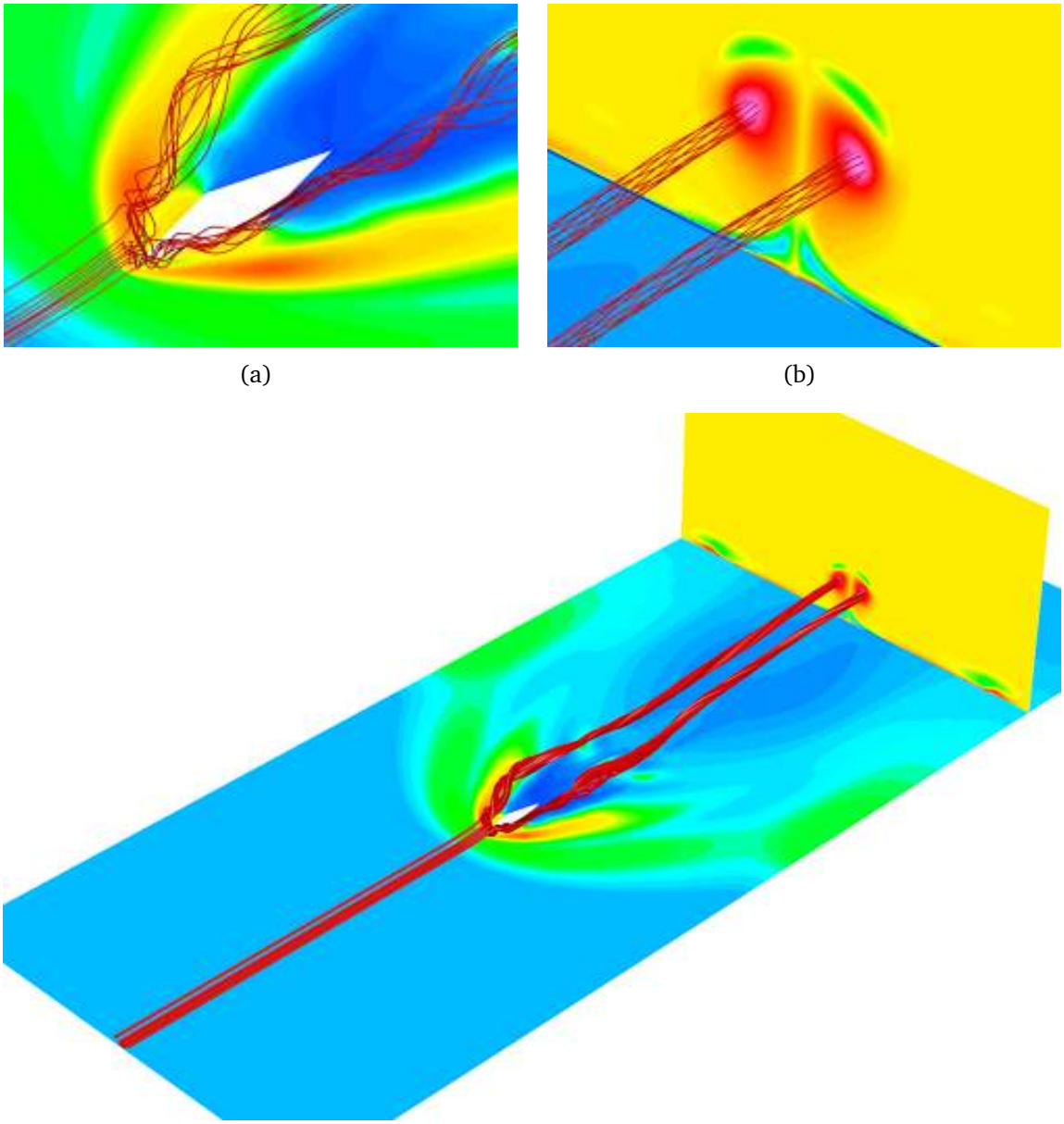

(a) (b)

(c)

Fig. 80 CVP, Layer 2.

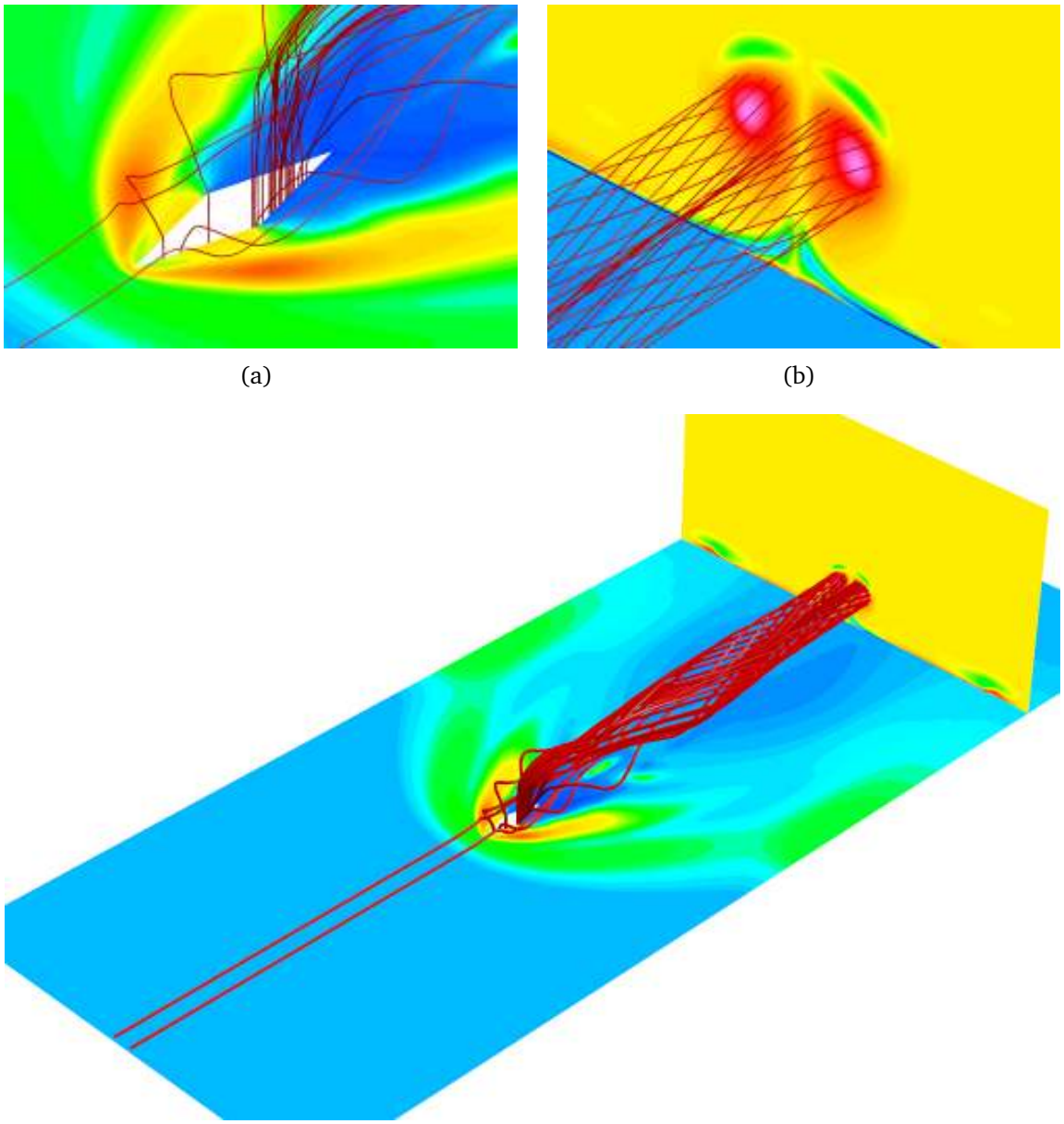

(a) (b)

(c)

Fig. 81 CVP, Layer 3.

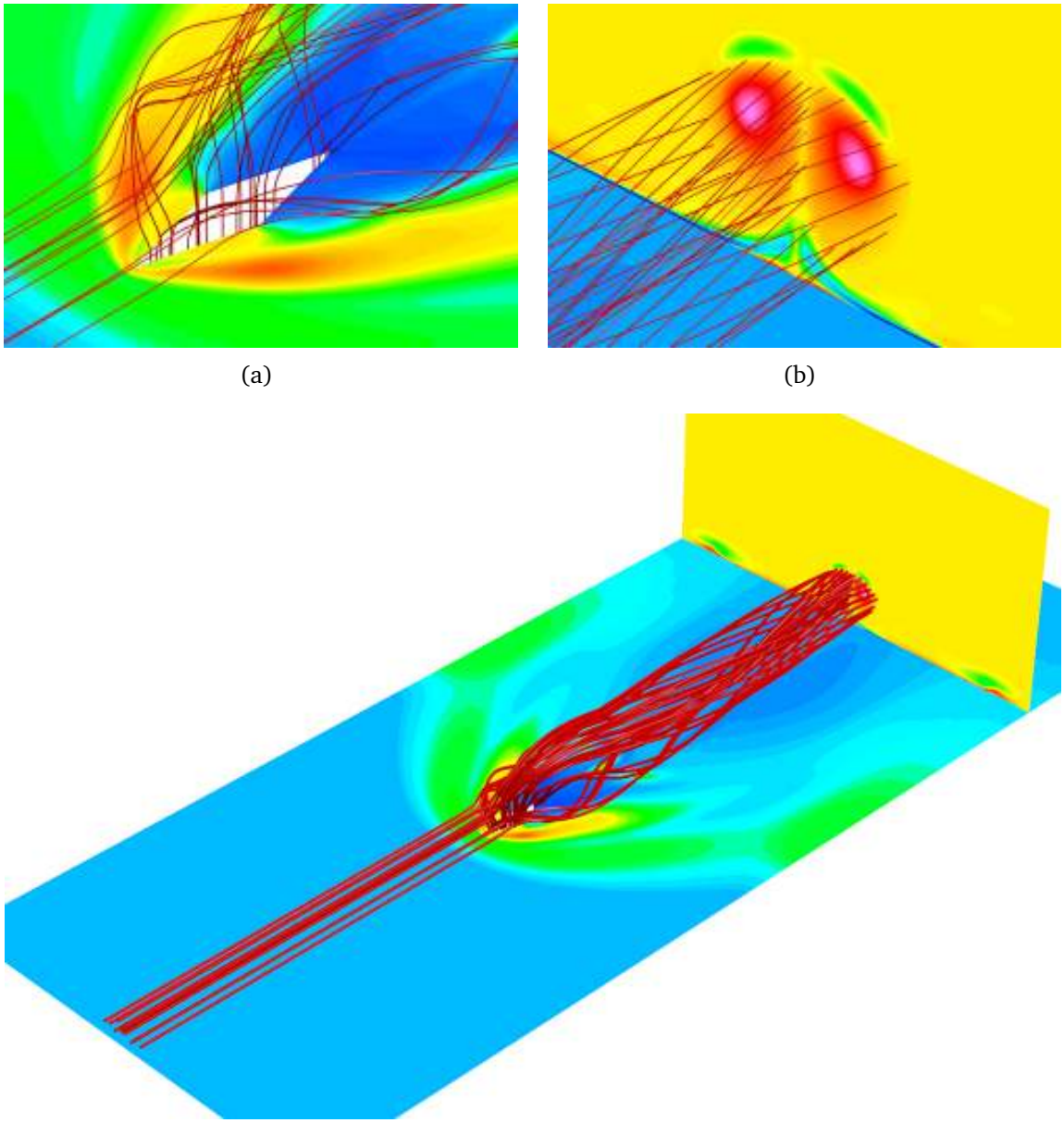

(a) (b)

(c)

Fig. 82 CVP, Layer 4.

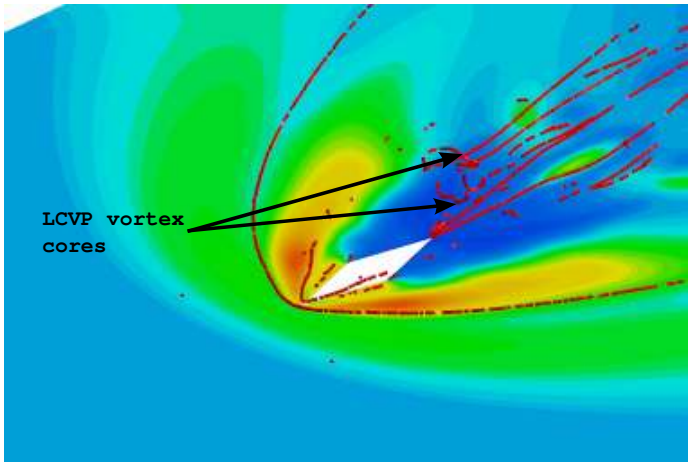

Fig. 83 LCVP vortex cores.

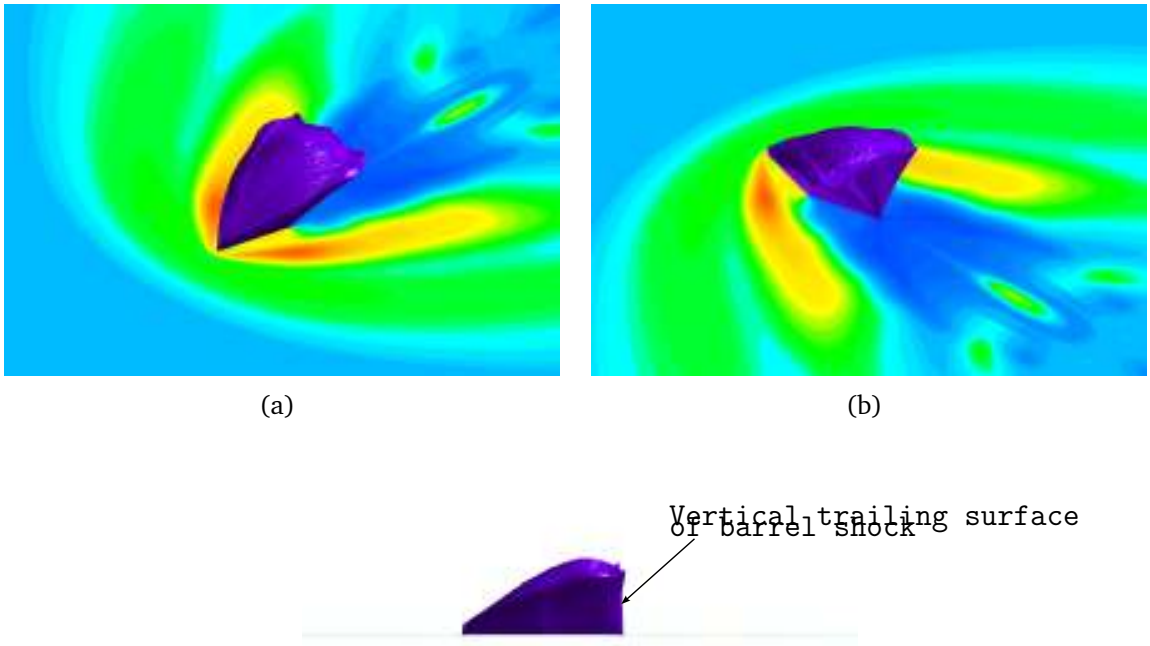

(a) (b)

(c)

Fig. 84 Barrel shock structure.

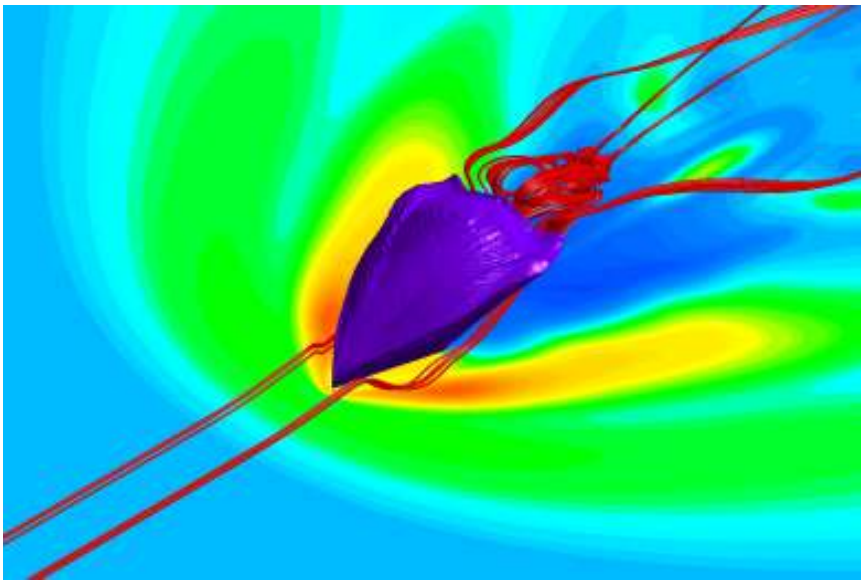

(a)

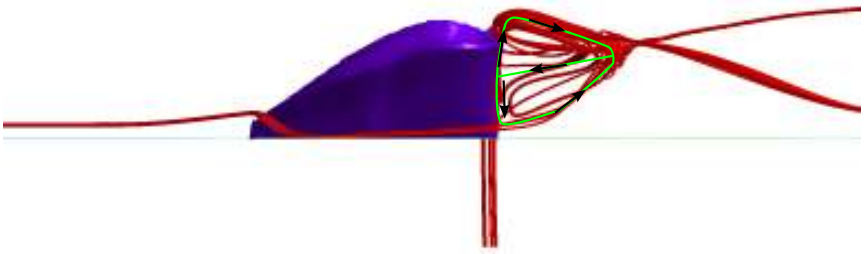

(b)

Fig. 85 LCVP structure.

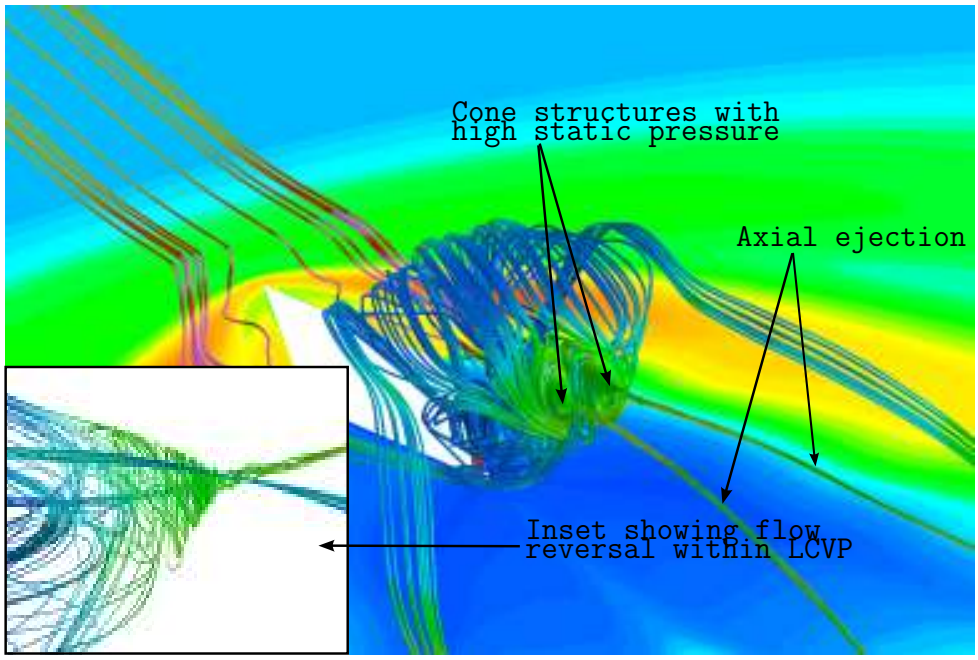

Fig. 86 Cone shaped structure downstream of LCVP.

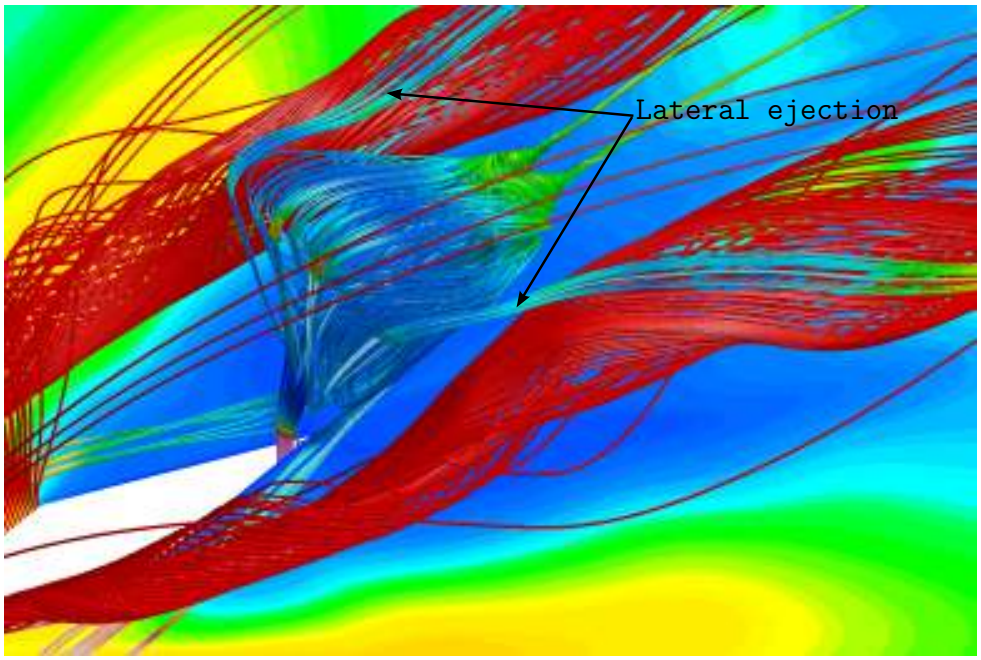

Fig. 87 Lateral ejection mechanism.

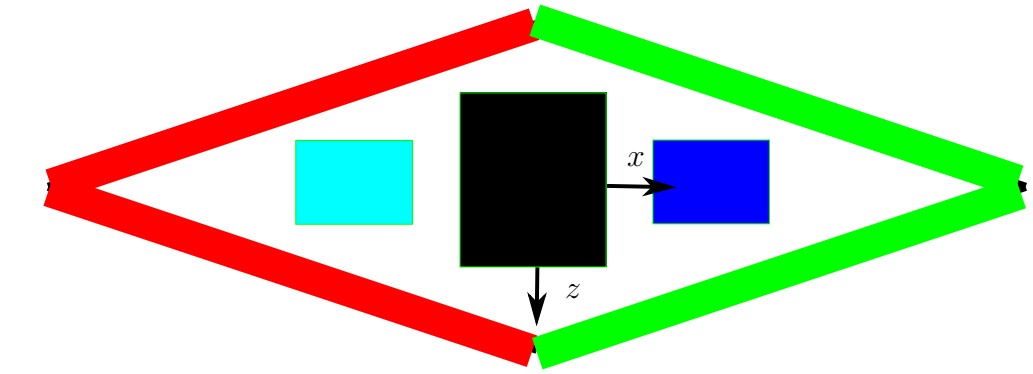

Region 1

Region 2

Region 3

Region 4

Region 5

Fig. 88 Jet orifice regions.

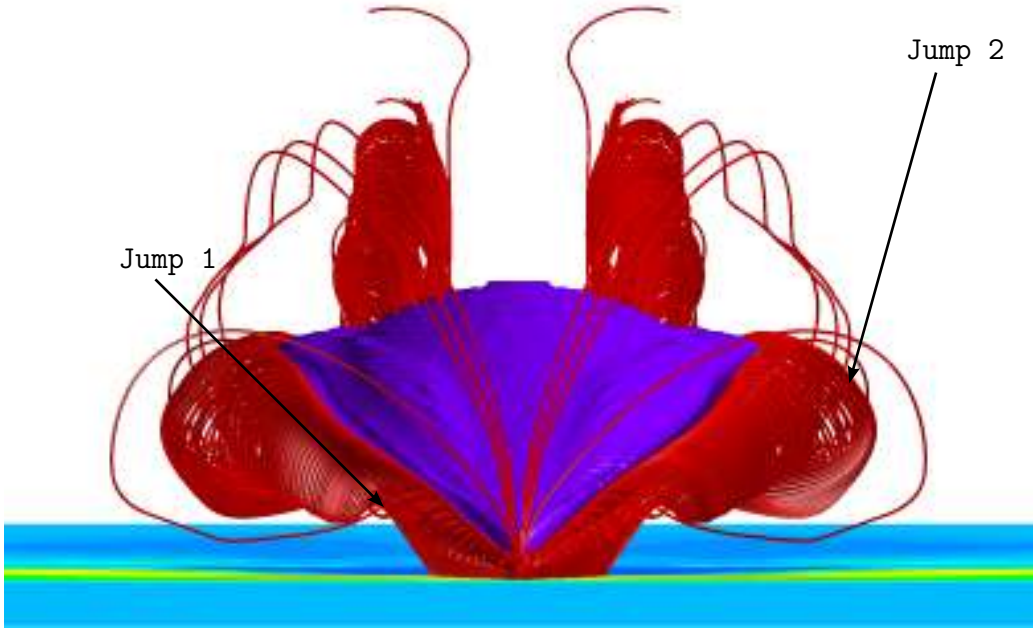

Fig. 89 Injector streamlines, Region 1.

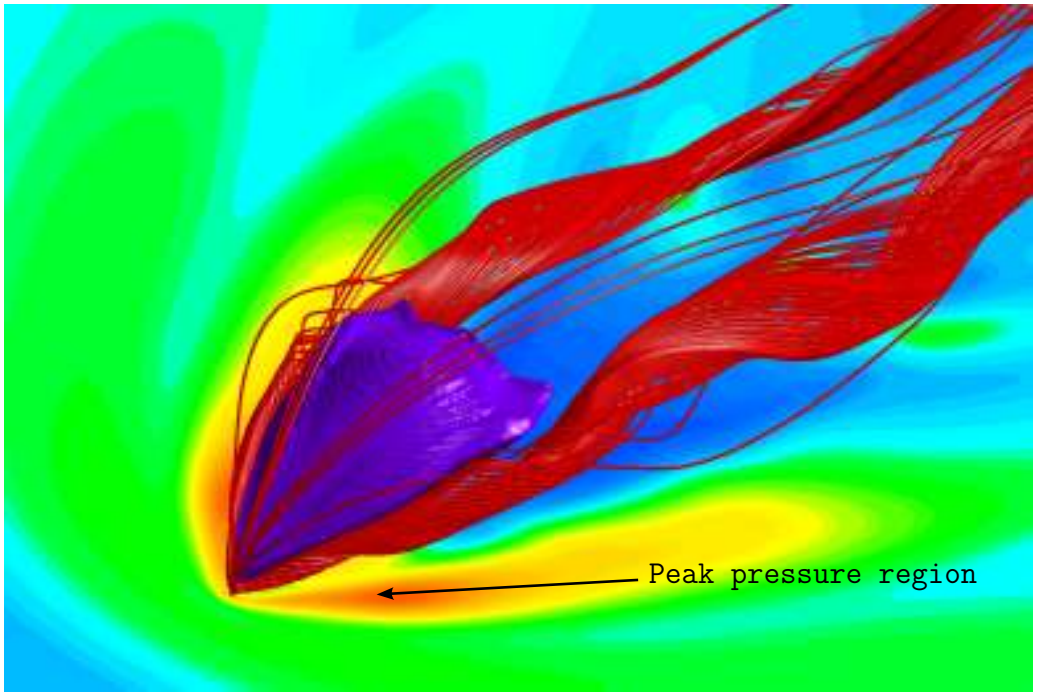

Fig. 90 Region 1 streamlines, cross-section change.

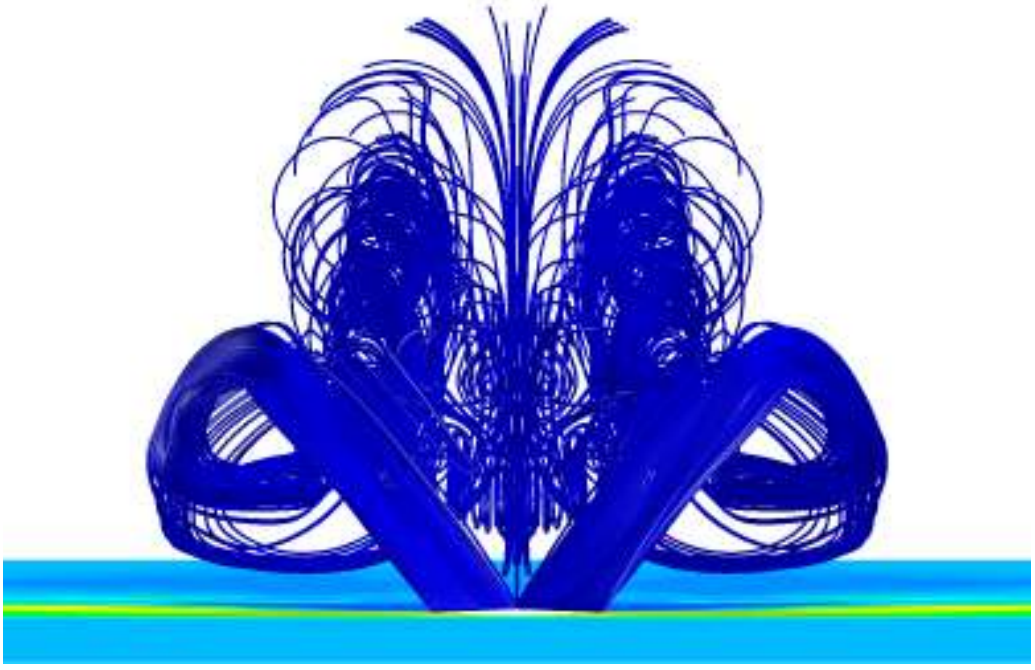

Fig. 91 Region 2 streamlines.

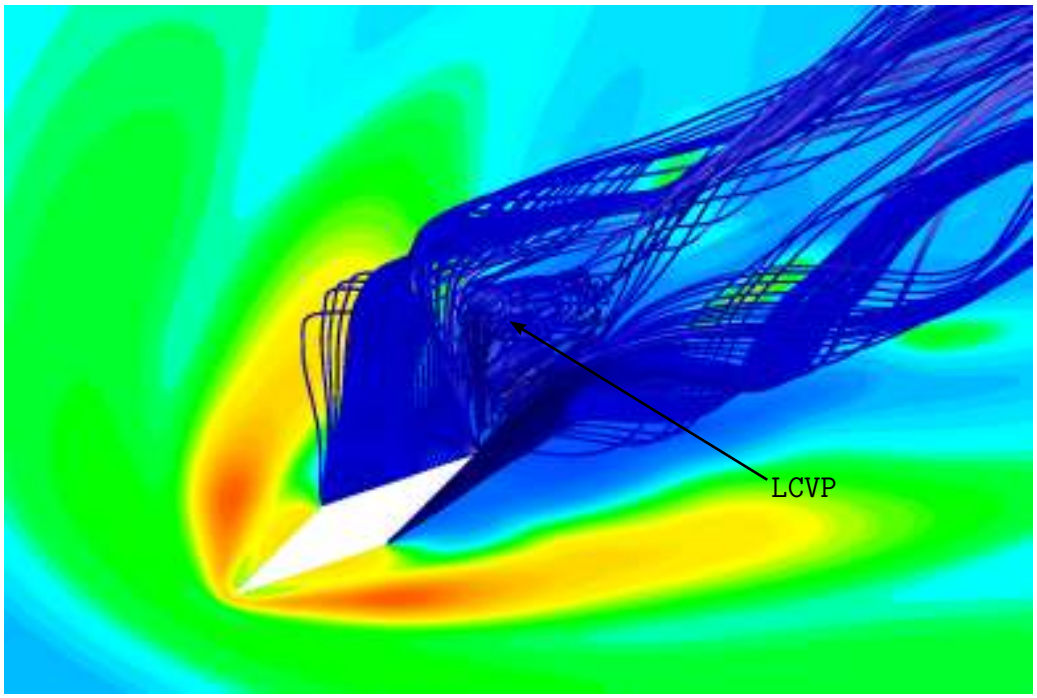

Fig. 92 Jet fluid entrainment in LCVP.

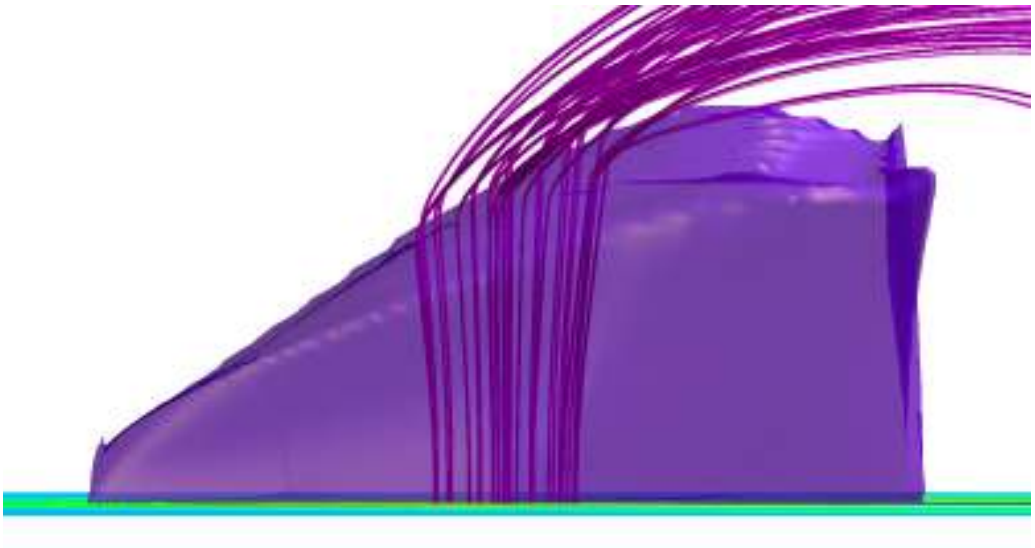

Fig. 93 Region 3 streamlines.

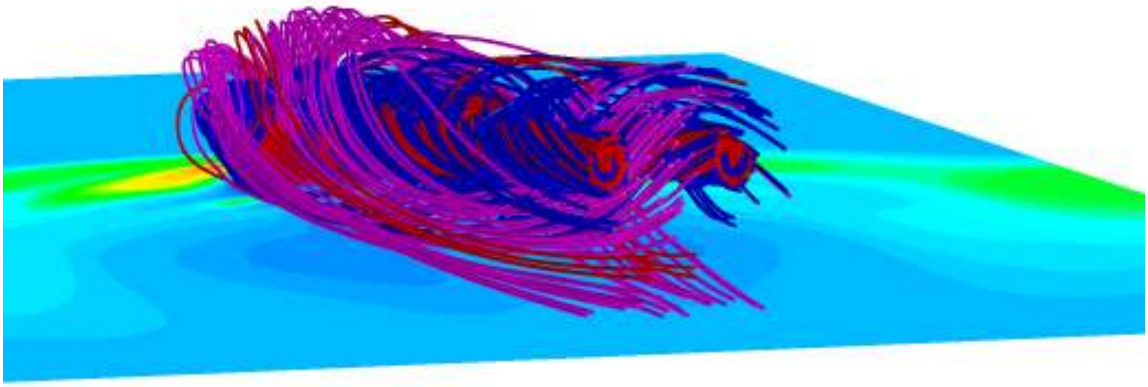

Fig. 94 Region 3 streamlines entrained in CVP.

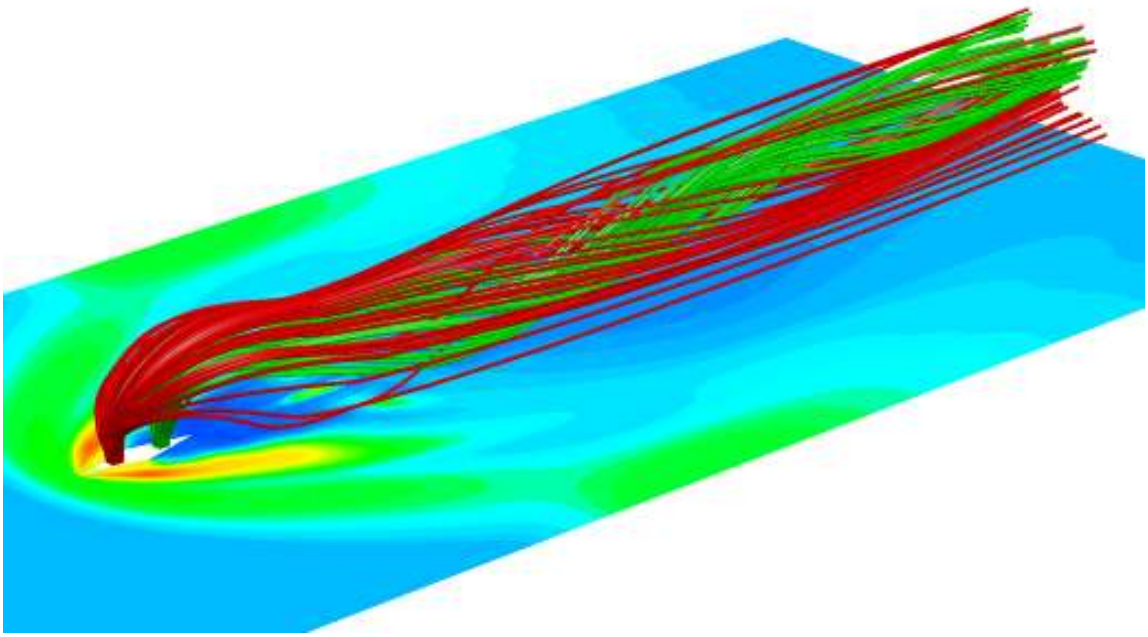

Fig. 95 Region 4 and 5 streamlines.

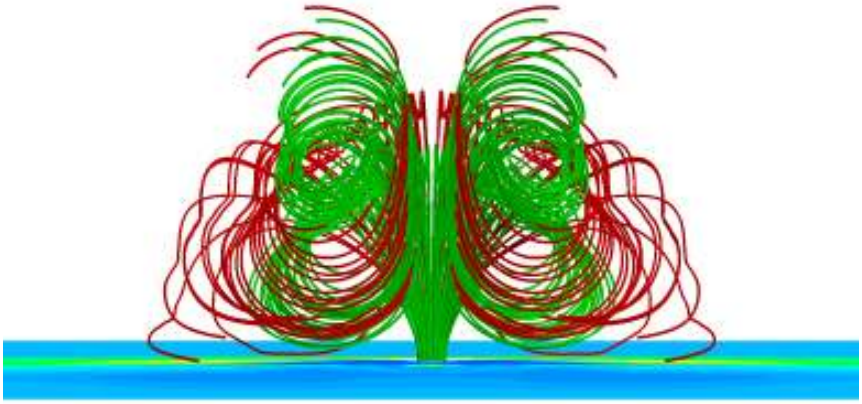

Fig. 96 Region 4 and 5 streamlines entrained in CVP.

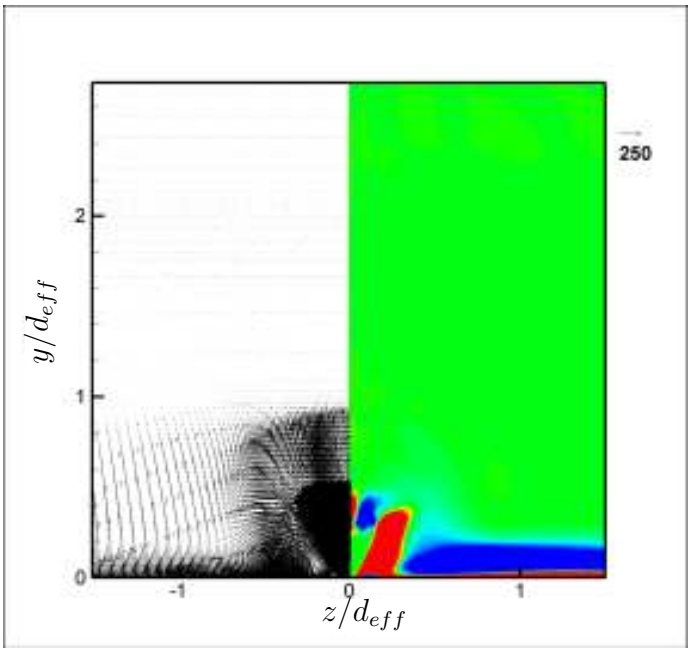

Fig. 97 $y-z$ **velocity and** x**-vorticity plot at** $x/d_{eff}=-1.0$**.**

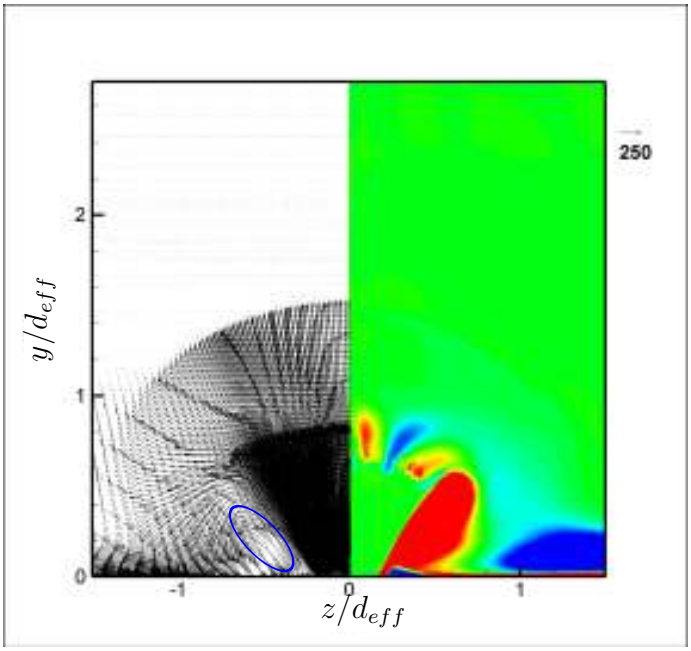

Fig. 98 $y-z$ **velocity and** x**-vorticity plot at** $x/d_{eff}=-0.5$**.**

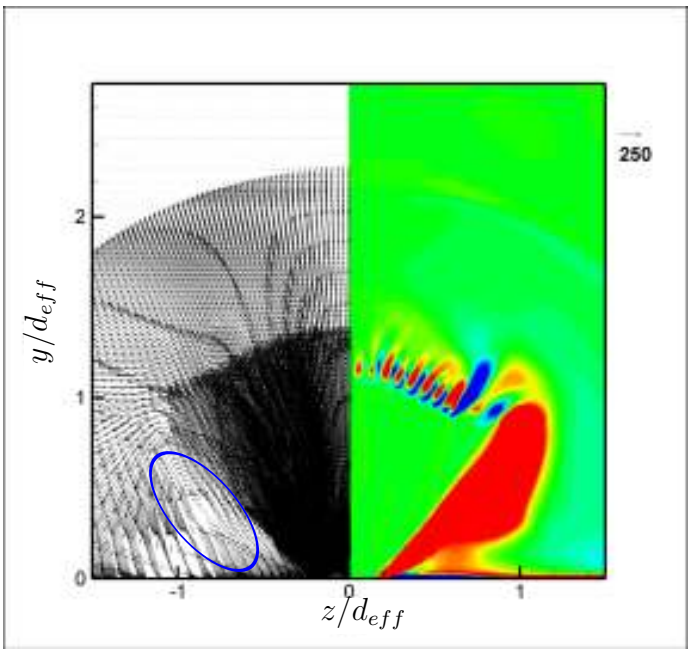

Fig. 99 $y-z$ **velocity and** x**-vorticity plot at** $x/d_{eff}=+$**0.5.**

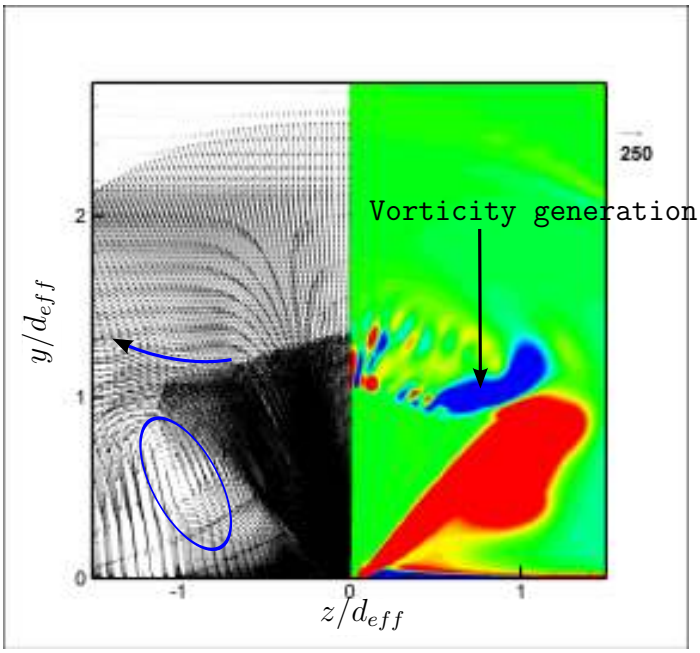

Fig. 100 $y-z$ **velocity and** x**-vorticity plot at** $x/d_{eff} = +1.0$**.**

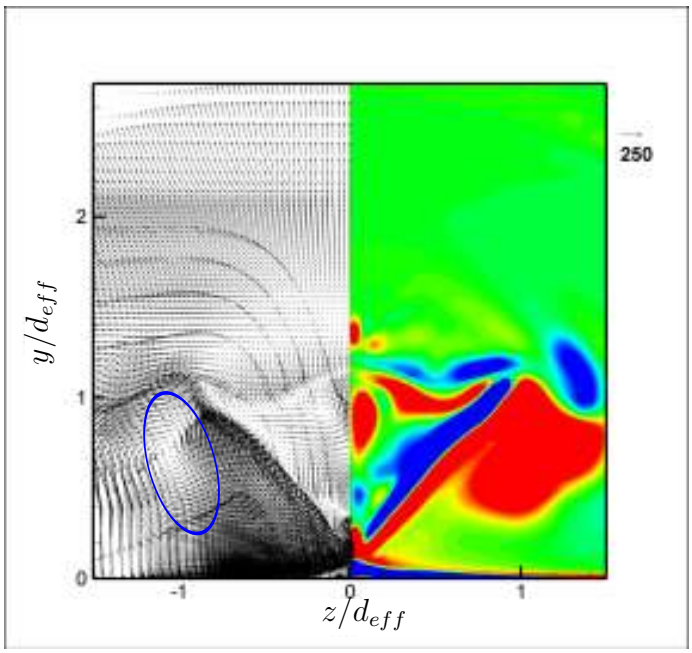

Fig. 101 $y-z$ **velocity and** x**-vorticity plot at** $x/d_{eff} = +1.5$**.**

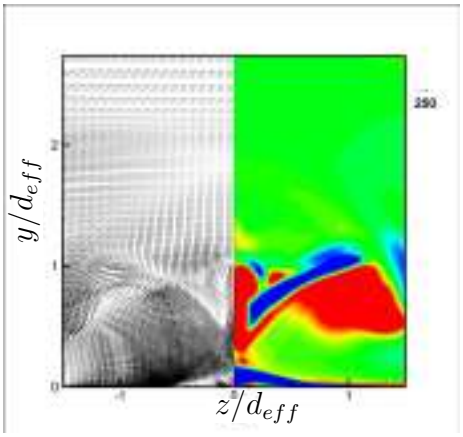

(a) $x/d_{eff} = +2.0$

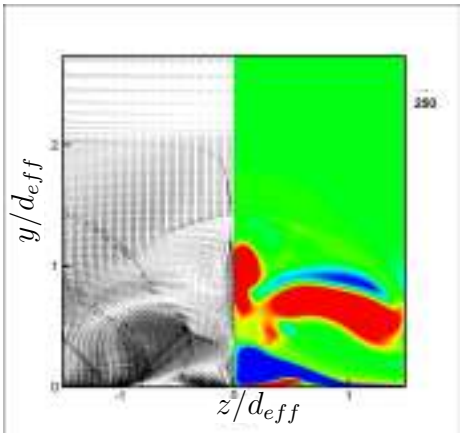

(b) $x/d_{eff} = +3.0$

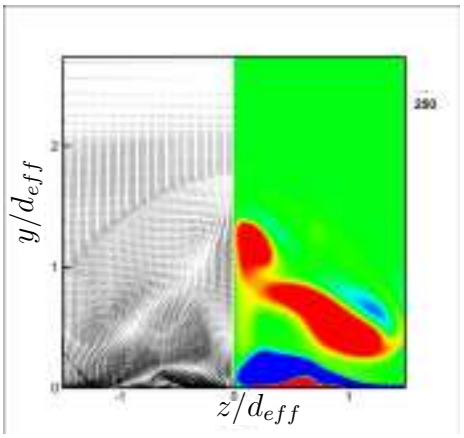

(c) $x/d_{eff} = +4.0$

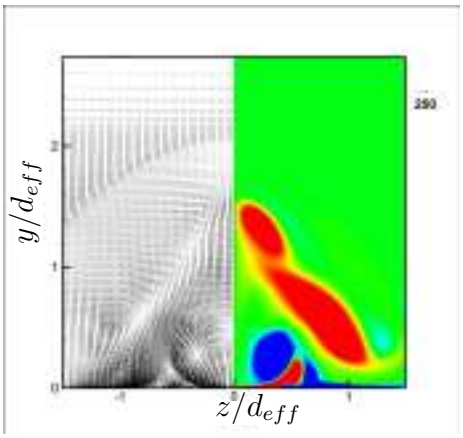

(d) $x/d_{eff} = +5.0$

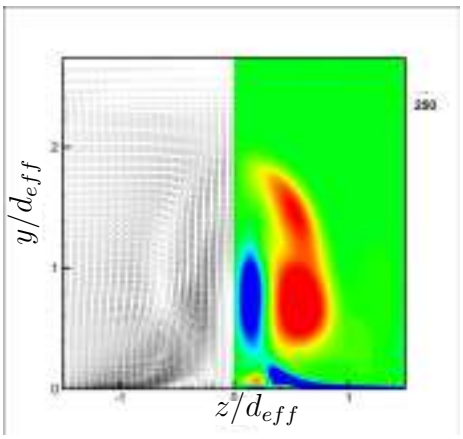

(e) $x/d_{eff} = +8.0$

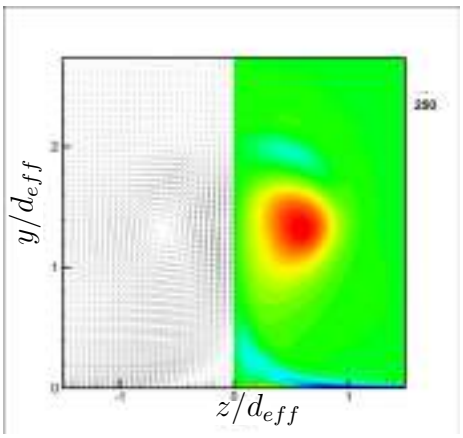

(f) $x/d_{eff} = +15.0$

Fig. 102 $y - z$ **velocity and** x**-vorticity plots.**

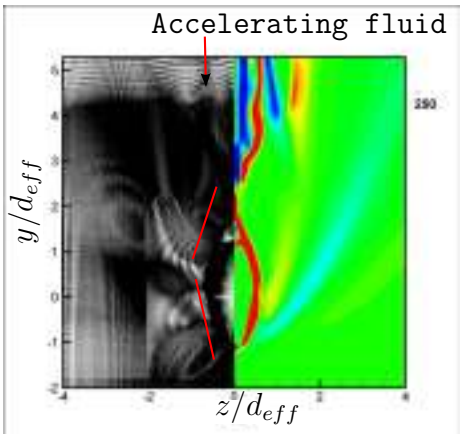

(a) $y/d_{eff} = +0.25$

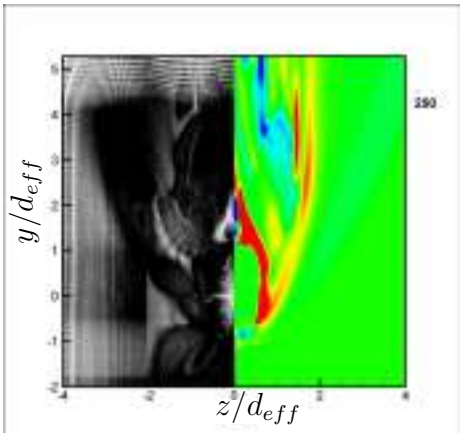

(b) $y/d_{eff} = +0.50$

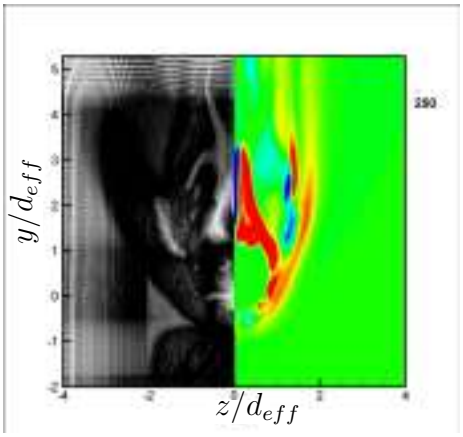

(c) $y/d_{eff} = +0.75$

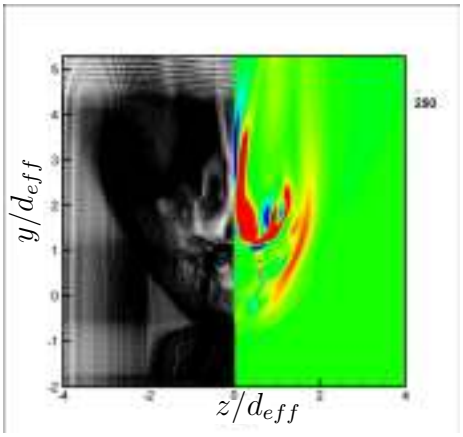

(d) $y/d_{eff} = +1.0$

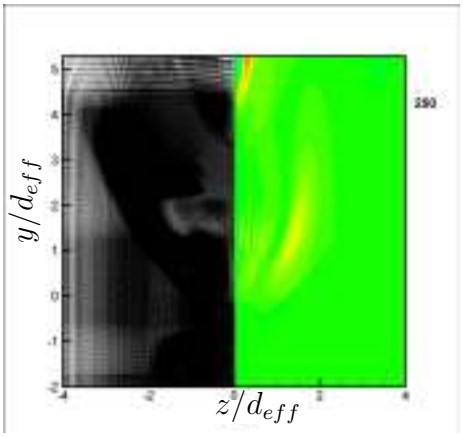

(e) $y/d_{eff} = +1.5$

Fig. 103 $z - x$ **velocity and** y**-vorticity plots.**

Fig. 104 Shear layers.

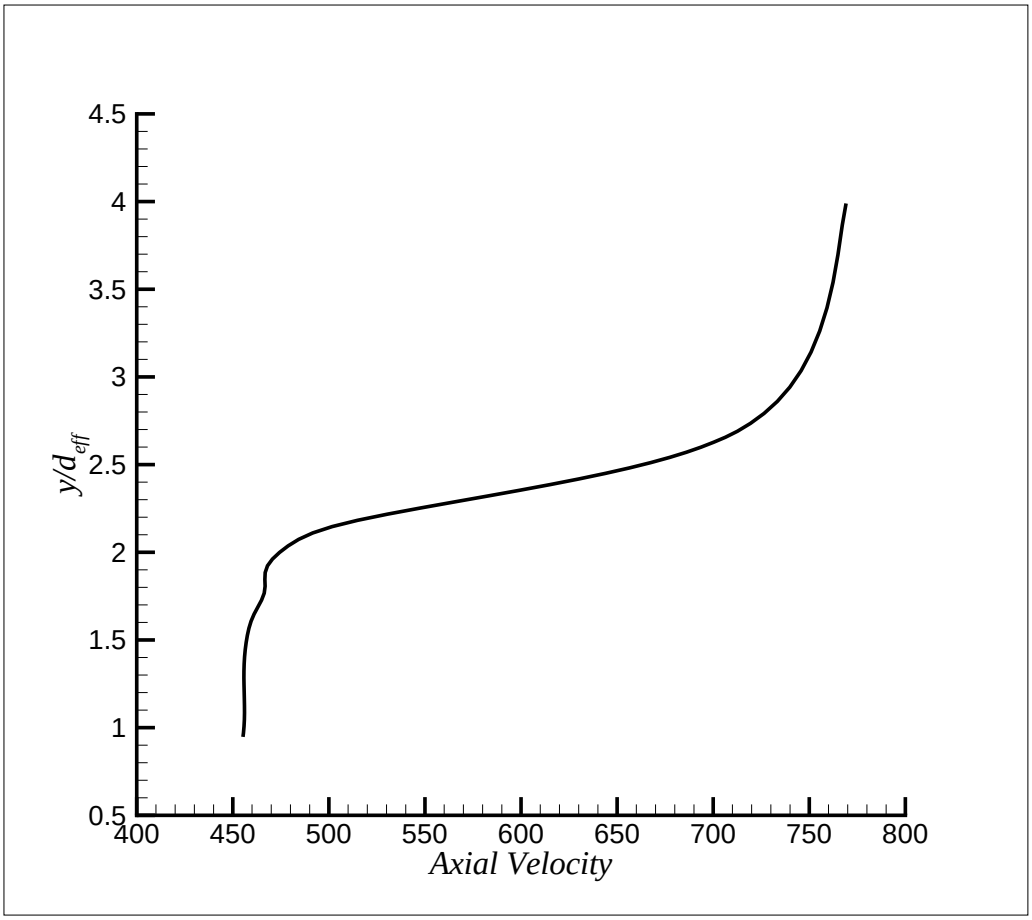

Fig. 105 Axial velocity difference across plume shear layer at $x/d_{eff} = +15.0$.

(a) 10-degree

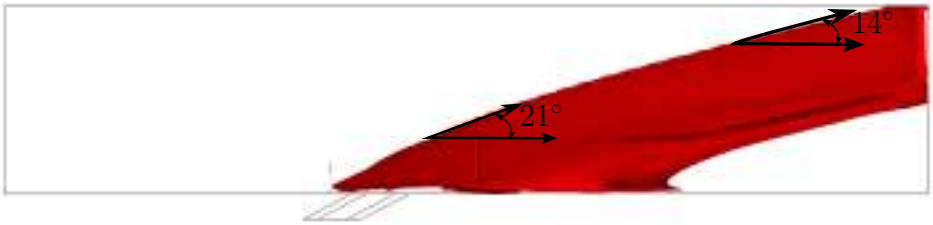

(b) 27.5-degree

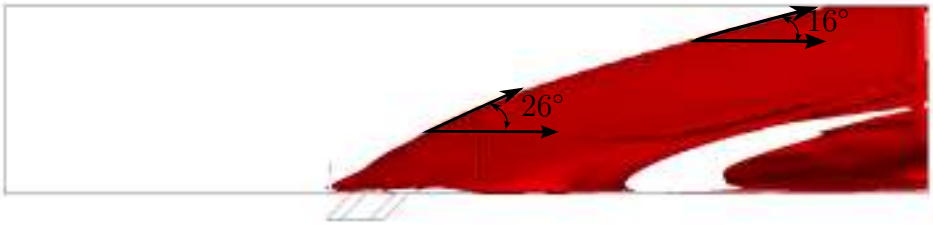

(c) 45-degree

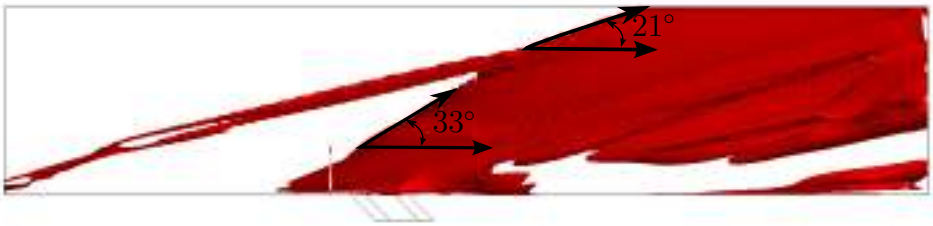

(d) 135-degree

Fig. 106 Interaction shocks for angled injection with J_1 momentum ratio.

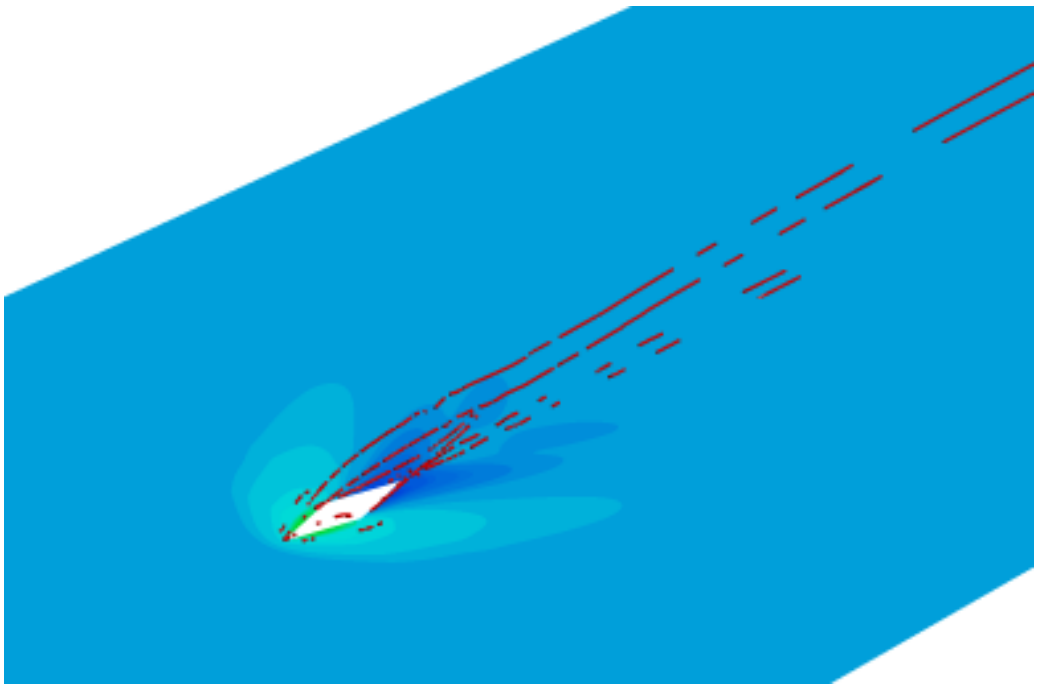

Fig. 107 Vortex cores, 10-degree J_1.

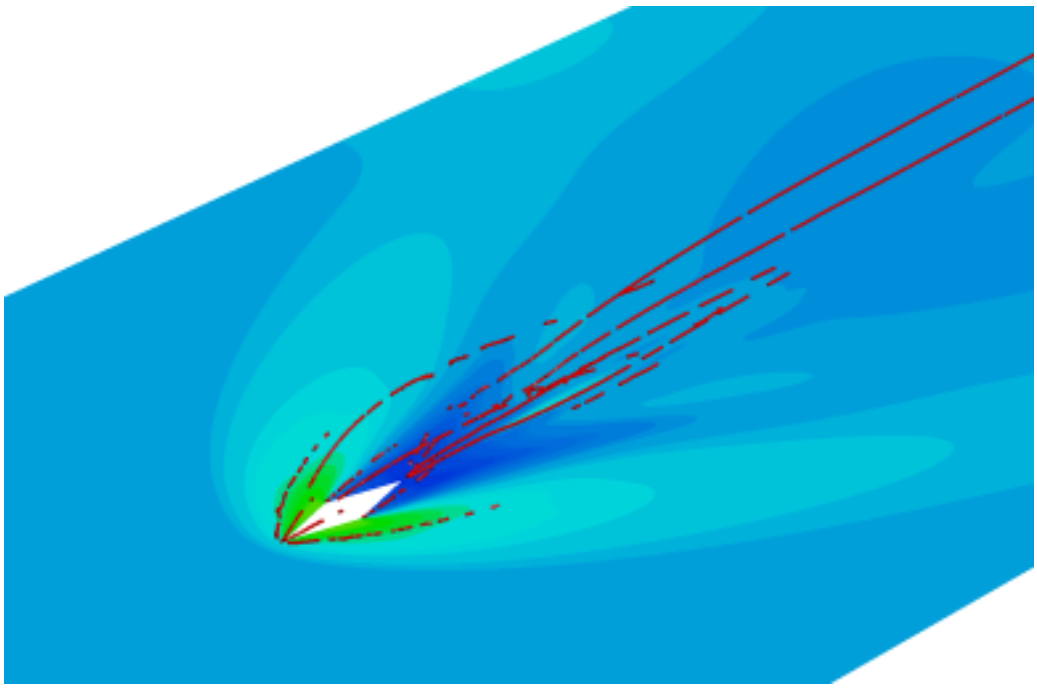

Fig. 108 Vortex cores, 27.5-degree J_1.

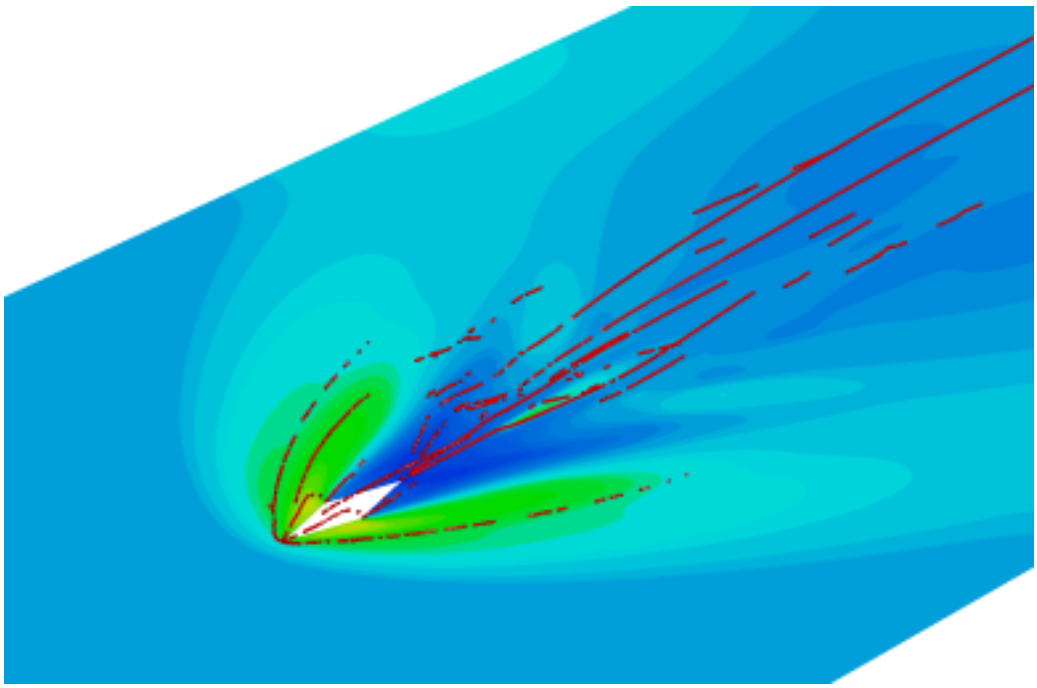

Fig. 109 Vortex cores, 45-degree J_1.

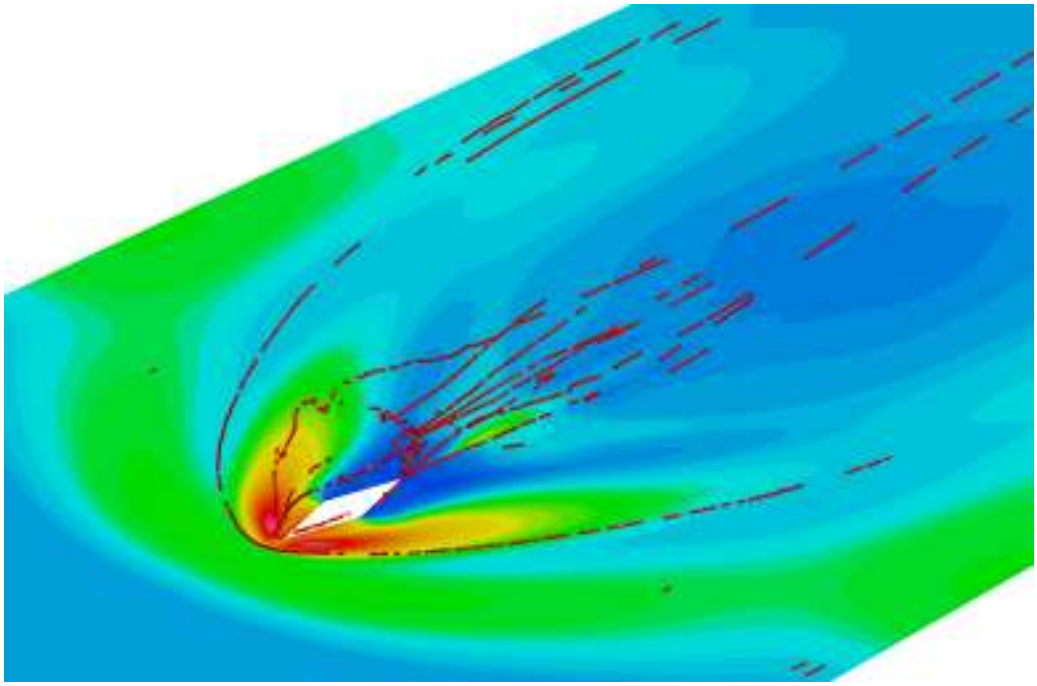

Fig. 110 Vortex cores, 135-degree J_1.

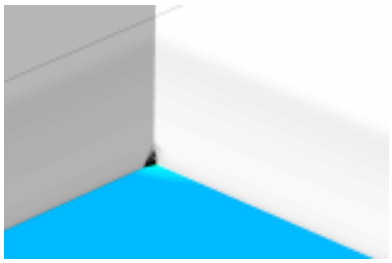

(a) x/d_{eff}=-1.0

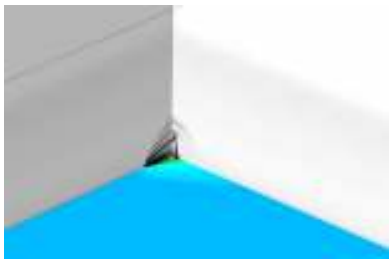

(b) x/d_{eff}=-0.5

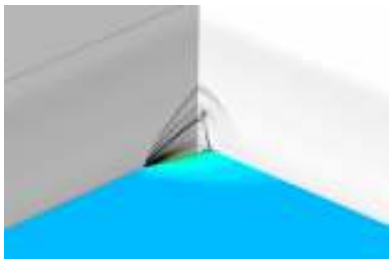

(c) x/d_{eff}= 0.0

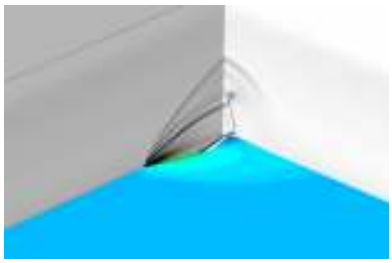

(d) x/d_{eff}=+0.5

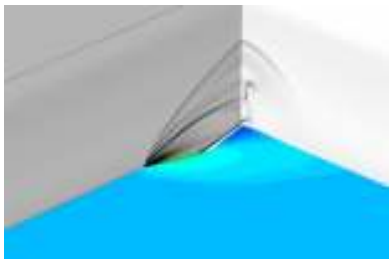

(e) x/d_{eff}= +1.0

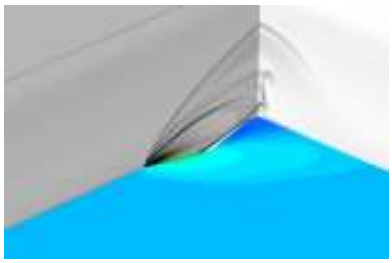

(f) x/d_{eff}=+1.5

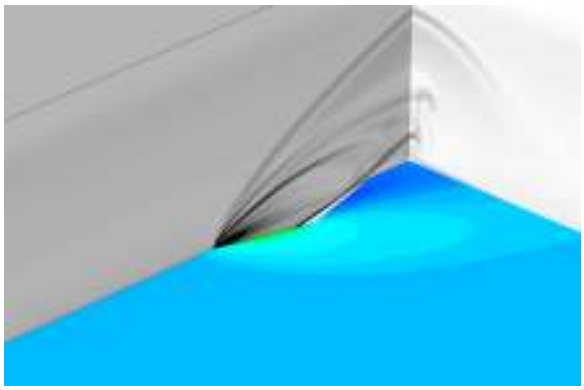

(g) x/d_{eff}=+2.0

Fig. 111 Numerical schlieren of barrel shock — 10-degree J_1.

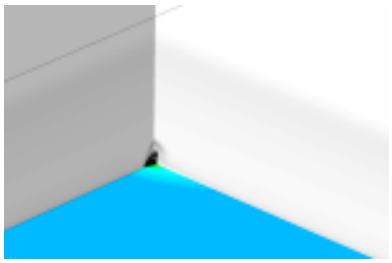

(a) x/d_{eff}=-1.0

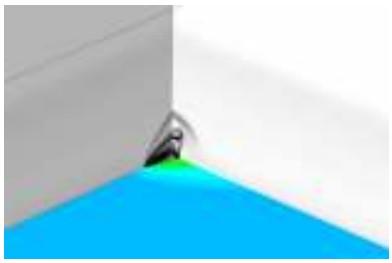

(b) x/d_{eff}=-0.5

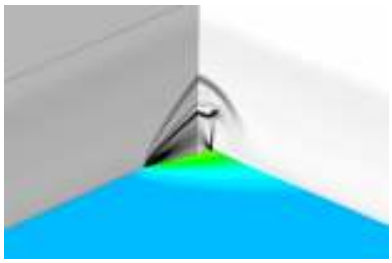

(c) x/d_{eff}= 0.0

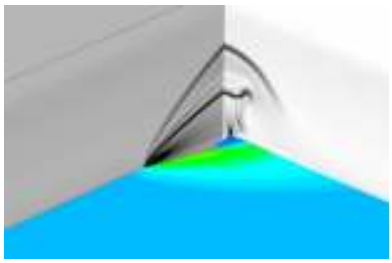

(d) x/d_{eff}=+0.5

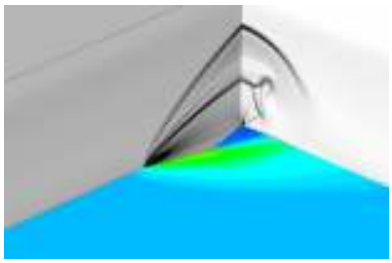

(e) x/d_{eff}= +1.0

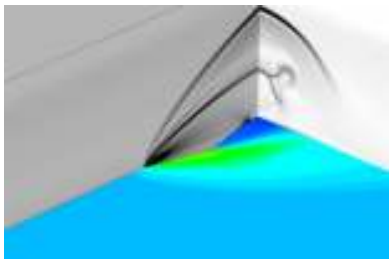

(f) x/d_{eff}=+1.5

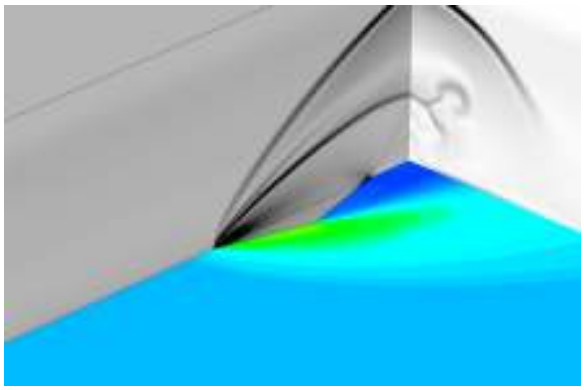

(g) x/d_{eff}=+2.0

Fig. 112 Numerical schlieren of barrel shock — 27.5-degree J_1.

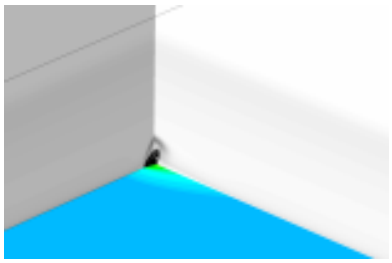

(a) x/d_{eff}=-1.0

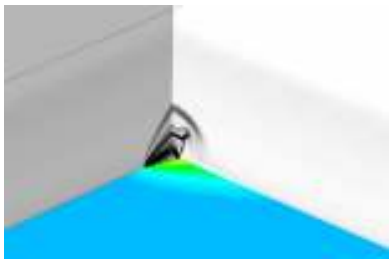

(b) x/d_{eff}=-0.5

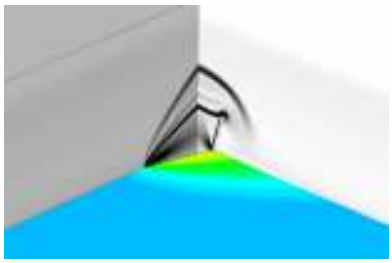

(c) x/d_{eff}= 0.0

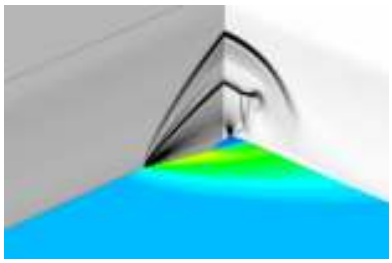

(d) x/d_{eff}=+0.5

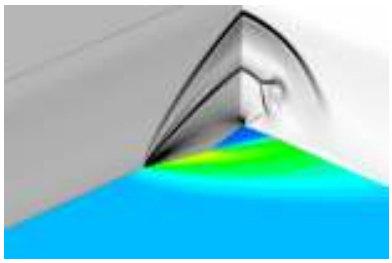

(e) x/d_{eff}= +1.0

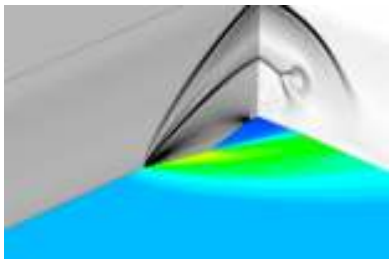

(f) x/d_{eff}=+1.5

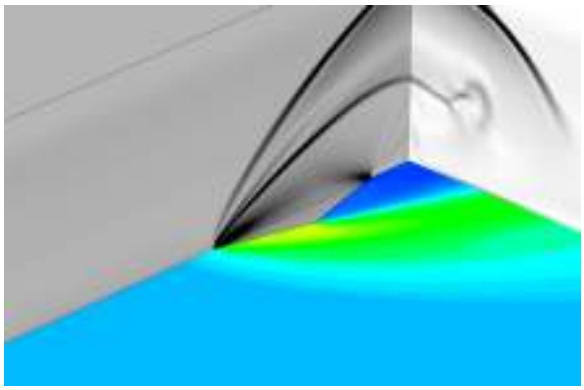

(g) x/d_{eff}=+2.0

Fig. 113 Numerical schlieren of barrel shock — 45-degree J_1.

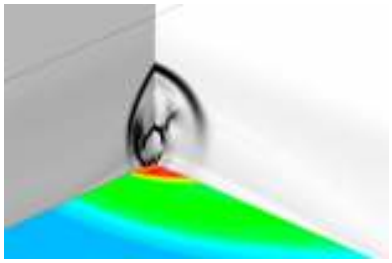

(a) x/d_{eff}=-1.0

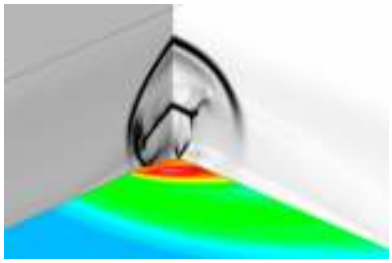

(b) x/d_{eff}=-0.5

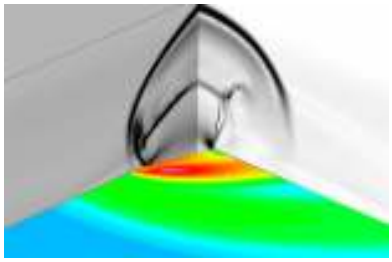

(c) x/d_{eff}= 0.0

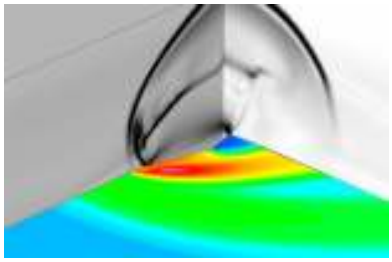

(d) x/d_{eff}=+0.5

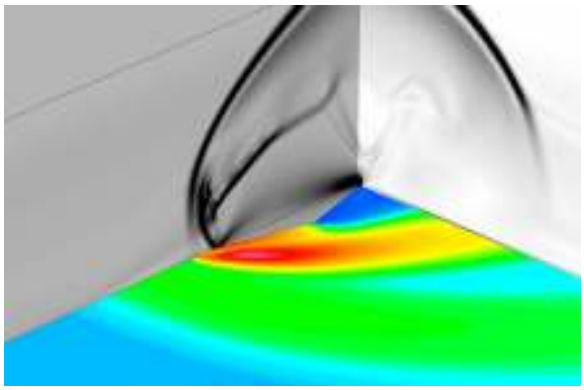

(e) x/d_{eff}=+2.0

Fig. 114 Numerical schlieren of barrel shock — 135-degree J_1.

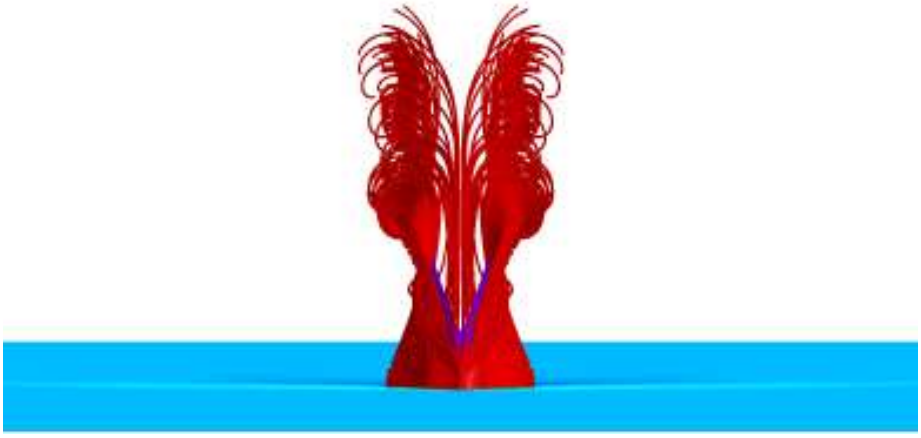

(a)

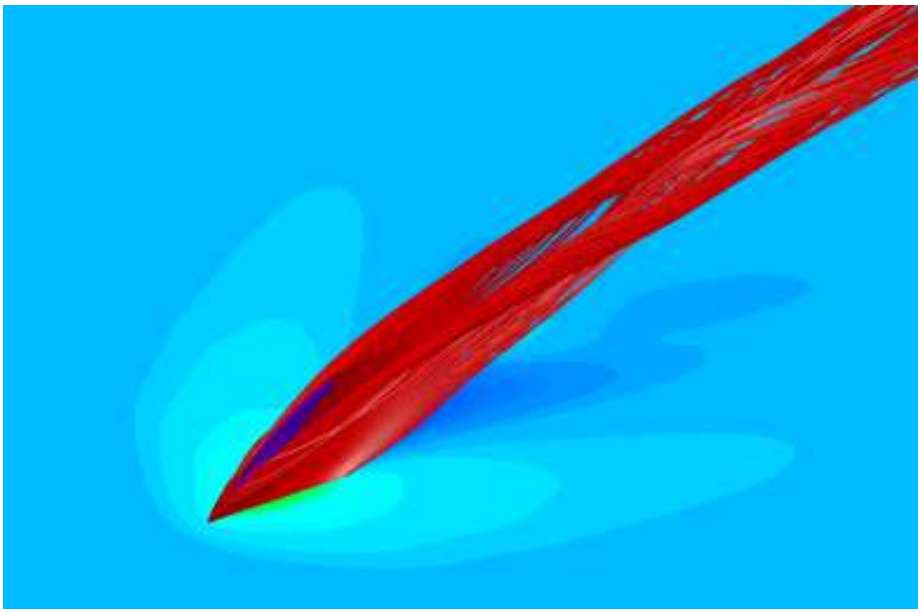

(b)

Fig. 115 Injector streamlines, Region 1, 10-degree J_1.

(a)

(b)

Fig. 116 Injector streamlines, Region 2, 10-degree J_1.

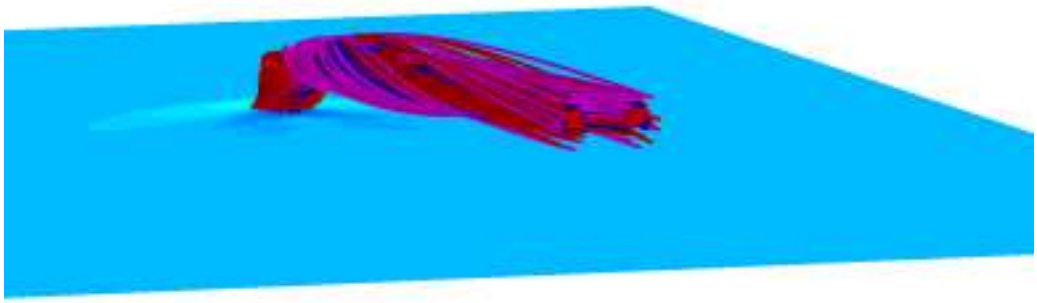

Fig. 117 Injector streamlines, Region 3, 10-degree J_1.

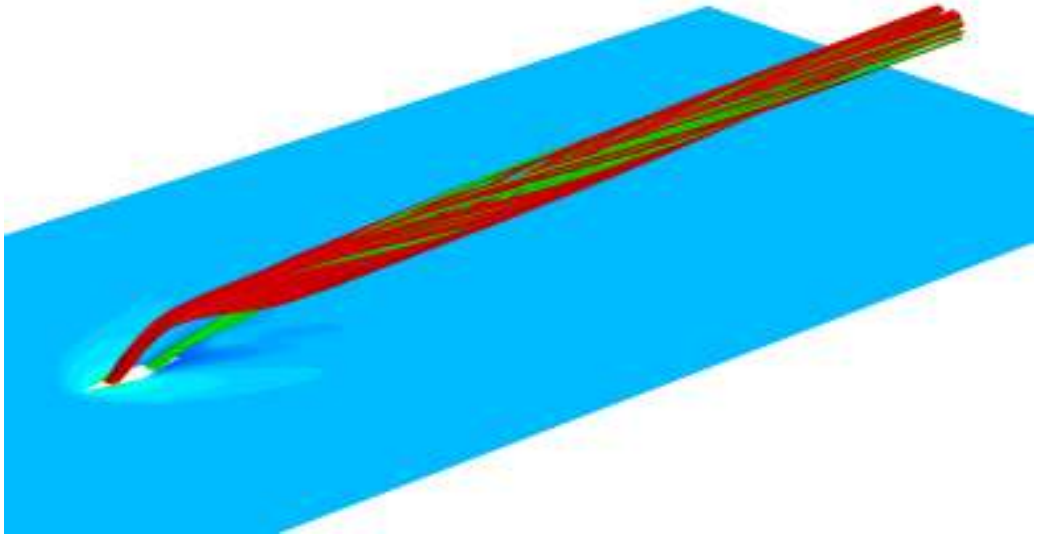

Fig. 118 Injector streamlines, Region 4 and 5, 10-degree J_1.

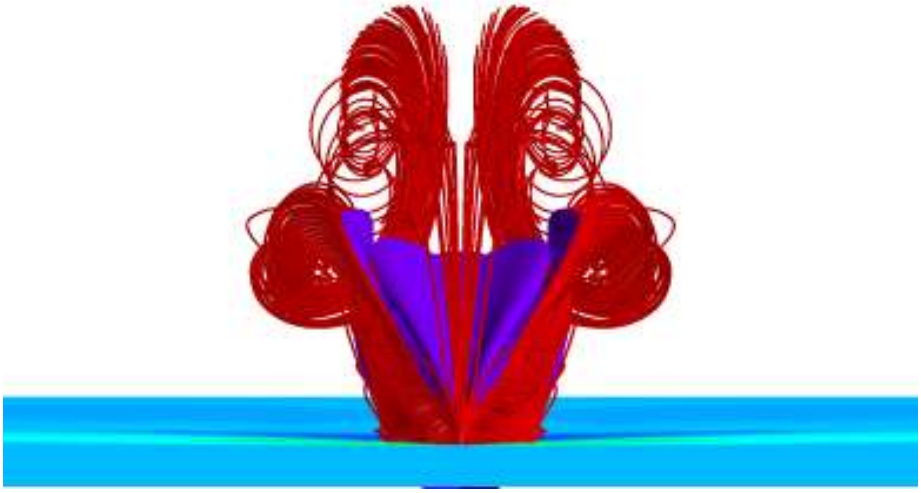

(a)

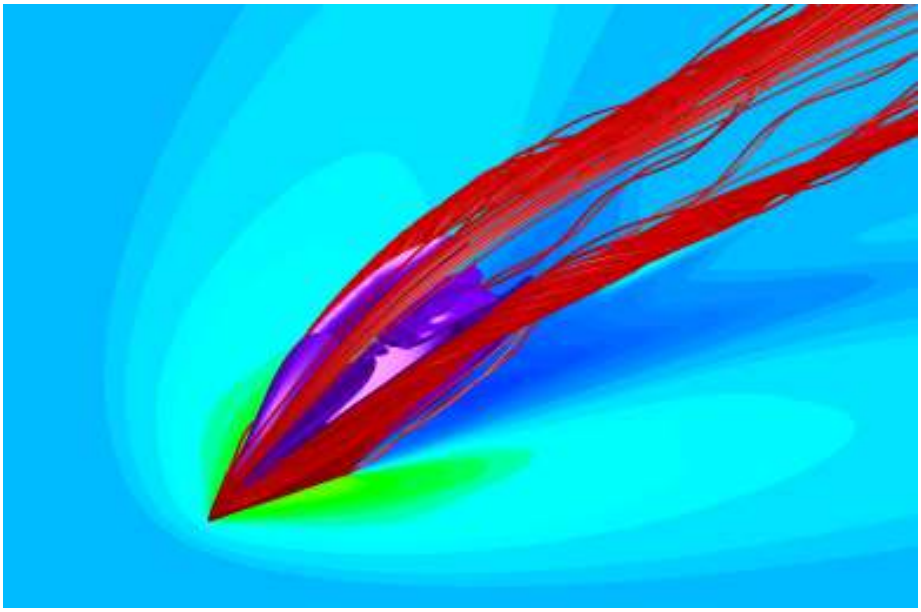

(b)

Fig. 119 Injector streamlines, Region 1, 27.5-degree J_1.

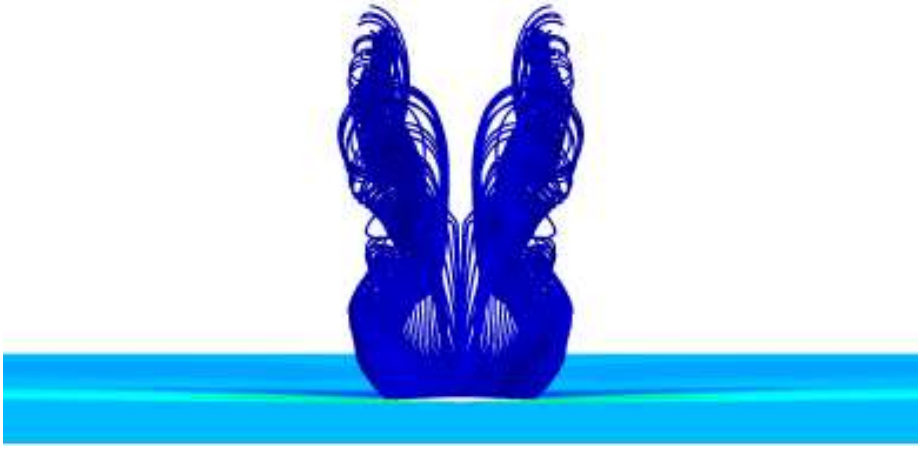

(a)

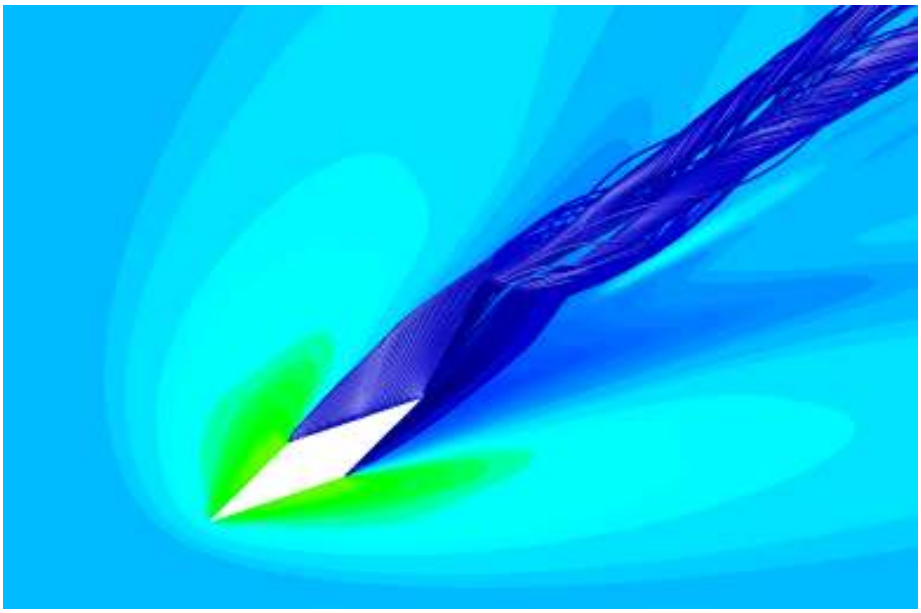

(b)

Fig. 120 Injector streamlines, Region 2, 27.5-degree J_1.

Fig. 121 Injector streamlines, Region 3, 27.5-degree J_1.

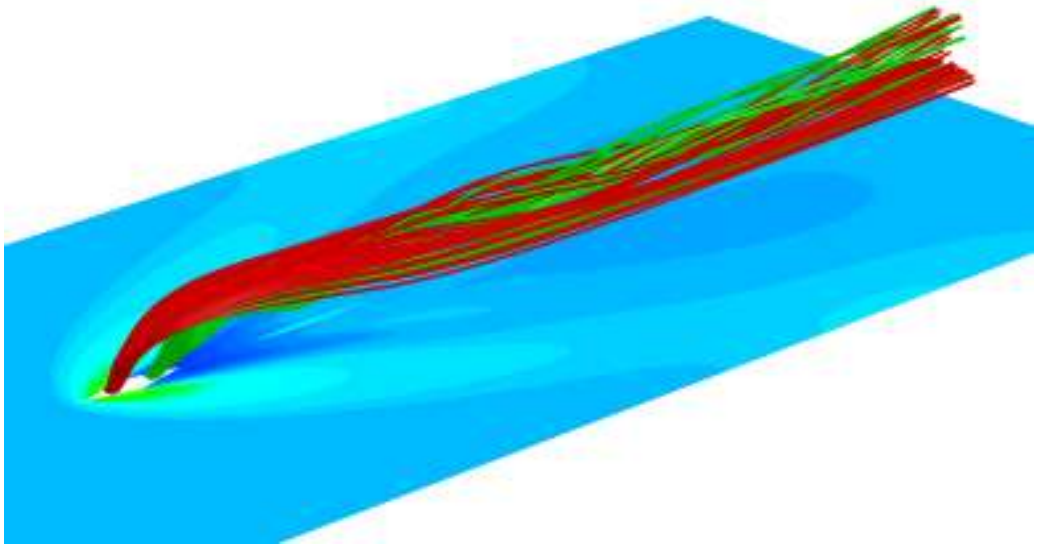

Fig. 122 Injector streamlines, Region 4 and 5, 27.5-degree J_1.

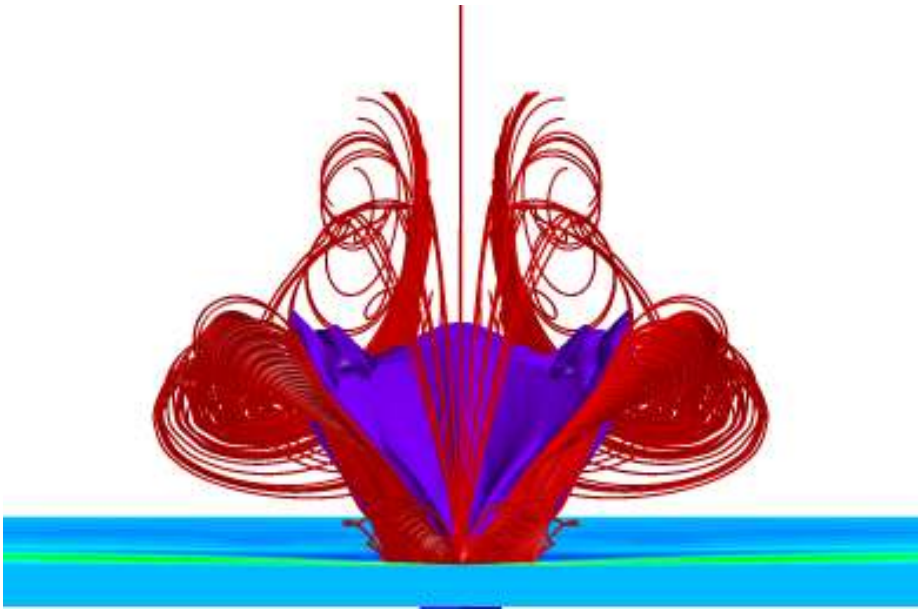

(a)

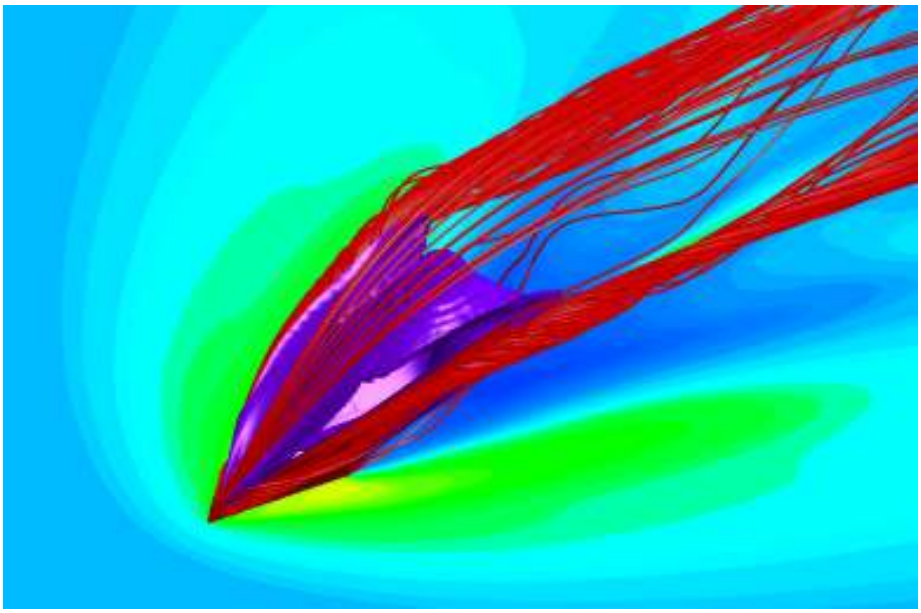

(b)

Fig. 123 Injector streamlines, Region 1, 45-degree J_1.

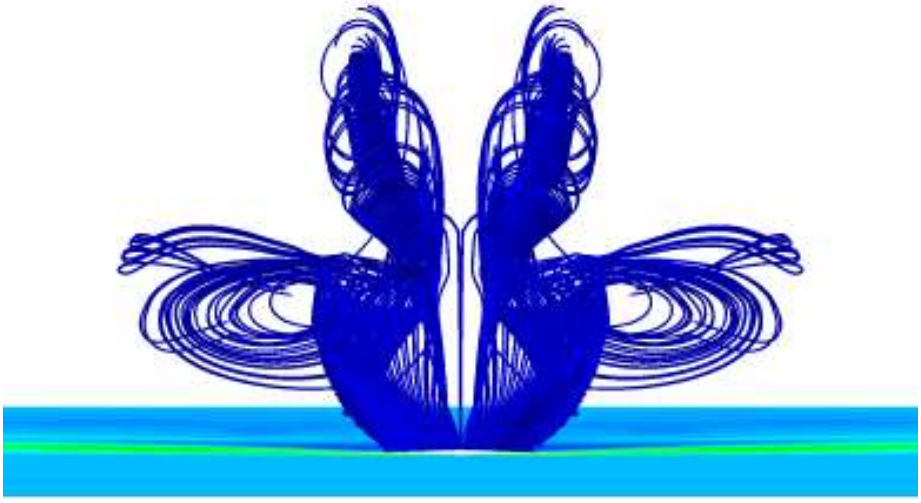

(a)

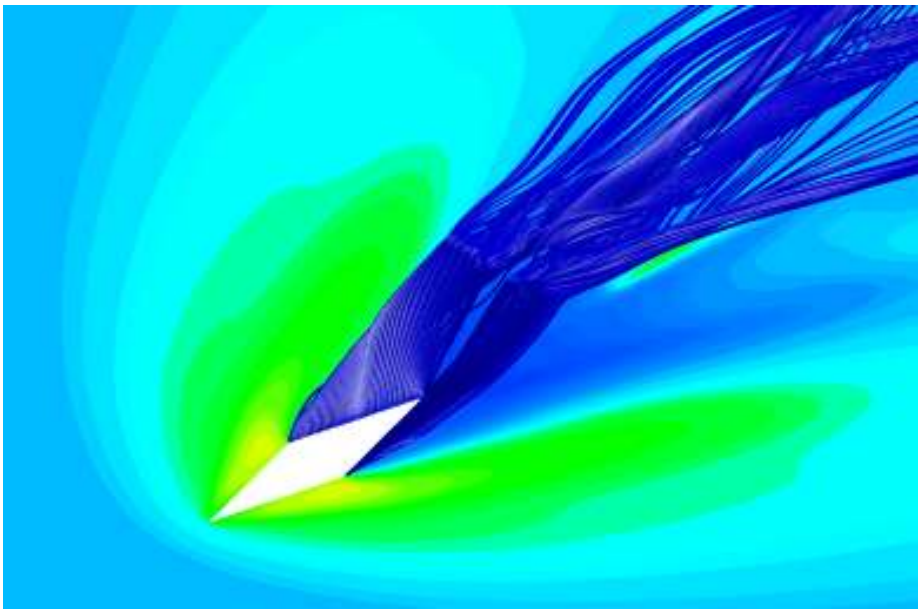

(b)

Fig. 124 Injector streamlines, Region 2, 45-degree J_1.

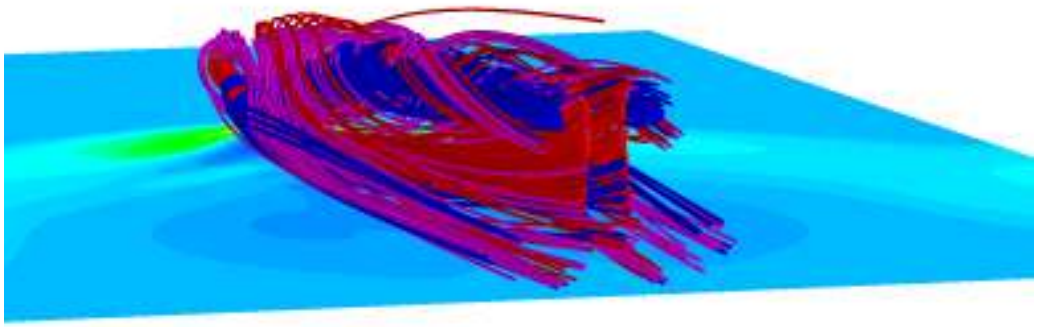

Fig. 125 Injector streamlines, Region 3, 45-degree J_1.

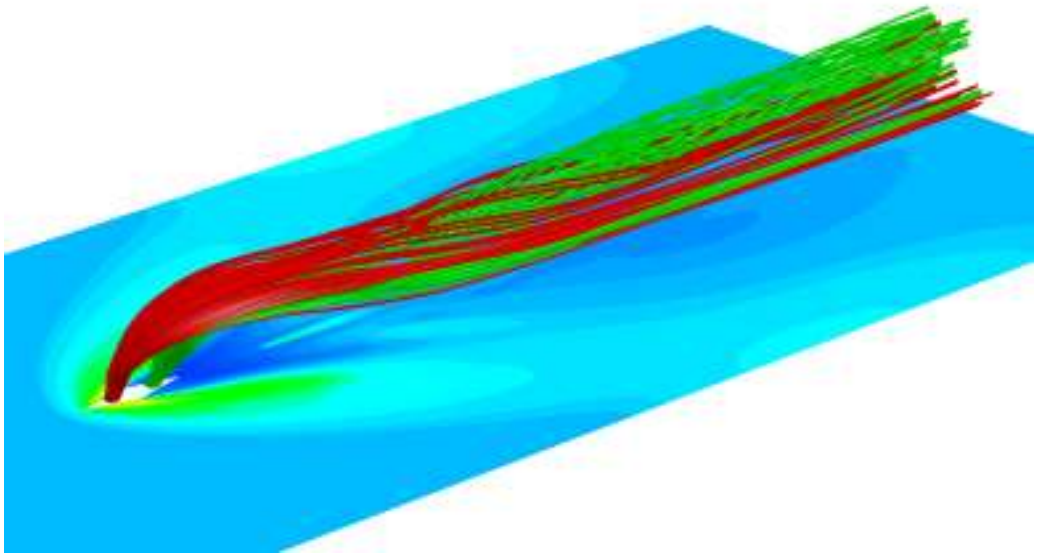

Fig. 126 Injector streamlines, Region 4 and 5, 45-degree J_1.

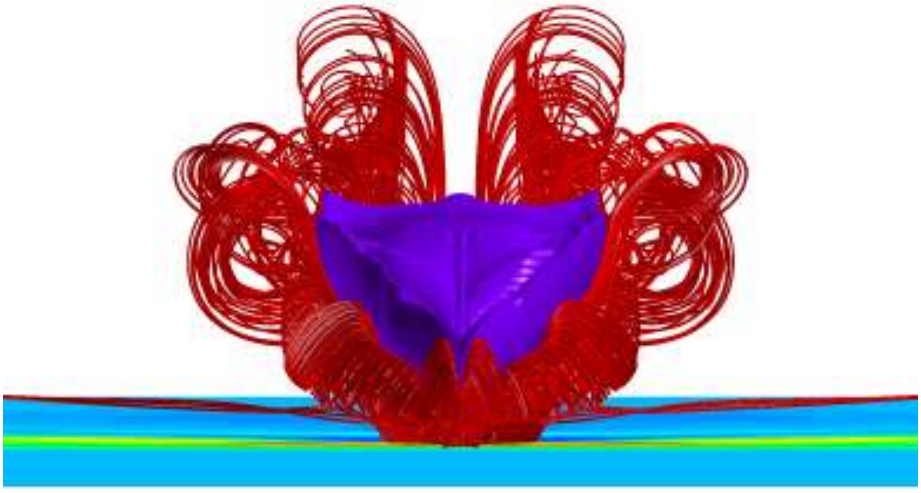

(a)

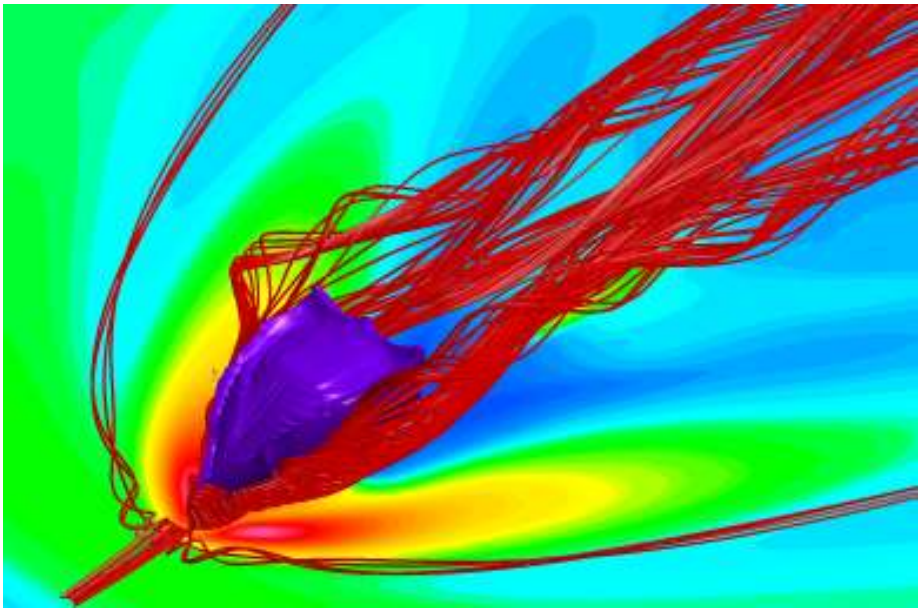

(b)

Fig. 127 Injector streamlines, Region 1, 135-degree J_1.

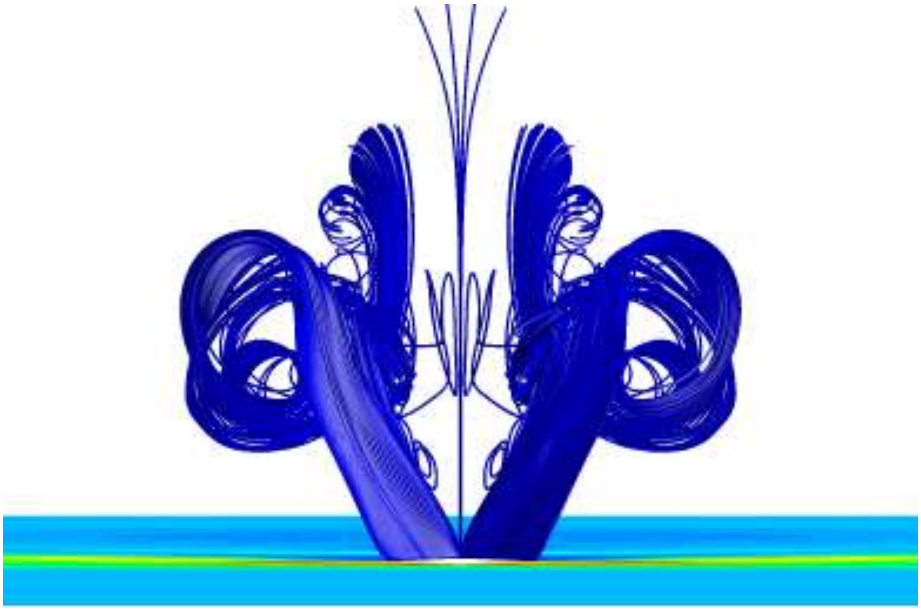

(a)

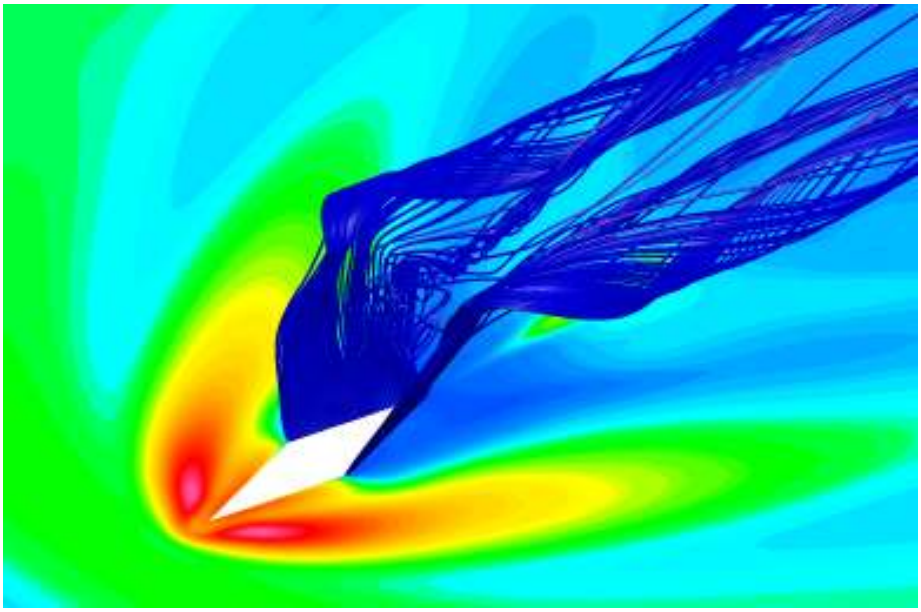

(b)

Fig. 128 Injector streamlines, Region 2, 135-degree J_1.

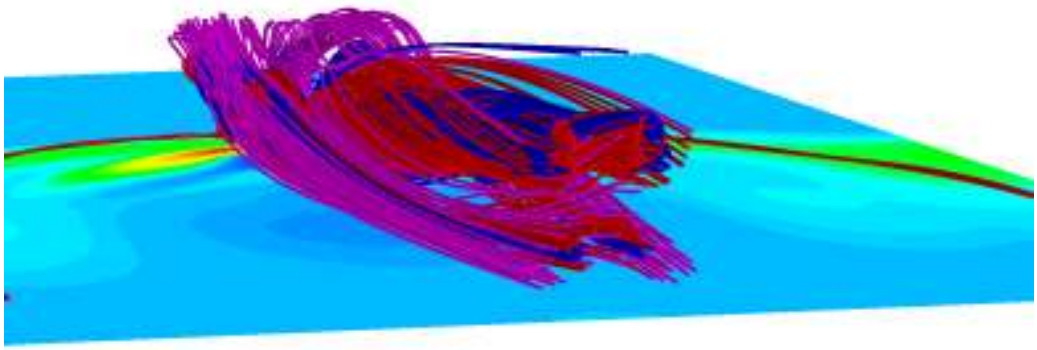

Fig. 129 Injector streamlines, Region 3, 135-degree J_1.

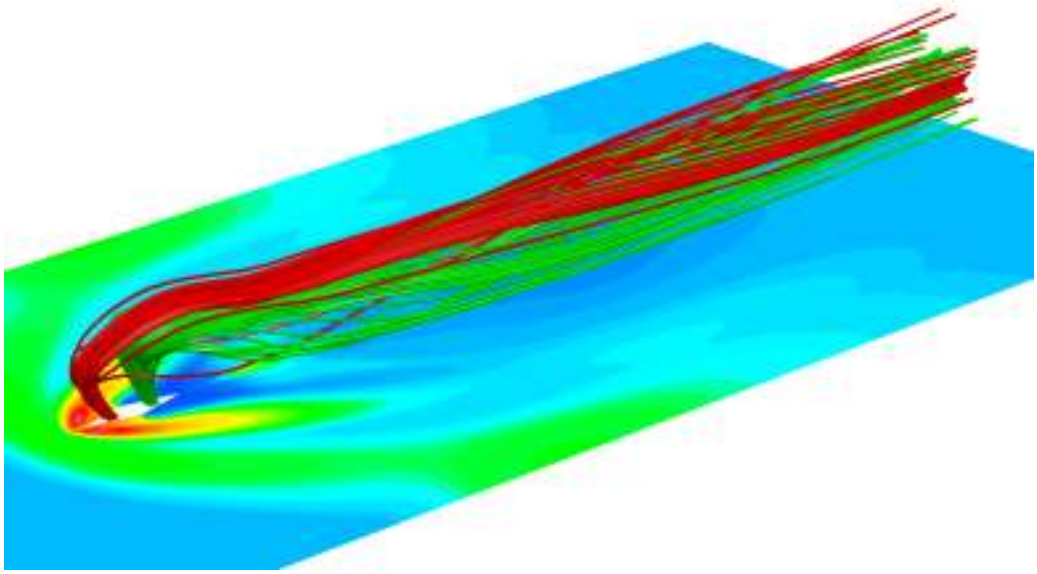

Fig. 130 Injector streamlines, Region 4 and 5, 135-degree J_1.

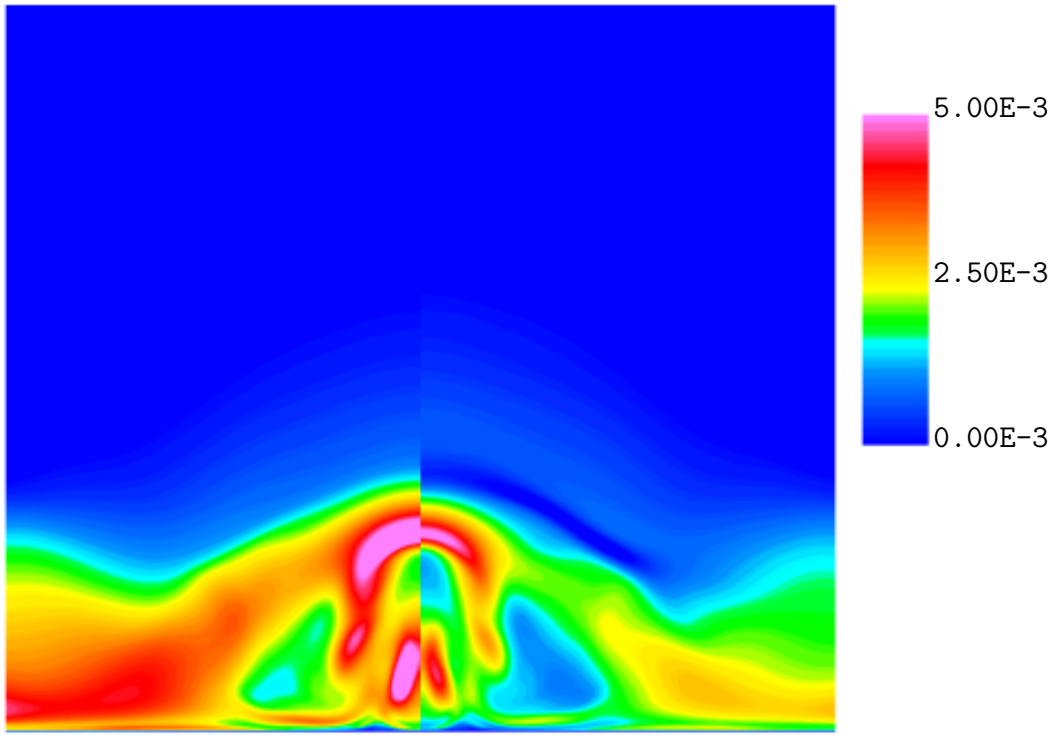

Fig. 131 Contour plot of TKE and τ_{11} at $x/d_{eff} = +8.0$, 90-degree J_1. The contours on the left are that of TKE while those on the right are τ_{11}

.

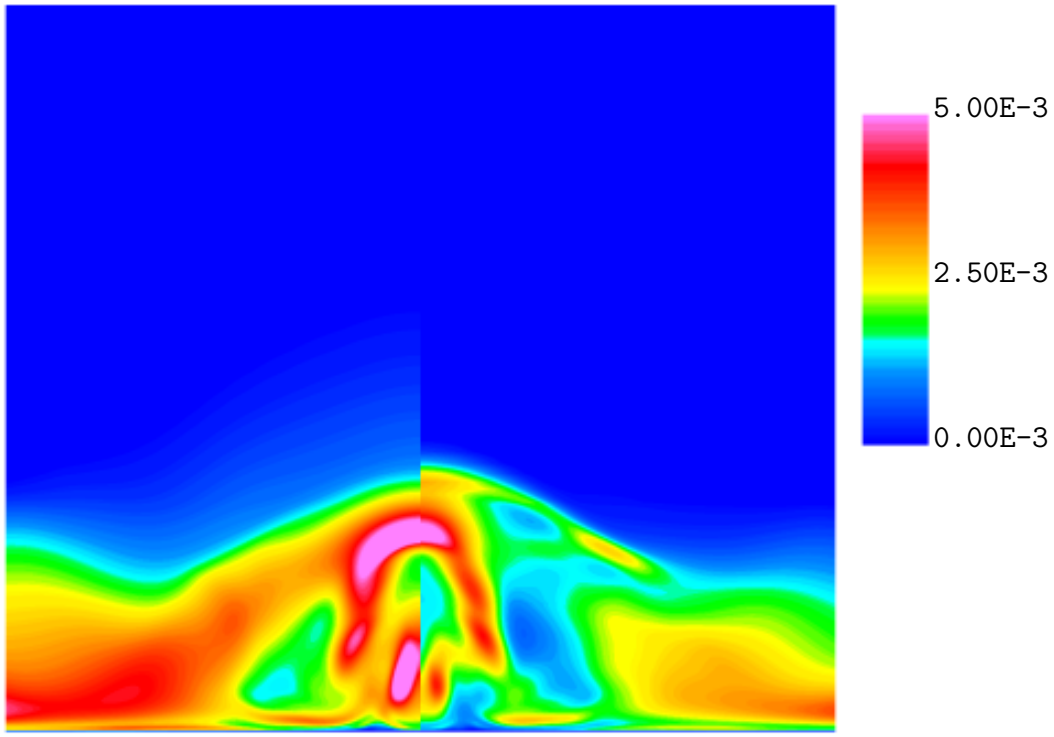

Fig. 132 Contour plot of TKE and τ_{22} at $x/d_{eff} = +8.0$, 90-degree J_1. The contours on the left are that of TKE while those on the right are τ_{22}

.

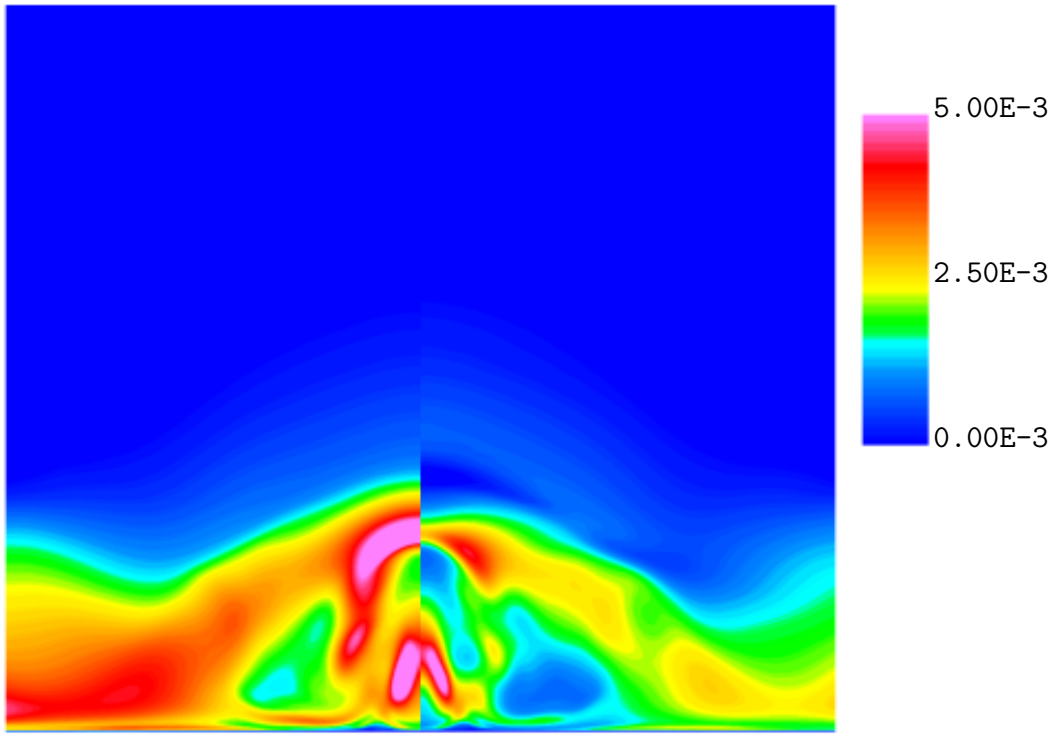

Fig. 133 Contour plot of TKE and τ_{33} at $x/d_{eff} = +8.0$, 90-degree J_1. The contours on the left are that of TKE while those on the right are τ_{33}

.

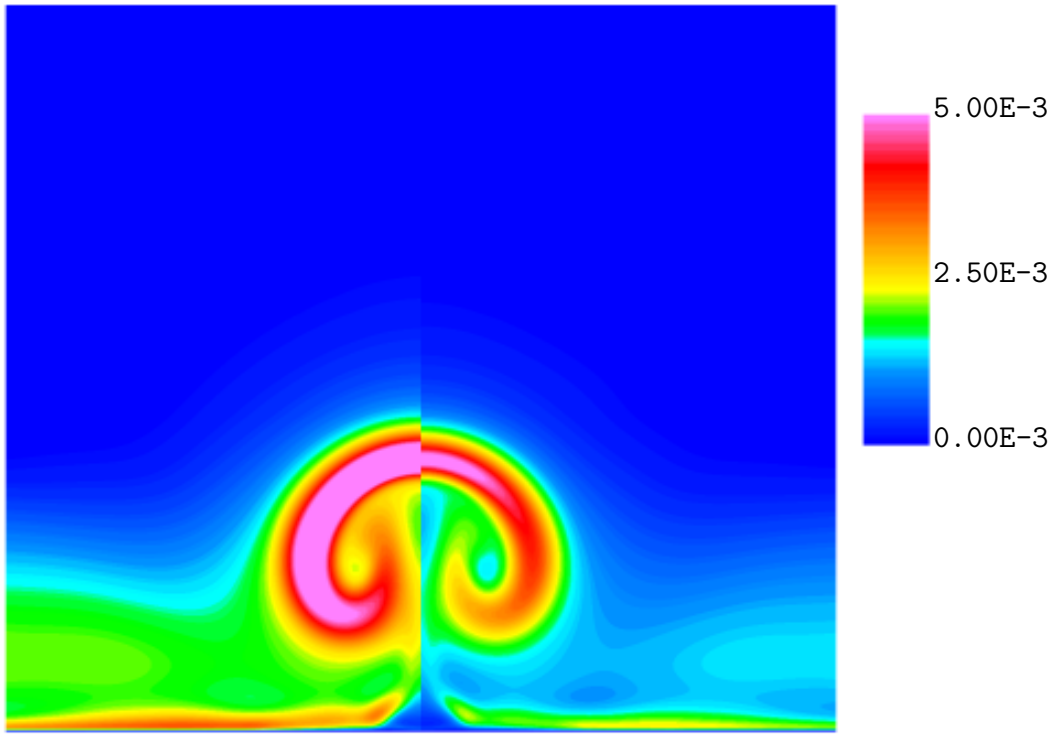

Fig. 134 Contour plot of TKE and τ_{11} at $x/d_{eff} = +23.0$, 90-degree J_1. The contours on the left are that of TKE while those on the right are τ_{11}

.

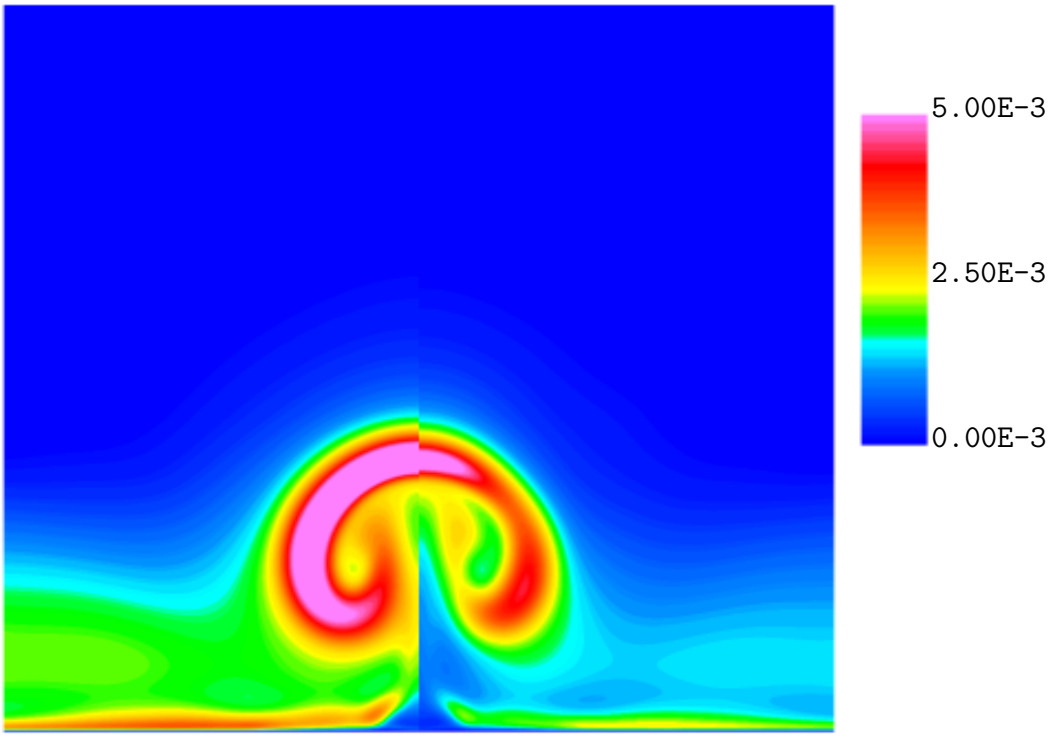

Fig. 135 Contour plot of TKE and τ_{22} at $x/d_{eff} = +23.0$, 90-degree J_1. The contours on the left are that of TKE while those on the right are τ_{22}

.

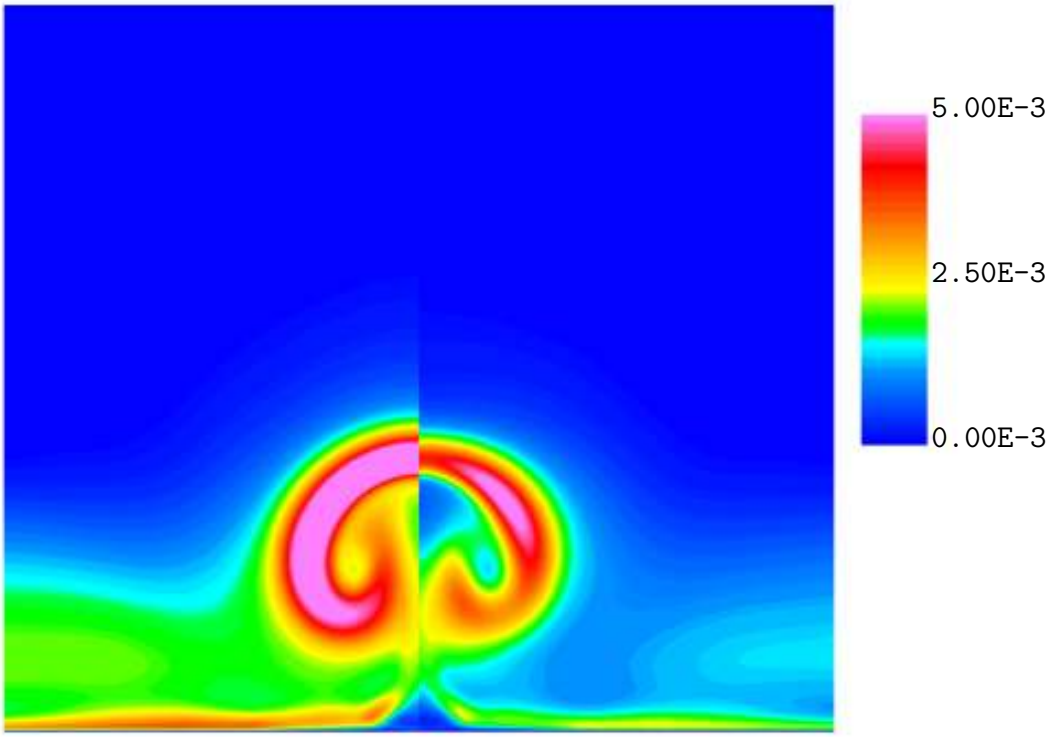

Fig. 136 Contour plot of TKE and τ_{33} at $x/d_{eff} = +23.0$, 90-degree J_1. The contours on the left are that of TKE while those on the right are τ_{33}

.

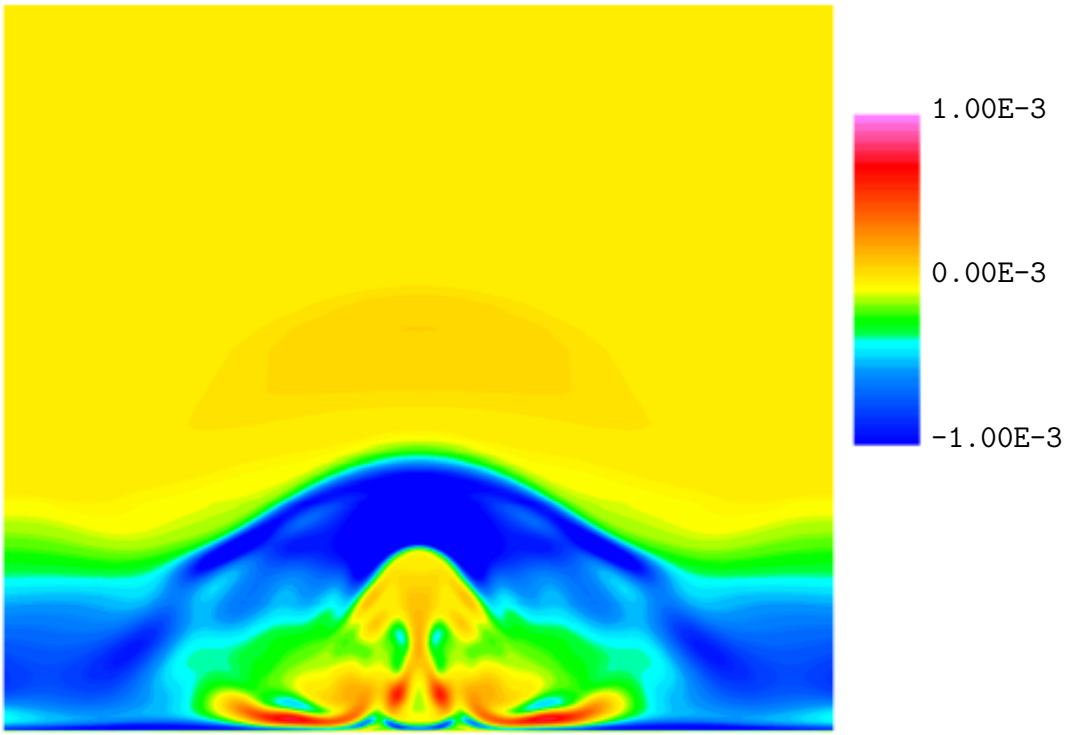

Fig. 137 Contour plot of τ_{12} at $x/d_{eff} = +8.0$, 90-degree J$_1$.

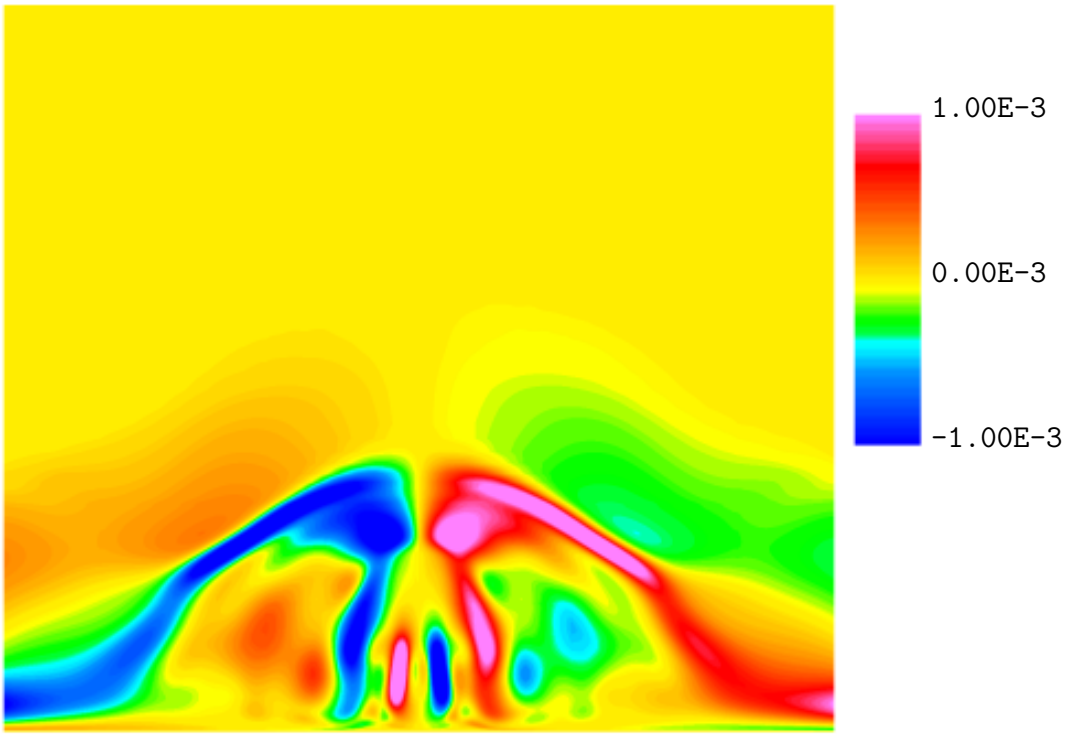

Fig. 138 Contour plot of τ_{23} at $x/d_{eff} = +8.0$, 90-degree J_1.

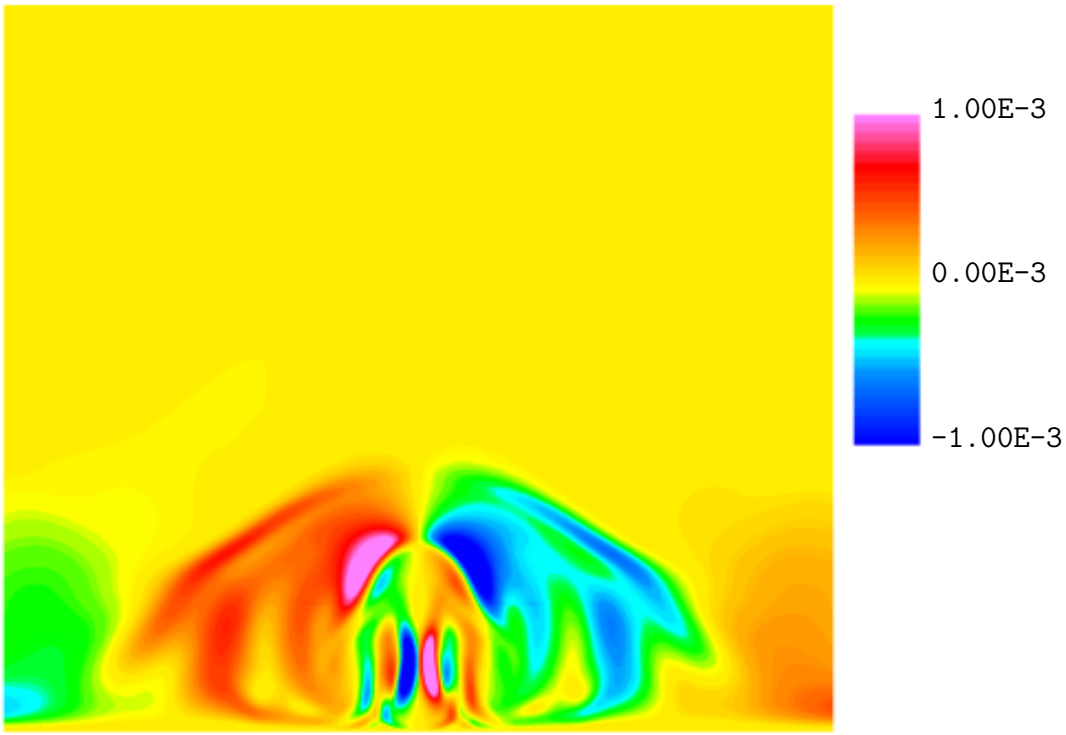

Fig. 139 Contour plot of τ_{31} at $x/d_{eff} = +8.0$, 90-degree J$_1$.

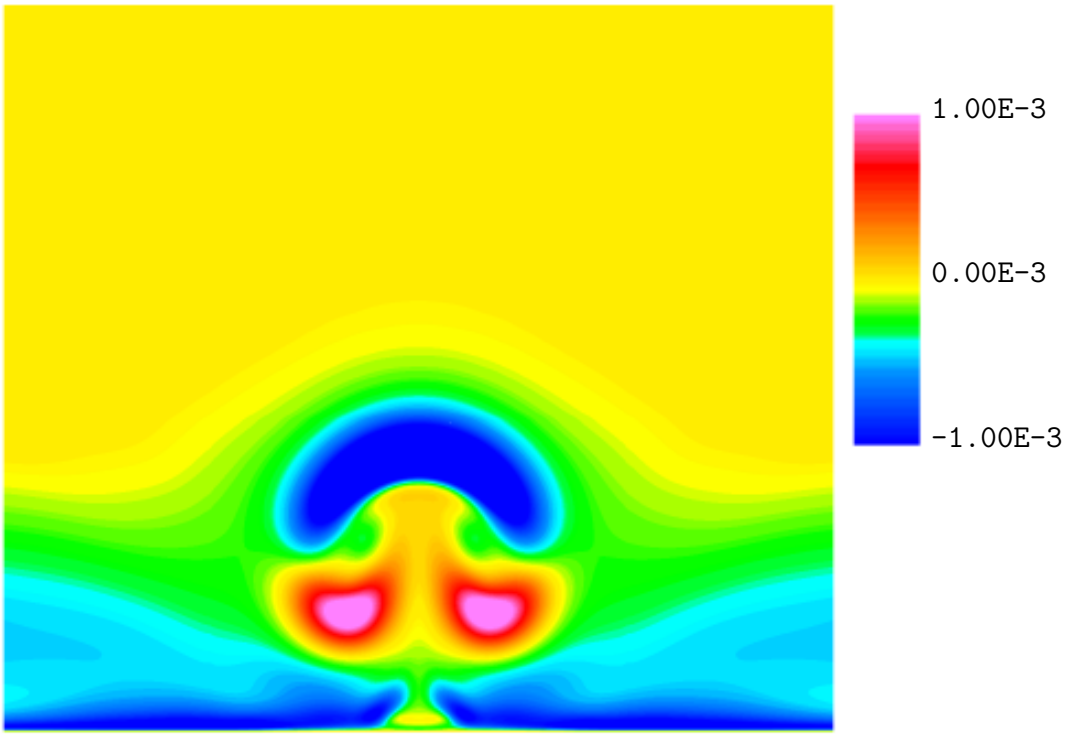

Fig. 140 Contour plot of τ_{12} at $x/d_{eff} = +23.0$, 90-degree J_1.

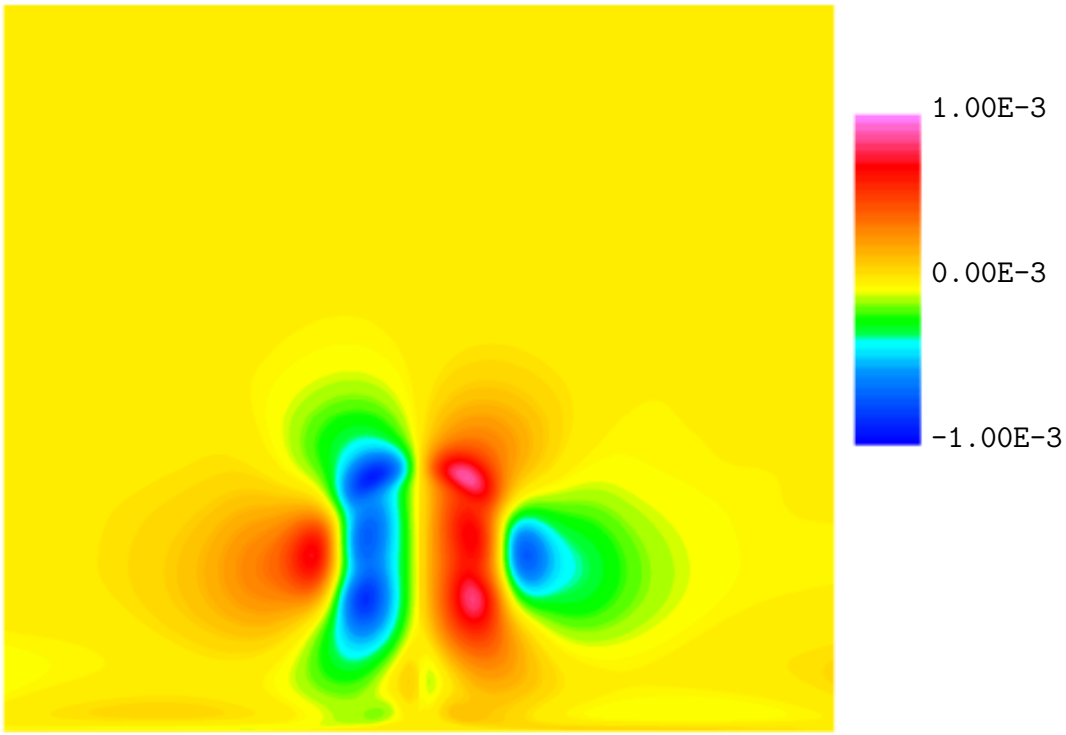

Fig. 141 Contour plot of τ_{23} at $x/d_{eff} = +23.0$, 90-degree J_1.

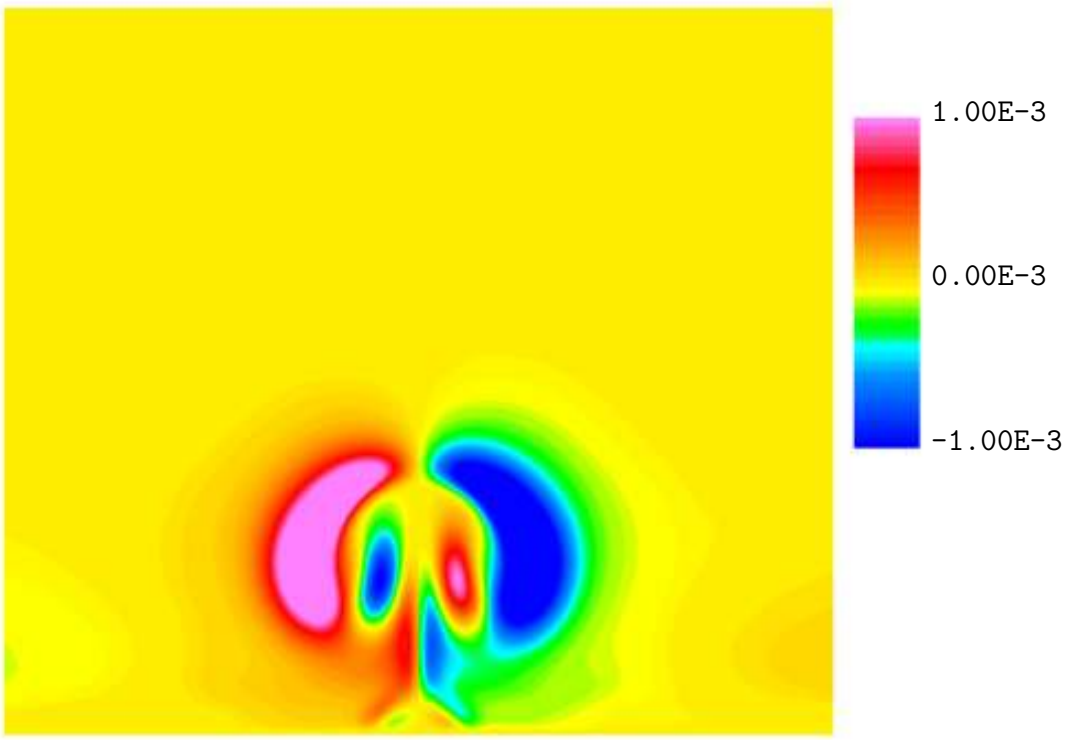

Fig. 142 Contour plot of τ_{31} at $x/d_{eff} = +23.0$, 90-degree J_1.

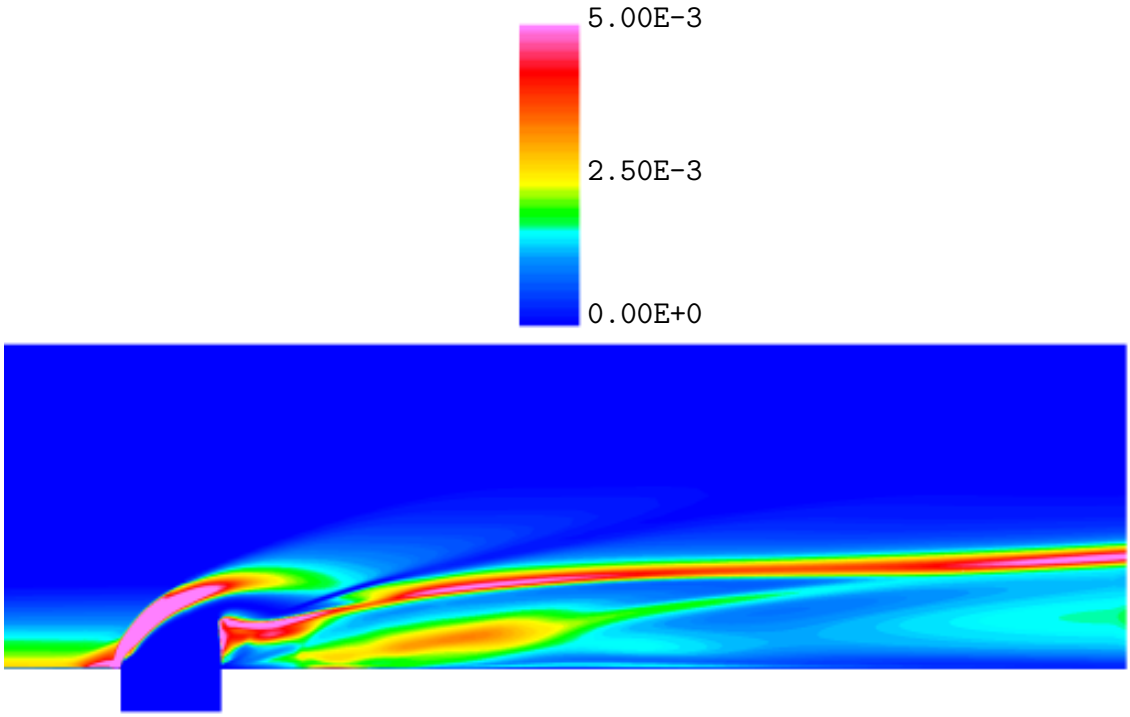

Fig. 143 Contour plot of τ_{11} at $z/d_{eff} = 0.0$, 90-degree J$_1$.

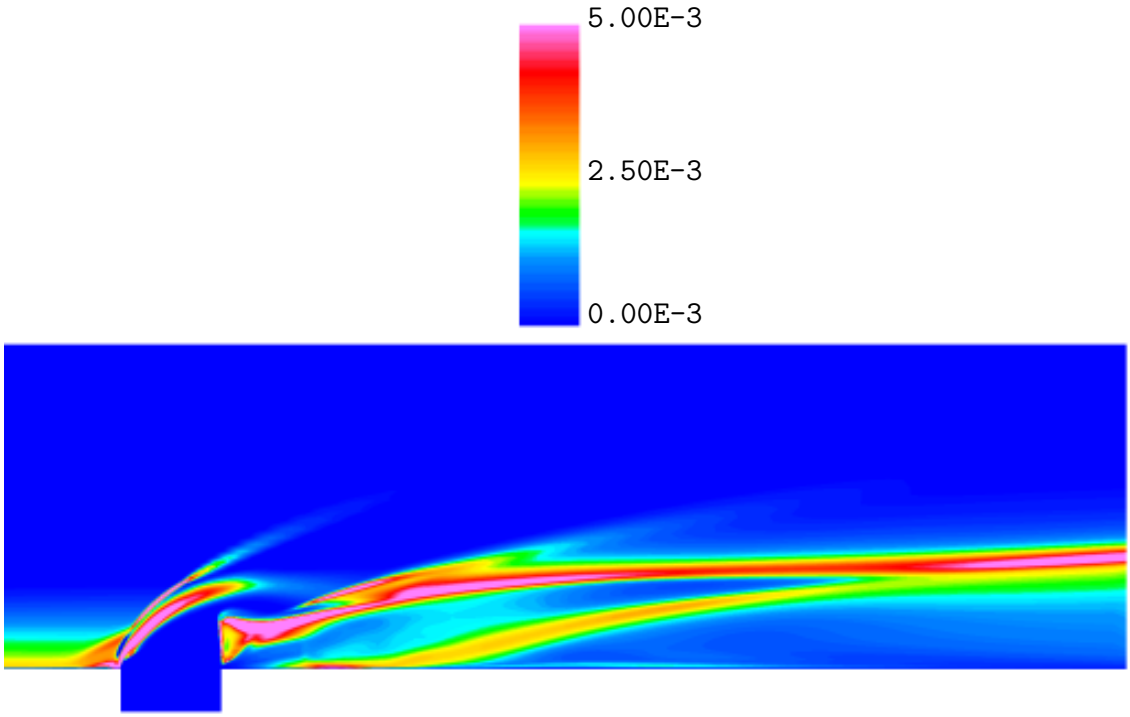

Fig. 144 Contour plot of τ_{22} at $z/d_{eff} = 0.0$, 90-degree J_1.

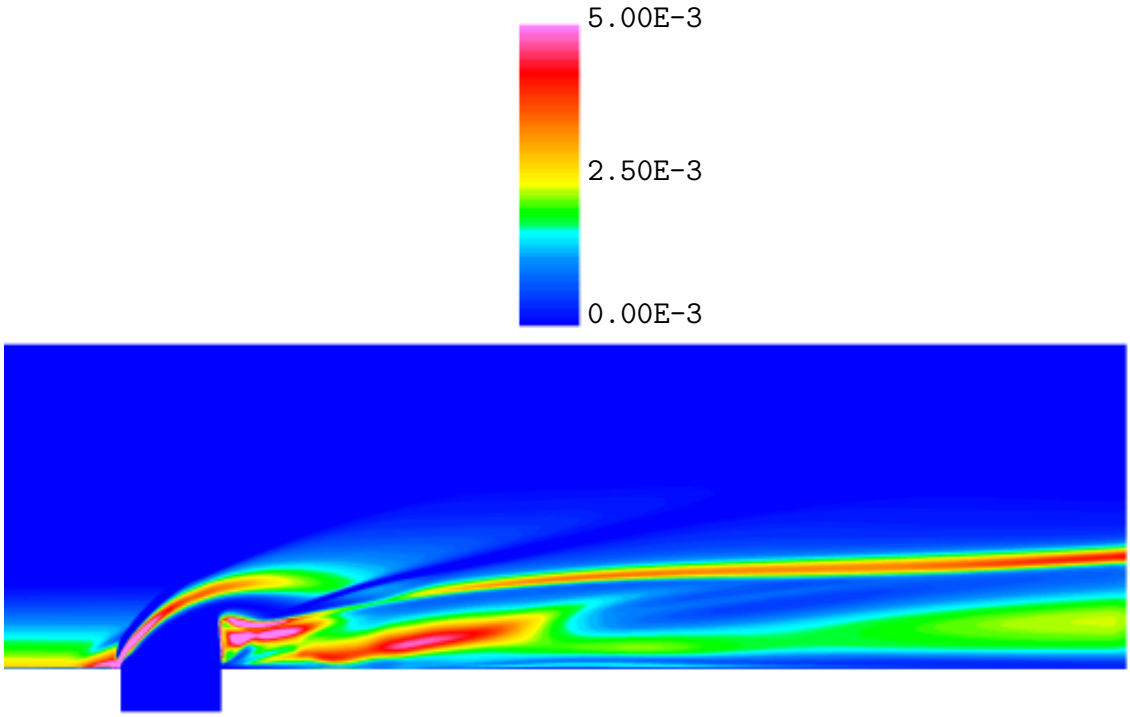

Fig. 145 Contour plot of τ_{33} at $z/d_{eff} = 0.0$, 90-degree J$_1$.

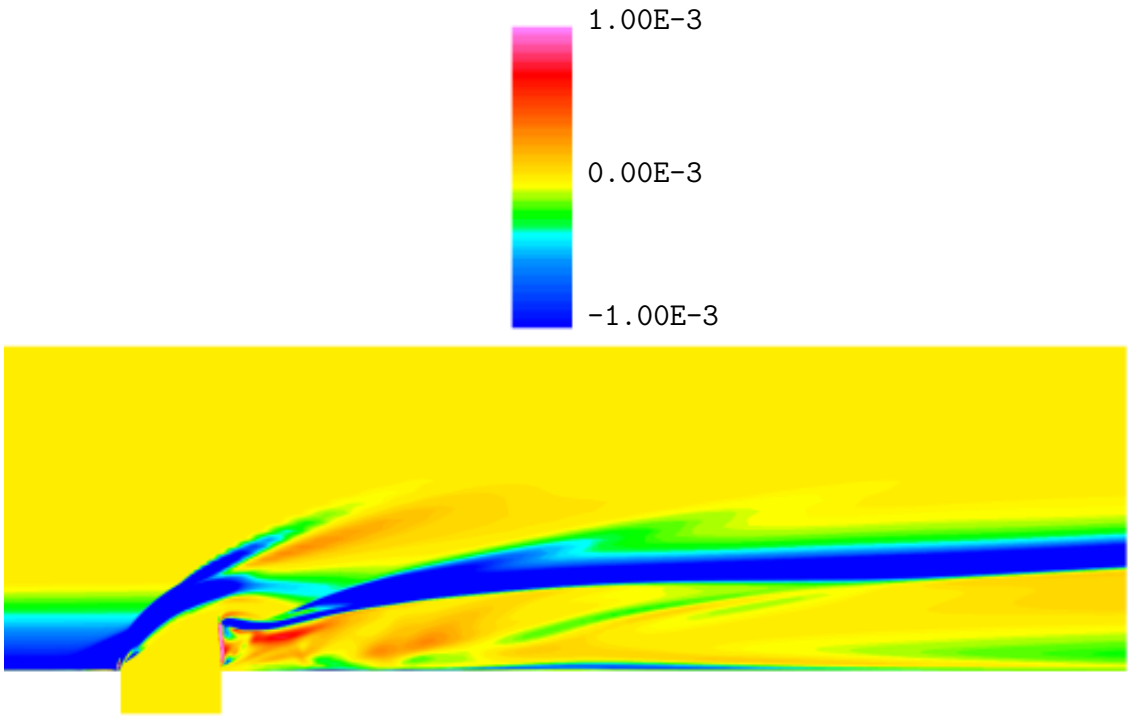

Fig. 146 Contour plot of τ_{12} at $z/d_{eff} = 0.0$, 90-degree J$_1$.

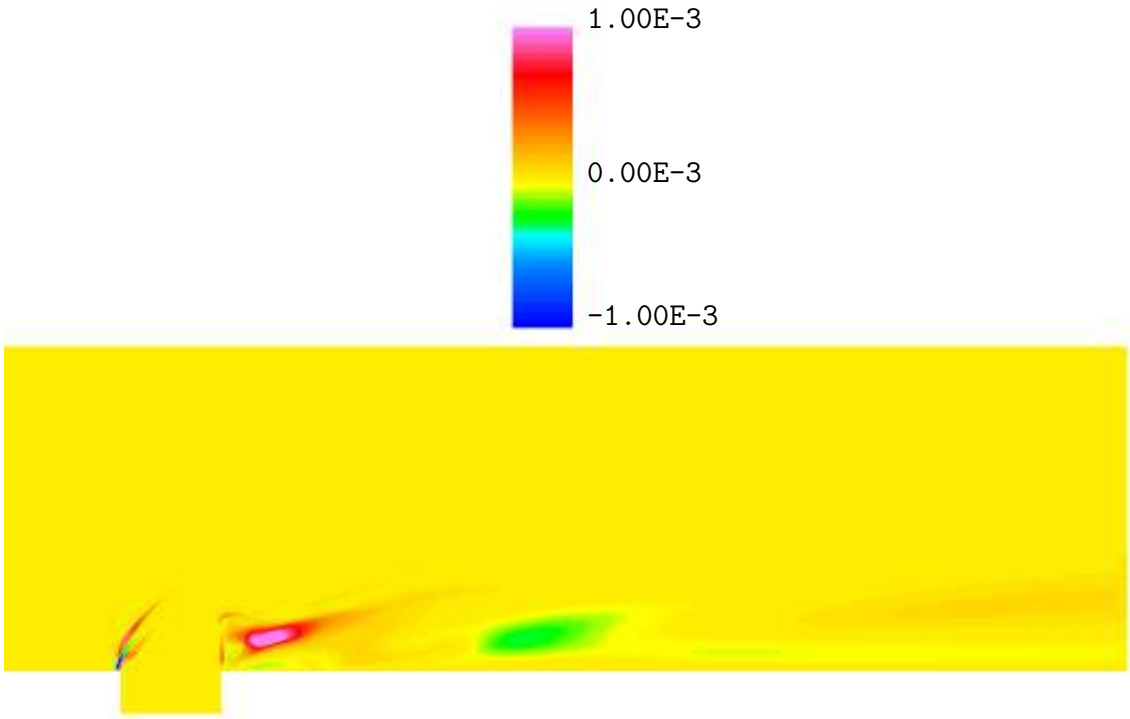

Fig. 147 Contour plot of τ_{23} at $z/d_{eff} = 0.0$, 90-degree J$_1$.

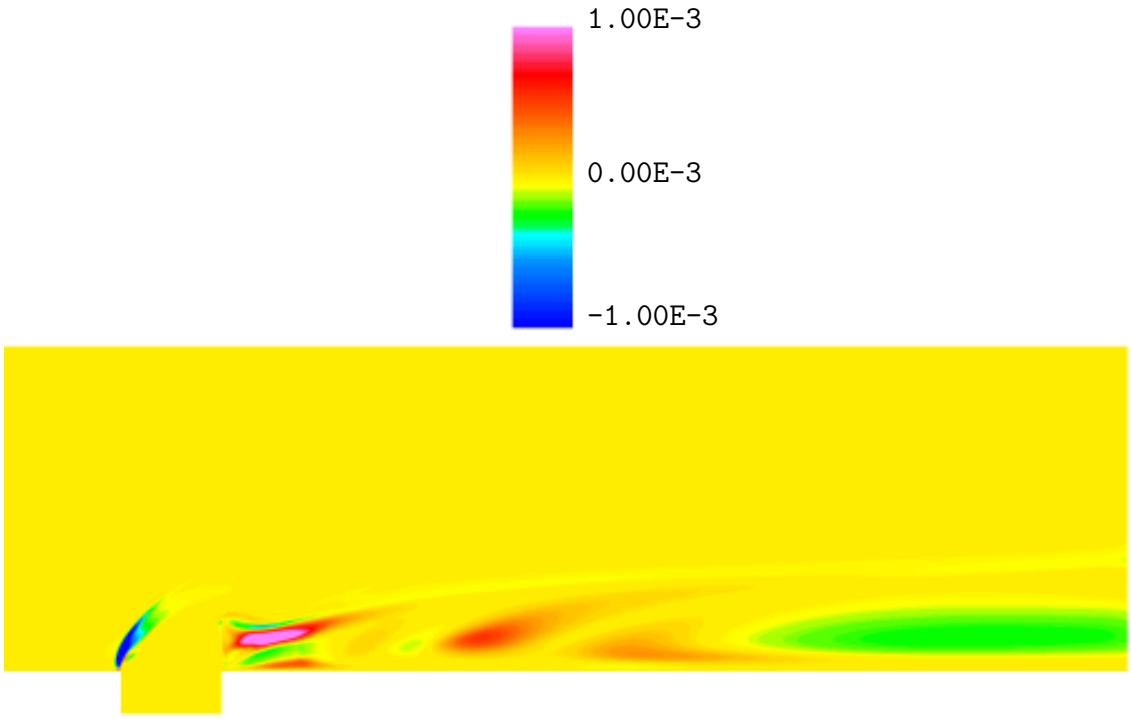

Fig. 148 Contour plot of τ_{31} at $z/d_{eff} = 0.0$, 90-degree J$_1$.

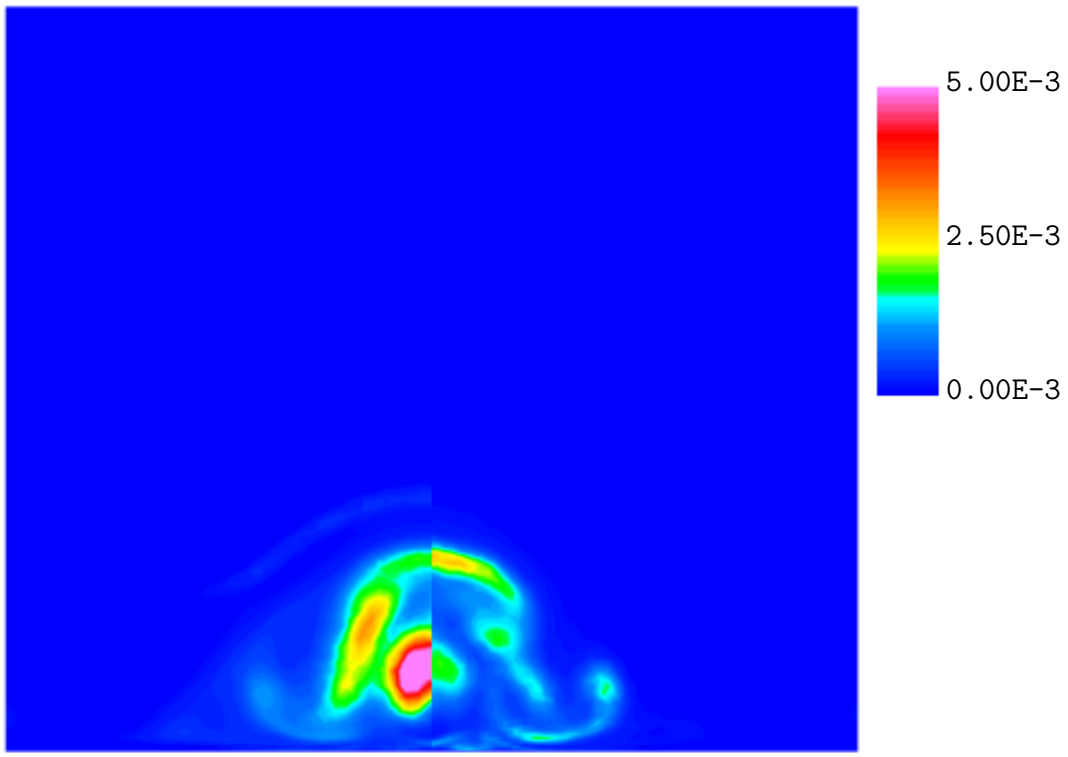

Fig. 149 Contour plot of TKE and τ_{11} at $x/d_{eff} = +8.0$, 90-degree J_1 — DES. The contours on the left are that of TKE while those on the right are τ_{11}

.

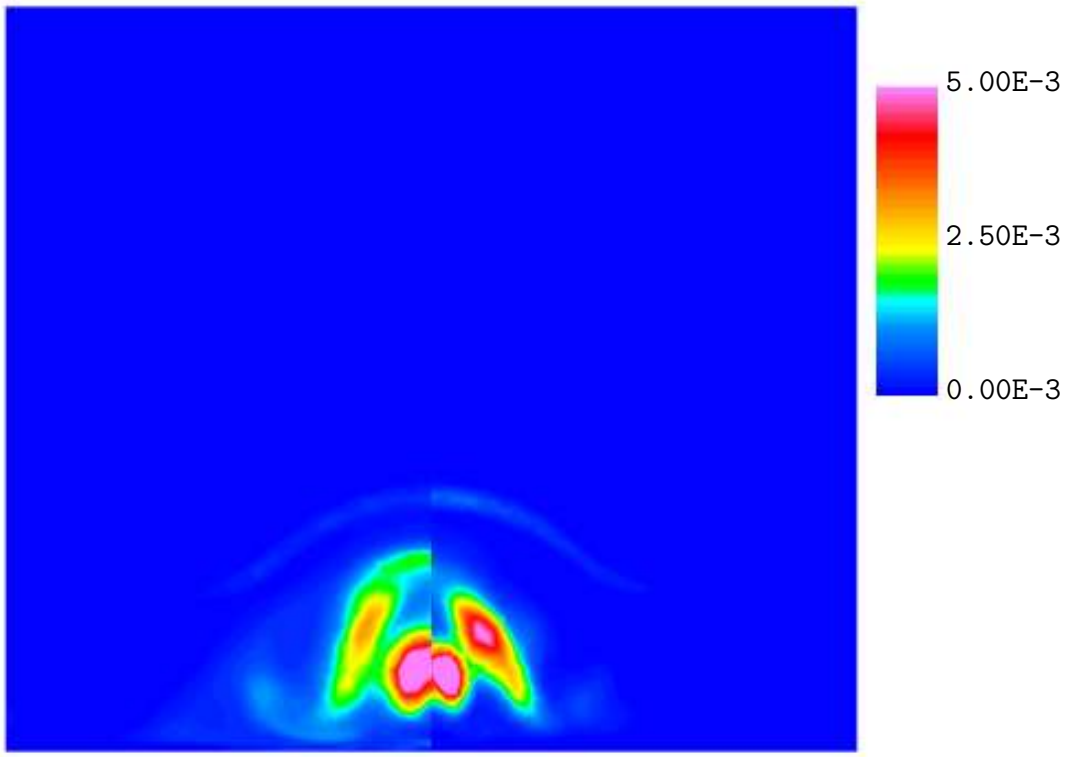

Fig. 150 Contour plot of TKE and τ_{22} at $x/d_{eff} = +8.0$, 90-degree J_1 — DES. The contours on the left are that of TKE while those on the right are τ_{22}

.

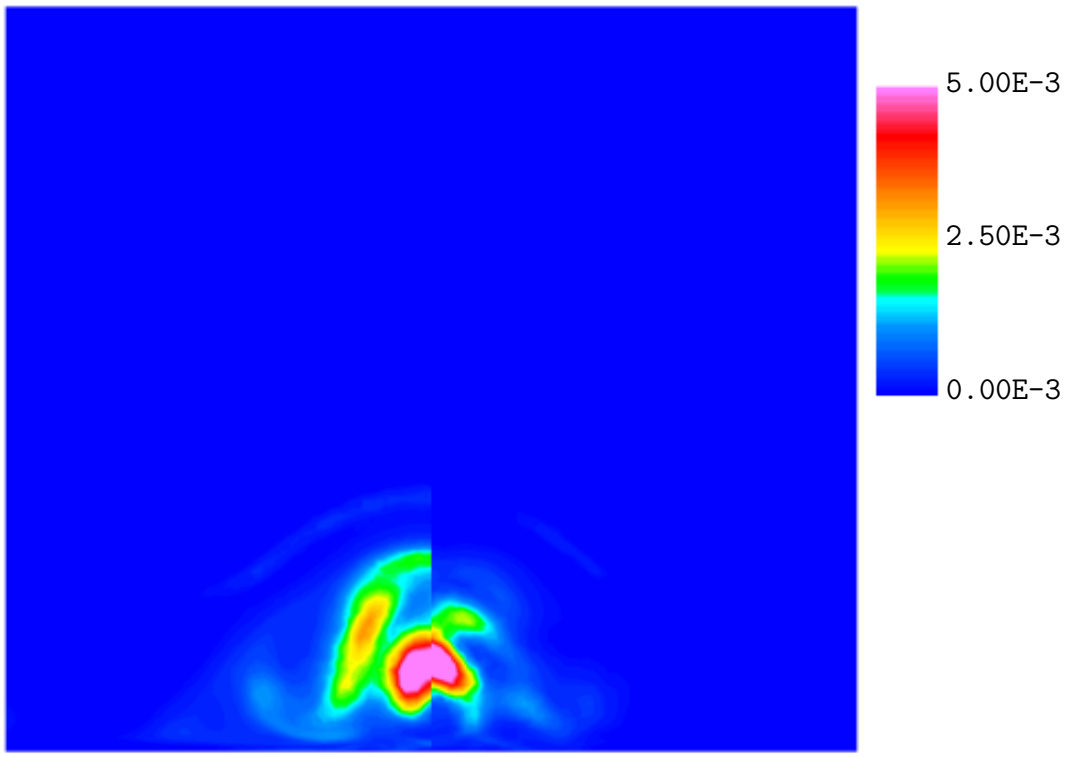

Fig. 151 Contour plot of TKE and τ_{33} at $x/d_{eff} = +8.0$, 90-degree J_1 — DES. The contours on the left are that of TKE while those on the right are τ_{33}

.

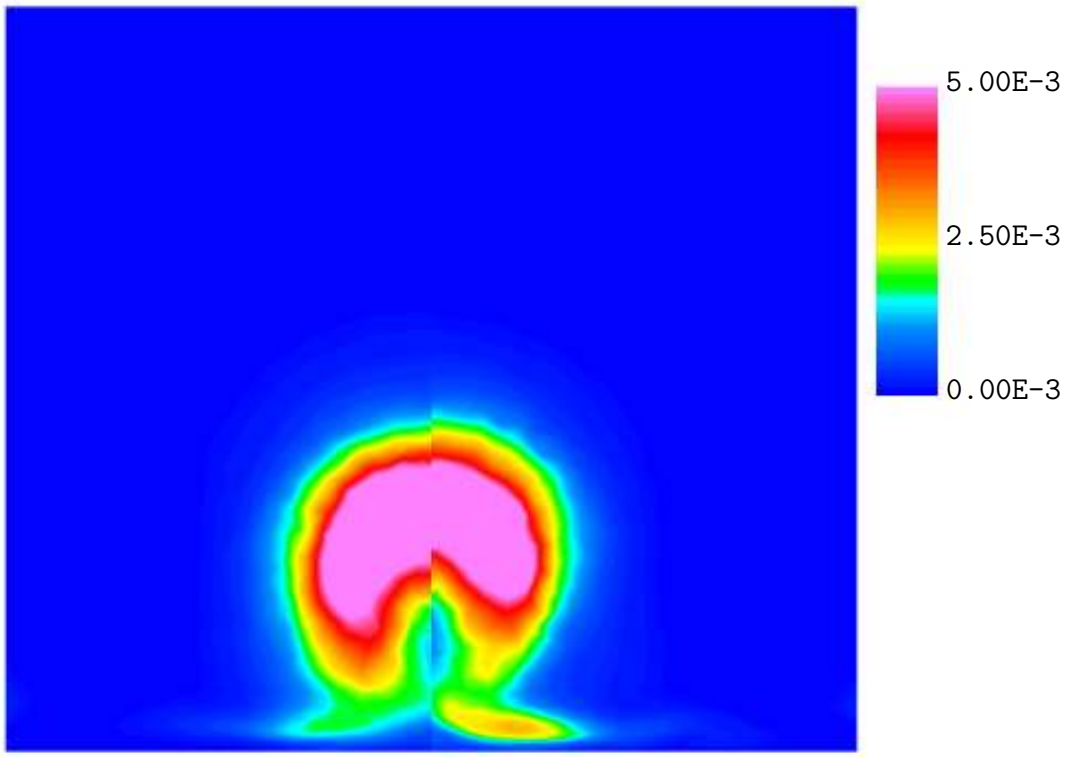

Fig. 152 Contour plot of TKE and τ_{11} at $x/d_{eff} = +23.0$, 90-degree J_1 — DES. The contours on the left are that of TKE while those on the right are τ_{11}

.

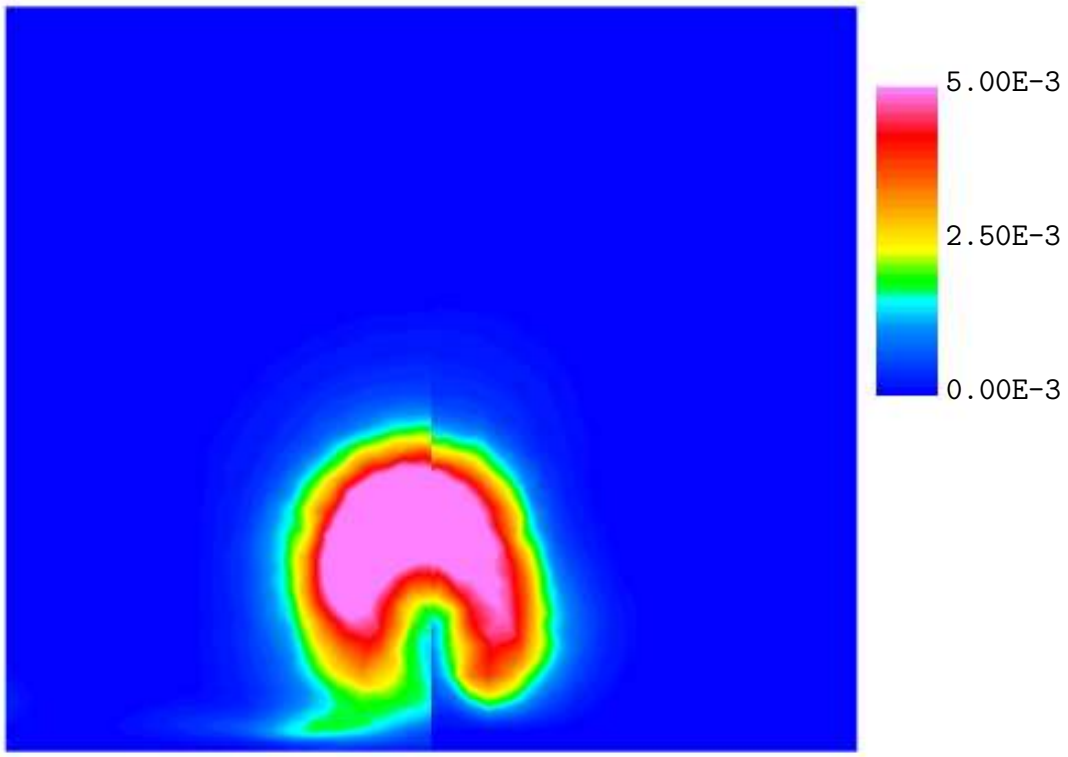

Fig. 153 Contour plot of TKE and τ_{22} at $x/d_{eff} = +23.0$, 90-degree J_1 — DES. The contours on the left are that of TKE while those on the right are τ_{22}

.

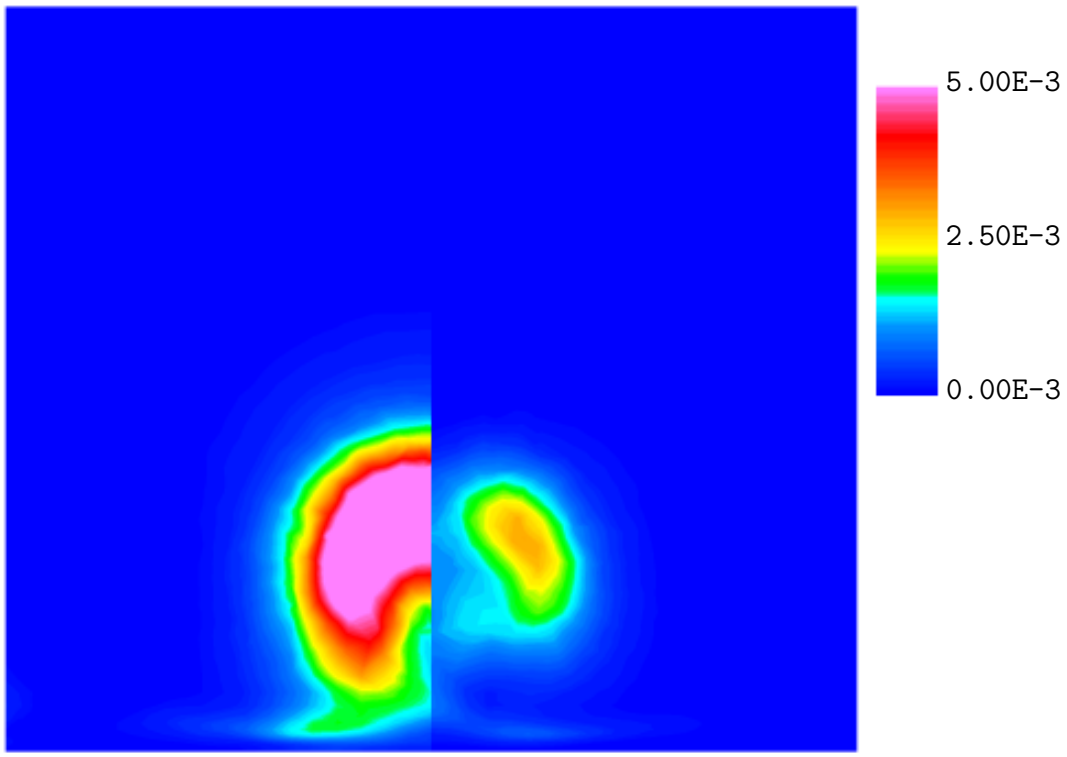

Fig. 154 Contour plot of TKE and τ_{33} at $x/d_{eff} = +23.0$, 90-degree J_1 — DES. The contours on the left are that of TKE while those on the right are τ_{33}

.

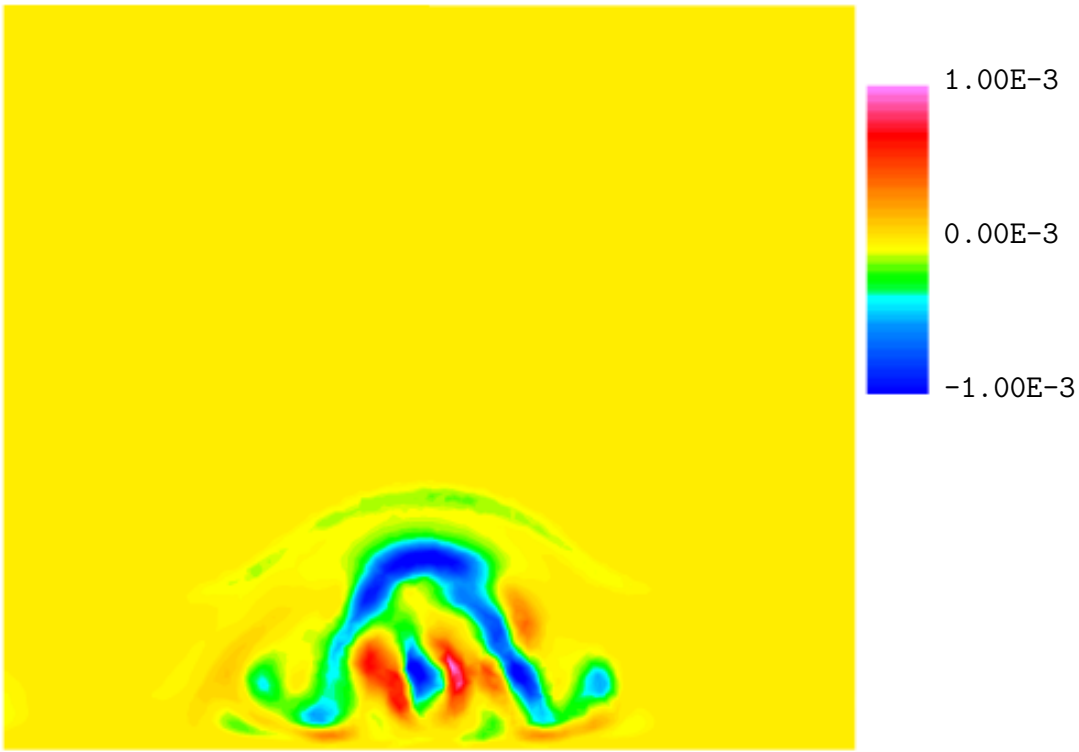

Fig. 155 Contour plot of τ_{12} at $x/d_{eff} = +8.0$, 90-degree J$_1$ — DES.

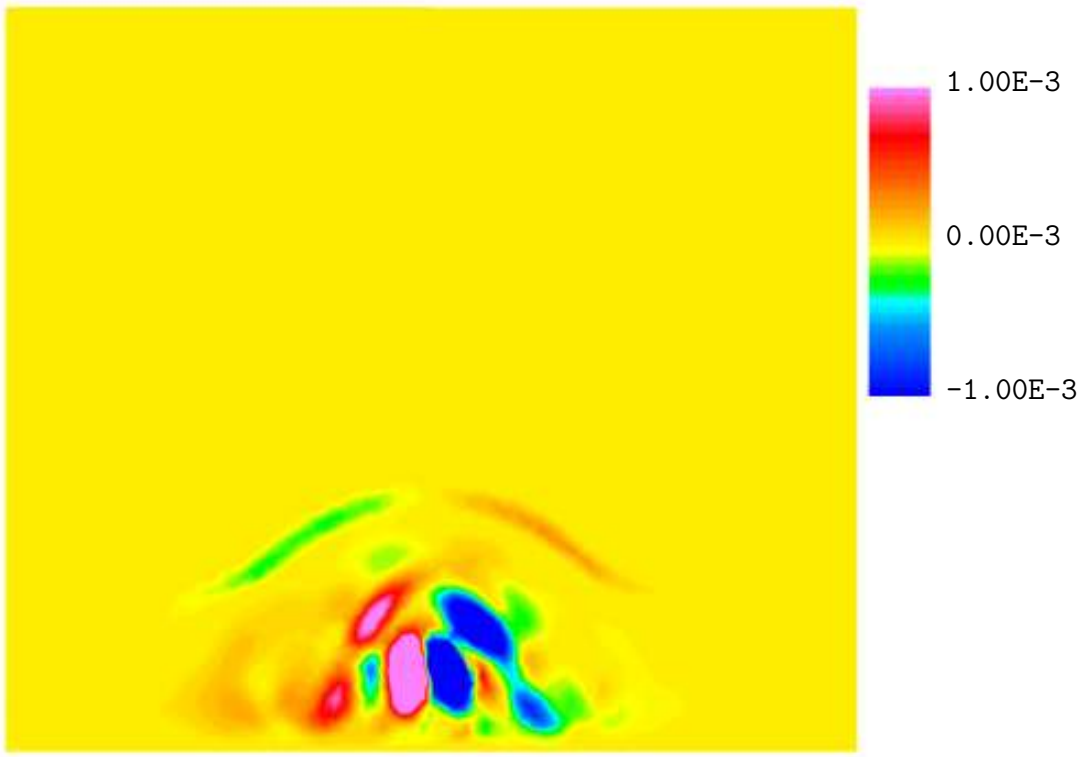

Fig. 156 Contour plot of τ_{23} at $x/d_{eff} = +8.0$, 90-degree J$_1$ — DES.

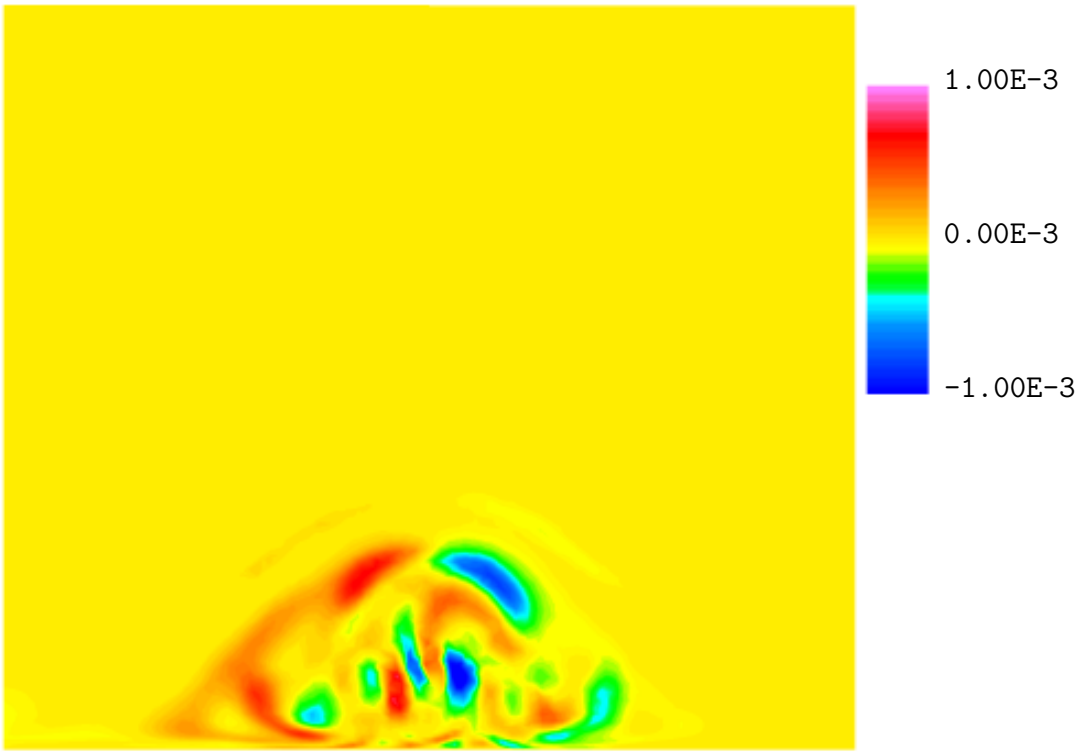

Fig. 157 Contour plot of τ_{31} at $x/d_{eff} = +8.0$, 90-degree J_1 — DES.

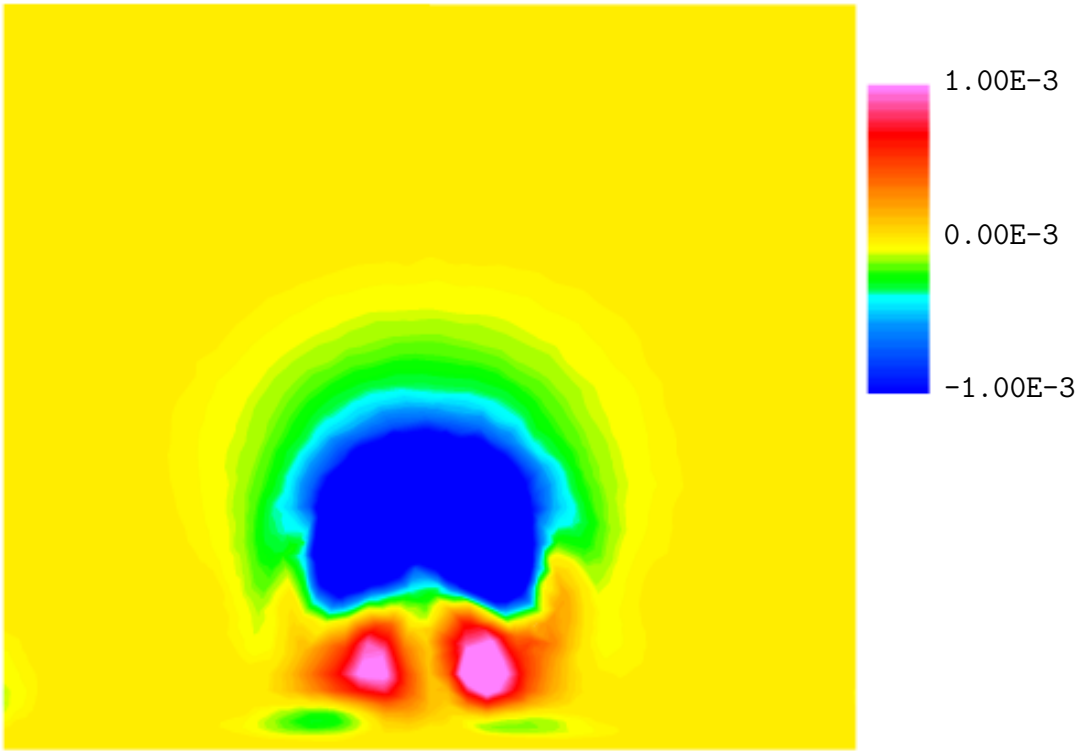

Fig. 158 Contour plot of τ_{12} at $x/d_{eff} = +23.0$, 90-degree J_1 — DES.

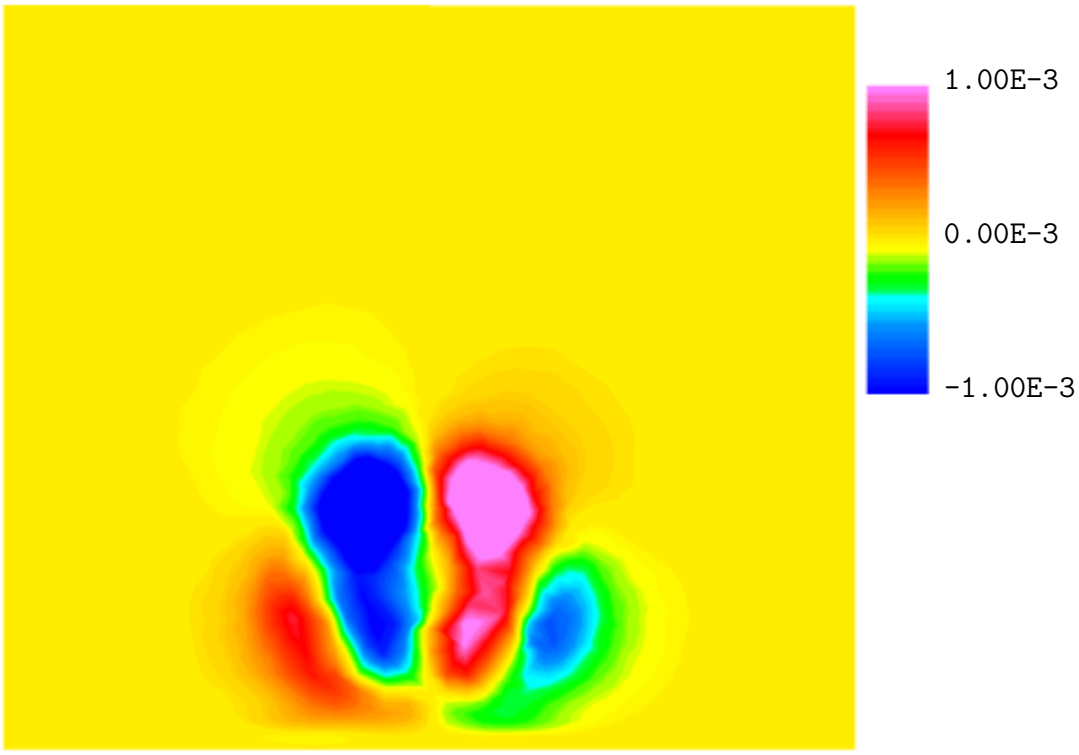

Fig. 159 Contour plot of τ_{23} at $x/d_{eff} = +23.0$, 90-degree J_1 — DES.

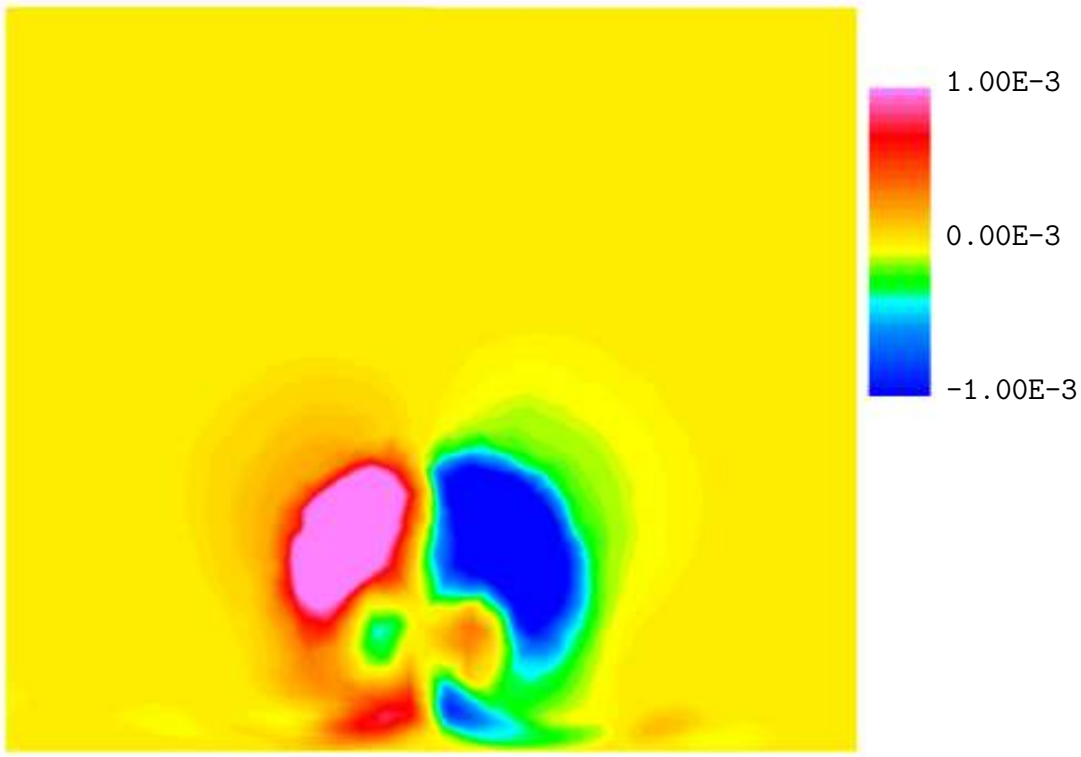

Fig. 160 Contour plot of τ_{31} at $x/d_{eff} = +23.0$, 90-degree J_1 — DES.

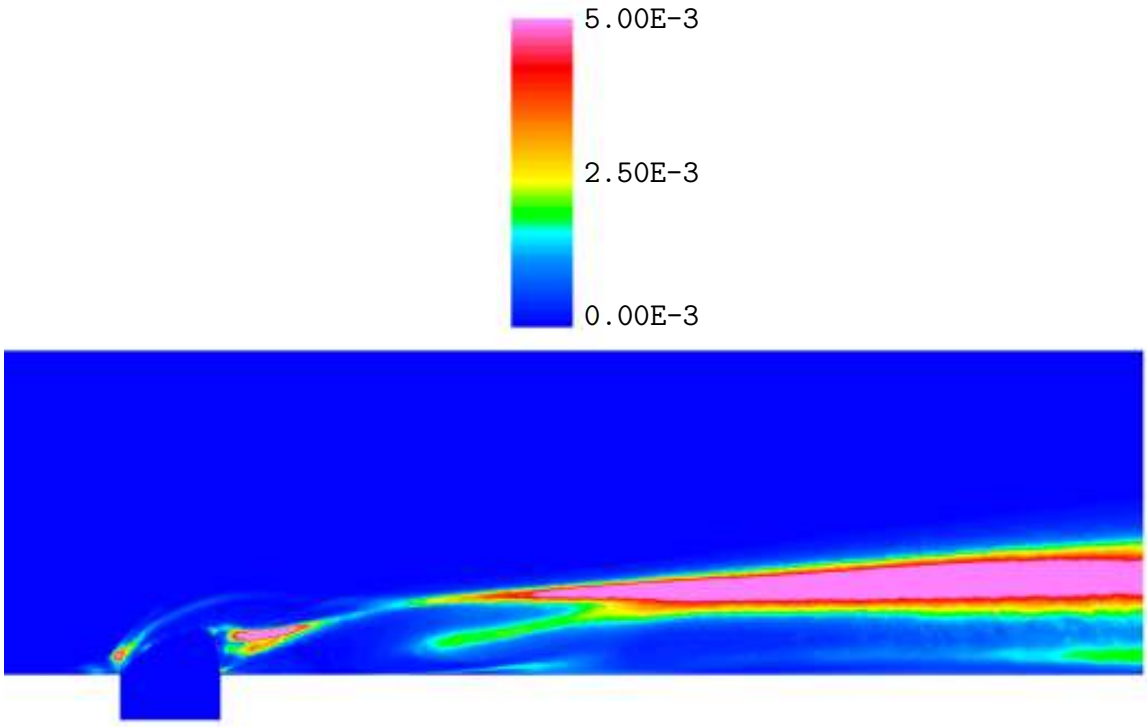

Fig. 161 Contour plot of τ_{11} at $z/d_{eff} = 0.0$, 90-degree J_1 — DES.

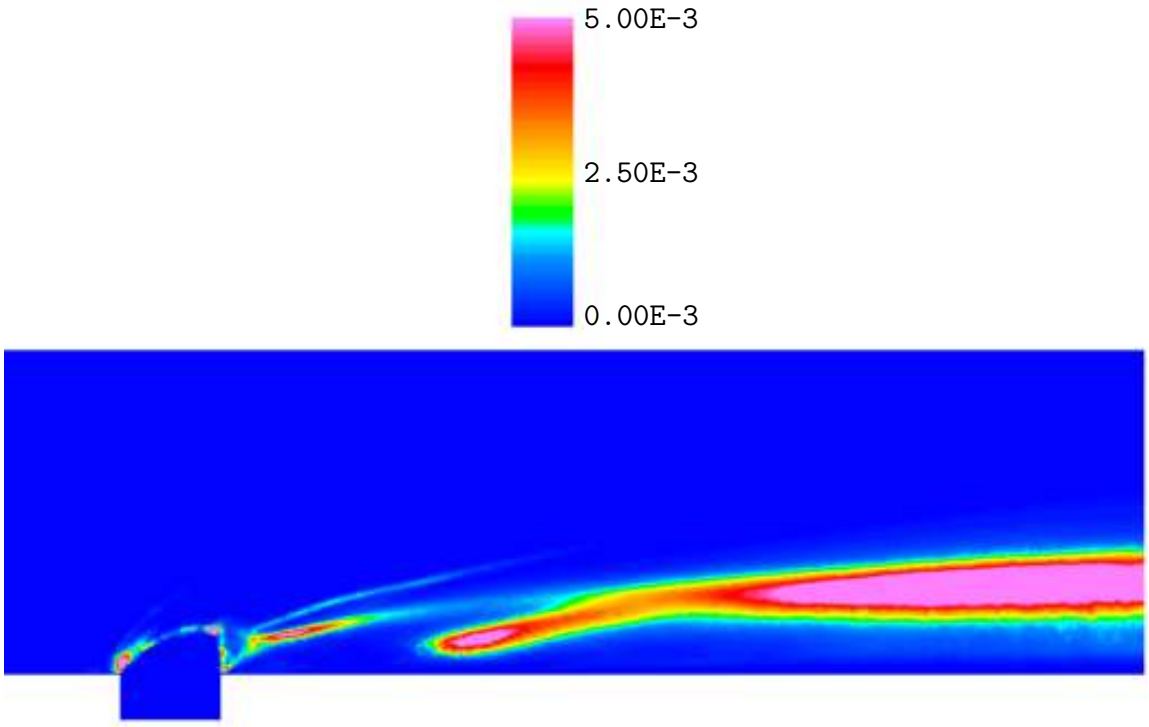

Fig. 162 Contour plot of τ_{22} at $z/d_{eff} = 0.0$, 90-degree J_1 — DES.

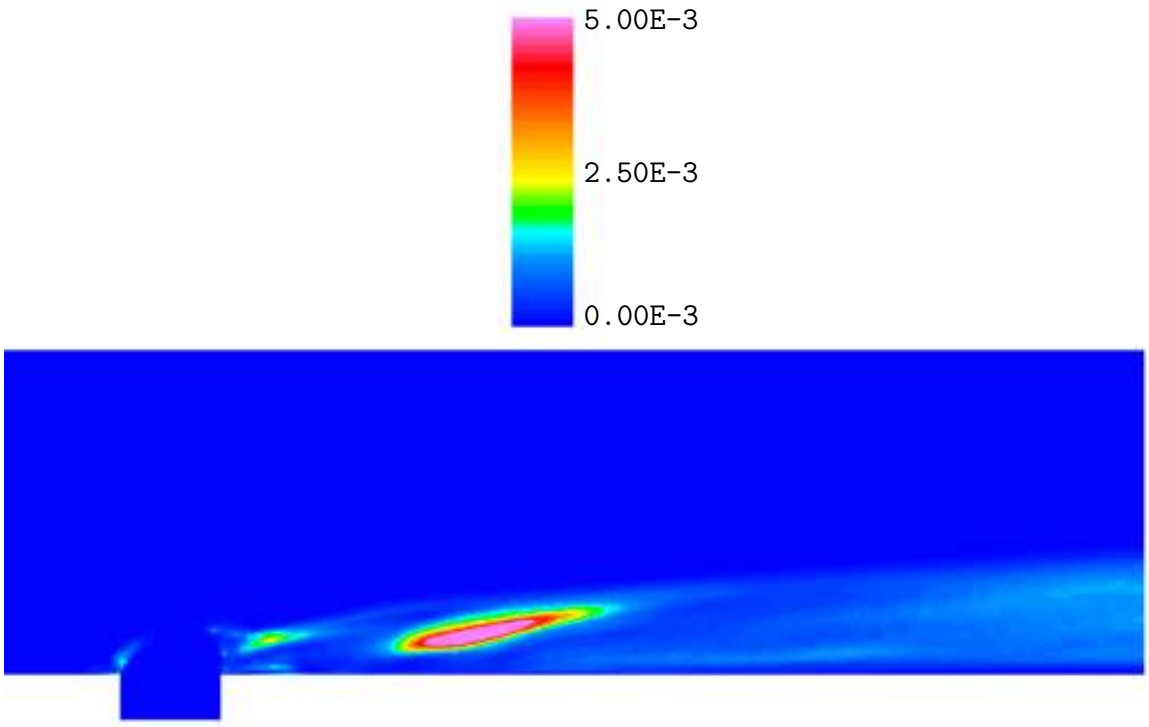

Fig. 163 Contour plot of τ_{33} at $z/d_{eff} = 0.0$, 90-degree J_1 — DES.

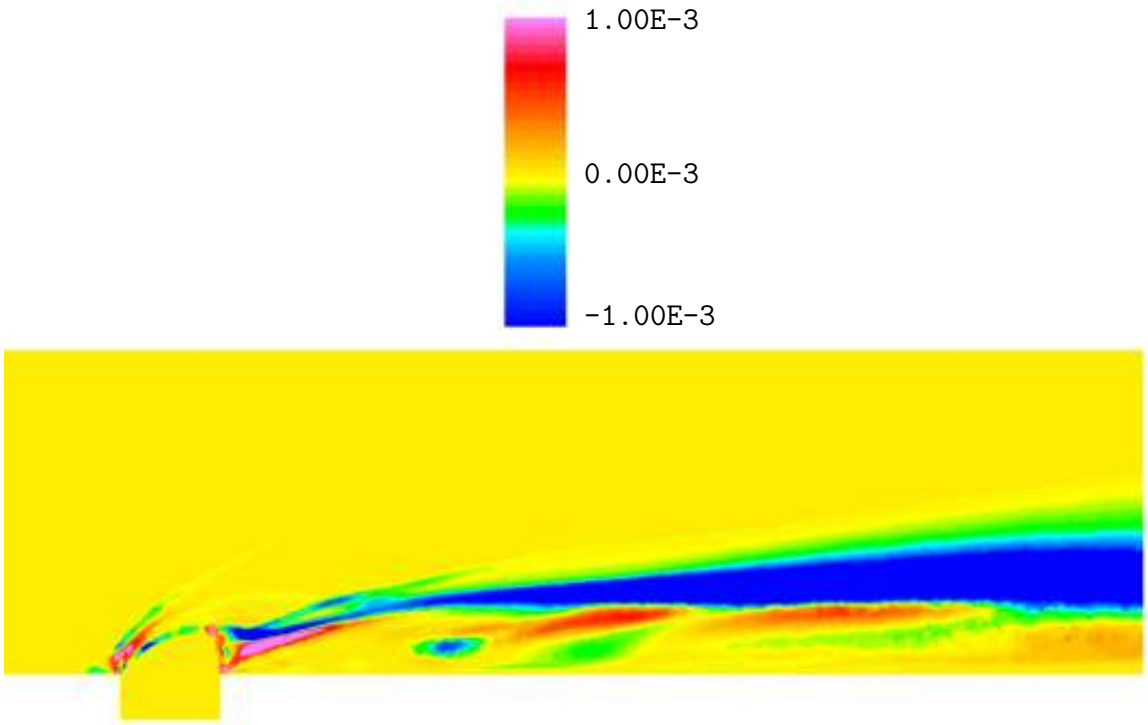

Fig. 164 Contour plot of τ_{12} at $z/d_{eff} = 0.0$, 90-degree J_1 — DES.

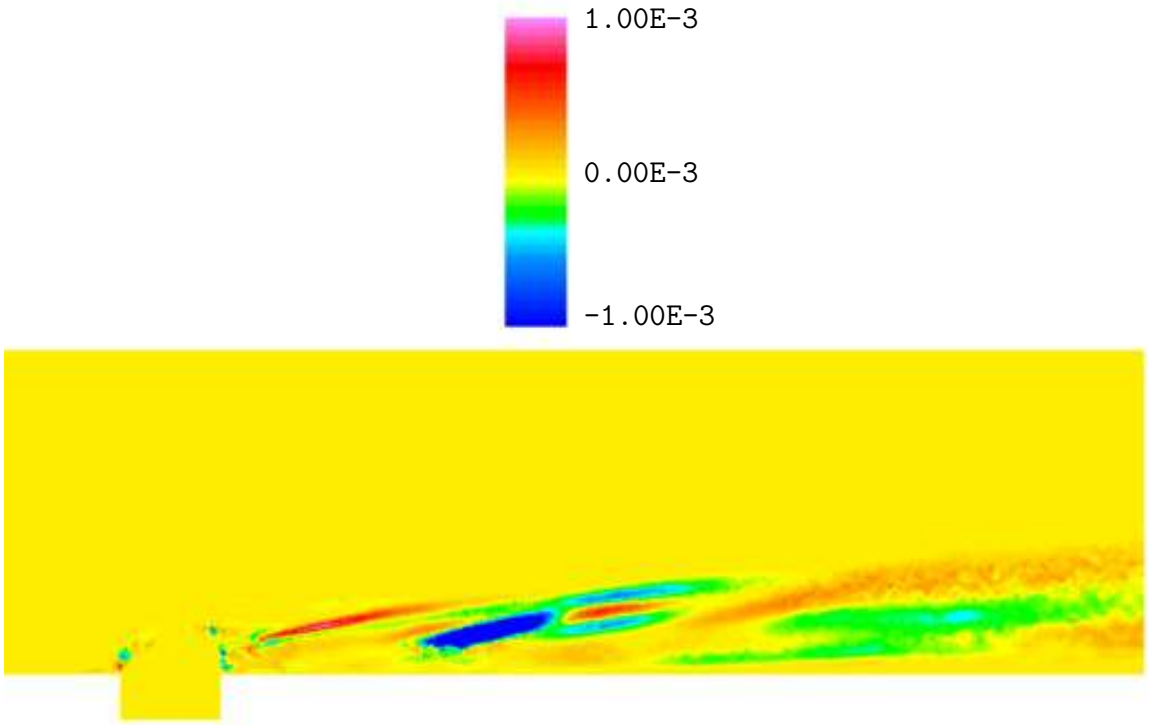

Fig. 165 Contour plot of τ_{23} at $z/d_{eff} = 0.0$, 90-degree J_1 — DES.

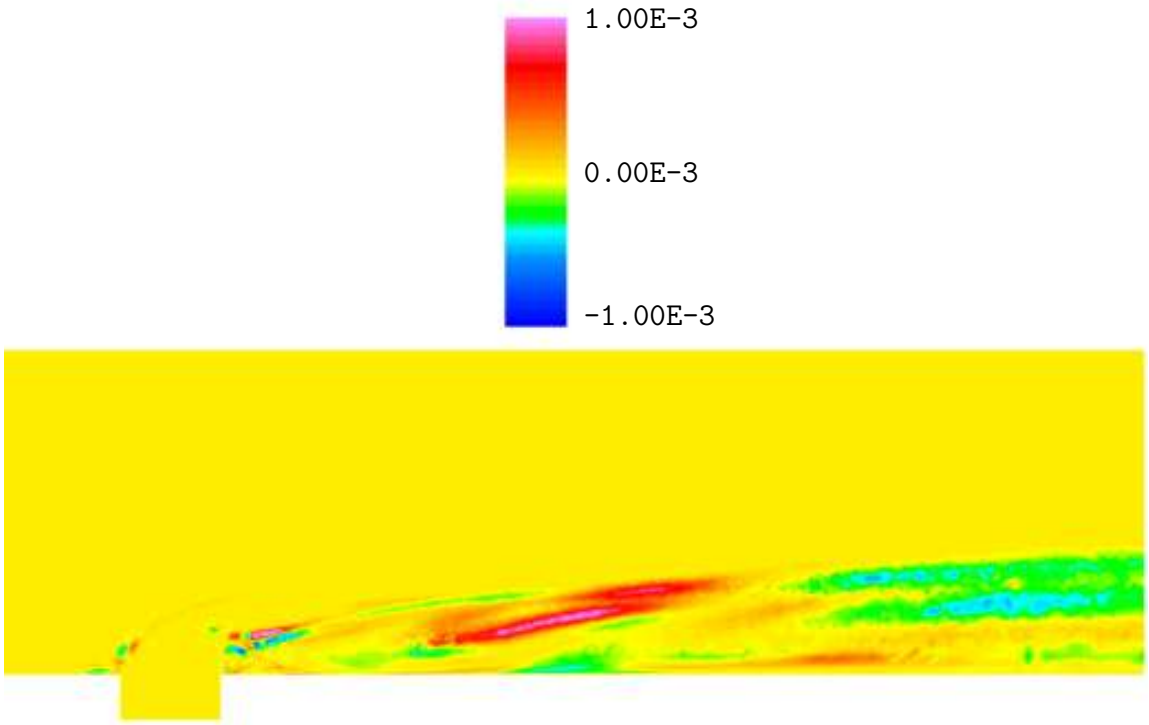

Fig. 166 Contour plot of τ_{31} at $z/d_{eff} = 0.0$, 90-degree J_1 — DES.

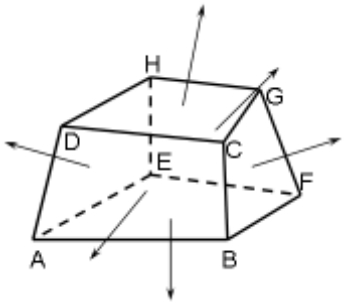

Fig. 167 Reference nodes for area vector calculation.

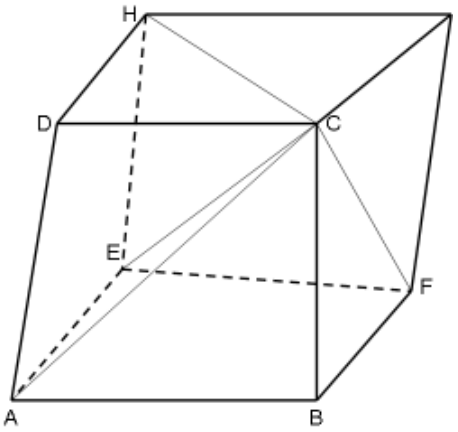

Fig. 168 Decomposition of hexahedron into pyramids.

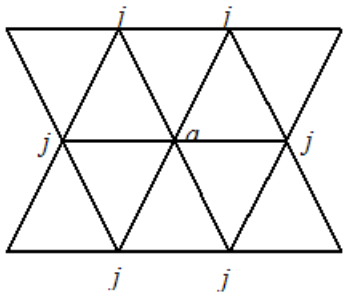

Fig. 169 Current grid point, a, and neighbors j.

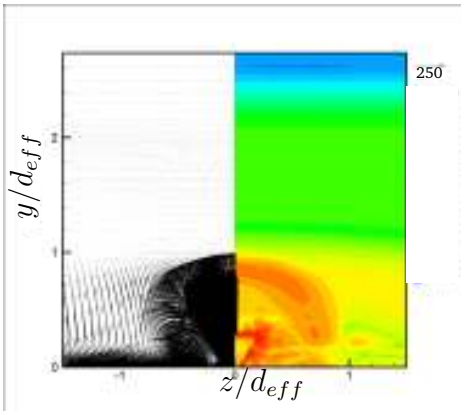

(a) $x/d_{eff} = -1.0$

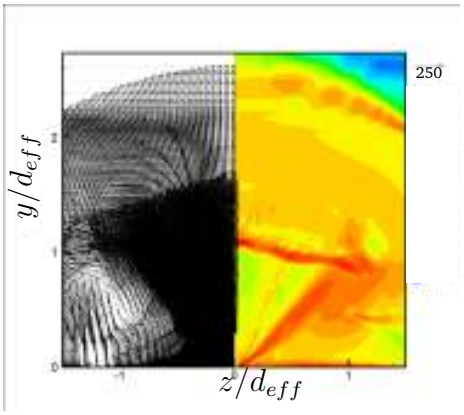

(b) $x/d_{eff} = +1.0$

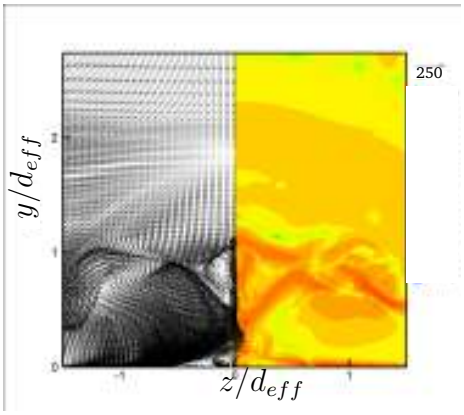

(c) $x/d_{eff} = +2.0$

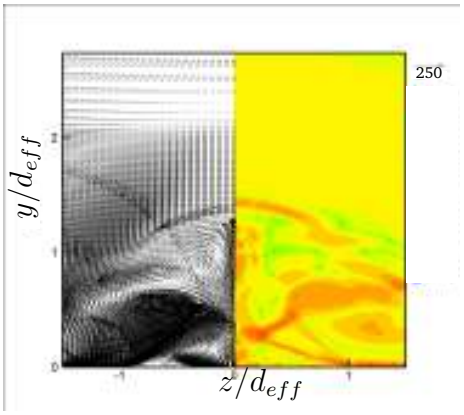

(d) $x/d_{eff} = +3.0$

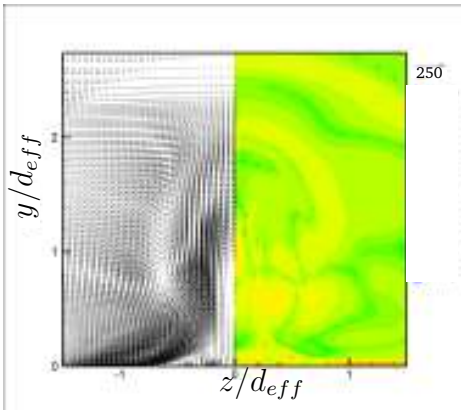

(e) $x/d_{eff} = +8.0$

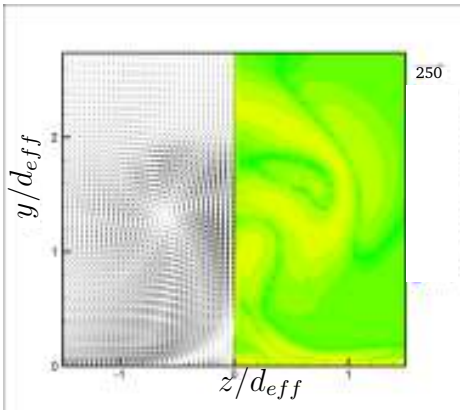

(f) $x/d_{eff} = +15.0$

Fig. 170 Compressibility contours at different axial locations. The values are plotted on a log scale.

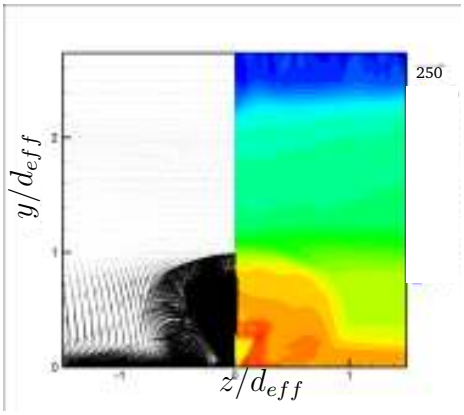

(a) $x/d_{eff} = -1.0$

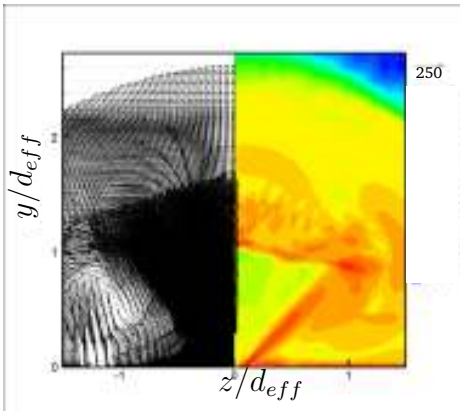

(b) $x/d_{eff} = +1.0$

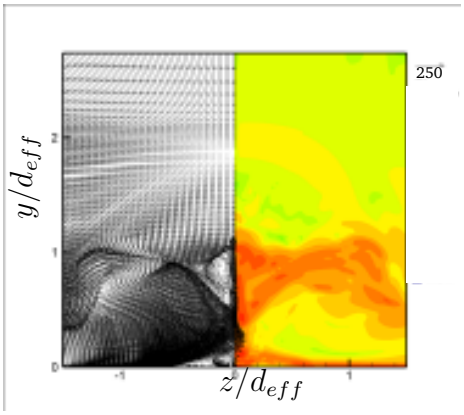

(c) $x/d_{eff} = +2.0$

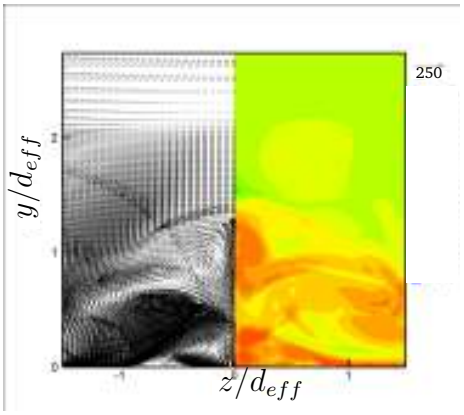

(d) $x/d_{eff} = +3.0$

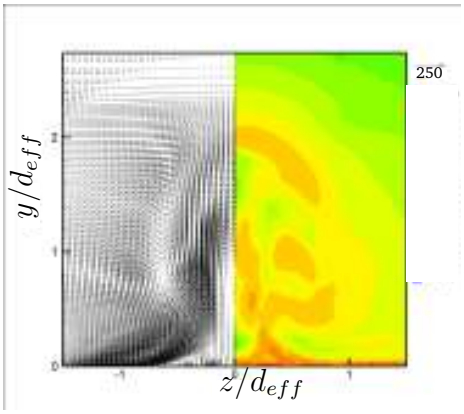

(e) $x/d_{eff} = +8.0$

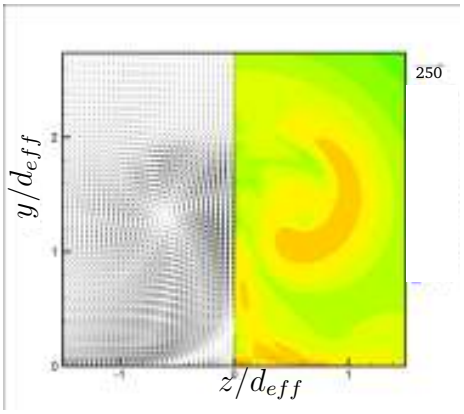

(f) $x/d_{eff} = +15.0$

Fig. 171 Vortex stretching contours at different axial locations. The values are plotted on a log scale.

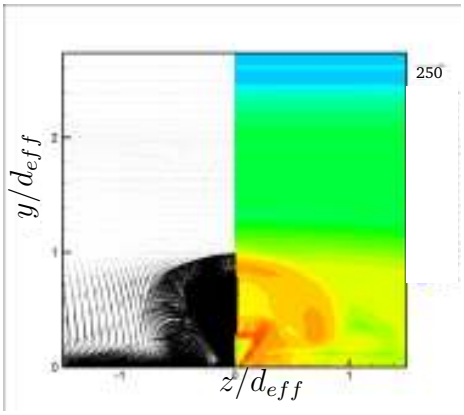

(a) $x/d_{eff} = -1.0$

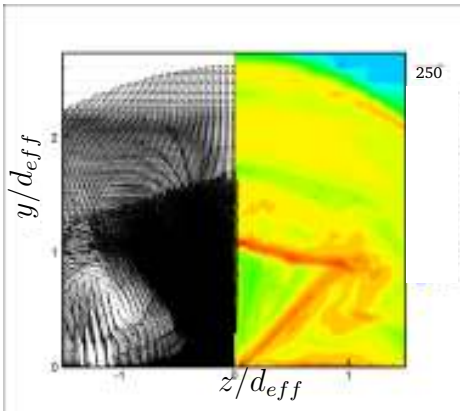

(b) $x/d_{eff} = +1.0$

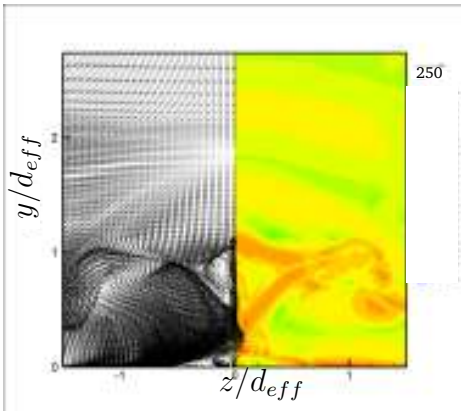

(c) $x/d_{eff} = +2.0$

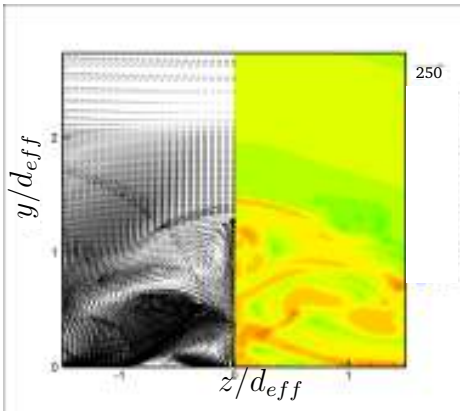

(d) $x/d_{eff} = +3.0$

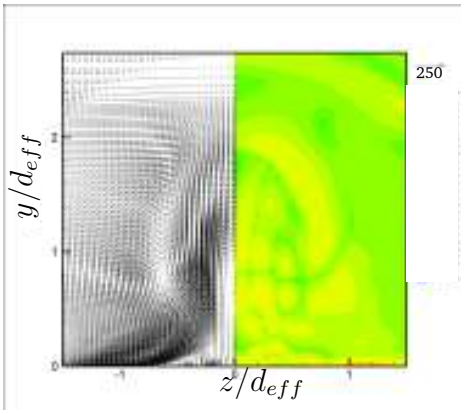

(e) $x/d_{eff} = +8.0$

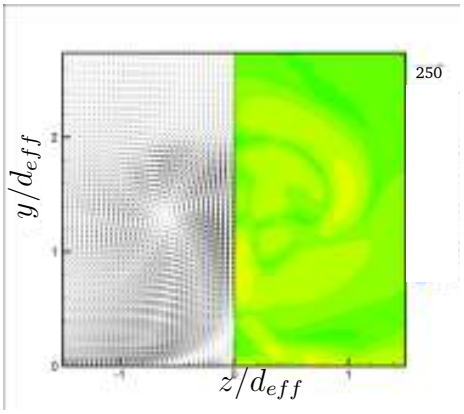

(f) $x/d_{eff} = +15.0$

Fig. 172 Baroclinic torque contours at different axial locations. The values are plotted on a log scale.

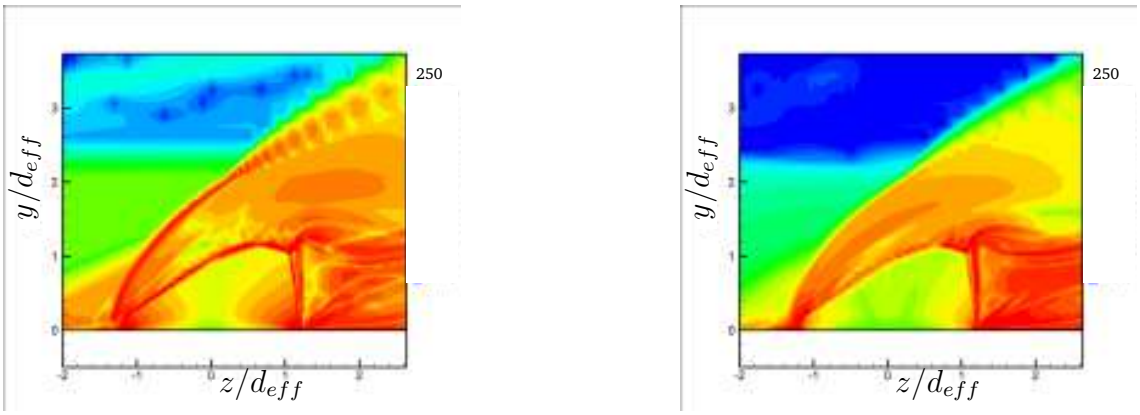

(a) Compressibility.

(b) Vortex stretching.

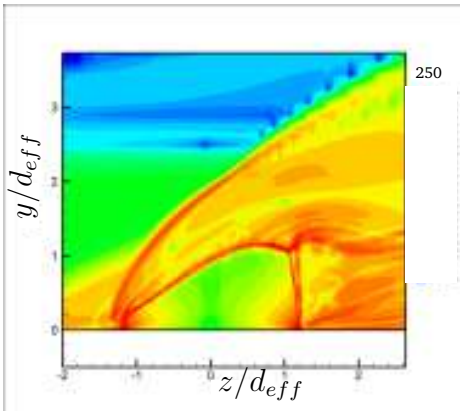

(c) Baroclinic torque.

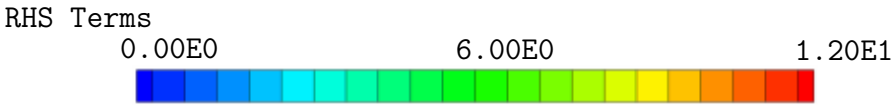

Fig. 173 Compressibility, vortex stretching and baroclinic torque around the barrel shock. The values are plotted on a log scale. The scale shown is applicable to all figures from 170 - 177.

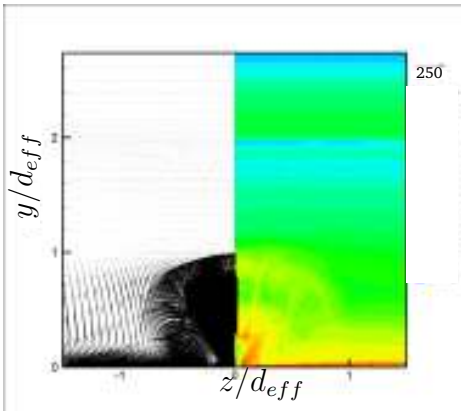

(a) $x/d_{eff} = -1.0$

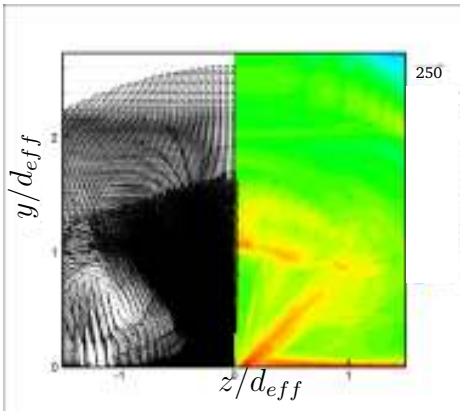

(b) $x/d_{eff} = +1.0$

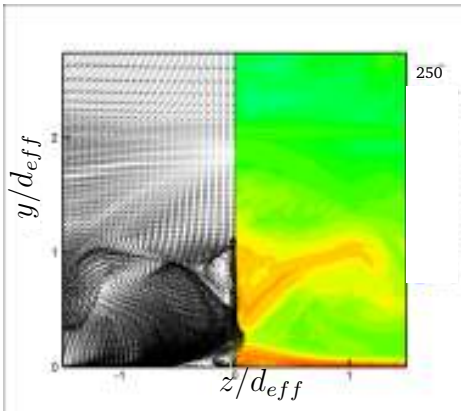

(c) $x/d_{eff} = +2.0$

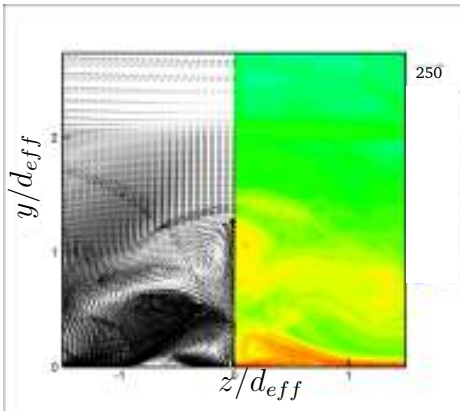

(d) $x/d_{eff} = +3.0$

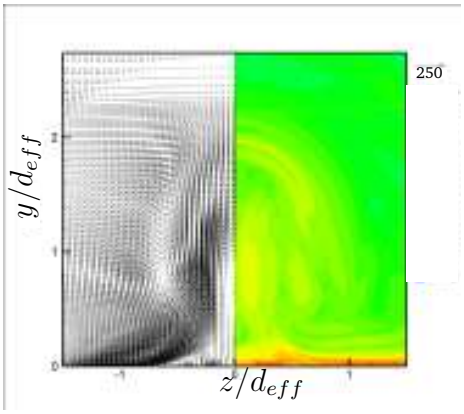

(e) $x/d_{eff} = +8.0$

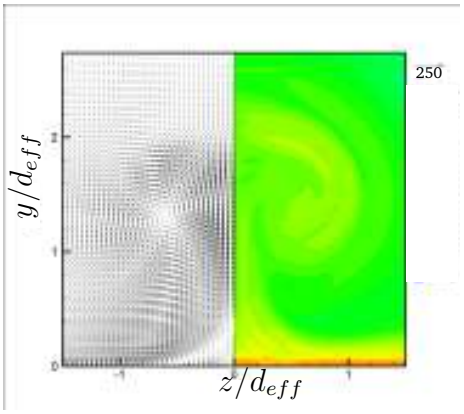

(f) $x/d_{eff} = +15.0$

Fig. 174 Laminar diffusion contours at different axial locations. The values are plotted on a log scale.

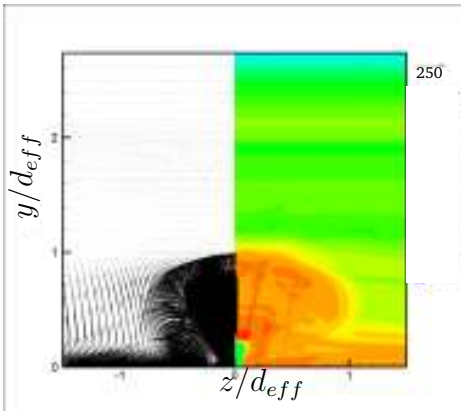

(a) $x/d_{eff} = -1.0$

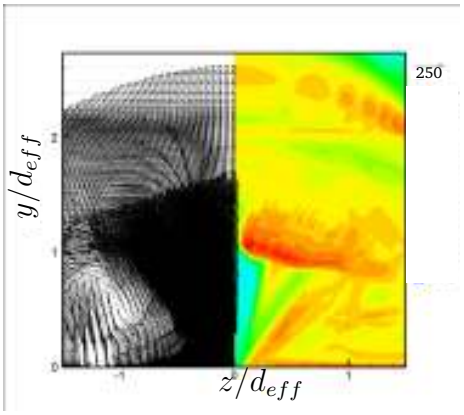

(b) $x/d_{eff} = +1.0$

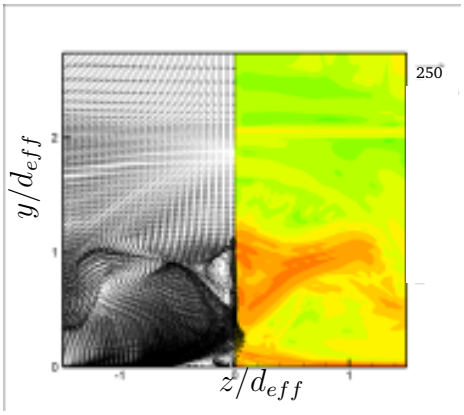

(c) $x/d_{eff} = +2.0$

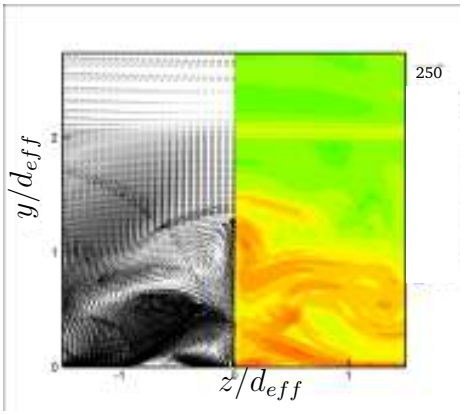

(d) $x/d_{eff} = +3.0$

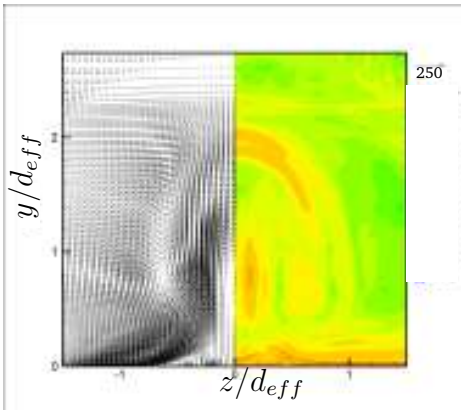

(e) $x/d_{eff} = +8.0$

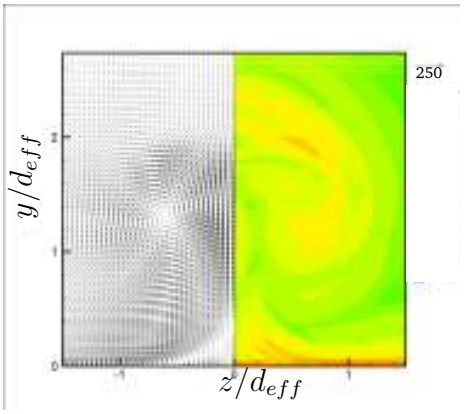

(f) $x/d_{eff} = +15.0$

Fig. 175 Turbulent diffusion contours at different axial locations. The values are plotted on a log scale.

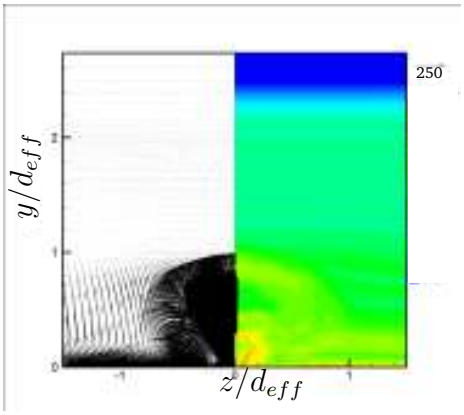

(a) $x/d_{eff} = -1.0$

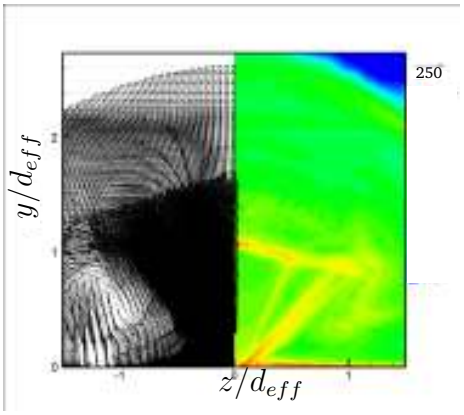

(b) $x/d_{eff} = +1.0$

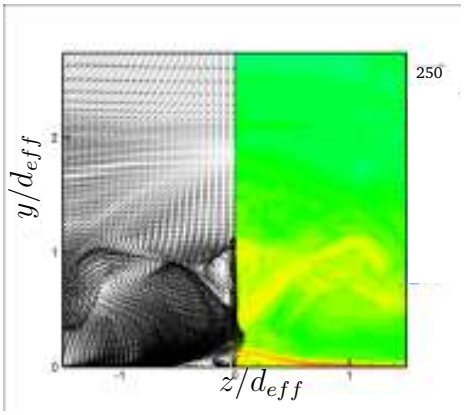

(c) $x/d_{eff} = +2.0$

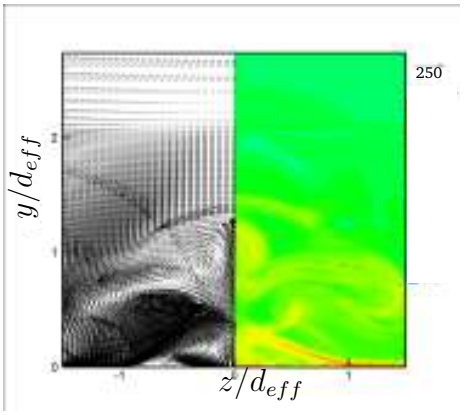

(d) $x/d_{eff} = +3.0$

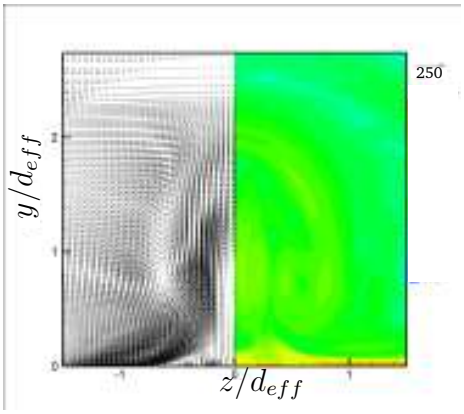

(e) $x/d_{eff} = +8.0$

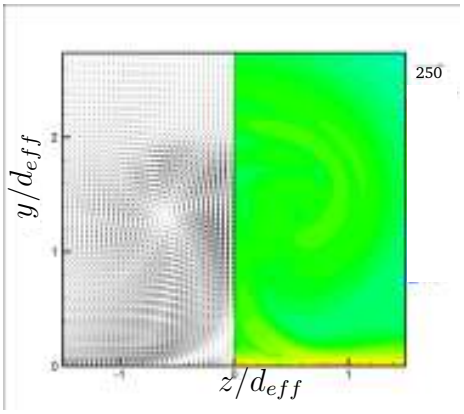

(f) $x/d_{eff} = +15.0$

Fig. 176 Anisosteric laminar diffusion contours at different axial locations. The values are plotted on a log scale.

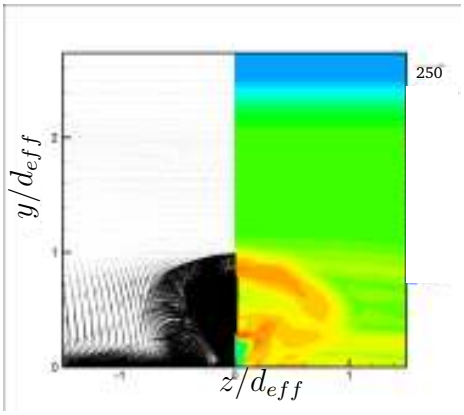

(a) $x/d_{eff} = -1.0$

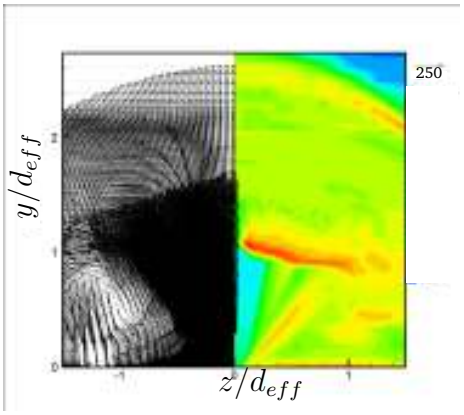

(b) $x/d_{eff} = +1.0$

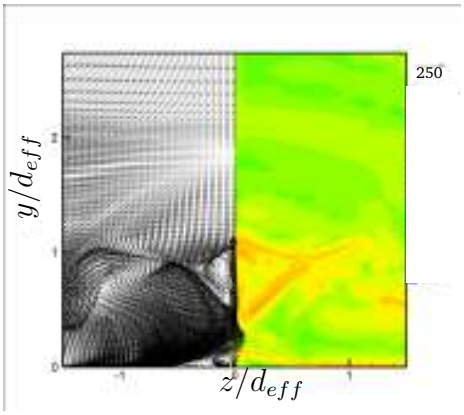

(c) $x/d_{eff} = +2.0$

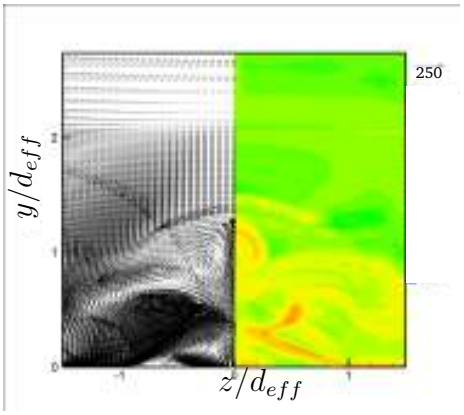

(d) $x/d_{eff} = +3.0$

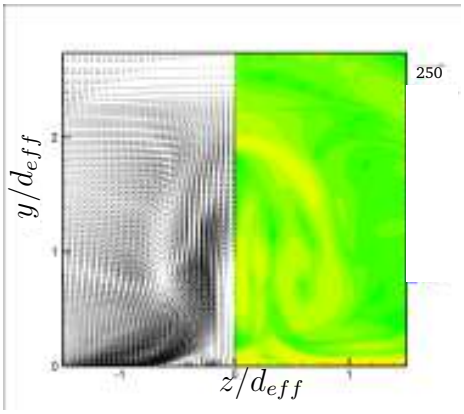

(e) $x/d_{eff} = +8.0$

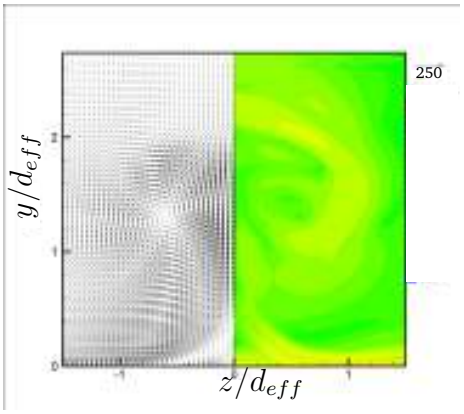

(f) $x/d_{eff} = +15.0$

Fig. 177 Anisosteric turbulent diffusion contours at different axial locations. The values are plotted on a log scale.

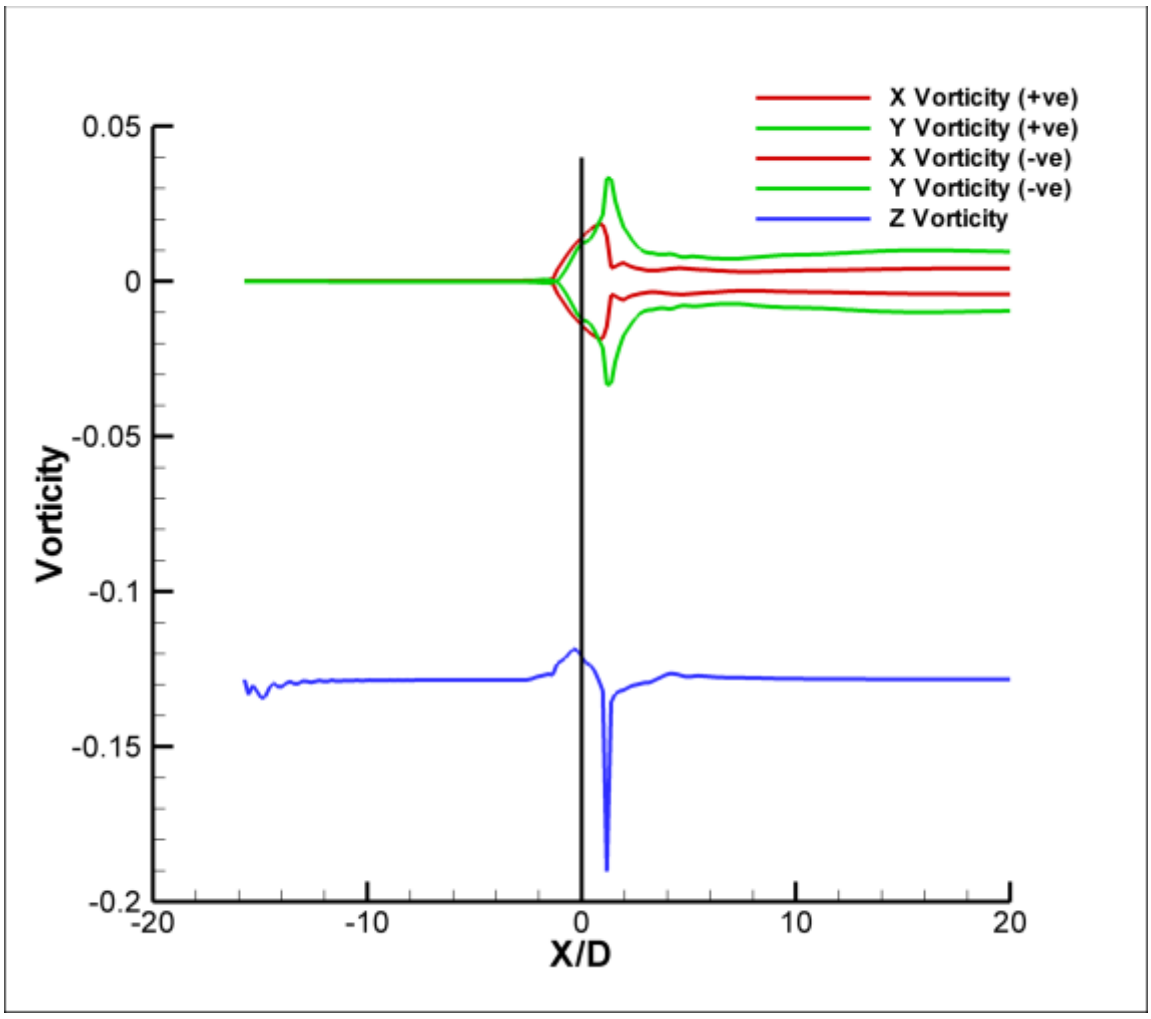

Fig. 178 Average x, y and z vorticity values on cross-sectional planes. The values are normalized by the d_{eff} and V_{inf}.

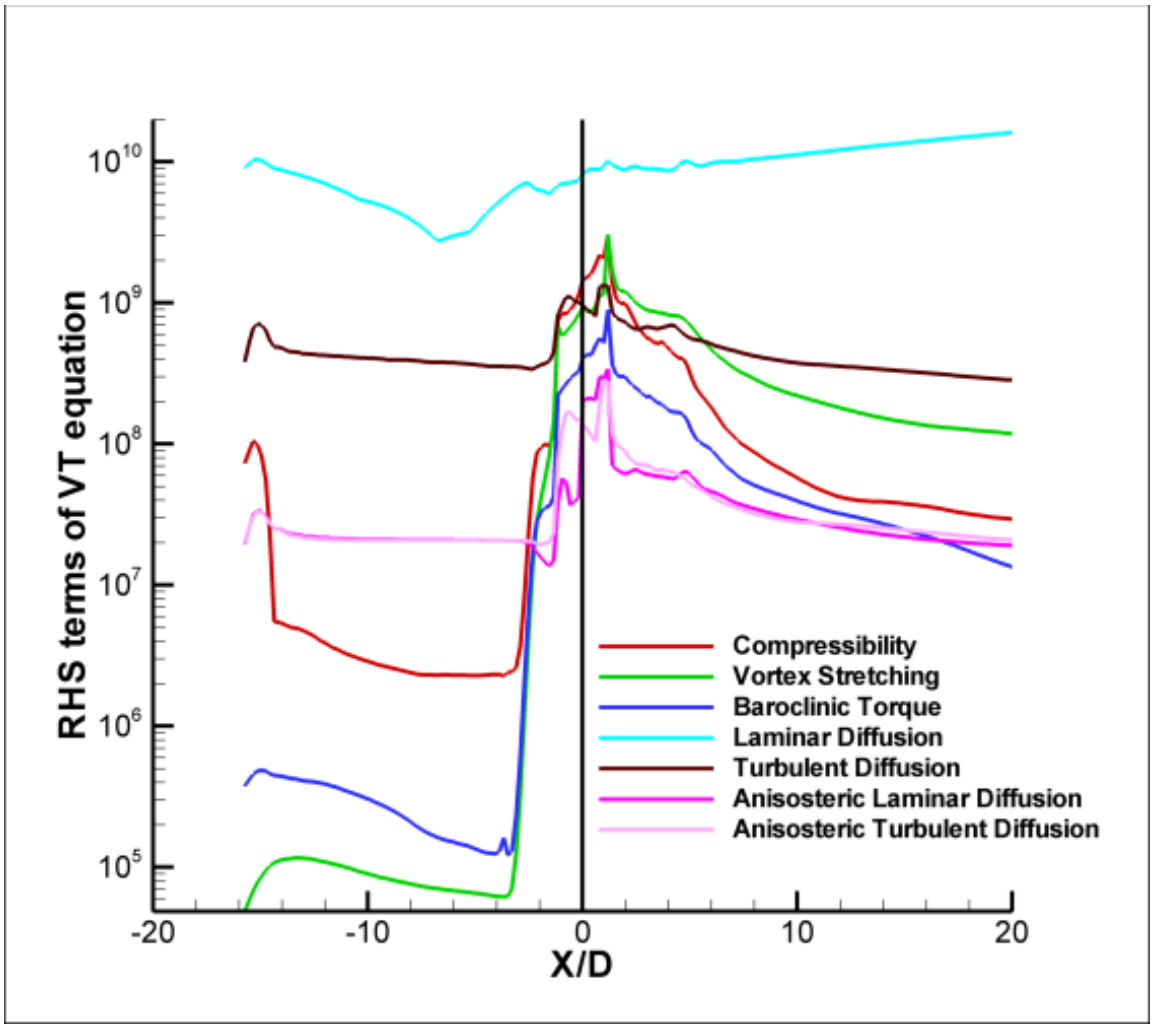

Fig. 179 Average values on cross-sectional planes of the RHS terms in the compressible vorticity transport equation. The y axis is plotted on a log scale.

APPENDIX B

Numerical results of additional jet injection runs are compared to experimental data in this appendix. Comparisons include cases with circular injectors as well as diamond injectors as higher jet total pressures. The circular injector cases are discussed first followed by the diamond injectors.

Circular Injectors

Circular injector configurations were simulated with RANS models (and structured grids) at two different jet total pressures and at 90-degree injection angles. These were done in order to compare to available experimental data. The circular injector configuration has been widely studied using both experimental and numerical approaches as outlined in chapter II. In the present study numerical results for the circular injector configurations are compared to experimental datasets that include shadowgraphs, surface oil flow, pitot pressure and surface pressure. In addition to the RANS simulations, DES simulations were performed using unstructured grids and for the J_1 momentum ration case, similar to the 90-degree diamond injector configuration discussed in chapter V. Results from these DES simulations are also compared to experimental data and corresponding RANS results.

Shadowgraphs

Results of experimental and numerical shadowgraphs from two-equation simulations are shown in Figs. 180 and 181 for the J_1 and J_2 momentum cases. A complete comparison between the results is difficult due to the resolution of the experimental image. The most discernable feature in the experimental images is the interaction shock. The angle of this shock as obtained in simulations is comparable

to that observed in the data. The shape of the barrel shock can be clearly seen in the numerical shadowgraphs. The size of the barrel shock increases with increasing jet momentum ration (or jet total pressure). Lambda shocks generated due the recirculation region ahead of the injector orifice can also be seen in these plots.

Instantaneous and time-averaged shadowgraphs from the low-momentum ratio (J_1) case detached-eddy simulations are shown in Fig. 182. The instantaneous and the time-averaged locations of the interaction shock are nearly the same in the two images. Significant changes are observed in the downstream region. The shear layer structure in the instantaneous results shows large scale features, while the time-averaged results are similar to the RANS results. The features seen in the instantaneous results appear to be more disorganized when compared to the instantaneous results from the diamond injector DES runs (see Fig. 46). Shock waves are seen to originate due to the presence of these structures. This was also observed in the diamond injector DES runs.

Surface Oil Flow Visualization

Results for the J_1 and J_2 cases from the two-equation simulations are shown in Figs. 183 and 184. In both these cases, the leading edge separation in both cases is seen to be higher in the simulation results. A possible cause of this discrepancy in the comparison is presented in chapter V. However, the downstream predictions of the horseshoe vortex region are good. The increased separation between the wake vortices for the J_2 case can be seen in Fig. 183. Comparing these to the time-averaged and instantaneous results from the detached-eddy simulation, we find that the separation region is slightly larger in DES, especially near the side walls. The downstream predictions are quite similar between the RANS and the

DES. Unsteady features are seen downstream, near the tunnel center line, in the instantaneous DES result.

Pitot Pressure and Mach Number

Plots of pitot pressure and Mach number results from experiments for the J_1 case and RANS results for the J_1 and J_2 case are shown in Figs. 185, 186 and 187. Experimental results for the J_2 case was not available. The overall prediction of pitot pressure and Mach number at locations $x/d_{eff} = +8.0$ and $x/d_{eff} = +23.0$ follows the trend of the diamond injector results. The simulations capture the salient flow features observed in experiments. The interaction shock location is approximately the same in experiments and simulations. The DES results (see Figs. 188 and 189) compare well to experimental data. Flow asymmetry is prominent in the instantaneous results at both axial locations.

Surface Pressure

Comparsion of surface pressure results from RANS and DES to experiments is shown in Fig. 190. The predictions compare well to experimental results for the J_1 case. RANS comparison to the J_2 experimental results at downstream locations are good. The upstream pressure prediction of the CFD is lower than experimentally measured values. This was also observed in the diamond injector simulations. DES results show unsteadiness in the instantaneous image. The time-averaged DES is similar to the RANS result.

Diamond Injectors

In addition to the cases discussed in chapter V, numerous simulations were performed with diamond injector configurations at two different jet total pressures. Representative results for the 90-degree injection case are compared to available experimental data in this section. Shadowgraphs

Increase in jet total pressure shows an increase in the interaction shock angles as seen in Figs. 191 and 192 for J_2 and J_3 cases of 90-degree injection through diamond orifices. The barrel shock outline denotes that it is larger than the J_1 case. However, the overall shape of the barrel shock is similar to the low pressure case. The vertical trailing edge observed in the low pressure case is also seen in the high pressure cases. The higher pressure fluid exiting into the tunnel creates a larger recirculation region upstream of the injector orifice. This leads to a stronger lambda shock which can be seen in both images. Comparing the results to experimental data, it is observed that the interaction shock angles predicted by the CFD are close to those obtained from experiments. A faint outline of the recompression shock and the shear layer can also be seen in experimental data. These are clearly visible in CFD results.

Surface Oil Flow Visualization

Numerical and experimental results for the surface oil flow visualization of J_2 and J_3 cases are seen in Fig. 193. The CFD results show separation further upstream from the injector as compared to the low pressure case. This was also observed with the formation of the lambda shock in the shadowgraphs. The experimental data agrees well with CFD results at downstream locations of the injector. The comparison at upstream locations follows the trend of other oil flow comparisons

and has been discusses in the section on circular injectors and in chapter V.

Pitot Pressure and Mach Number

Experimental data for the J_2 case was available only at the far field location while none were available for the J_3 case. The contour plots of pitot pressure and Mach number are shown in Figs. 194 and 195. The interaction shock outline is observed at the top of the displayed cross-section. Far field comparisons for the J_2 case shows a trend similar to the comparisons of the low pressure case in chapter V. The CFD captures the salient flow features seen in experiments. However, near the outer edges of the wake region, higher diffusion is observed in experimental results. Comparing the J_2 and J_3 cases, we find that the overall structure of the flow is similar. An increase in the interaction shock height is observed at location $x/d_{eff} = +8.0$. The structure of the inner core of the wake is slightly different between the two cases.

Surface Pressure

Plots of the surface pressure comparison for the two high pressure cases are shown in Fig. 196. The structure of the high pressure region upstream and around the sides of the injector in CFD results is similar to experiments. The area of the low pressure region downstream of the injector is larger in CFD results. This was also observed in the low pressure cases. Again, in comparison to experimental data, the results from CFD follow the trend set by the low pressure cases.

Numerical simulation results for the angles injection cases with increased jet total pressure were examined and compared to available experimental data. Overall, the comparison for the diamond and circular injector simulation results with

experimental data follow the same trend across all the jet total pressure cases and injection angles.

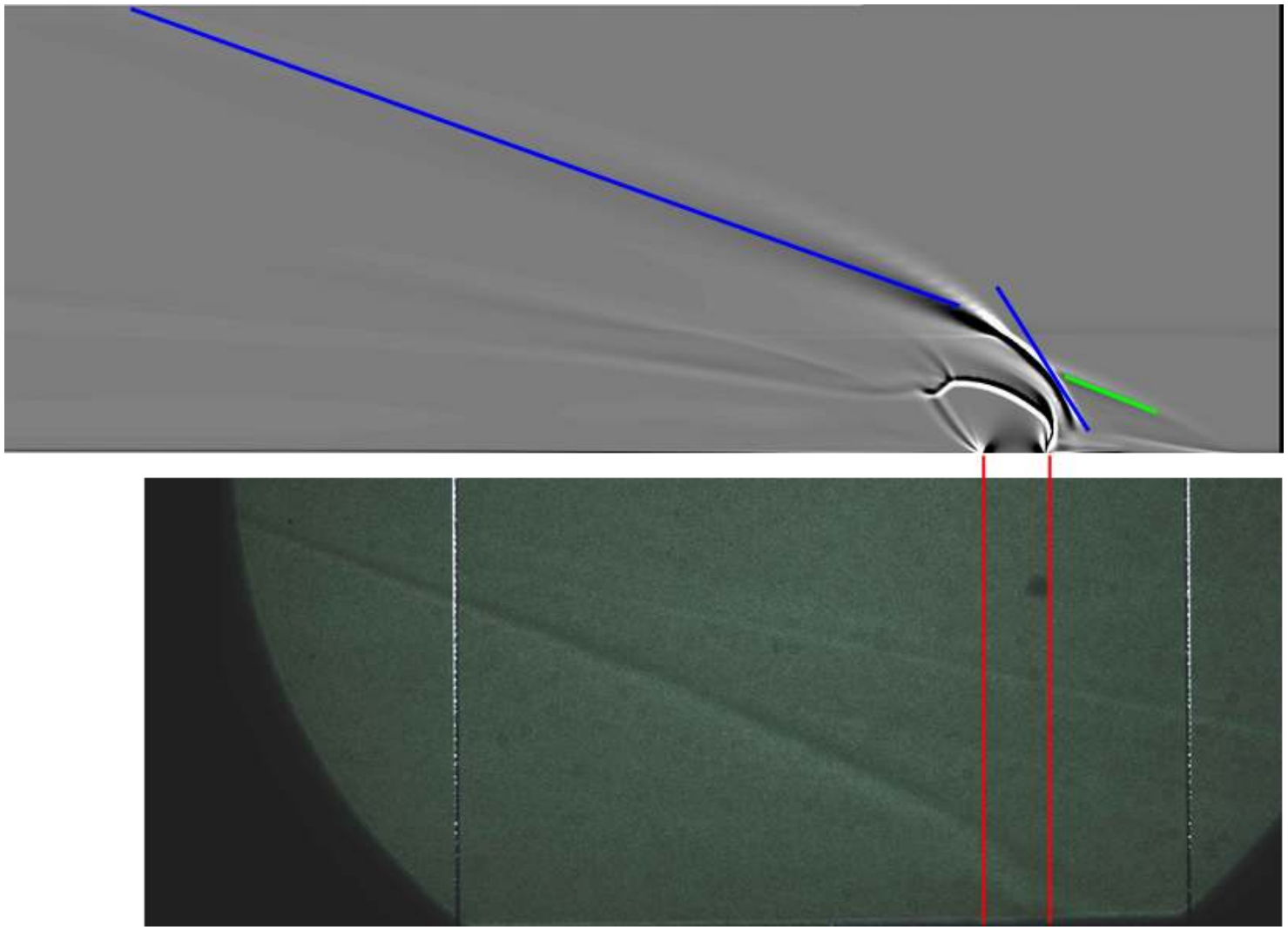

Fig. 180 Shadowgraph comparison of RANS results with experiments — 90-degree J_1, circular.

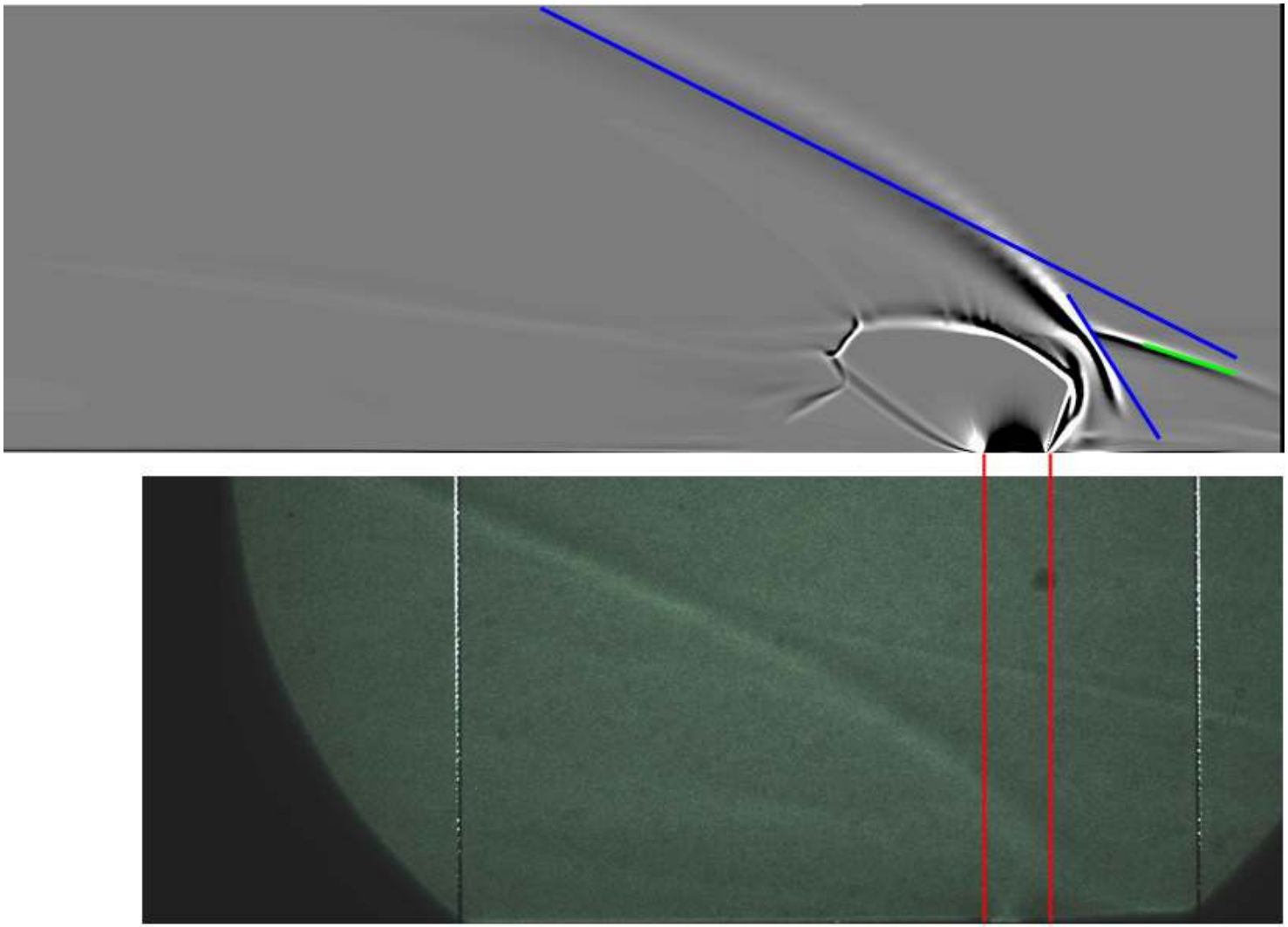

Fig. 181 Shadowgraph comparison of RANS results with experiments — 90-degree J_2, circular.

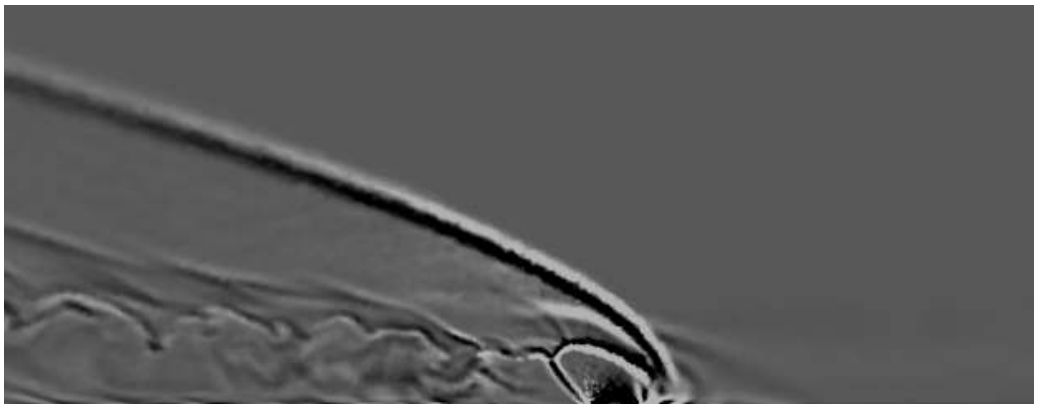

(a) Instantaneous

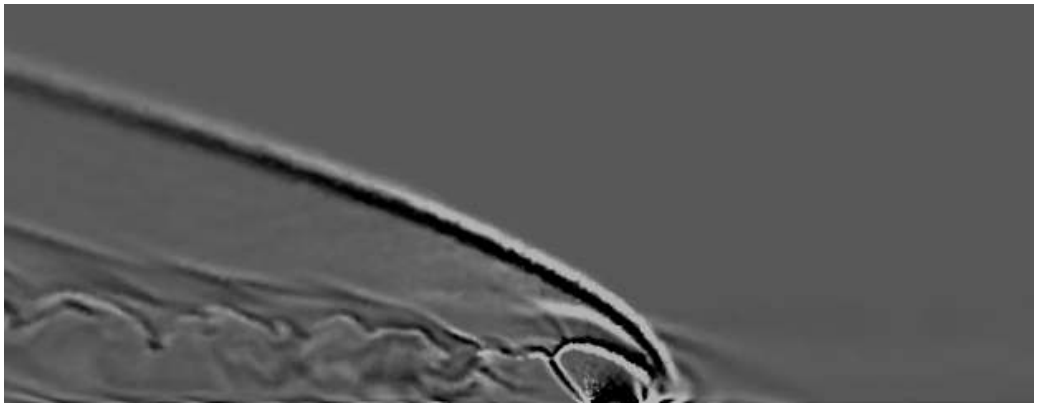

(b) Time-averaged

Fig. 182 Shadowgraph results from detached-eddy simulations — 90-degree J_1, circular.

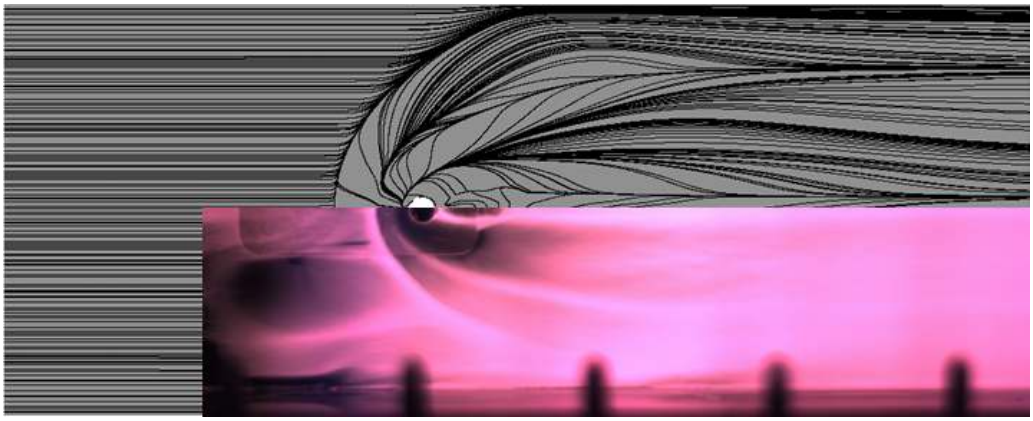

(a) 90-degree J_1, Circular

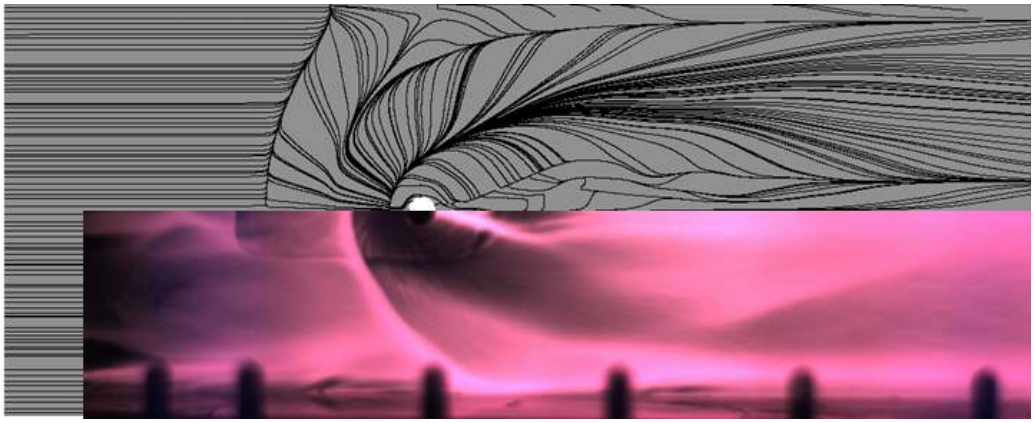

(b) 90-degree J_2, Circular

Fig. 183 Oil flow comparison of RANS results with experiments.

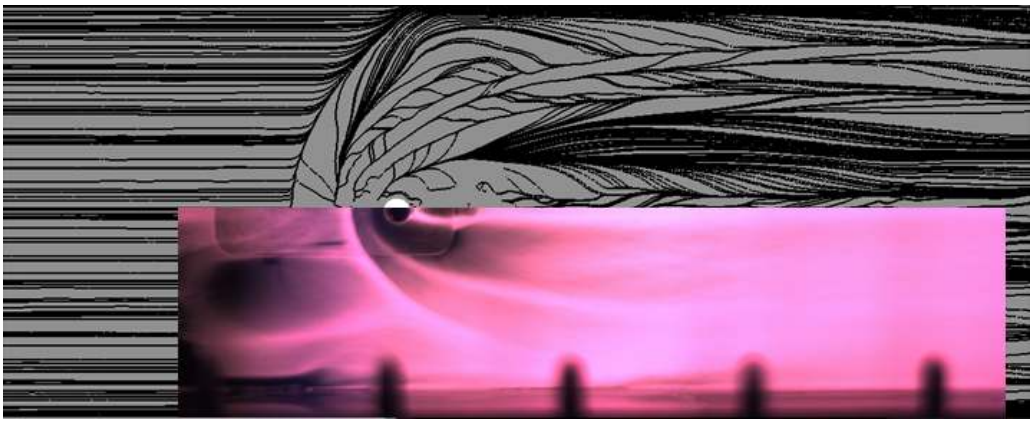

(a) Instantaneous

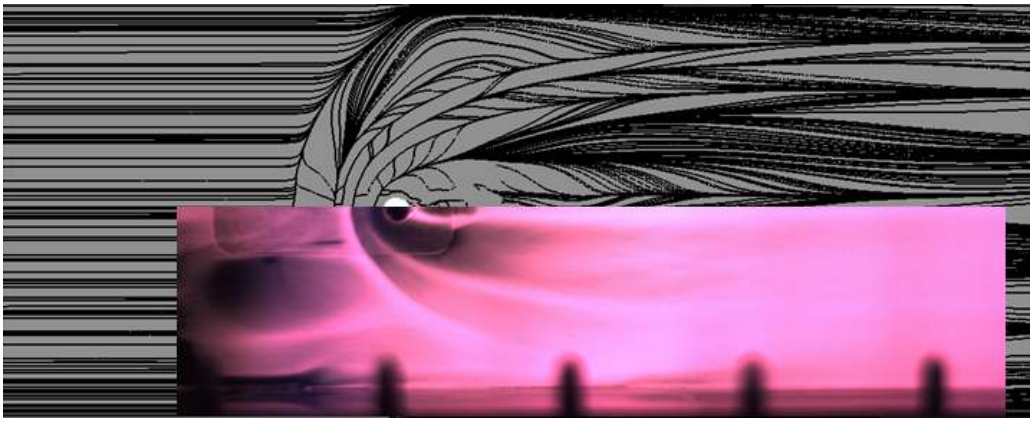

(b) Time-averaged

Fig. 184 Oil flow results from detached-eddy simulations — 90-degree J_1, circular.

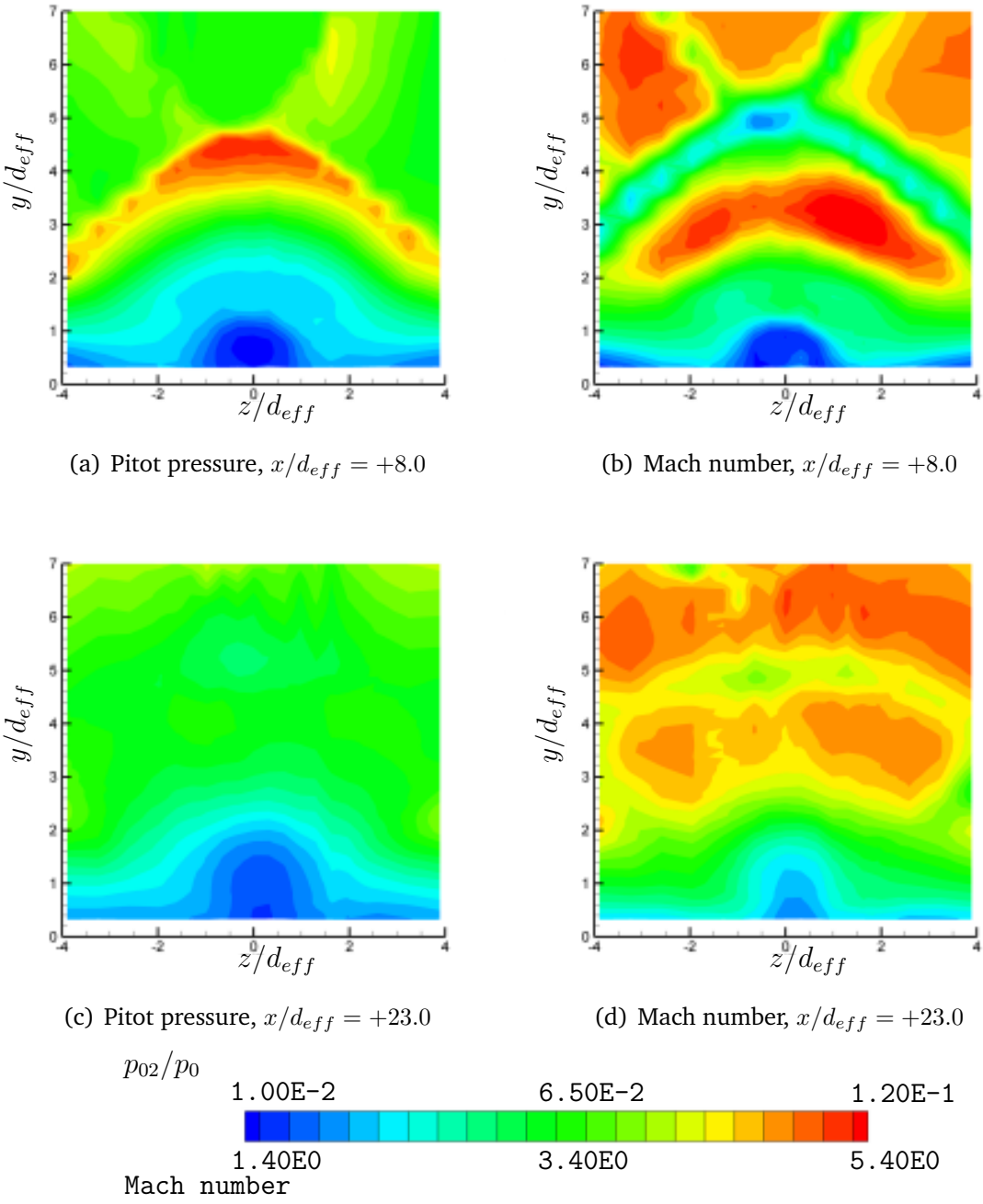

(a) Pitot pressure, $x/d_{eff} = +8.0$

(b) Mach number, $x/d_{eff} = +8.0$

(c) Pitot pressure, $x/d_{eff} = +23.0$

(d) Mach number, $x/d_{eff} = +23.0$

Fig. 185 Experimental pitot pressure and Mach number contours at $x/d_{eff} = +8.0$ and $x/d_{eff} = +23.0$ — 90-degree J_1, circular. The pitot pressure is normalized by the freestream total pressure. The axial locations x/d_{eff} are measured from the leading edge of the injector.

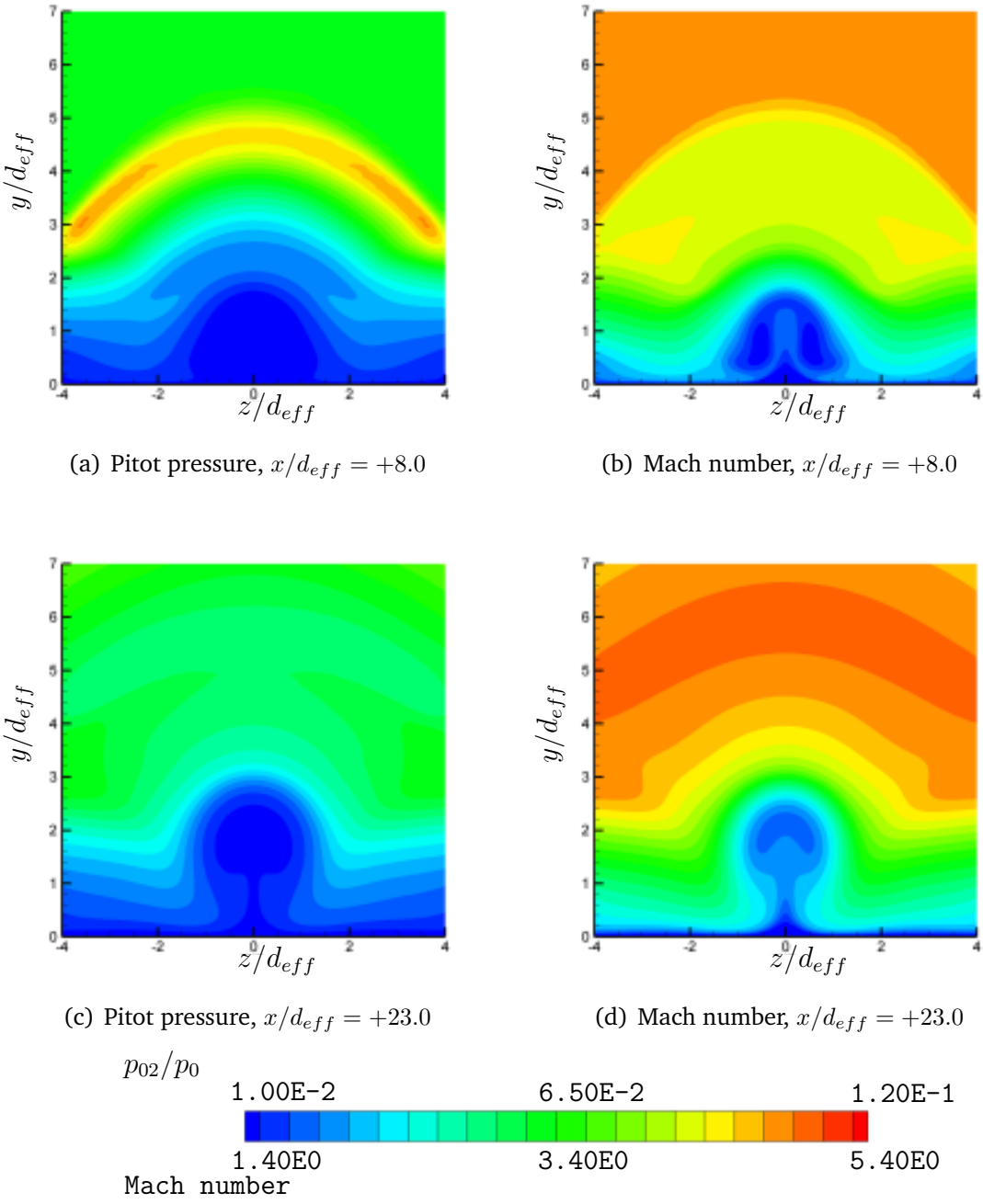

(a) Pitot pressure, $x/d_{eff} = +8.0$

(b) Mach number, $x/d_{eff} = +8.0$

(c) Pitot pressure, $x/d_{eff} = +23.0$

(d) Mach number, $x/d_{eff} = +23.0$

Fig. 186 Pitot pressure and Mach number contours at $x/d_{eff} = +8.0$ and $x/d_{eff} = +23.0$ — 90-degree J_1, circular. The pitot pressure is normalized by the freestream total pressure. The axial locations x/d_{eff} are measured from the leading edge of the injector.

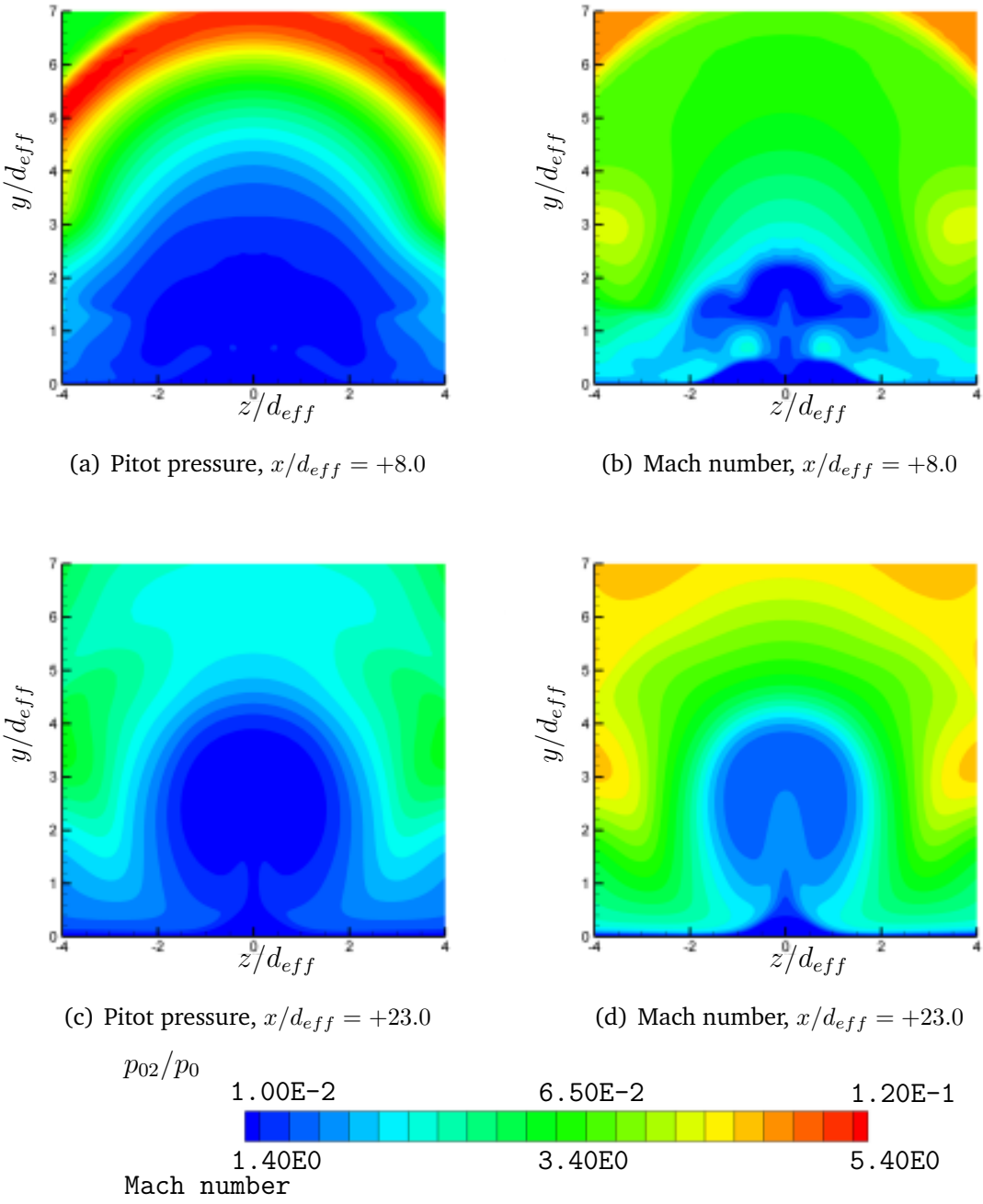

(a) Pitot pressure, $x/d_{eff} = +8.0$

(b) Mach number, $x/d_{eff} = +8.0$

(c) Pitot pressure, $x/d_{eff} = +23.0$

(d) Mach number, $x/d_{eff} = +23.0$

Fig. 187 Pitot pressure and Mach number contours at $x/d_{eff} = +8.0$ and $x/d_{eff} = +23.0$ — 90-degree J_2, circular. The pitot pressure is normalized by the freestream total pressure. The axial locations x/d_{eff} are measured from the leading edge of the injector.

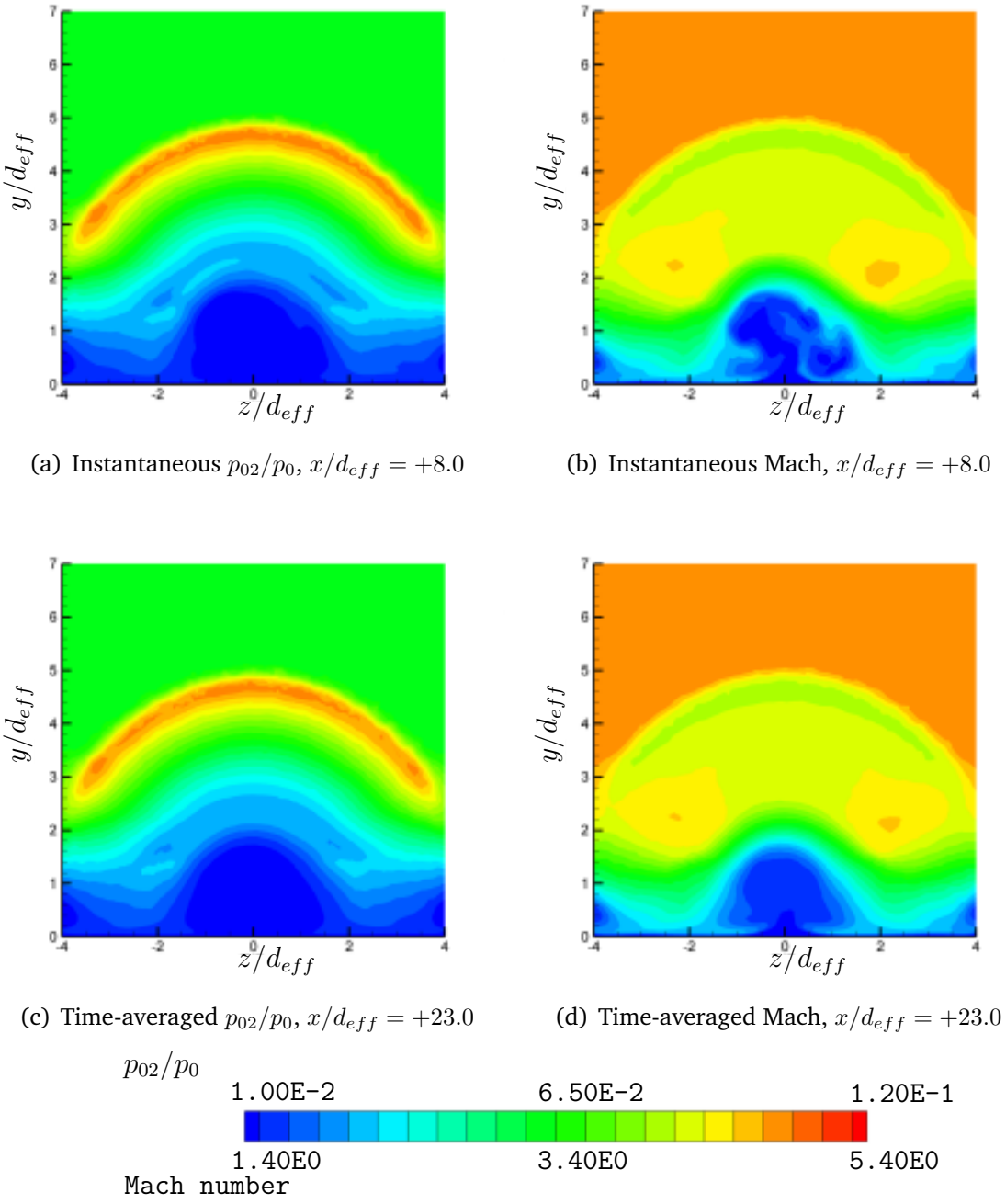

(a) Instantaneous p_{02}/p_0, $x/d_{eff} = +8.0$

(b) Instantaneous Mach, $x/d_{eff} = +8.0$

(c) Time-averaged p_{02}/p_0, $x/d_{eff} = +23.0$

(d) Time-averaged Mach, $x/d_{eff} = +23.0$

Fig. 188 DES results of pitot pressure and Mach number contours at $x/d_{eff} = +8.0$ — 90-degree J_1, circular. The pitot pressure is normalized by the freestream total pressure. The axial locations x/d_{eff} are measured from the leading edge of the injector.

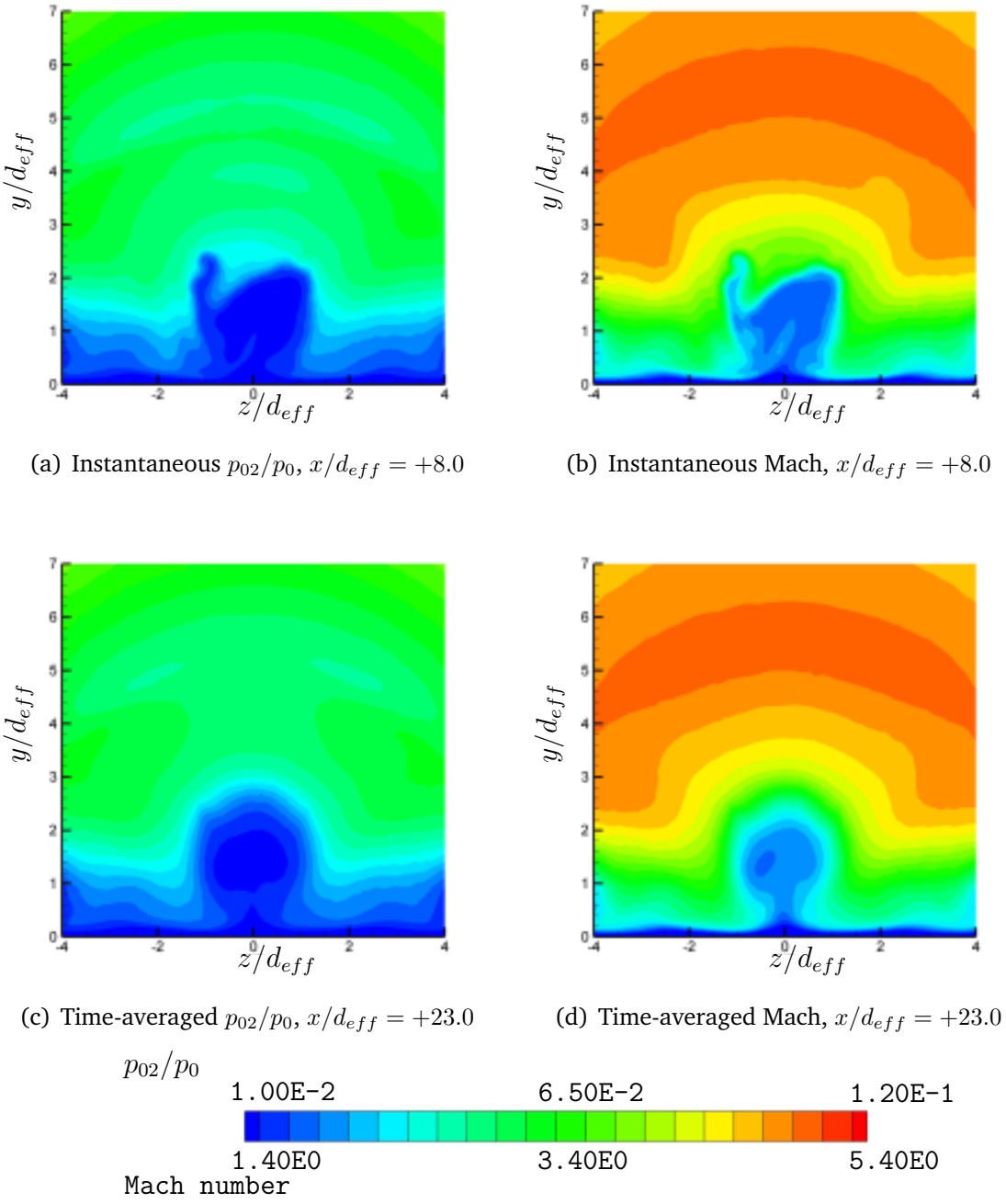

(a) Instantaneous p_{02}/p_0, $x/d_{eff} = +8.0$

(b) Instantaneous Mach, $x/d_{eff} = +8.0$

(c) Time-averaged p_{02}/p_0, $x/d_{eff} = +23.0$

(d) Time-averaged Mach, $x/d_{eff} = +23.0$

Fig. 189 DES results of pitot pressure and Mach number contours at $x/d_{eff} = +23.0$ — 90-degree J_1, circular. The pitot pressure is normalized by the freestream total pressure. The axial locations x/d_{eff} are measured from the leading edge of the injector.

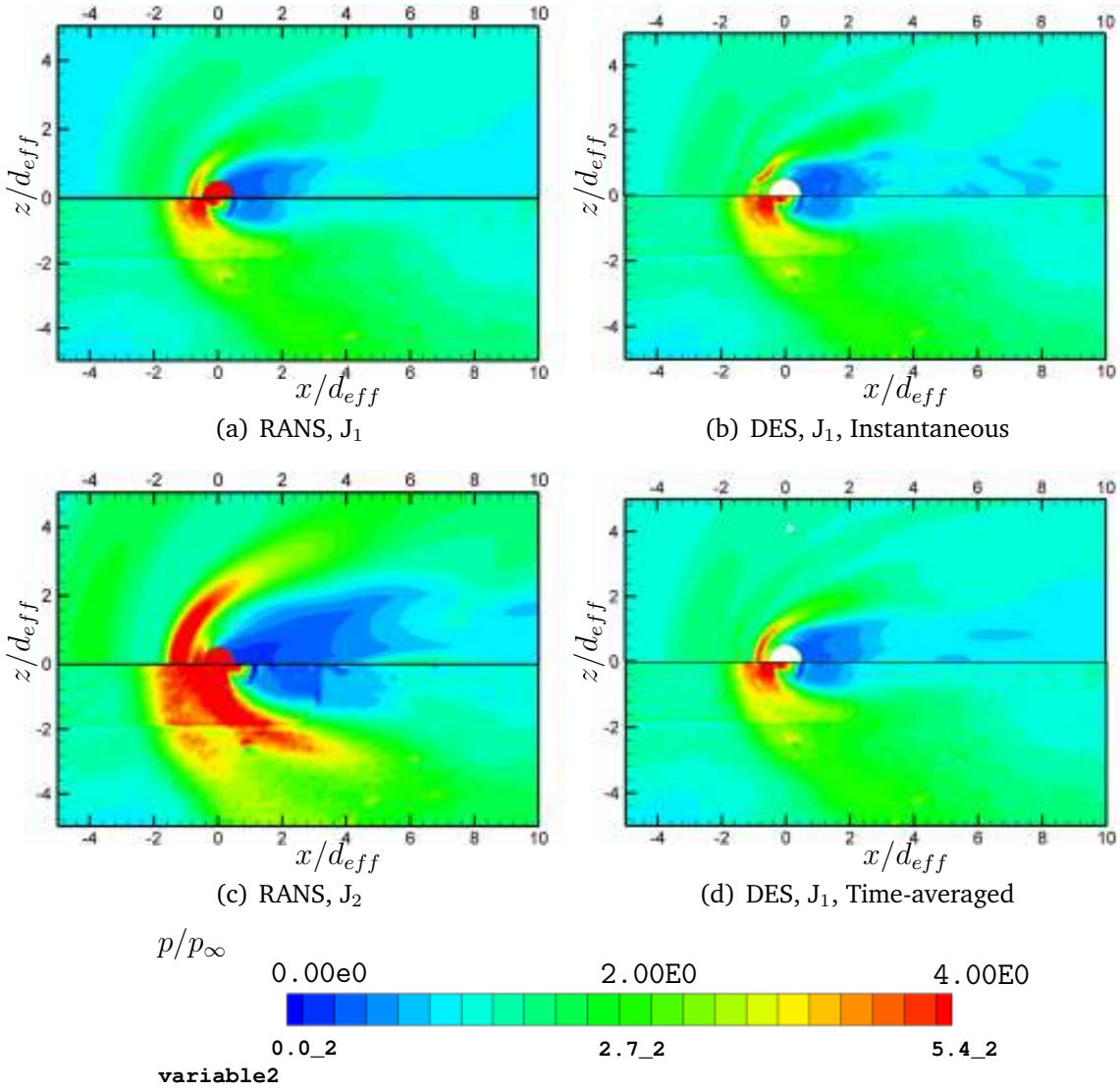

(a) RANS, J_1 (b) DES, J_1, Instantaneous

(c) RANS, J_2 (d) DES, J_1, Time-averaged

Fig. 190 Surface pressure comparison of RANS and DES results with experiments. The surface pressure is normalized by the freestream static pressure.

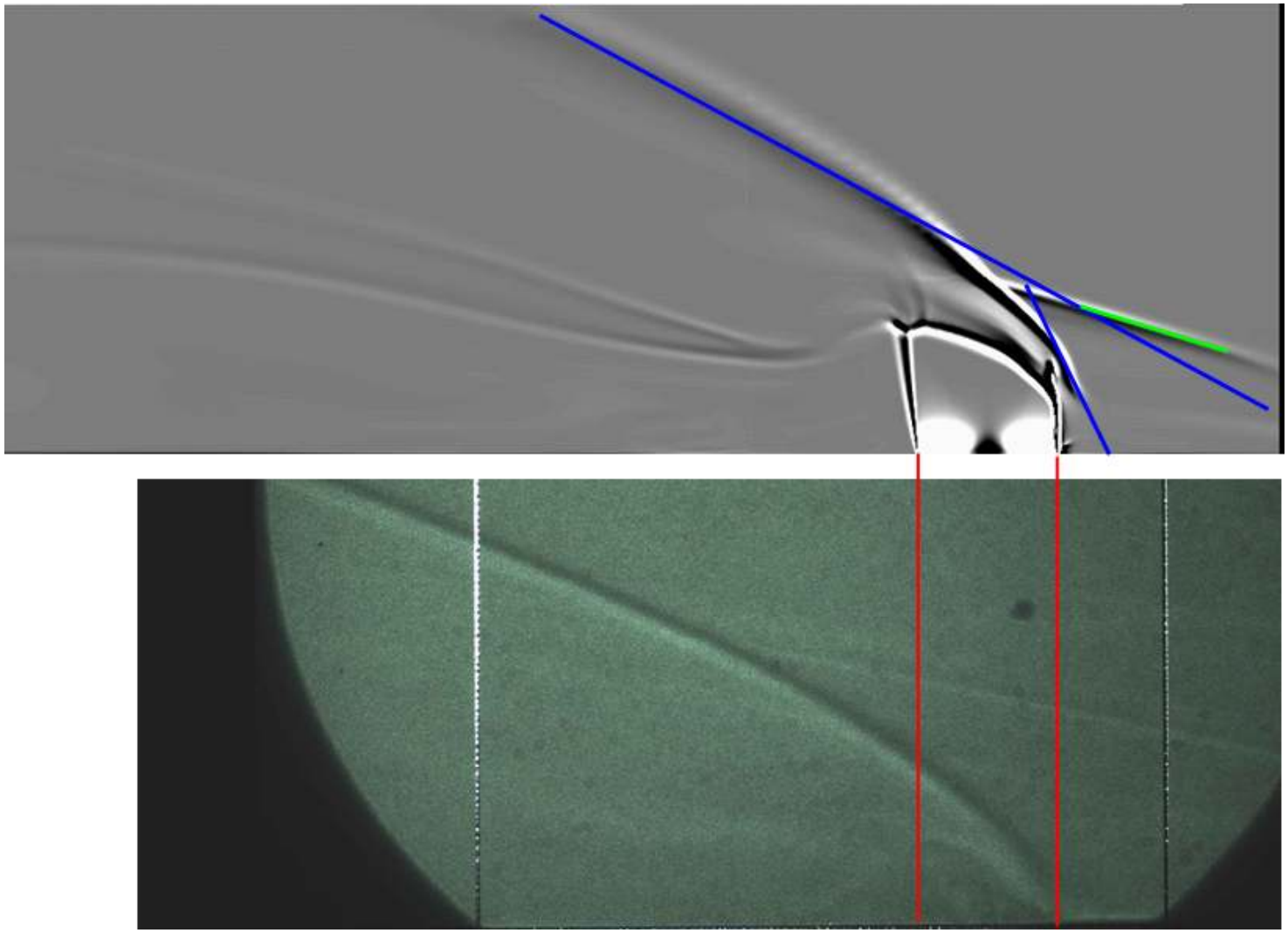

Fig. 191 Shadowgraph comparison of RANS results with experiments — 90-degree J_2.

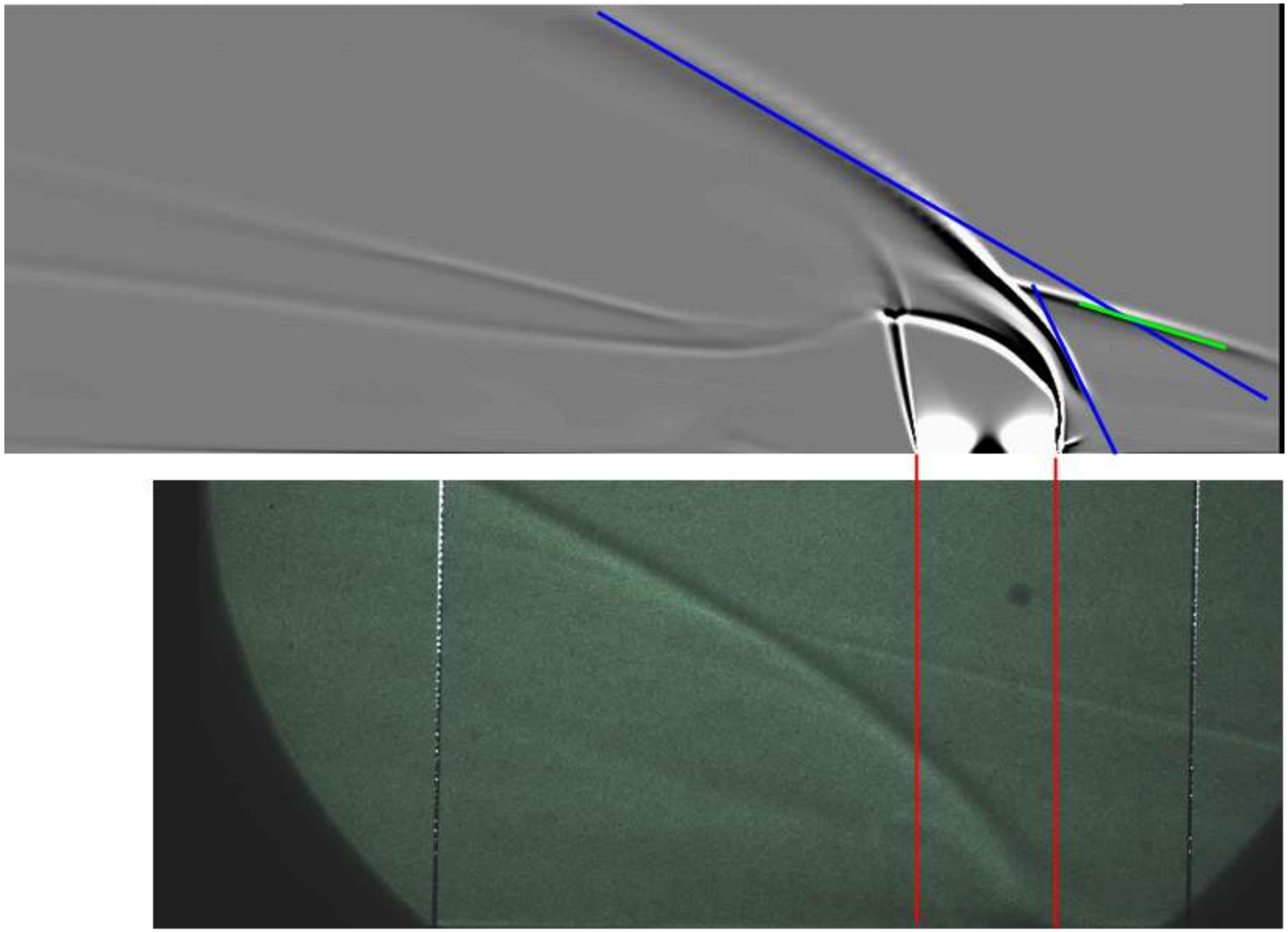

Fig. 192 Shadowgraph comparison of RANS results with experiments — 90-degree J_3.

(a) 90-degree J_2

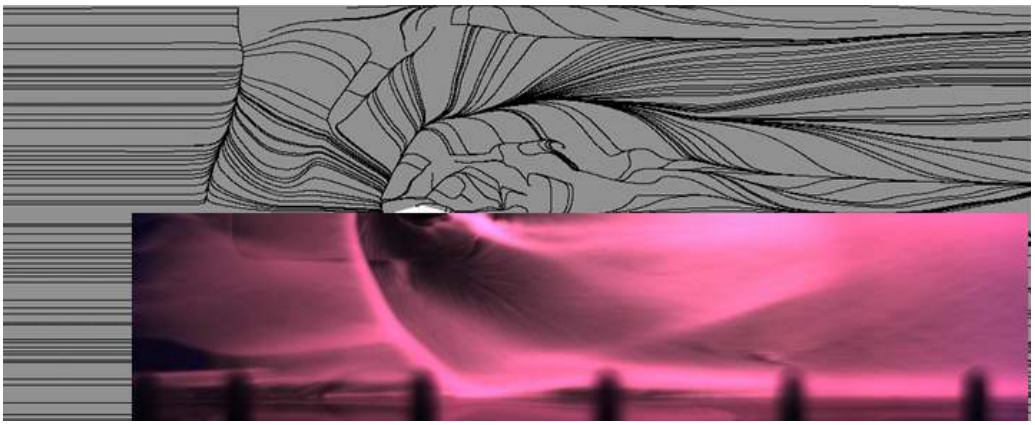

(b) 90-degree J_3

Fig. 193 Oil flow comparison of RANS results with experiments.

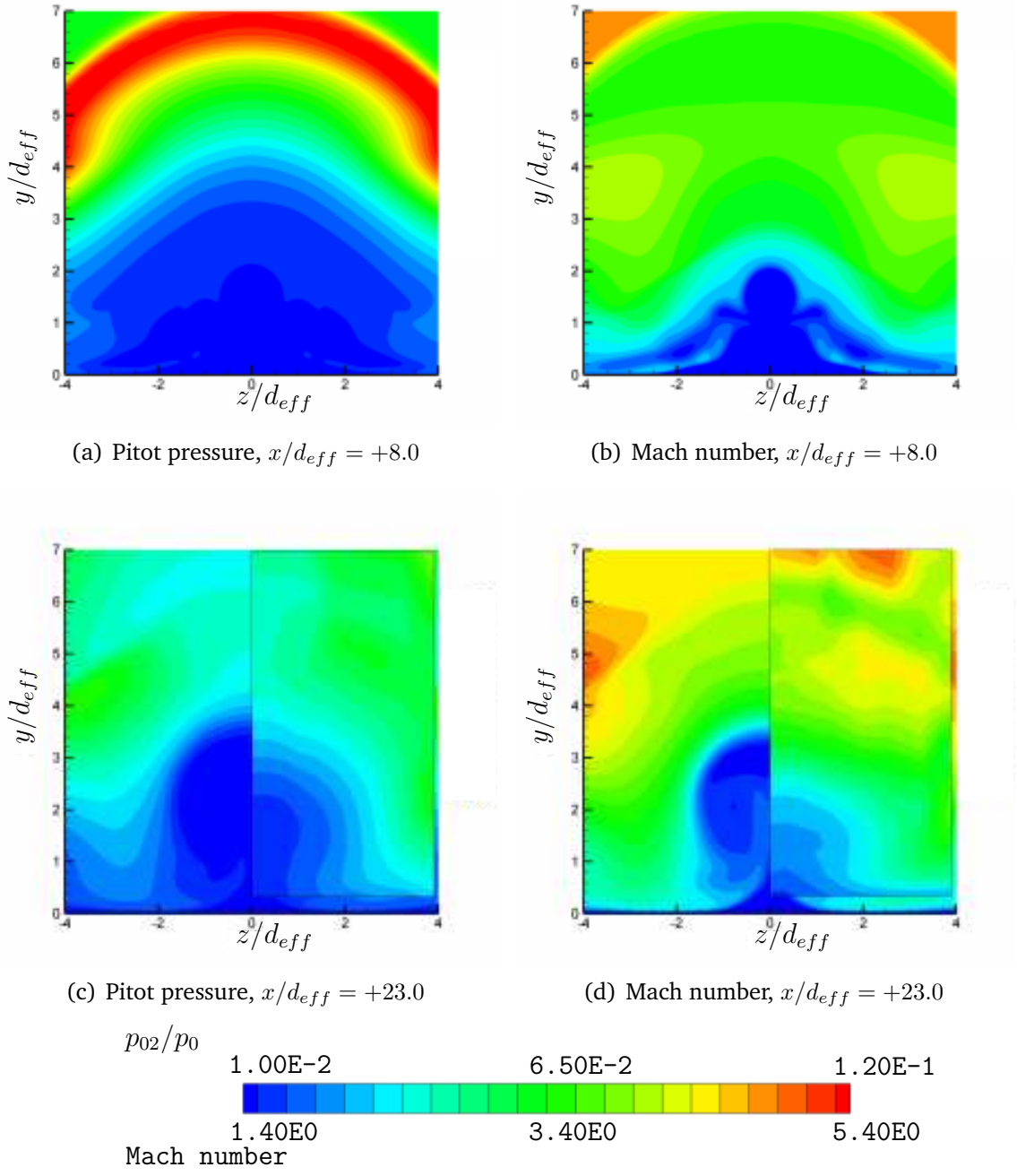

(a) Pitot pressure, $x/d_{eff} = +8.0$

(b) Mach number, $x/d_{eff} = +8.0$

(c) Pitot pressure, $x/d_{eff} = +23.0$

(d) Mach number, $x/d_{eff} = +23.0$

Fig. 194 Experimental pitot pressure and Mach number contours at $x/d_{eff} = +8.0$ and $x/d_{eff} = +23.0$ — 90-degree J_2. The pitot pressure is normalized by the freestream total pressure. The axial locations x/d_{eff} are measured from the leading edge of the injector.

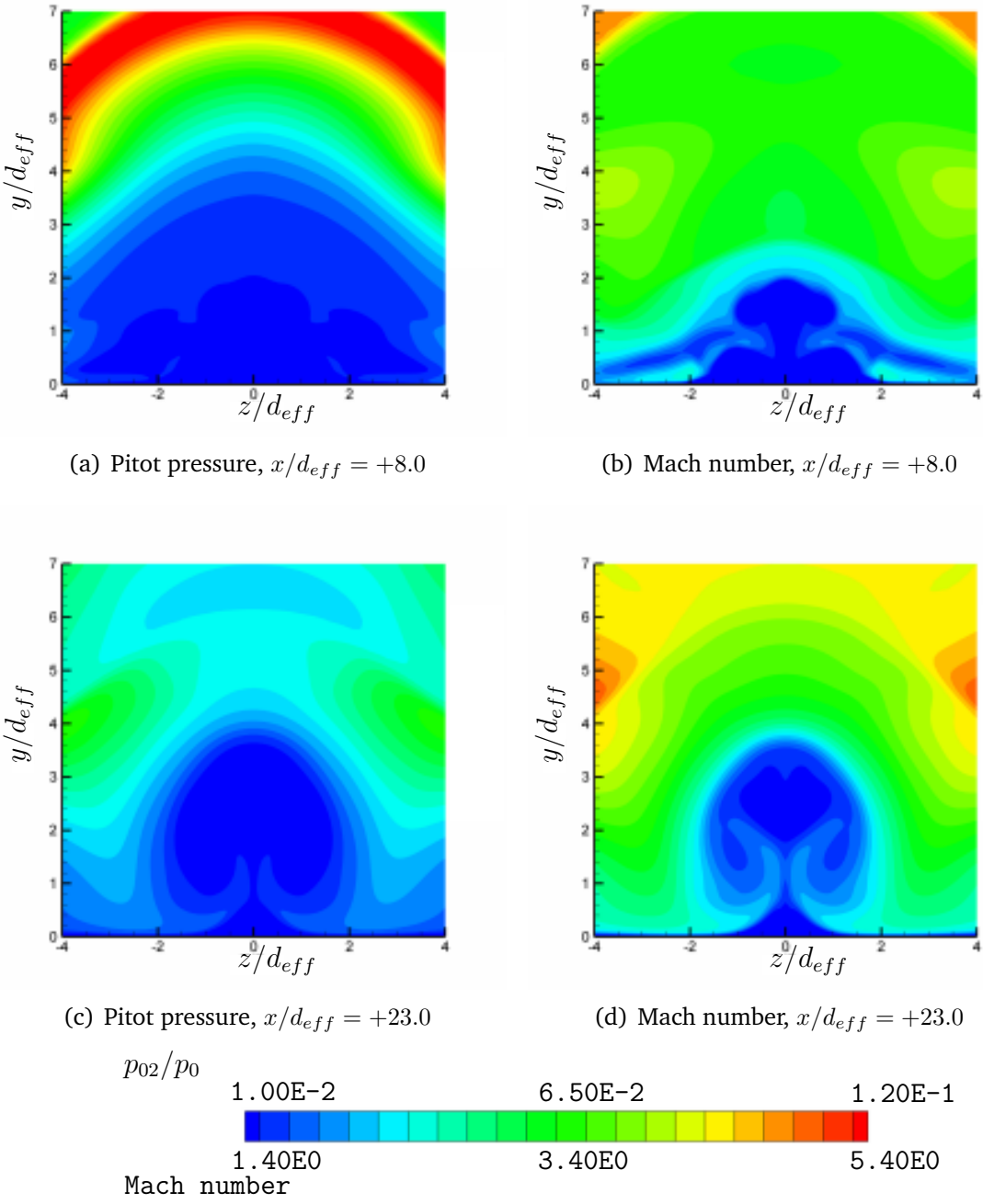

(a) Pitot pressure, $x/d_{eff} = +8.0$

(b) Mach number, $x/d_{eff} = +8.0$

(c) Pitot pressure, $x/d_{eff} = +23.0$

(d) Mach number, $x/d_{eff} = +23.0$

Fig. 195 Experimental pitot pressure and Mach number contours at $x/d_{eff} = +8.0$ and $x/d_{eff} = +23.0$ — 90-degree J_3. The pitot pressure is normalized by the freestream total pressure. The axial locations x/d_{eff} are measured from the leading edge of the injector.

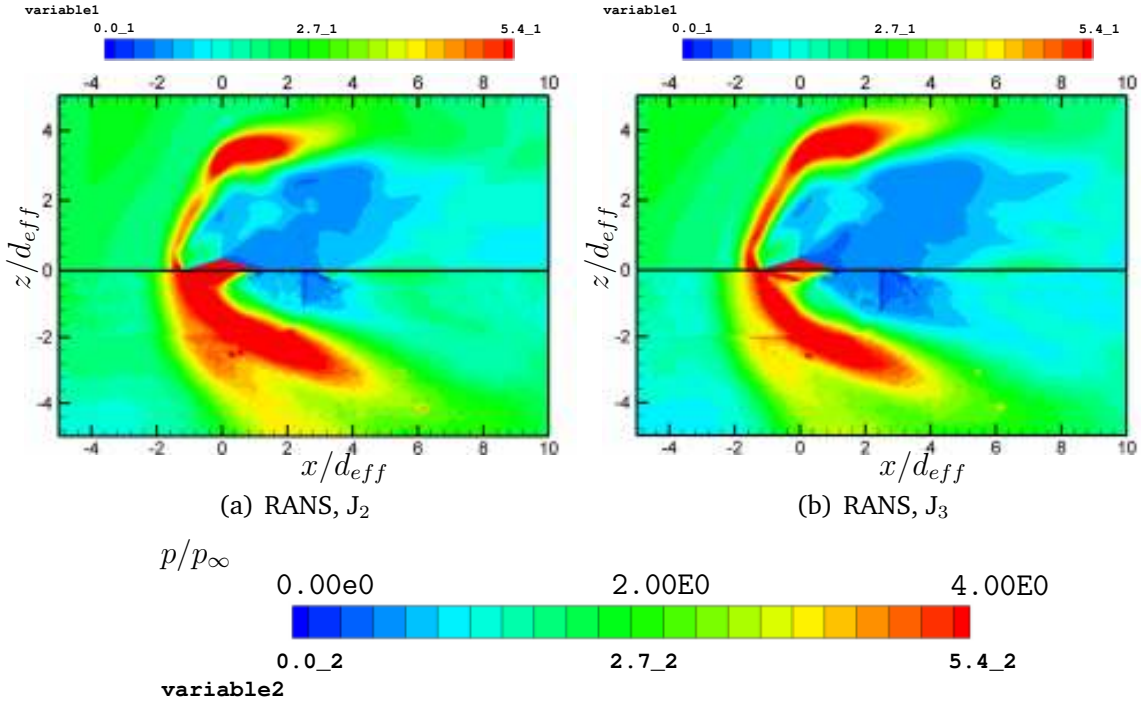

(a) RANS, J_2 (b) RANS, J_3

Fig. 196 Surface pressure comparison of RANS results with experiments for cases J_2 and J_3. The surface pressure is normalized by the freestream static pressure.

APPENDIX C

Diamond Injectors

The change is the key aspects of the mean and turbulent flow structure for the high pressure 90-degree diamond injector cases are presented in this appendix.

The primary flow feature of interest that is modified due to increase in injector total pressure is the barrel shock. The isosurface of entropy representing the barrel shock surface for the two high pressure cases is shown in Figs. 197 and 198. It is observed that the lateral spread of the barrel shock is considerably larger as compared to the low pressure case. The lateral spread leads to the increase in the included angle of the vertical trailing surface. The bounding edges of the vertical trailing surface are closer to the tunnel floor. This leads to change in the boundary layer fluid inflow into the low pressure region downstream of the barrel shock. Consequently, the structure of the LCVP vortex changes as seen in Fig. 199. The structure of the vortex in both these cases is not as organized as the one in the low pressure case. Hence, the vortex structure down stream of the barrel shock has a diminished capacity to act as a gasdynamic flame holding device. The scales used for the contour plots in all the images are identical to the one used for corresponding figures in chapter VI.

The increased lateral spread of the barrel shock is accompanied by an increase in the lateral penetration of the injector fluid. Streamlines from region 1 of the injector orifice are shown in Fig. 200. The extents of the plotted domain are the same as that of the corresponding low pressure plots. It can be seen that the lateral spread of these streamlines is considerably larger as compared to the low pressure case. This could possibly lead to increased entrainment of the freestream fluid. Streamlines from region 2 (see Fig. 201) provide an approximate indication of the

width of the barrel shock trailing surface. Region 3 and 4 streamlines, shown in Fig. 202 show that the axial CVP is much larger as compared to the low pressure case (see Fig. 96). Results for the J_3 (see Figs. 203 - 205) case are similar to the J_2 case.

Turbulent kinetic energy and axial stress plots for the J_2 and J_3 cases are shown in Figs. 206 - 211. Compared to the low pressure case discussed in chapter VI, we observe that the there is an increase in the levels of turbulent kinetic energy in the plume region down stream of the injector. The plots indicate the presence of an energetic wake vortex system that is almost the size of the CVP core in the J_2 case. In the J_3 case the wake vortices are a little further apart but are still high in TKE content. Also, the TKE contours of the plume in the J_3 case has a slightly different structure.

These results show that an increase in the injector total pressure changes some of the salient feature observed in the low pressure case. While some of these changes are not beneficial to the flame holding applications, others such as the increase in TKE will lead to enhanced mixing properties in the flow field.

Hybrid Injectors

As described earlier in chapter VI, the shape of the barrel shock in the 90-degree injection simulation at momentum ratio J_1 resulted in the formation of the LCVP. In the low pressure angled injection cases of 45-degrees and 27.5-degrees, we observed an enhanced leading edge mixing vortex. A preliminary optimized injector was studied by combining the the geometries of the angled and the normal injectors. The leading edge of the injector was angled at 27.5-degrees and 45-degrees for the two cases, while the trailing edge was maintained at 90-degrees. This re-

sults from these simulations are shown in Figs. 212 and 213. The results indicate that the LCVP structure is still present in these configurations. The leading edge mixing vortex strength is enhanced as compared to the normal injection case. It was also found that the total pressure loss for the hybrid injectors were reduced by about 5 percent as compared to the normal injection.

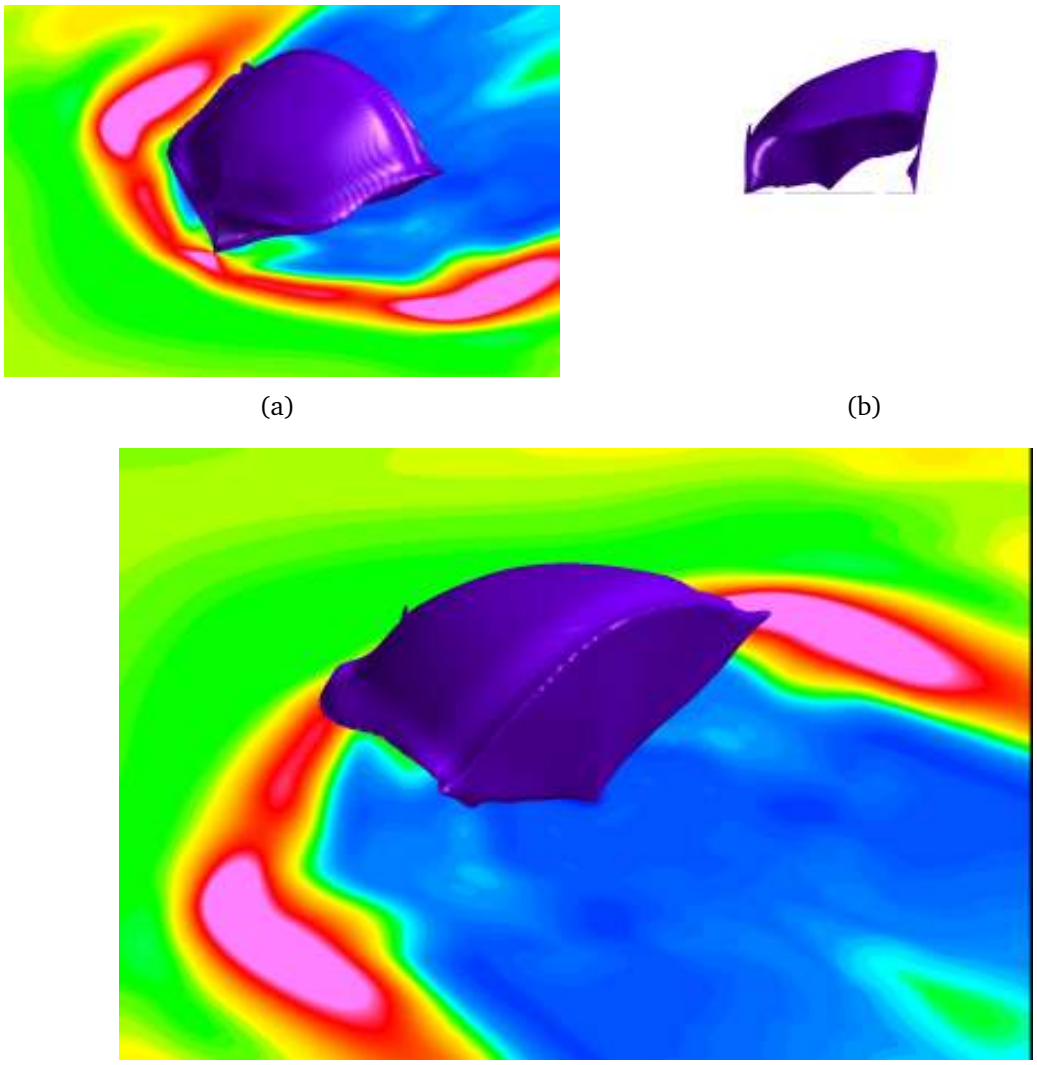

(a) (b)

(c)

Fig. 197 Barrel shock structure for 90-degree J_2 case.

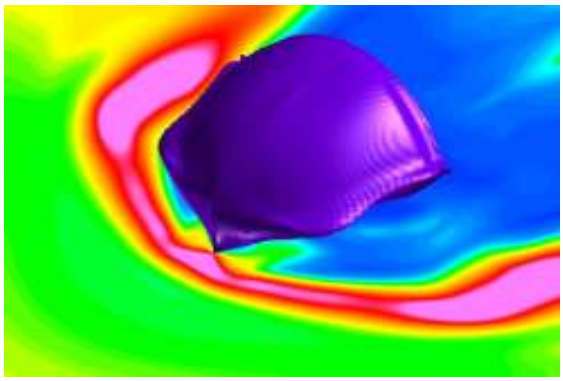

(a)

(b)

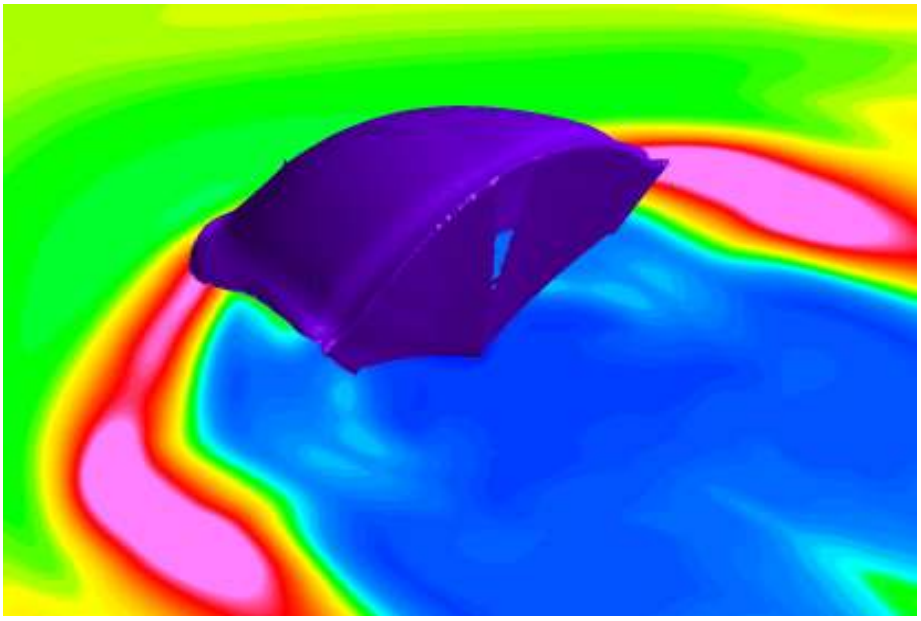

(c)

Fig. 198 Barrel shock structure for 90-degree J_3 case.

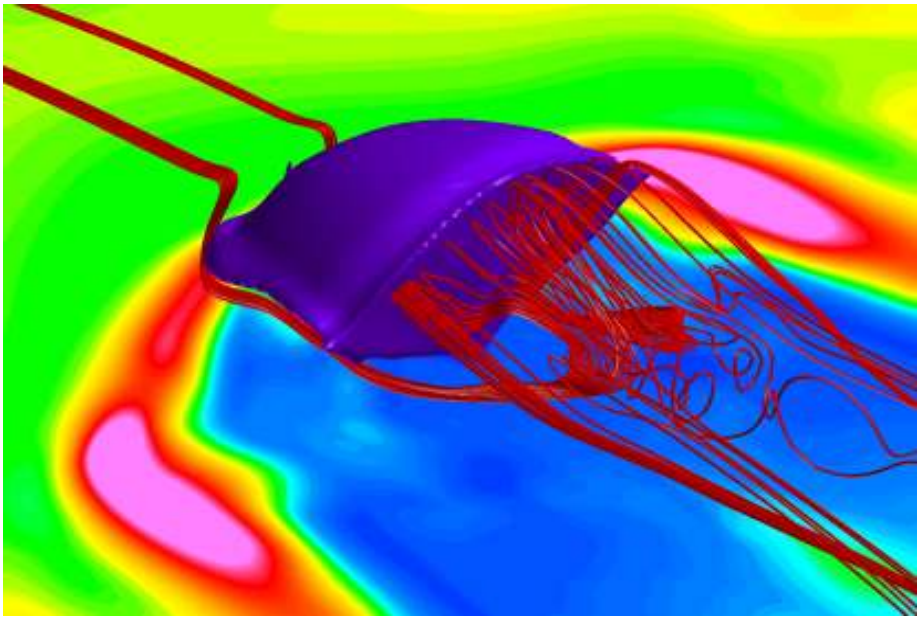

(a)

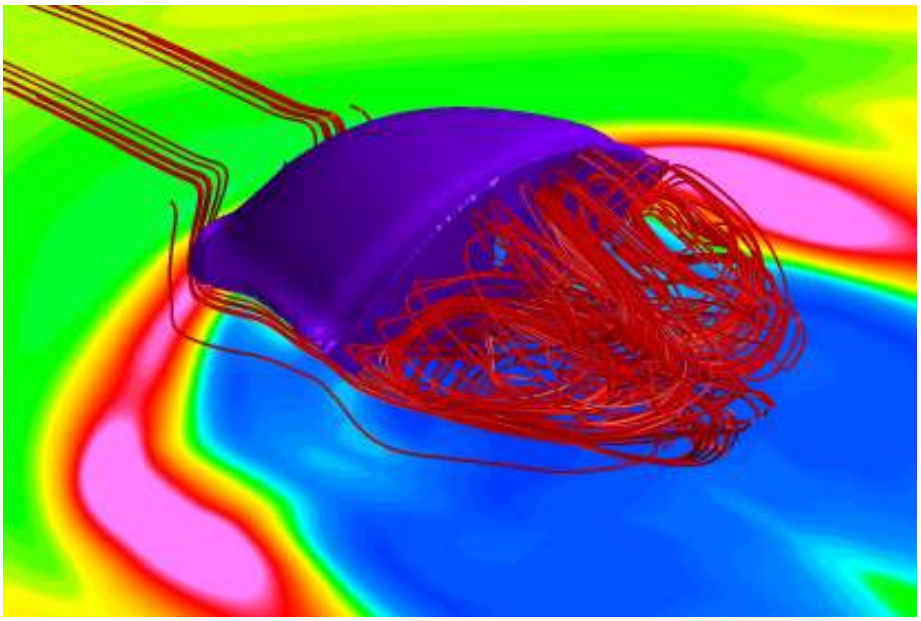

(b)

Fig. 199 Structures downstream of the barrel shock for cases J_2 and J_3.

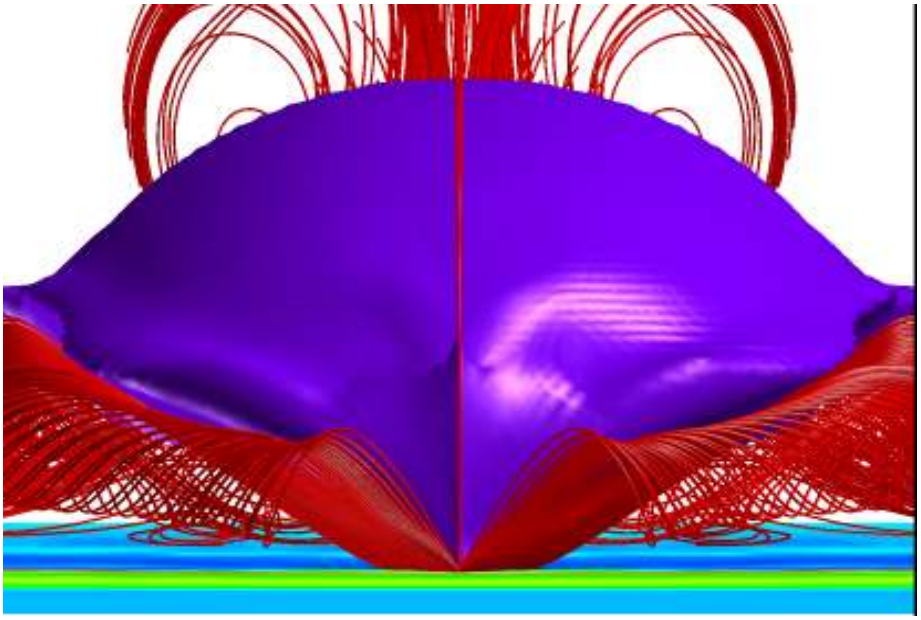

(a)

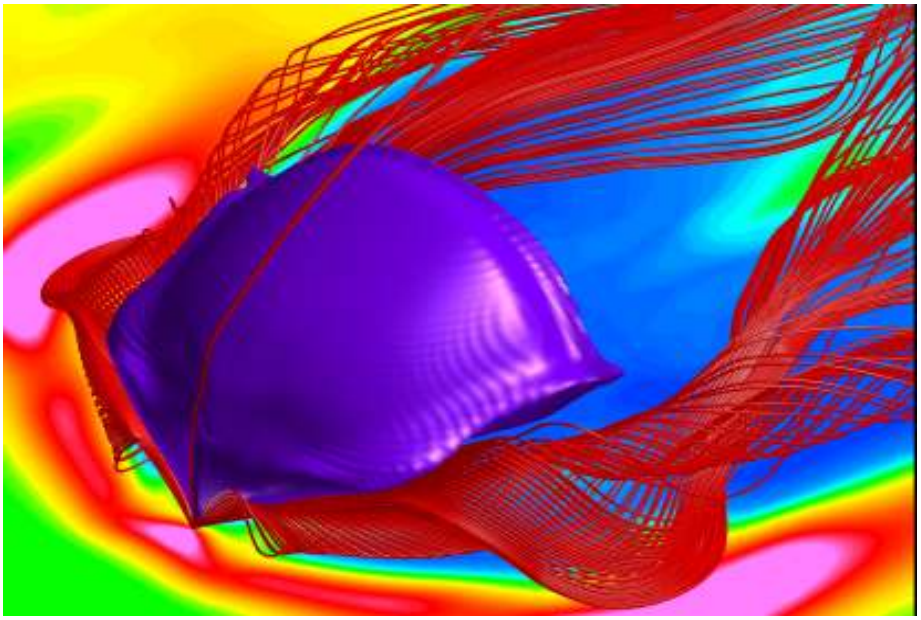

(b)

Fig. 200 Injector streamlines from region 1 for the J_2 case.

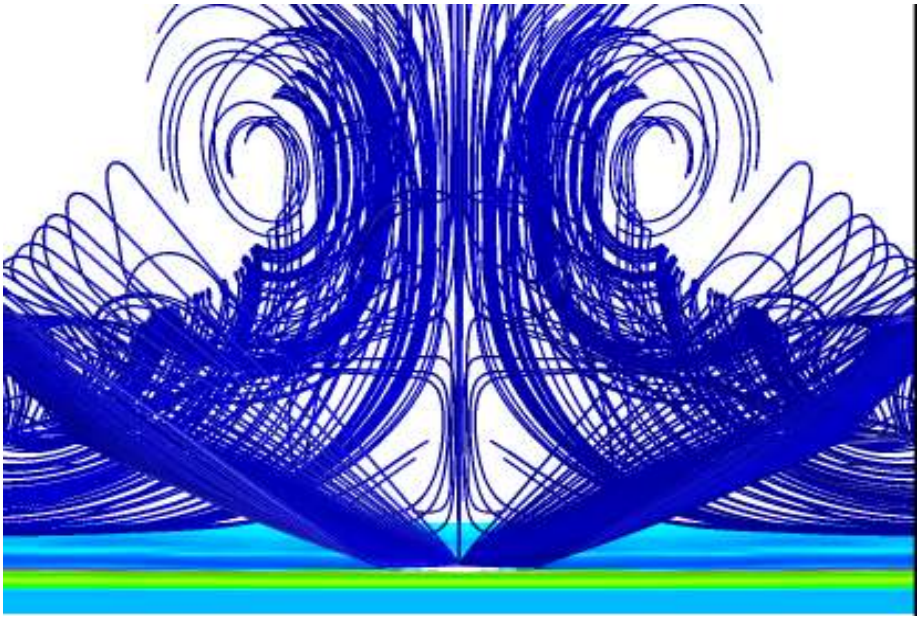

(a)

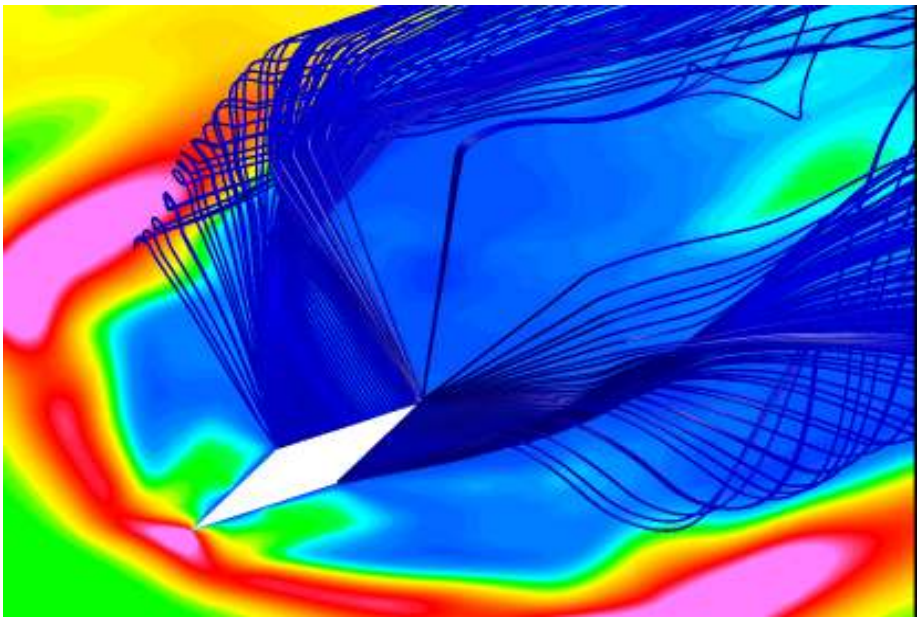

(b)

Fig. 201 Injector streamlines from region 2 for the J_2 case.

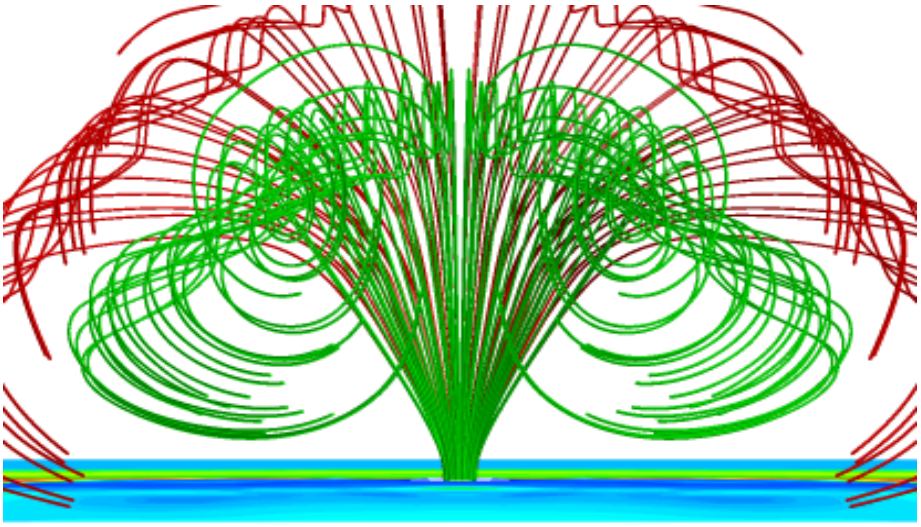

Fig. 202 Injector streamlines from region 5 for the J_2 case.

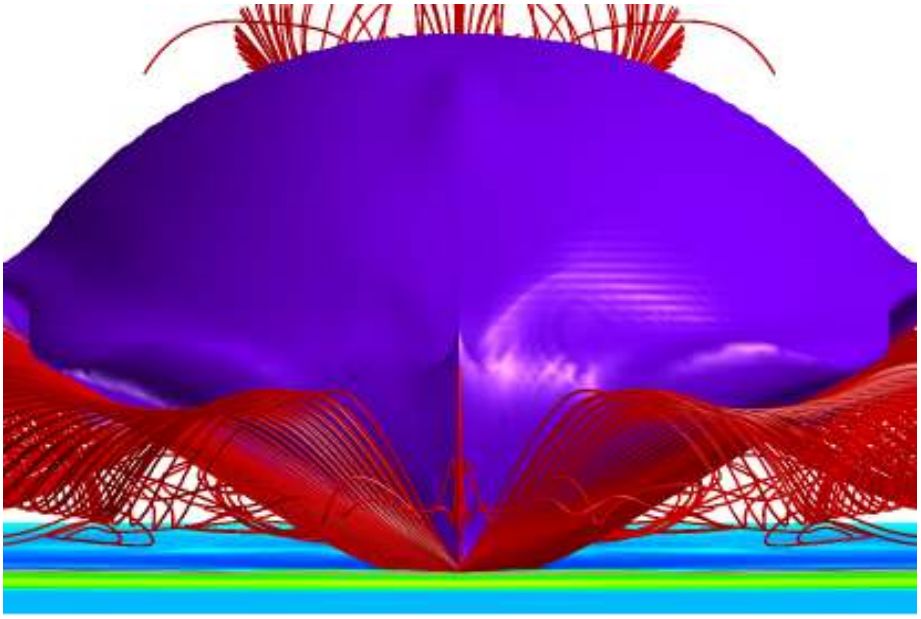

(a)

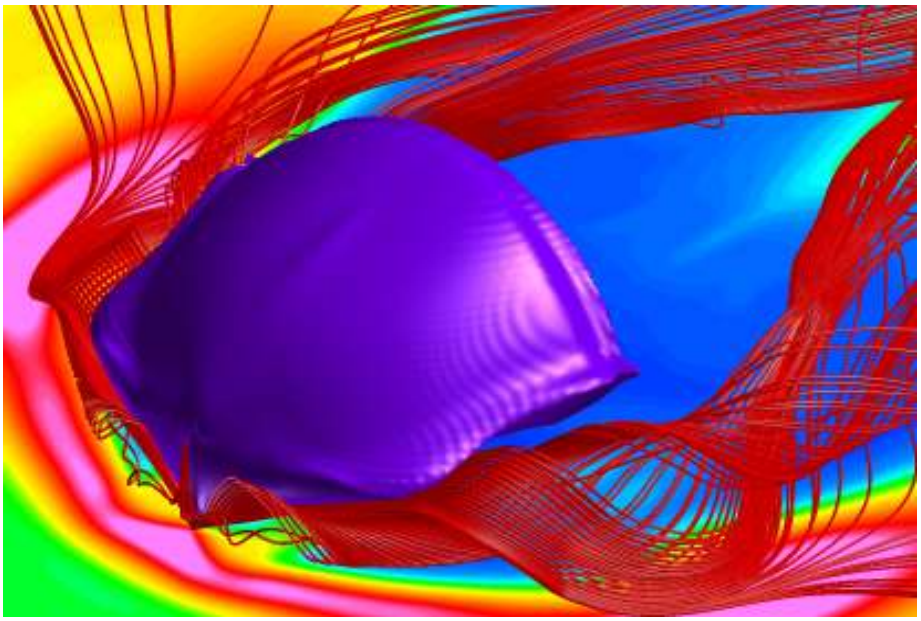

(b)

Fig. 203 Injector streamlines from region 1 for the J_3 case.

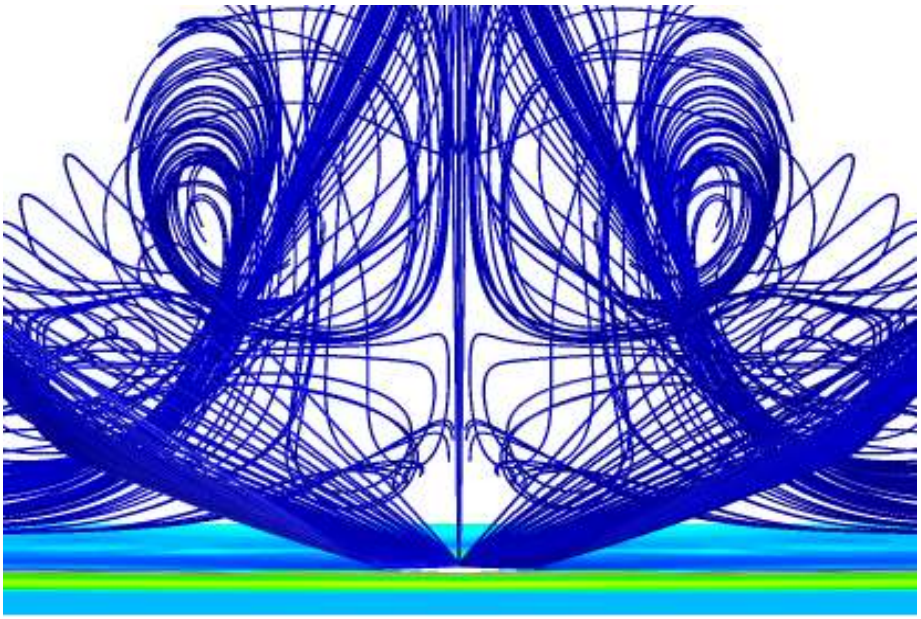

(a)

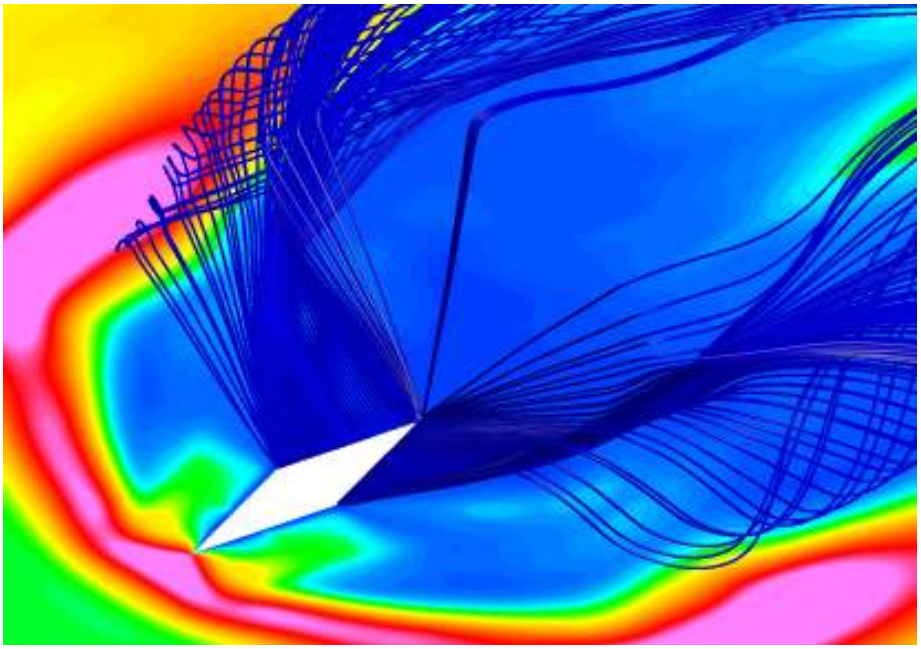

(b)

Fig. 204 Injector streamlines from region 2 for the J_3 case.

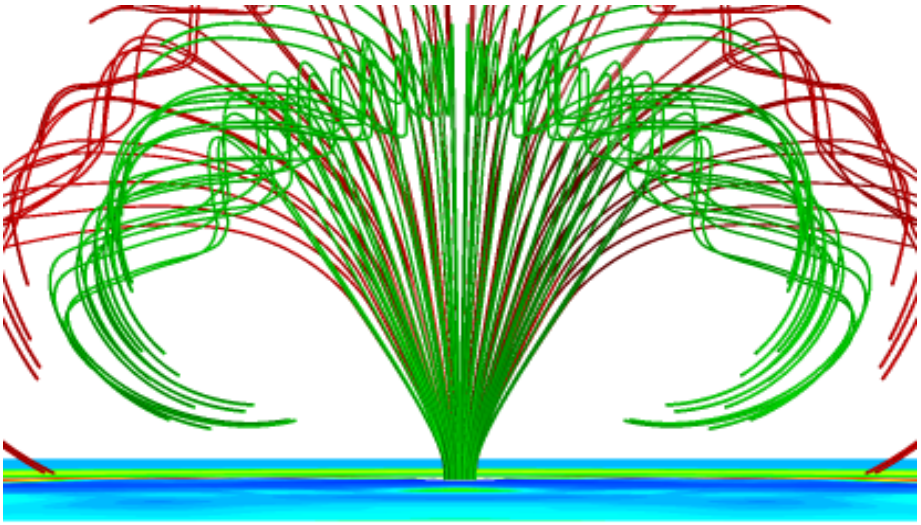

Fig. 205 Injector streamlines from region 5 for the J_3 case.

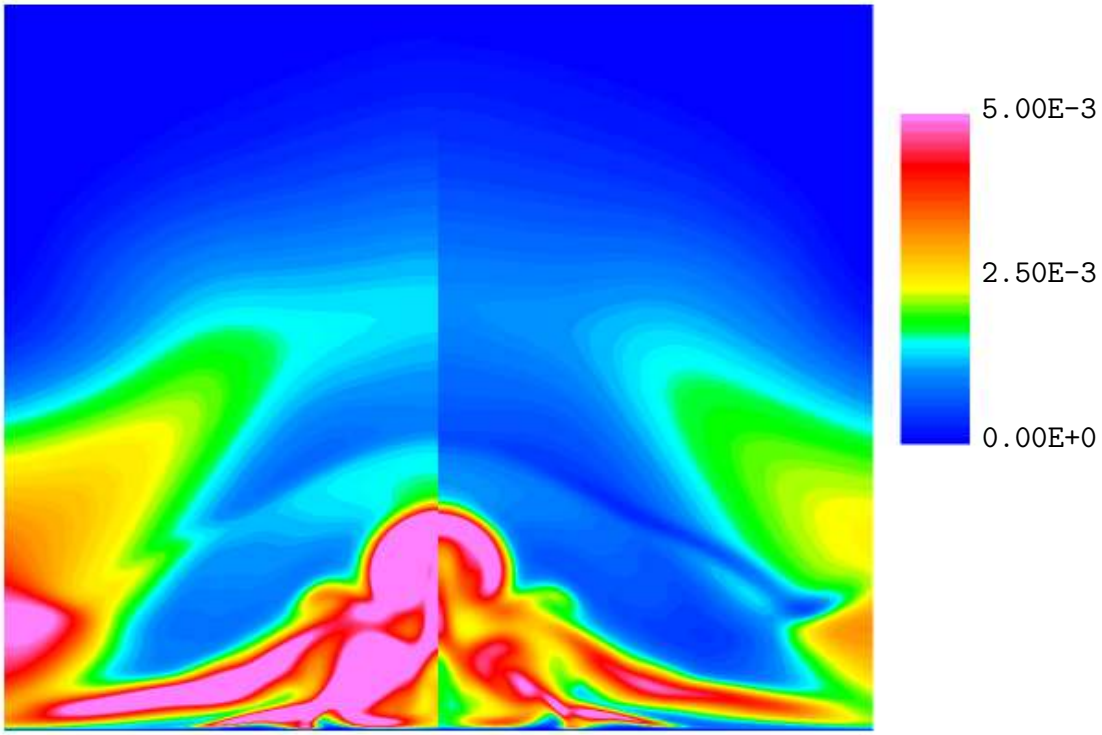

Fig. 206 Contour plot of τ_{11} and TKE at $x/d_{eff} = +8.0$, 90-degree J_2.

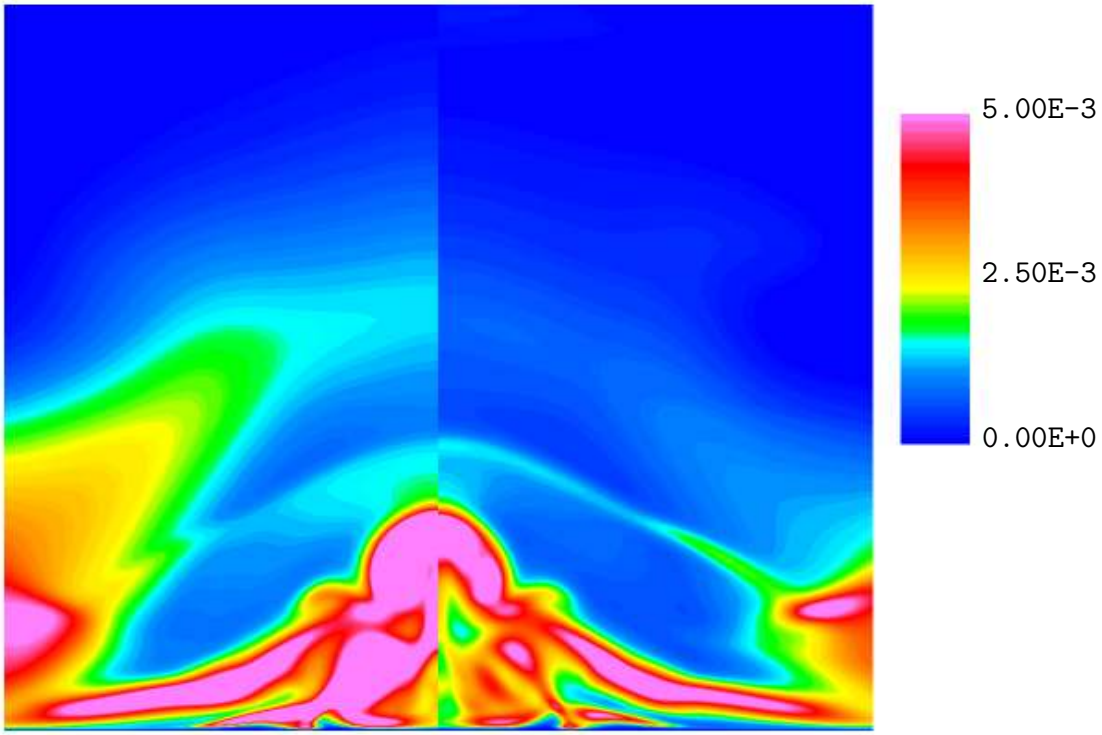

Fig. 207 Contour plot of τ_{22} and TKE at $x/d_{eff} = +8.0$, 90-degree J_2.

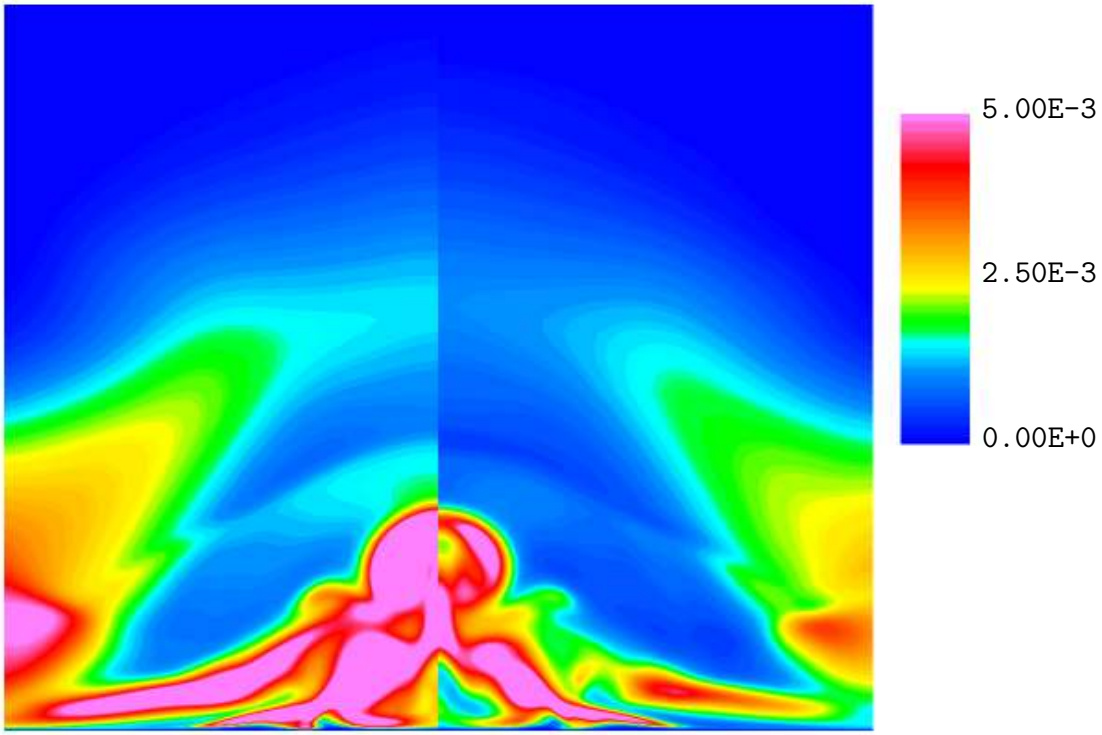

Fig. 208 Contour plot of τ_{33} and TKE at $x/d_{eff} = +8.0$, 90-degree J_2.

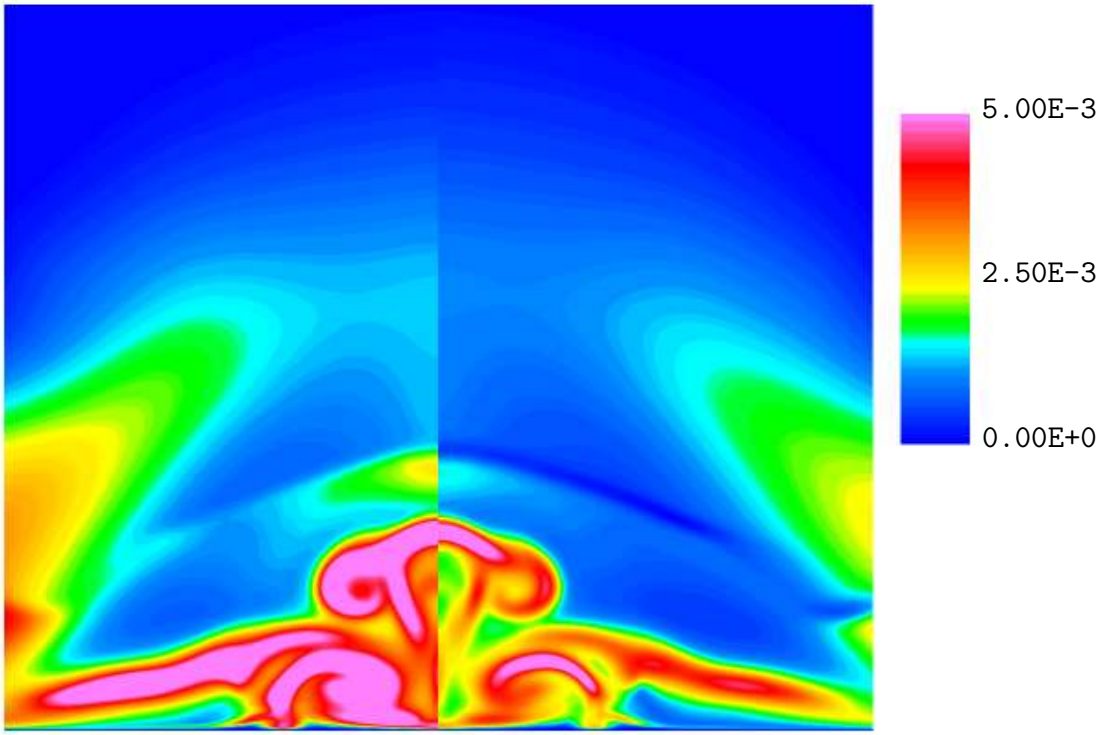

Fig. 209 Contour plot of τ_{11} and TKE at $x/d_{eff} = +8.0$, 90-degree J_3.

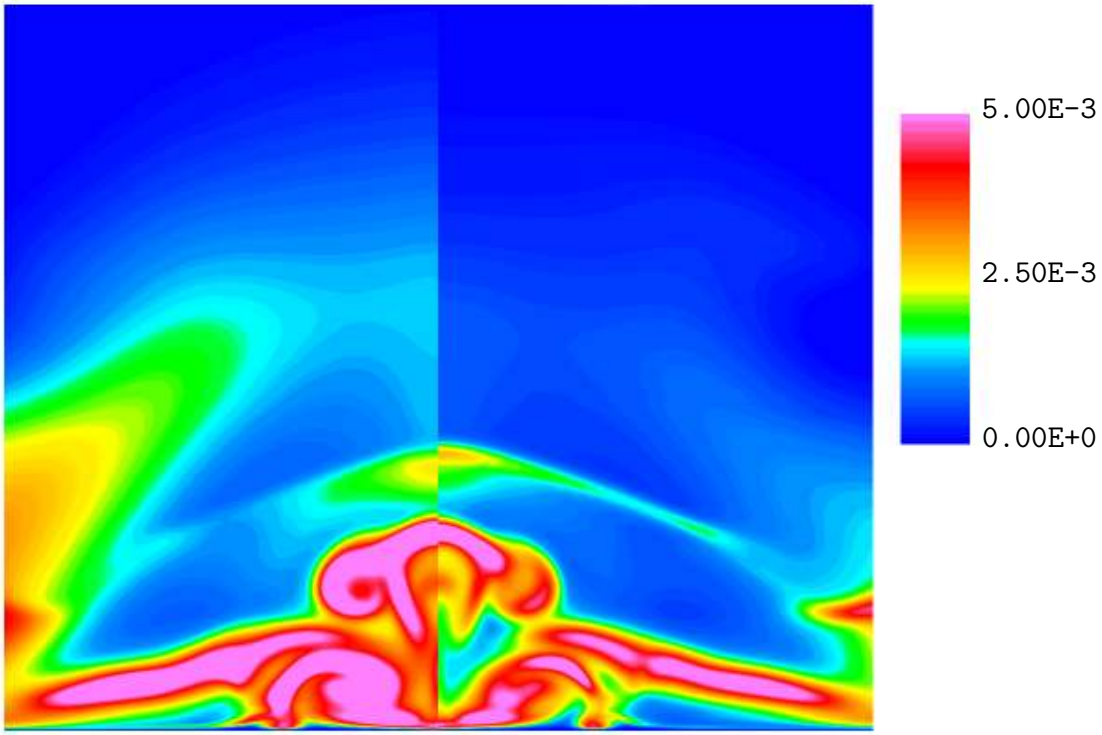

Fig. 210 Contour plot of τ_{22} and TKE at $x/d_{eff} = +8.0$, 90-degree J$_3$.

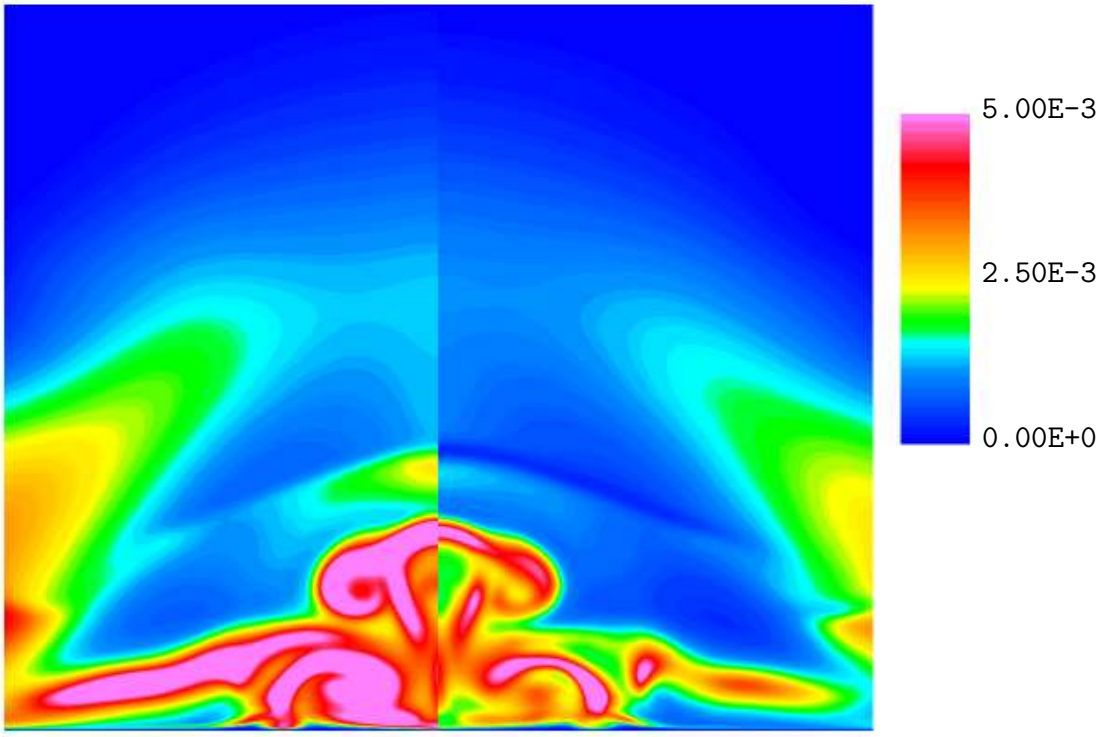

Fig. 211 Contour plot of τ_{33} and TKE at $x/d_{eff} = +8.0$, 90-degree J$_3$.

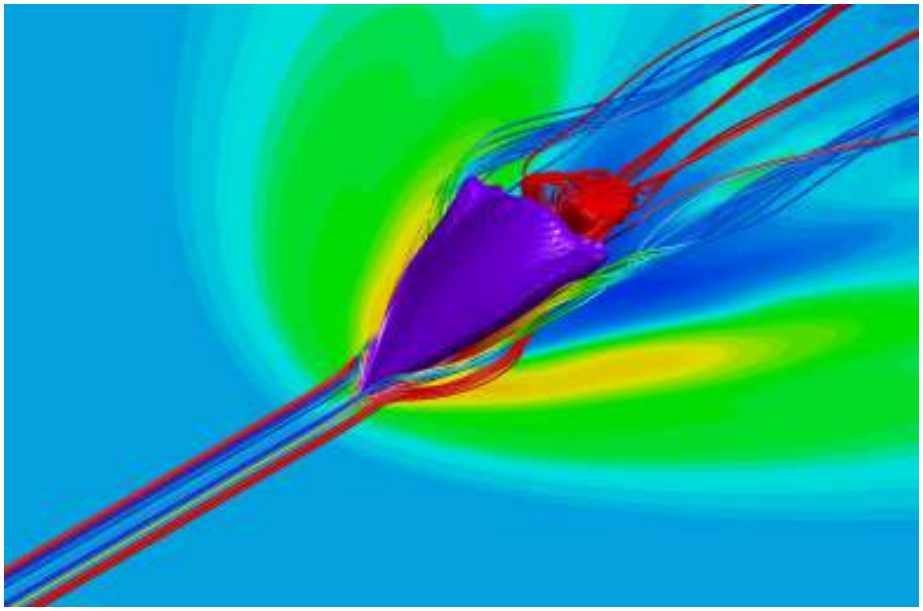

(a)

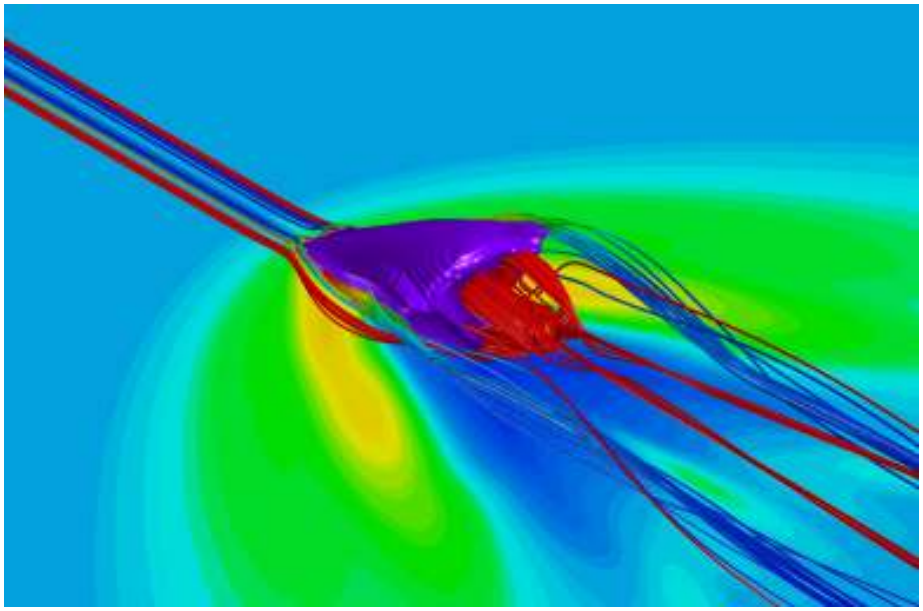

(b)

Fig. 212 LCVP and leading edge mixing in the 27.5-degree hybrid injector case.

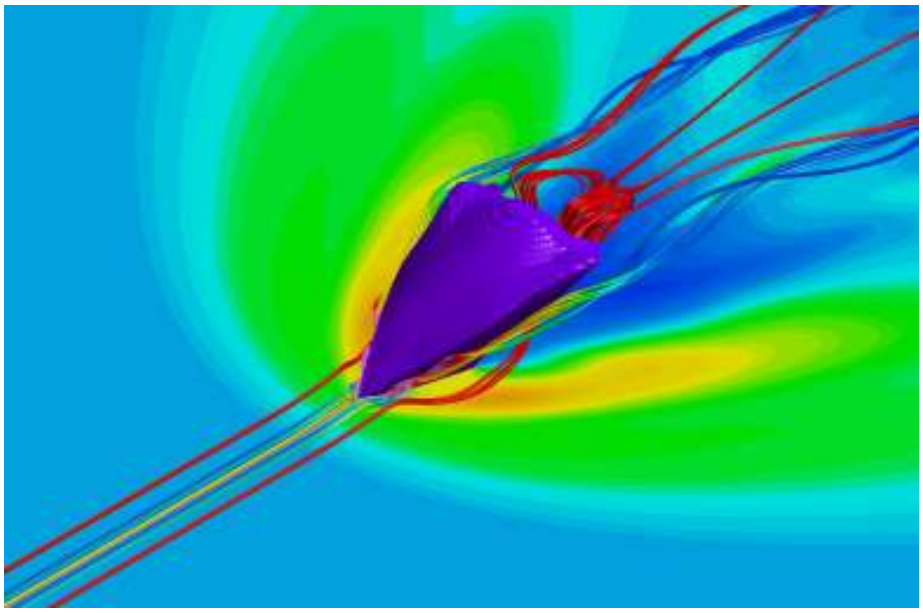

(a)

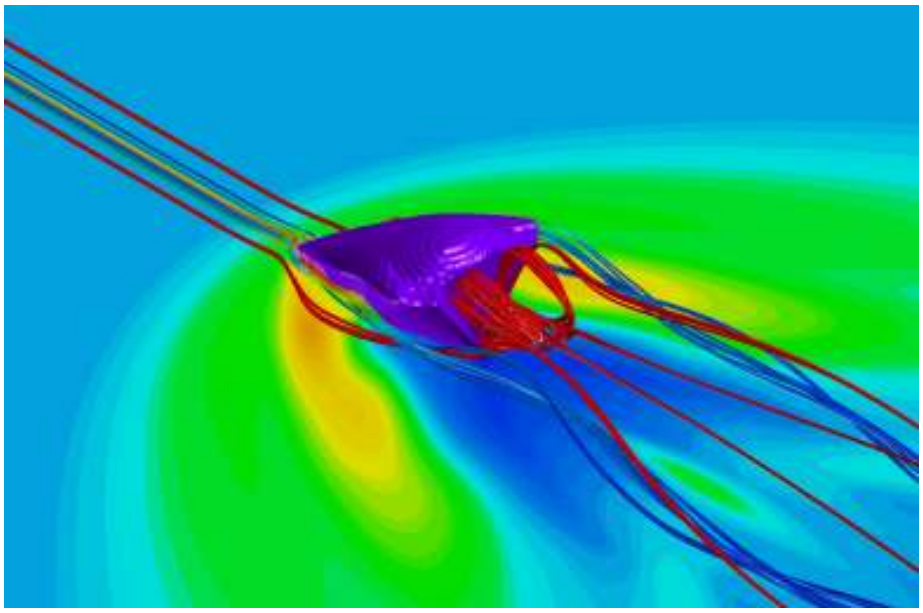

(b)

Fig. 213 LCVP and leading edge mixing in the 45-degree hybrid injector case.

VITA

Name:	Ravichandra Srinivasan
Address:	Department of Aerospace Engineering, Texas A&M Univerisity, MS 3141, College Station, TX 77843
Email Address:	rsrinivasan@tamu.edu
Education:	B.E., Mechanical Engineering, Bangalore University. M.S., Mechanical Engineering, The University of Alabama. Ph.D., Aerospace Engineering, Texas A&M University.